On the Limits of Precision Glass Molding for Diffractive Optical Elements

THÈSE N^{O} 8033 (2017)

PRÉSENTÉE LE 20 OCTOBRE 2017
À LA FACULTÉ DES SCIENCES ET TECHNIQUES DE L'INGÉNIEUR
LABORATOIRE D'OPTIQUE APPLIQUÉE
PROGRAMME DOCTORAL EN PHOTONIQUE

ÉCOLE POLYTECHNIQUE FÉDÉRALE DE LAUSANNE

POUR L'OBTENTION DU GRADE DE DOCTEUR ÈS SCIENCES

PAR

Karin PRATER

acceptée sur proposition du jury:

Prof. L. Thévenaz, président du jury
Prof. H. P. Herzig, Dr T. Scharf, directeurs de thèse
Prof. M. Roussey, rapporteur
Dr A. Hermerschmidt , rapporteur
Prof. P. Hoffmann, rapporteur

ÉCOLE POLYTECHNIQUE
FÉDÉRALE DE LAUSANNE

Suisse
2017

Abstract

Diffractive optical elements (DOEs) consist of surface reliefs with dimensions in the micrometer range and nanometer precision. Two technologies dominate: Elements replicated in plastic and directly microfabricated elements in fused silica. Plastic DOEs are mostly used in mass production because they can be fabricated very cost-efficient by replication technologies such as plastic injection molding and hot embossing. Glass DOEs are only used when its superior characteristics e.g. higher temperature stability, higher form accuracy due to a low reaction to humidity and stress are necessary for the specific application. Today, glass DOEs are fabricated by cleanroom technology based on direct structuring of fused silica. In this thesis, we investigate the possibility to use precision glass molding to fabricate glass DOEs. Up to now, precision glass molding is used only for continuous surfaces like in aspherical lenses or freeform elements. Diffractive optical elements with more complex structures including surface discontinuities (steps) are not found. One reason is the lack of a suitable mold material that can withstand the high molding temperatures and can be microstructured with the necessary accuracy.

One potential candidate to close this technology gap is glassy carbon. Glassy carbon is a fullerene-like carbon with extreme temperature resistance and unmatched chemical inertness. The key factor of applying glassy carbon is the possibility to structure its surface with the suitable dimensions and conformity. We tested and developed microstructuring processes to overcome limitations such as process compatibility, etch selectivity, structural integrity, and surface roughness.

Our major objective of this work aimed to investigate the limits of precision glass molding for DOEs. Of special interest are the minimal feature size and maximal aspect ratio that can be obtained by keeping the optical quality of surfaces. We showed that precision glass can replicate features down to 800 nm and the process is stable. With this newly established processes, the whole fabrication chain could be tested for the first time including lifetime tests of the stamp. For each step, extensive characterization was done. Measuring the optical performance was the last step that allowed us to develop a complete guideline for the fabrication of diffractive optics with precision glass molding. Beamsplitting elements were chosen as test designs, because they allow a rigorous evaluation of the optical performance by measuring the diffraction efficiencies and uniformity distribution.

As the main results, we could show that precision glass molding of DOEs can reach a comparable optical performance as directly etched fused silica DOEs, which is the state-of-the-art technology. We could confirm that glassy carbon is an excellent mold material for precision glass molding of complex optical surfaces.

Keywords: Diffractive optical element, glassy carbon, reactive ion etching, multilevel fabrication, electron-beam lithography, precision glass molding, fused silica molding, RCWA simulations.

Zusammenfassung

Diffraktive optische Elemente (DOE) bestehen aus Oberflächereliefs mit Dimensionen im Mikrometer Bereich und Nanometerpräzision. Zwei Technologien dominieren: Elemente repliziert in Kunststoff und direkt mikrostrukturierte Elemente in Quarzglas. Kunststoff DOE sind bevorzugt in der Massenproduktion, weil sie sehr kosteneffizient gefertigt werden können auf Grund von Replikationstechnologien wie dem Kunststoff-Spritzguss und dem Heißprägen. Glas wird nur verwendet, wenn seine überlegenen Eigenschaften wie z. B. höhere Temperaturstabilität, höhere Formgenauigkeit durch eine geringe Reaktion auf Feuchtigkeit und Stress für die jeweilige Anwendung notwendig sind. Derzeit besteht die Herstellung von Glass DOE auf der direkten Strukturierung von Quarzglas, was auf der Reinraumtechnologie basiert. In dieser Arbeit untersuchen wir die Möglichkeiten Glass DOEs mit Hilfe von Präzisionsblankpressen zu fertigen. Bislang wird Präzisionsblankpressen nur für kontinuierliche Oberflächen wie asphärischer Linsen oder Freiform-Elemente verwendet. Diffraktive optische Elemente mit komplexeren Strukturen einschließlich Oberflächendiskontinuitäten (Stufen) werden nicht gepresst. Ein Grund dafür ist das Fehlen eines geeigneten Materials für das Presswerkzeug, das den hohen Temperaturen standhalten und mit der nötigen Genauigkeit mikrostrukturiert werden kann.

Ein potenzieller Kandidat diese technologische Lücke zu schließen ist Glassy Carbon. Glassy Carbon ist ein Fulleren ähnlicher Kohlenstoff mit extremer Temperaturbeständigkeit und unübertroffene chemische Inertheit. Der entscheidende Faktor zur Anwendbarkeit von Glassy Carbon besteht in der Notwendigkeit seine Oberfläche mit den geeigneten Abmessungen und Konformität zu strukturieren. Wir haben Mikrostrukturierungsprozesse getestet und entwickelt um die bestehenden Grenzen bezüglich Prozess-Kompatibilität, Ätzselektivität, struktureller Vollständigkeit und Oberflächenrauheit zu überwinden.

Das wesentliche Ziel dieser Arbeit ist die Untersuchung der Grenzen des Präzisionsblankpressens für DOE. Von besonderem Interesse sind die minimale Strukturgröße und das maximale Aspekt Verhältnis, die erreicht werden können bei gleichzeitiger Erhaltung der optischen Qualität der Oberfläche. Wir zeigten, dass mit Präzisionplankpressen Strukturgrössen von 800 nm replizieren werden können und dass der Prozess stabil ist. Mit den neu entwickelten Prozessen konnten wir erstmalig die Prozesskette als Ganzes betrachten. Darin sind vielversprechende Lebensdauertests der Prozesswerkzeuge inbe-

griffen. Für jeden Schritt erfolgte eine umfassende Charakterisierung.
Im letzten Schritt wurden Messungen der optischen Leistungen durchgeführt und mit Simulationen verglichen. Diese vollständige Analyse erlaubte uns komplette Leitlinien für die Herstellung von diffraktiven Optiken mit Hilfe von Präzisionsblankpressens zu entwickeln. Strahlteiler Elemente wurden als Test-Designs ausgewählt, weil sie eine rigorose Bewertung der optischen Leistung auf Grund der gemessenen Beugungseffizienzen und der Uniformitätsverteilung erlauben.
Als wichtigste Ergebnisse konnten wir zeigen, dass Präzisionsblankpressens eine ähnliche optische Leistung erreichen kann wie direkt geätzten Quarzglassoptiken, die dem Stand der Technik entsprechen. Wir konnten bestätigen, dass Glassy Carbon eine ausgezeichnete Wahl als Stempelmaterial für Präzisionsblankpressens von komplexen optischen Oberflächen ist.

Stichwörter: Diffraktive optische Elemente, Glassy Carbon, reaktives Ionenätzen, Multiniveau Fabrication, Electron-Strahl Lithographie, Präzisionsblankpressen, Quarzglass Pressen, RCWA Simulationen.

Contents

1 Introduction

Diffractive optical elements (DOEs) are used in a wide variety of applications. They usually have a microrelief surface (continuous or binary) with features ranging from submicrometer to millimeter dimensions laterally and vertical dimensions of a few hundred nanometer. The design freedom is much higher than for refractive optical elements. Some optical functionalities are only possible with diffractive optics and multiple operations such as beamshaping and focusing can be integrated into one single element [Kress2009, Herzig1997, Gale2002]. This leads to a more compact optical arrangement and allows miniaturization of optical systems. The main market is illumination and beam shaping.

Plastic DOEs are preferred, because of their low cost. However, glass has some very strong advantages over plastic: the high-temperature stability allows an unmatched form stability over a large temperature range; the high range of operation temperature and low reaction to humidity is especially advantageous for high power light throughput and for outdoor applications. But due to their high costs, glass DOEs are only used, when the application requires the superior characteristics.

High power light throughput is given for diffusers for illumination high power LED systems or for manufacturing applications, where laser beamshaping, homogenization, and focusing are used for laser surface treatment, cutting and welding. Beamplitting allows parallel processing. Specific beam shaping can be realized for e.g. logo engraving. Beam shaping can also be used for direct laser writing of photoresist and direct laser ablation to optimize the spot shape. DOEs allow amplitude mode selection of high-power laser systems to improve the quality of the focal spot. Beam samplers can provide a small percentage of the laser light to monitor the laser power. Biomedical applications like laser skin treatment and surgical laser treatment for cutting and suturing are also common applications. The low reaction to humidity and stress allows to use glass DOEs in endoscopic systems for 3D imaging. The DOEs generate diffractive projected patterns that are used for calculating 3D information. A large demand exists for 3D imaging in the automotive and factory automation with infrared light, where the transmission of plastic decreases remarkably [Kress2009].

The reason why plastic DOEs are much cheaper than glass DOES is the availability of different replication processes such as plastic injection molding, hot embossing, and soft lithography. The cost decreases especially for very large scale mass production [Hansen2011, Gale2005]. Specific molds (Ni-plated steel) are easily machined by diamond turning or by electroforming of Si masters fabricated by cleanroom technology. Whereas glass binary DOEs are directly fabricated into fused silica by cleanroom technologies such as photolithography and plasma etching, which cause much higher costs and require operational demanding equipment [Kress2009, Herzig1997]. Continuous surface reliefs for e.g. micro-Fresnel lenses can be fabricated by direct diamond turning or laser ablation. A molding technique for glass seems therefore interesting to decrease production costs of high performance DOEs with superior characteristics.

For replication of glass precision glass molding has been developed [Wolz2015] [Mertus2012, Klocke2012]. The glass is heated to a temperature higher than the glass transition temperature and the surface relieve is imprinted into the glass under isothermal conditions. The industrial use of precision glass molding for optical elements has been so fare limited to macroscopic optical surfaces such as aspherical lenses and freeform elements. Typically, tungsten carbide is used as a mold material. It is structured by precision diamond grinding. Since glass is very reactive in the molding temperature range, tungsten carbide needs to be coated with an anti-adhesion coating e.g. Pt-Ir.

A number of challenges need to be addressed, when going to precision glass molding of diffractive optical elements: the choice of the mold material is important due to the much harsher environment of glass molding in comparison to plastic replication and secondly a microstructuring technology for this mold material needs to be available with the necessary feature size and quality on a large scale. We believe that the lack of a suitable mold material, which can fulfill these requirements, is the main reason why precision glass molding for microrelief surfaces has not been established yet in industry. The molding temperatures are very high. Depending on the glass, temperatures are ca. 400 to 800 °C for low glass transition materials and can reach 1400 °C for fused silica. The glass is much more viscose than plastic during the imprinting process, therefore the mold material needs to be hard enough in order to prevent mold deformations and to reach a reasonable long mold lifetime. An anti-adhesive surface is preferred. Coatings can be applied, but include a longer and more expensive fabrication process. Also, a high stress at the interface of coating and mold appears for each temperature cycle and will eventually cause a failure of the mold coating. Additionally, coating thickness range typically at 300 nm, which will limit the resolution fof diffractive optical elements.

Tungsten carbide can be operated at high temperatures, but is limited in possible feature size due to the used diamond turning for its structuring [Mertus2012]. Nickel is limited to temperatures below 400 °C, at which a phase transition appears. In what concerns microstructuring Silicon (Si) is a preferred material, because of the large amount of available cleanroom processes. However, Si is too brittle to withstand many molding cycles [Kang2004]. Fused silica can be operated for high enough temperatures and microfabrication process with the necessary quality are easily available. Fused silica has

been successfully used for selected applications low transition temperature glasses in precision glass molding, when an anti-adhesion coating was used. Only a very limited amount of materials are chemically inert enough to be used directly. Diamond fulfills this requirement. However, focused ion beam etching of chemical vapor deposited diamond is too slow on large areas [Komori2008]. The microcrystalline structure of diamond coating limits the use of etching techniques.
One very interesting material already used for precision glass molding for replication of conventional lenses is Glassy carbon (GC). Glassy carbon shows many advantages: operation temperature range up to 2000 °C, high hardness, form stability and a low chemical reactivity, which makes coatings unnecessary [6]. However, only a few manufacturers are able to deliver high-quality GC wafers. The microstructuring technologies for glassy carbon are not well explored and seem very limited. Glassy carbon etching with a surface roughness Ra below 20 nm was only recently accomplished by Youn et al. [Youn2009]. Structures with submicrometer features were replicated in Pyrex glass (not an optical glass), aluminum and borosilicate glass. However, diffractive optical elements were not included in research papers. Precision glass molding of DOEs was demonstrated with GC molds elsewhere [Chen2008, Mori2008], but the surface roughness was too high (more than 20 nm).

We believe that glassy carbon has a high potential to fill the gap as a mold material for diffractive optical elements. Our objective is to investigate this potential and to find the limits arriving for precision glass molding for surface relieve features in the submicrometer range. Precision glass molding of diffractive optical elements could allow a strong decrease of the cost compared to direct fabricated elements [Gale2002], which could allow glass diffractive optical elements to enter into existing application fields or to promote new applications, which would otherwise be too expensive to enter the market for instance in the automotive industry.

1.1 Outline of the Thesis

The process chain of the fabrication of diffraction optical elements with precision glass molding is illustrated in Fig. 1.1. For the first time, the entire process chain was taken into consideration. The results obtained from the mold fabrication and precision glass molding can help to optimize the design. Also, requirements specified by the design were determined for precision glass molding.

First, **Chapter 2** will discuss the design of diffractive optical elements in general. The simulation tools are explained, which will later be used to compare the different fabrication constraints. It is important to use different kinds of test elements to analyze the potential of our approach. This includes the limits of the smallest feature size (critical

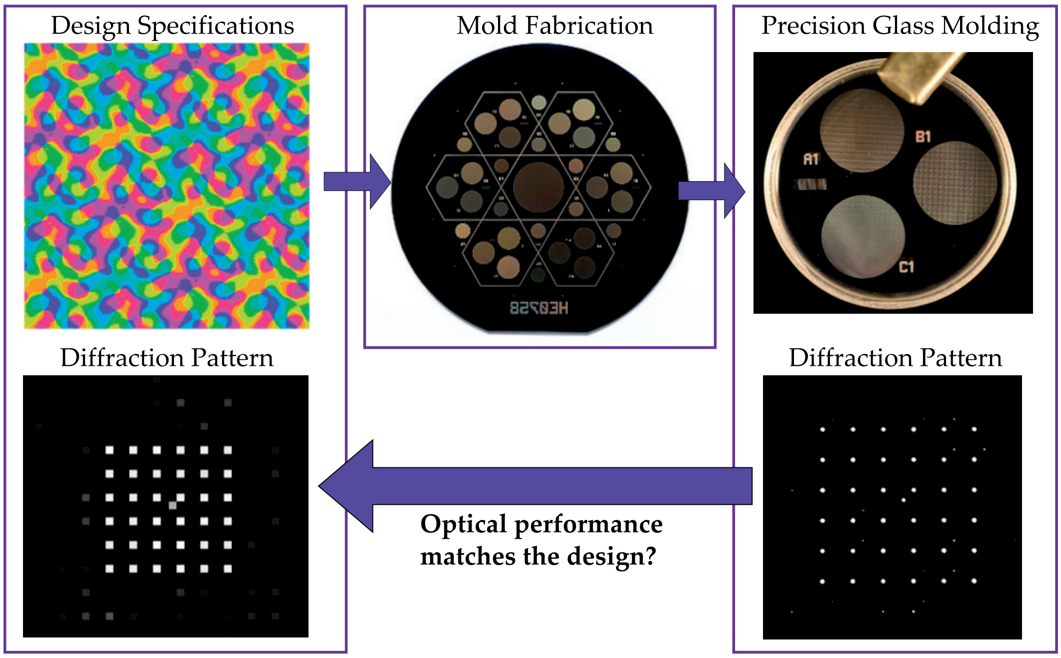

Figure 1.1: Process chain of the fabrication of diffraction optical elements with precision glass molding. Simulations are the key tool to link the individual steps with the final optical performance.

dimension), which can, on the one hand, be structured on the glassy carbon mold and on the other hand be replicated. We use fan-out elements as test designs, since their quality of optical performance can be easily interpreted. The diffraction efficiency is a key parameter and can be easily distinguished from stray light and the 0^{th} order efficiency. The light distribution of the individual beam spots is important for applications such as parallel laser processing. A uniform light distribution is characteristic for the fabrication quality and therefore used as an additional test parameter. Multilevel binary DOEs allow higher efficiency and non-centrosymmetric light patterns. They are thus preferred for many applications, but are limited due to much higher fabrication costs. Multilevel binary DOEs would benefit strongly from a replication approach, where the high cost of one master is distributed over many replications. We therefore extend our test designs by different multilevel binary elements.

In **Chapter 3** we describe the investigated microfabrication processes for glassy carbon molds. The objectives for the glassy carbon microfabrication are driven by the need to expand the available processes. The process of Youn et al. showed the necessary etch quality [Youn2009], but show process limitation (Au is not allowed in cleanroom facilities, where semiconductor devices are fabricated). First, different hard mask material for the plasma etching of glassy carbon were tested. We found silicon hard masks a very good choice. An optimization of the plasma etching condition resulted in an excellent selectivity GC to Si of 19:1. This allowed us to fabricate microstructured molds with feature sizes down to 200 nm by using electron-beam lithography. The main novelty of the GC microfabrication consists of the investigations for continuous surface relief structuring with e.g. multilevel elements.

Chapter 4 deals with the precision glass molding. In contrast to previous work, we mold glass on large areas (diameter 18 mm) and investigate limitation effects especially for microstructures on flat surfaces. A low transition temperature glass and fused silica were molded.
The glass can shrink significantly, when cooled down from the molding temperature to room temperature. It is thus preferred to use a glass with a low coefficient of thermal expansion. The introduced form errors for aspherical lenses are compensated by adapting the mold surface [Klocke2012]. To the best of our knowledge effects introduced by thermal shrinkage for glass microstructures have not been reported. This is especially important for small features with high aspect-ratios on large areas. The quality of the molding is investigated by scanning electron microscope images of the mold surface and the corresponding glass replication. The influence of the molding parameters such as temperature, pressure and time need to be analyzed by investigating the filling of the microstructures. The viscosity plays a major role, because it determines the formability of the glass. The mold lifetime needs to be high and molding parameters that favor long mold lifetimes are preferred.
In addition to glassy carbon, we test fused silica as a mold material, where a coating is necessary for easy glass mold release. For precision glass molding of microrelief surfaces the importance of coating layers has so far not been discussed. We found that coatings will limit the lifetime of the mold significantly and should be avoided. They are however acceptable for macroscopic surfaces.
The main objectives for precision glass molding are to find the minimal feature size and maximum aspect-ratio that can be replicated with high accuracy. A high-performance DOE with a minimum feature size of 800 nm could be molded and we obtained state of the art optical quality.

Thereafter, in **Chapter 5** we will present the results we obtained for the optical performance of the molded diffractive optical elements. Simulations will help to interpret our results and to analyze especially the limitations of precision glass molding.
The most important criteria are the optical performance tests. The test of the diffraction efficiency, 0^{th} order efficiency and uniformity errors of the different beamsplitting elements need to be measured and compared to state-of-the-art technology. Since multiple fabrication steps are involved, it is not possible to tell easily which part of the process chain and therefore which tolerance parameters determine the final optical performance. As a novelty, simulations of molded glass profiles were included into the simulations and gave valuable information on the limitations of precision glass molding.
The main question of this work is the influence of the molding on the performance of the

DOEs. We found that for larger feature sizes (> 2 µm) the molding plays a minor role and the performance is determined by the mold structuring. This included the testing of multilevel DOEs, which have not been included in research so far. A significant performance change could be seen for a DOE with a critical dimension of 800 nm. We tested the molding parameters for optimal performance and were thus able to prove for the first time that precision glass molded DOEs with a high performance can reach the same performance as state-of-the-art fabricated DOEs in fused silica.
Lastly, we summarize our findings in **Chapter 6**.

2 Theory of Diffractive Optical Elements

A diffractive optical element (DOE) is an optical element that manipulates light by segmenting and interference of the light coming from the different segments. In case of an amplitude modulation, the light in certain segments is not transmitted and only the light passing through the transparent areas is interfering with each other. Instead of manipulation the amplitude it is also possible to change the phase. The light in the different zones is experiencing a retardation by a modulation of the refractive index or by a variation of the surface height profile. Phase elements are preferred over amplitude elements, because the light throughput is much better for phase elements.

Nowadays diffractive optical elements are penetrating more and more mass markets for end customer products [Kress2009, Herzig1997, **?**]. The shape of a unit cell of the periodic structure dictates the power distribution between the different diffraction orders and thus optical functionality and efficiency. This is illustrated for different situations in Figure 2.1. With a refractive prism, all light is bent by an angle θ. Since the phase of

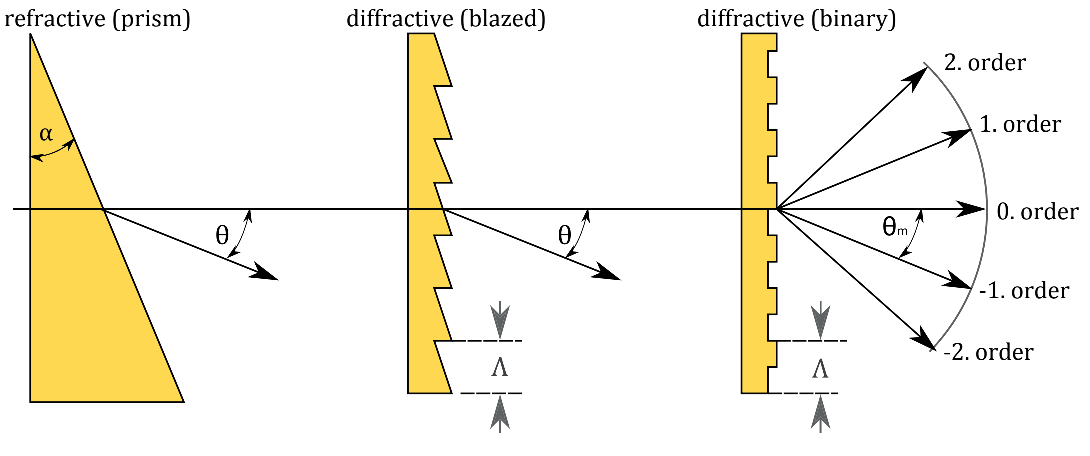

Figure 2.1: Comparison of a refractive, a blazed and a binary component resulting in the same optical functionality. With a refractive prism, all light is bent by an angle θ. For a blazed diffractive element the surface of a prism is wrapped onto the fundamental phase interval 2π. A binary element in its simplest form is translated into 2 discrete levels.

light is periodic by 2π, the same phase modulation of a coherent light source reached for a continuous surface can be achieved by wrapping the surface by onto multiples of the fundamental phase interval 2π. For a blazed diffractive element the surface of a prism is wrapped onto the fundamental phase interval 2π. 100% of the light is directed in the -1^{st} diffraction order. A binary element with the same grating period Λ and depth is given by a discrete number of phase controlling areas. In its simplest form, this is done by 2 discrete levels, where the light is diffracted in 40.5% both in the $+1^{st}$ and -1^{st} order because it shows the same symmetry for both diffraction orders. In order to increase the diffraction efficiency, more levels need to be employed.

Today the markets expects only diffractive optical elements with complex optical functionalities and very high efficiency. Thus, the surface complexity is high. Depending on the application the surface can be binary (two level), multilevel or continuous-relieve (blazed). Combinations of diffractive and refractive surfaces are needed to decrease the size of an optical system and increase its functionality. Optical elements with 2 structures sides are also desired, but the 2 surfaces need to be aligned to each other with high precision.

In practice, the technological manufacturability very often limits the possibilities for applications. The size and shape of the smallest structure define whether a DOE can be realized or not. Therefor specification for the allowed tolerances must be established during the whole manufacturing chain starting with the design, fabrication and finally the optical testing. Simulations are key tools to understand the individual steps since the fabrication influences can be investigated individual, whereas for the fabricated elements all influences will be seen together.

In section 2.1 the Fraunhofer approximation and Rigorous Coupled Wave Analysis (RCWA) are introduced, which are used for the simulation of the fabricated gratings. In section 2.2 the design of diffractive optical elements is discussed. The design of the different test elements, which are used in this work, are described in section 2.2.3.

2.1 Simulation Models

This chapter, which is based on the book of Kress [Kress2009], will focus on two different simulation approaches available to model the light propagation through DOEs. In the center of interest is the simulation of systematic fabrication errors introduced by the various fabrication techniques both in the mold fabrication and the glass molding.

The first section will deal with modeling of DOEs in the scalar diffraction regime. If the DOE contains structures with dimension sizes in the range of the wavelength, more complex models have to be used. A vector electromagnetic model will be described in section 2.1.2. As a rule of thumb, the scalar approach can be used for blazed DOEs with the smallest period Λ to wavelength λ ratio of

$$5 \geq \frac{\Lambda}{\lambda}. \tag{2.1}$$

Binary elements have smaller features. The smallest feature present in the DOE is referred to as critical dimension (CD). The critical dimension is an important parameter for DOE fabrication technologies. For the binary element in Fig. 2.1 the critical dimension is equal to $\Lambda/2$. This means that scalar theory can be used for binary DOEs when,

$$\mathrm{CD} \leq 10\lambda \tag{2.2}$$

is fulfilled. Otherwise, rigorous models need to be used.

2.1.1 Scalar Theory

Scalar diffraction is valid under the following assumptions [Voelz2011, Goodman1996]:

- the medium is linear dielectric,
- the medium is isotropic (independent of polarization),
- the medium appears homogeneous (permittivity is independent of position),
- the medium is non-dispersive (permittivity is independent of wavelength),
- the medium shows no magnetic dependency (medium with magnetic permittivity of vacuum).

Figure 2.2 illustrates the light propagation through an optical element. Let z be the propagation direction. The DOE is parallel to the x-y plane. The source field variables are indicated with the subscript 1 and the observation plane variables with 2. The input field is assumed as $U_1(x_1, y_1) = \exp(jkz)$ with $k = 2\pi/\lambda$, a unit-amplitude, monochromatic

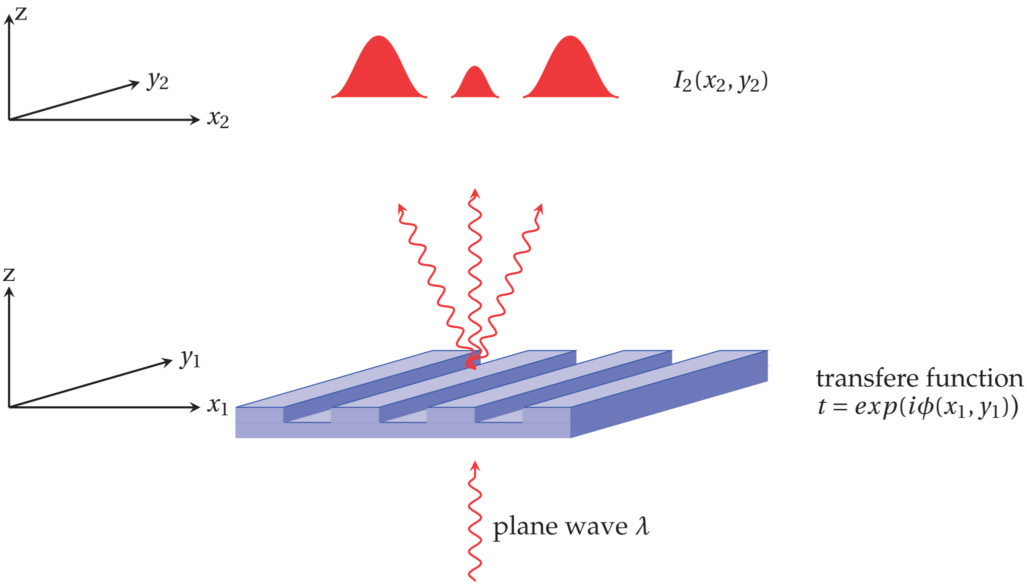

Figure 2.2: Propagation of plane wave through a phase grating. The phase grating can be described by the phase function $\phi(x_1, y_1)$, which is introduced by a surface profile variation. The irradiance in the far field is given by $I_2(x_2, y_2)$.

plane wave.

The transmission function for a phase grating shows no absorption loss. No amplitude change can be seen over the grating. With the thin element approach the transmission function is determined by a phase function $\phi(x_1, y_1)$:

$$t(x_1, y_1) = exp\left(i\phi(x_1, y_1)\right). \tag{2.3}$$

If the optical element is illuminated with this field under normal incident, then the field distribution at the optical element is equal to the transmission function of the optical element

$$U(x_1, y_1) = U_1(x_1, y_1) * t(x_1, y_1) = \exp(jkz) * exp\left(i\phi(x_1, y_1)\right). \tag{2.4}$$

In order to calculate the far field of the input field $U(x_1, y_1)$, Fraunhofer approximation can be used [Voelz2011]. The irradiance in the far field $I_2(x_2, y_2)$ is given by:

$$I_2(x_2, y_2) = \left(\frac{1}{\lambda z}\right)^2 \left|\int\int U(x_1, y_1)\exp\left[-j\frac{2\pi}{\lambda z}(x_2 x_1 + y_2 y_1)\right] dx_1 dy_1\right|^2. \tag{2.5}$$

The Fraunhofer expression can be seen as a Fourier transformation $\widetilde{U}$ of the input field U with a multiplication factor and a simple variable substitution:

$$I_2(x_2, y_2) = \left(\frac{1}{\lambda z}\right)^2 \widetilde{U}\left(\frac{x_2}{\lambda z}, \frac{y_2}{\lambda z}\right). \tag{2.6}$$

The criteria to use the Fraunhofer approximation are summarized in Tab. 2.1. The approximation can be used for DOEs with feature sizes much greater than the wavelength. For blazed gratings, the smallest feature is the grating period. For binary elements, the smallest feature is given by the critical dimension.

For the implementation of the simulation a standard tool, Matlab is used, where the Fourier transformation is done by a fast Fourier algorithm (FFT) with discrete sampling. Thus, the discrete coordinates in the source plane (plane of the phase grating) and the observation plan are connected with each other. The source plane side length is L_1 and

1.	Fresnel number $N_f = \frac{w^2}{\lambda z}$	far field $N_f << 1$
2.	Ratio of grating period Λ to wavelength λ for Critical Dimension CD smaller λ	$\Lambda >> \lambda$ $CD >> \lambda$
3.	Discrete sampling	$\frac{CD}{\Delta x_1} \geq 5$

Table 2.1: Criteria for Fraunhofer Approximation with numerical simulation. The Fresnel number attributes to the fact that the propagation length z needs to be large enough. The limits of thin elements approximation are given by the 2^{nd} criteria, which talks about a critical dimension to wavelength ratio. The distance of the discrete points Δx of the phase grating profile needs to be high enough, which is described by the 3^{rd} criteria.

the observation plane side length is L_2. The source plane sampling Δx_1 and observation plane sampling Δx_2 are connected as following:

$$L_2 = \frac{\lambda z}{\Delta x_1}; \qquad \Delta x_2 = \frac{\lambda z}{L_1}; \qquad x_2 = \lambda z \left[\frac{-1}{2\Delta x_1} : \frac{1}{L_1} : \frac{1}{2\Delta x_1} - - \frac{1}{L_1} \right]. \tag{2.7}$$

Because discrete sampling is used, enough sampling points per period need to be chosen (Nyquist–Shannon sampling theorem). Criteria 3. in Tab. 2.1 attributes to this restriction. More than 5 discrete points per critical dimension should be implemented. If Δx_1 is the distance of 2 discrete points, the criteria for the sampling reads as:

$$\frac{CD}{\Delta x_1} \geq 5. \tag{2.8}$$

The definition of the grating size D in the numerical observation window L_1 can be chosen in two different ways: finite grating or infinite grating. For finite elements, the grating size should be smaller than the numerical window. Outside the grating area, the transfer function needs to be set to zero, which is equivalent to situations where all light passes through the optical element. The light distribution in the far field will consist of diffraction orders with a finite width, which can be seen in Fig. 2.2 by the irradiance I_2. In the numerical simulations, the order intensity is calculated by summation over a chosen area containing the diffraction order. The width of diffraction order decreases with the number of periods used in the grating. For smaller grating periods Λ the angle of the diffraction orders decreases. Thus, the definition of the angular area needs to be chosen carefully.

For infinite gratings the situation simplifies strongly. In the case, where the grating size is equal to the numerical window and an integer number of periods P spans the numerical window $L_1/\Lambda = P$, the simulations will give the resulting diffraction pattern of an infinite grating. The output field consists of delta functions and the diffraction orders are localized in single discrete entries. This is why for all simulations based on the Fraunhofer approximation settings with infinite gratings are used.

2.1.2 Rigorous Models

In case the critical dimension of the DOE is to close to the wavelength (see Equation 2.2), scalar theory cannot be used and rigorous methods need to be used. For rigorous simulations, we used the Matlab code RETICOLO written by J.P. Hugonin and P. Lalanne [Hugonin2005]. It is based on Rigorous Coupled wave Analysis (RCWA), which is a frequency-domain modal method. It calculates the efficiencies of diffraction orders. It includes routines to compute the near-field electromagnetic field through the grating.

Figure 2.3 depicts the definition and sampling of the grating necessary for RCWA. The grating can be illuminated from the top or from the bottom by a plane wave of wavelength λ. The polarization state can be set to TM, TE or conical polarization. We choose the bulk glass substrate to be on the bottom and the air on the top. The grating is usually

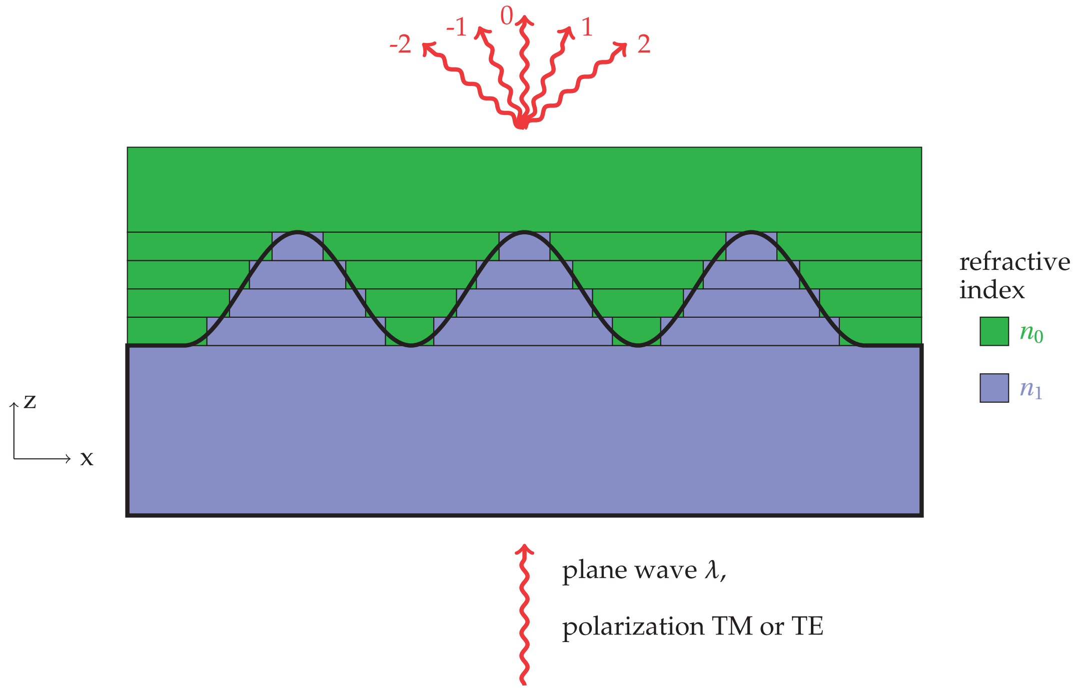

Figure 2.3: Definition of a phase grating into discrete layers. The top (air) and the bottom layer (substrate) have uniform textures.

illuminated from the bottom.
The input window will be periodically expanded. The grating period is equal to multiples of the input window. One-dimensional gratings are considered (invariant grating in y-direction). The grating is composed of a stack of layers. Each layer is modeled by rectangular regions with homogenous refractive indexes. The input for RETICOLO consists of the layer thickness and the texture, which is given by the local transition points and the corresponding refractive indexes. Two level binary surfaces with vertical (90°) edges can be implemented by only 3 layers: a top layer (predefined as air), a bottom layer (predefined as substrate) and one grating layer. An arbitrary continuous surface profile like in Fig. 2.3 needs to be discretized into layers. The position of the transition point is set as the surface height in the middle of the layer. For very flat surfaces the number of layers N needs to be increased accordingly. However, the computational time is proportional to the number of layers N. Also caused by the nature of discrete layers, the influence of surface roughness cannot be easily computed with RCWA. For this, Fraunhofer simulation is more feasible. In general, a higher surface roughness will decrease the overall diffraction efficiency.
Once the layers are defined, RETICOLO calculates the eigenmodes in each layer of the grating in a plane-wave basis. After the calculation of the eigenmodes, a scattering matrix approach is used to recursively relate the mode amplitudes in the single layers with each other. At last, RETICOLO gives the diffraction efficiencies in the transmitted and the reflected orders.

The eigenmodes are also referred to as Fourier orders. The number of eigenmodes taken into consideration needs to be chosen carefully for the numerical implementation. The parameter is defined as M and is equal to $2M+1$ Fourier harmonics spanning form -M to M. The accuracy of the simulation depends solely on this parameter [Moharam1995]. The number of Fourier orders taken into consideration should be higher than the number of design diffraction orders of the grating. The convergence of the calculations should be checked by simulating the diffraction efficiency as a function of the number of Fourier orders. If the efficiency reaches a stable value, the number of Fourier orders is high enough to ensure reliable results. Also, more orders need to be used for deeper gratings and larger periods. TM polarization converges much slower than TE polarization [Moharam1995]. On should keep in mind that the computational time increases as

$$CPU_{time} \propto NM^3. \tag{2.9}$$

This is usually reasonable for one-dimensional surfaces with 2 levels, but can become very slow for multilayer gratings and two-dimensional elements.

2.2 Optical Design

When light passes through periodic elements with features in the diffraction regime, multiple orders will be seen in the far field. The grating period Λ determines the angular separation θ_m between the diffraction order m and the 0^{th} order beam. The separation angle is governed by the grating equation:

$$\sin(\theta_m) = \frac{m\lambda}{\Lambda}. \tag{2.10}$$

To reach greater angles the period needs to be decreased. The grating equation only gives information of the direction of the light, but not about the amount of light going in the individual orders. This is determined by the surface shape in the fundamental period. Phase elements have low losses and the function is encoded as height profile at the surface of the elements. The depth (or height) of the surface structure $h(x,y)$ is equal to a phase retardation $\phi(x,y)$, which light experiences when going through the substrate material n_1 and the surrounding medium n_0:

$$h(x,y) = \frac{\phi(x,y)}{2\pi}\frac{\lambda}{n_1 - n_0}. \tag{2.11}$$

If the phase retardation is equal to π (or $\lambda/2$ in terms of wavelength) and if the area size of π and 0 are equal, the 0^{th} order light will experience destructive interference and the light will be guided to higher orders. As an example, let the grating be a 2 level binary grating with a height difference h_0, then the highest efficiency for the higher orders will be seen at:

$$h_0 = \frac{\lambda}{2(n_1 - n_0)}. \tag{2.12}$$

In some designs, the 0^{th} order should reach a certain efficiency and is part of the design diffraction orders. This can be done by adopting the step height or changing the design so that the areas for 0 and π phase have a different extension.
The height depends directly on the wavelength. The wavelength dependency of the refractive index does play a smaller role. The wavelength dependence of the refractive index $n_1(\lambda)$ for a transparent material can be described by the Sellmeirs formula:

$$n^2 = 1 + \frac{B_1\lambda^2}{\lambda^2 - C_1} + \frac{B_2\lambda^2}{\lambda^2 - C_2} + \frac{B_3\lambda^2}{\lambda^2 - C_3} \quad [\lambda \text{ in } \mu\text{m}]. \tag{2.13}$$

The Sellmeier coefficients $B_{1,2,3}$ and $C_{1,2,3}$ are experimental determined. In Tab. 2.2 the coefficients for the two investigated materials are given for a glass L-BAL42 from OHARA and for fused silica. This formulation is used for the refractive index calculations for all simulations. The wavelength dependency of the refractive index is plotted in Fig. 2.4 (a) for the visible wavelength region. The height difference h_0 for a 2 level binary grating given with equation 2.12 is depicted in Fig. 2.4 (b).

Sellmeier coefficient	L-BAL42	fused silica
B_1	1.39528097	0.6961663
B_2	0.072551952	0.4079426
B_3	1.66335848	0.8974794
C_1	0.011186203	0.0684043
C_2	0.0246748575	0.1162414
C_3	167.717958	9.896161

Table 2.2: Sellmeier coefficients for L-BAL42 and fused silica [5].

The two investigated materials L-BAL42 and fused silica require two different depths for the same optical functionality and for the same wavelength. For a replication approach, this means two molds of different depth would be needed for L-BAL42 and fused silica when the same wavelength is intended. It is also possible to fabricate one mold, which is used for both materials and the wavelength has to be chosen accordingly.

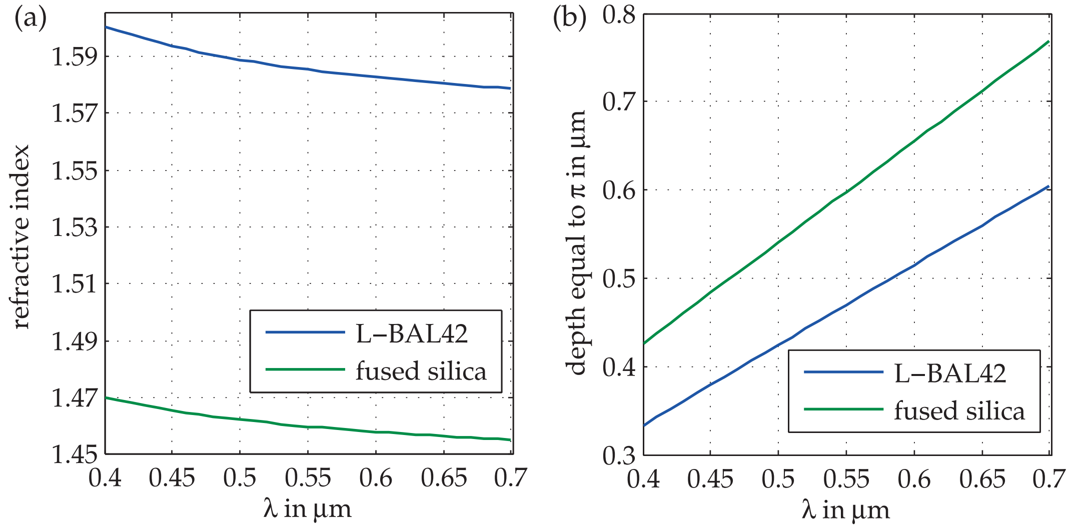

Figure 2.4: Wavelength dependence of refractive index (a) for a glass L-BAL42 and fused silica and depth equal to a π phase difference (b) (surrounding medium air $n_0 = 1$).

As an example, a 1x2 beamsplitter is discussed. A possible design has design parameters as given in Tab. 2.3.

He: Ne laser	λ=633nm	
diffraction angle $\theta_{1,-1}$	±9.1°	
period Λ	4 µm	
feature size	2 µm	
fused silica (incident medium air)	n_1 =1.457	h = 692 nm
L-BAL42 (incident medium air)	n_1 =1.581	h = 545 nm

Table 2.3: Design parameters of a 2 level binary 1:2 beamsplitter.

One has to note that 9.1° deviation angle is still not very high and leads to geometrical dimensions in the micron range. The efficiency η_m of the m^{th} order for a 2 level binary grating with duty cycle 0.5 is governed by:

$$\eta_m = \left(\frac{2}{m\pi}\right)^2. \tag{2.14}$$

The diffraction efficiency of the $+1st$ and $-1st$ order are both 40.5%. The diffraction efficiencies calculated with Fraunhofer approximation do not include reflection loss. To compare the measurement results with the theoretical values the reflection losses of 2 surfaces need to be added. As an approximation Fresnel coefficient R is used [Saleh1991]:

$$R = \left(\frac{n_1 - n_2}{n_1 + n_2}\right)^2. \tag{2.15}$$

Eq. 2.15 is valid for a perpendicular incident. If the DOE is surrounded by air, then $n_1 = 1$. For the refractive index of the substrate material n_2 we use the Sellmeier formula 2.13 (plotted in Fig. 2.4. (a)). The reflection coefficients are depicted in Fig. 2.5. For a wavelength of 532 nm the reflection loss per surface is 3.5% for fused silica and 5.14% for the glass L-BAL42. Thus fused silica DOEs have the advantage of a higher efficiency. However, the lower refractive index of fused silica results also in higher step heights and higher aspect ratios, which might be more challenging during the fabrication process.

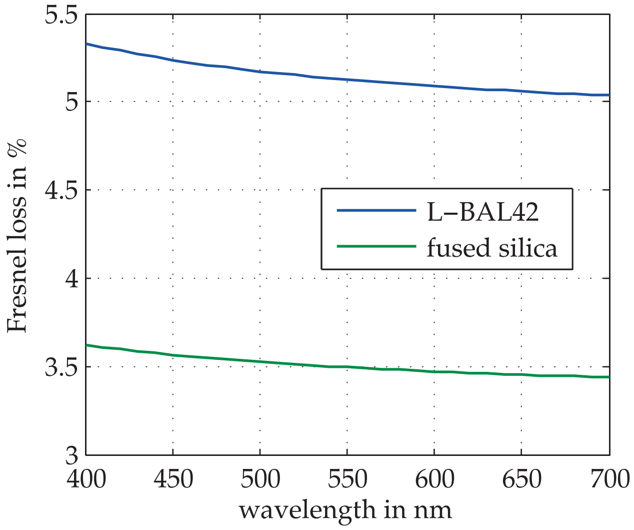

Figure 2.5: Reflection loss per surface for L-BAL42 and fused silica in perpendicular incident calculated with the Fresnel coefficient (Eq. 2.15).

2.2.1 Blazed Elements

The performance of a DOE is discussed in terms of the achievable diffraction efficiency that is how much of the incoming light is transferred into the desired diffraction orders. Surface roughness smaller than 20 nm show a negligible influence (Rossi and Hessler 1999; Michael T. Gale et al. 1994). The theoretical efficiency of blazed diffractive surfaces can achieve 100% if reflection losses are not taken into consideration. Some of the most common parameters which influence the efficiency are described in Tab. 2.6.

To achieve maximum efficiency one needs to fabricate blazed structures with sharp profiles. For classical surface structuring like grinding and milling features in the 10 µm range are very challenging, because the tooling needs to show the same size. Even if the tool tip had a very small radius, wear during the fabrication can cause a considerable enlargement of the tip radius [Dambon2016]. The final surface will show thus stronger edge rounding and will suffer from an efficiency drop.

Binary surface structuring techniques in the µm range are available due to the large effort in the semiconductor industry. This is why blazed elements are often approximated with N binary levels. If the number of photolithography masks used is q, then the

parameter	graph	example calculation
different operation wavelength λ $\eta_m(\lambda)=\left\|\frac{\sin\left(\pi\left[(\lambda_0/\lambda)-m\right]\right)}{\pi\left[(\lambda_0/\lambda)-m\right]}\right\|^2$ λ_0 … design wavelength m … diffraction order	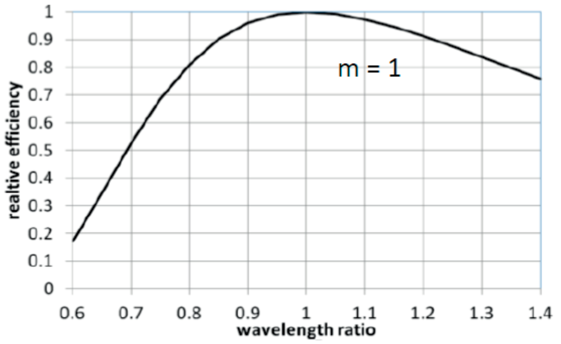	m = 1 λ = 696nm λ_0= 633nm λ_0/λ = 1.1 η = 0.97
operated for finite spectral range $\lambda_0 \pm \Delta\lambda$ Integrated diffraction efficiency $\eta = 1 - \left(\frac{\pi\, \Delta\lambda}{6\, \lambda_0}\right)^2$	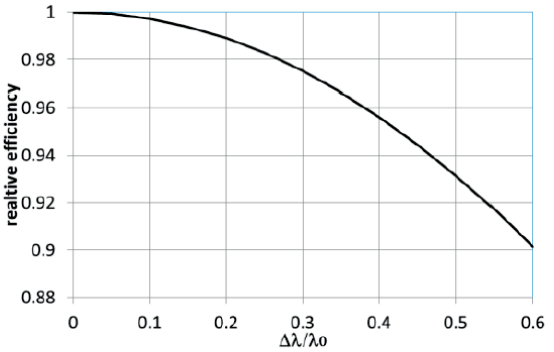	$\Delta\lambda/\lambda_0$ = 40% Δλ = 253nm η = 95.6%
aspect ratio (fabrication error): $\eta = (1-\Delta\Lambda/\Lambda)^2$ 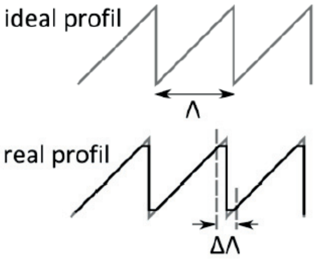	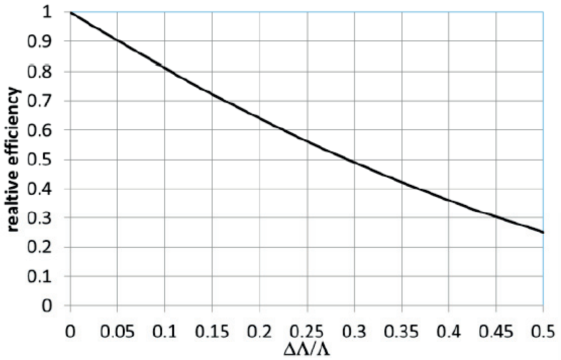	Λ=4µm ΔΛ=0.2 µm η = 0.9 ΔΛ=0.1 µm η = 0.95
height (fabrication error): $\eta_m(\lambda)=\left\|\frac{\sin\left(\pi\left[(h/h_0)-m\right]\right)}{\pi\left[h/h_0-m\right]}\right\|^2$ 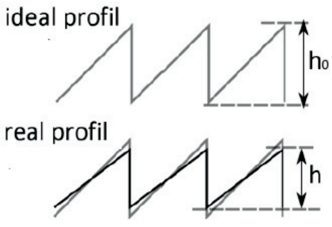	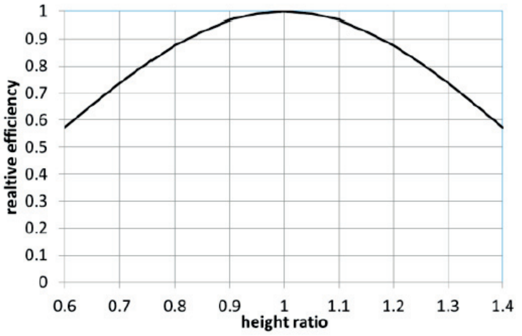	m = 1 h_0=692nm Δh=+/-20nm height ratio =0.97 η = 0.997

Figure 2.6: The efficiency η of blazed elements depends on the operation wavelength λ, profile height h and the fabrication accuracy [Herzig1997, Kress2009].

number of fabricated levels reaches $N = 2^q$. The first order efficiency will drop due to this fabrication method like:

$$\eta_1 = \left(\frac{sin(\pi/N)}{\pi/N} \right)^2 . \tag{2.16}$$

An 8 level structure will have a maximum efficiency of only 94.9% and a 16 level system can reach 98.7%.

2.2.2 Fan-Out Elements

Fan-out elements generate spot arrays. They are used for optical computing, laser material processing or structured illumination. Special binary fan-out elements are Dammann gratings, which generate spot arrays of equal power [Dammann1977]. The grating period Λ determines the angle of the diffraction orders according to the grating equation 2.10. However, the shape inside the period $t(x, y)$ distributes the power between the orders. For binary optics, the transfer function t can take the values 1 and -1. Fig. 2.7 shows the profile of a 1 dimensional Dammann grating. The grating is determined by the number and position of the phase transitions x_s. The number of phase transitions S per half period can be linked to the number of design orders M. For an uneven number of design orders, the 0^{th} order is included and the relationship reads as

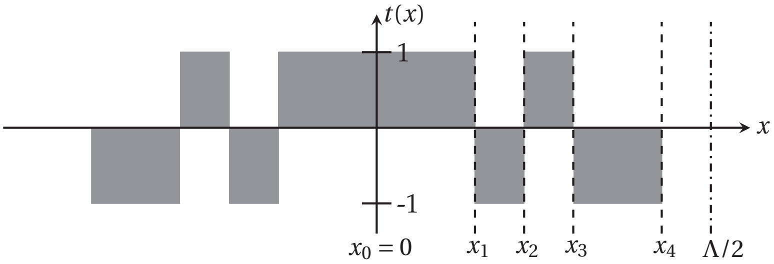

Figure 2.7: Grating transmittance of a 1 dimensional Dammann grating with 4 transition points S. This element will act as a spot array with $2S + 1 = 9$ spots.

$$M = 2S + 1. \tag{2.17}$$

For an even number of design orders, the 0^{th} order is excluded and the diffraction pattern has non-zero entries only for the uneven diffraction orders. The number of orders is then given by

$$M = 2S. \tag{2.18}$$

Symmetric phase grating designs result in a uneven number of spot arrays and asymmetric gratings exclude the 0^{th} order. It is desired that the amount of light and thus the efficiency of the design orders is as high as possible. The uniformity error UE is a parameter specific for fan-out elements, where a uniform power distribution over all design orders is desired and the fabricated element is tested against this criteria. The UE is defined as the difference between the maximal power P_{max} and the weakest diffraction order power P_{min} as

$$\mathrm{UE} = \frac{P_{max} - P_{min}}{P_{max} + P_{min}}. \tag{2.19}$$

Jahns et al. [Jahns1989] presented a feasibility study of Dammann gratings. They analyzed the influence of the number and position of the phase transitions and the etching depth. If Δx_s are the shifts of the phase transition points x_s, then the power of the diffraction orders P_m changes by dP_m. Jahns et al. made an estimation for the worst case. The relative change is given by:

$$\frac{dP_m}{P_m} = \frac{8\sqrt{2}}{\sqrt{\eta}} S^{3/2} \frac{1}{Q}, \tag{2.20}$$

where Q is the relative position error: $Q = \frac{\Lambda}{\Delta x}$. To investigate the influence on the uniformity error, we assume the maximum power to increase to $P_{max} = P_{av} + dP$ and the minimum power to decrease by $P_{min} = P_{av} - dP$ from the average order power P_{av}. The uniformity error will be changed by the accuracy of the phase transition as follows:

$$UE \approx \frac{dP_m}{P_m} = \frac{8\sqrt{2}}{\sqrt{\eta}} S^{3/2} \frac{1}{Q}. \tag{2.21}$$

From equation 2.21 it can be seen that for larger numbered arrays the accuracy of the position of the phase transition has to be better in order to remain at low uniformity errors. This will lead to very demanding constraints in fabrication. The relative positioning error Q should be high for low uniformity errors. This is easier to fulfill for larger grating periods. The position error Δx_n is introduced during the grating fabrication. Possible reasons would be pixelation of the photolithography mask, over-or underexposure of the photoresist and underetching during dry etching (see chapter 3). For the approach presented here it is also possible that such errors are introduced during the precision glass molding (see chapter 4).

It should be noted that equation 2.20 is only an estimation for the efficiency change. The influence of the positions of the phase transition points can vary strongly for different grating designs. To understand the influence, each grating needs to be analyzed individually.

A grating depth error or wavelength change ($\lambda \neq \lambda_0$) will result in a scaling change of the grating phase:

$$t(x, y) = exp(i\phi(x, y) - \epsilon). \tag{2.22}$$

The scaling factor ϵ is given for a phase grating in transmission with equation 2.11. Jahns et al. showed that the power of the orders changes by a factor:

$$P_m = \frac{1+cos(\epsilon)}{2} P_m^{\epsilon=0}, \qquad P_0 = 1 - \frac{1+cos(\epsilon)}{2} \sum_{m\neq 0} P_m^{\epsilon=0}. \tag{2.23}$$

Thus, the power of the higher orders decreases, but the uniformity does not change. At the same time, the power of the 0^{th} order increases much stronger, since it attracts the power of all higher orders. This is especially important when the 0^{th} order is one of the design orders. Then the uniformity will change with the phase scaling error ϵ. Equation 2.23 is true for all Dammann gratings, which fulfill the requirements for Fraunhofer approximation, that is if $\Lambda \geq 5\lambda$.

Another effect discussed by Jahns et al. is an area dependent phase change R. For example, if the etching depth is varying over the active area and the depth reaches π in some areas but reaches other phase values at different positions. This can happen when the etching is not uniform during the reactive ion etching. A power change can be estimated like:

$$\frac{dP_m}{P_m} \leq \sqrt{2}\frac{2S+1}{\eta} R. \tag{2.24}$$

As an example, for a 10% deviation and a 70% efficiency of an 11 spot array ($S = 5$) the phase change R needs to be smaller than 0.0045. This corresponds to a $\Delta h/\lambda$ of 0.0014.

Kemme [Kemme2010] studied the influence of edge roundings on the performance of Dammann gratings. A 2 level fused silica grating with 2.55 µm period, 1.94 µm depth for a wavelength of 1.55 µm was simulated with RCWA. The simulated profiles are shown in Fig. 2.8 (a)-(f). The radius of the edge R was varied, where the max. value for R is equal to half the feature size. Amongst the symmetric profiles, the strongest effect was seen for the element in Fig. 2.8 (b). The efficiency of the $+1^{st}$ and -1^{st} orders decreased from 43% to 40.7%, which mostly was distributed to the 0^{th} order. The asymmetric profiles Fig. 2.8 (e)-(f) result in unequal power distribution between the $+1^{st}$ and -1^{st} order.

Kemme also analyzed a 4 level grating given in Fig. 2.8 (g)-(i) and an 8 level system. In both cases, only an insignificant drop in the efficiency is seen. He concluded that edge roundings do not change the performance of blazed gratings fundamentally except when a strong asymmetry is introduced.

Table 2.4 summarizes the influence of the main parameters on the optical performance. The strongest increase of the uniformity error is given by the positions of the transition points.

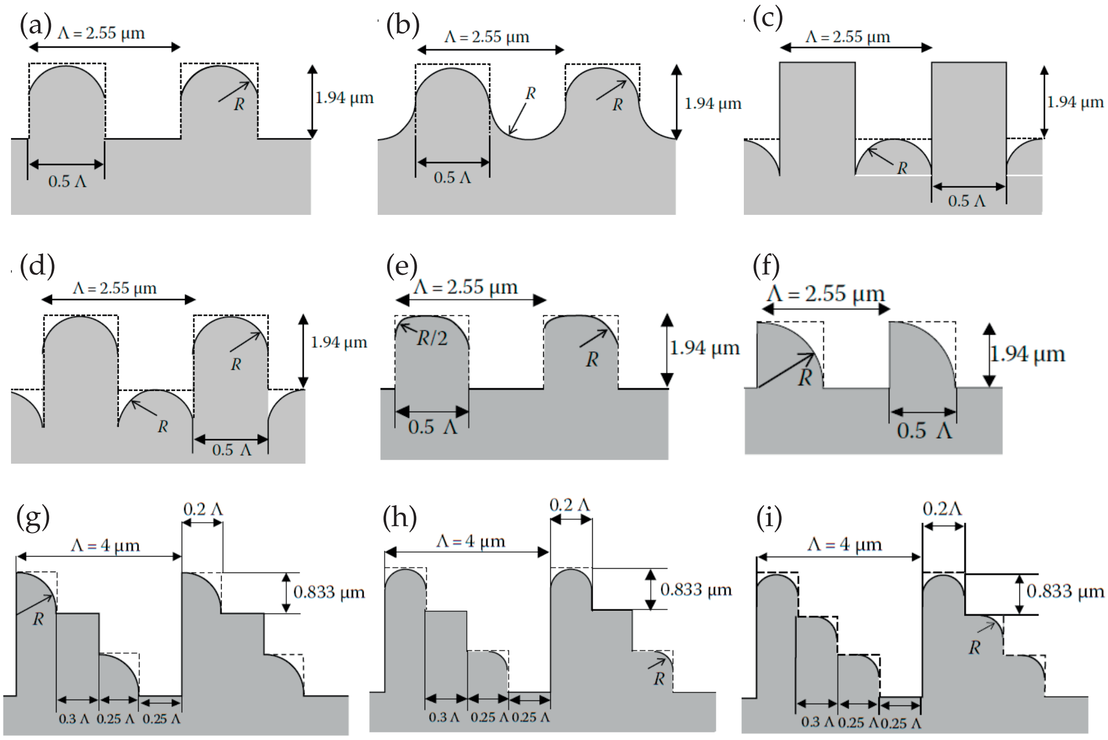

Figure 2.8: Layout for the height profiles including edge roundings used by Kemme (images taken from [Kemme2010]). For 2 level system (a)-(f) and for 4 level system (g)-(h), with symmetric and asymmetric profile roundings.

	eff.	UE	0^{th}	caused by
phase mismatch ϵ	reduced	const. (0^{th}order no design order); high (0^{th}order is design order)	strong increase	etch depth, wavelength mismatch
shift of transition points		strong influence		pixilation grid, over- or underexposure (linked to CD, scales with period)
alignment of features	$\propto$ const. (light is scattered to higher orders)	strong influence	const.	mask to mask misalignment

Table 2.4: Influence of the main parameters on the optical performance of Dammann gratings.

2.2.3 Mask Design

The diffraction patterns of our samples consist of spot arrays, a typical Fan-out element that can be qualified with values for the efficiency of the design orders, the 0^{th} order efficiency and the uniformity. These give a clear and significant judgment about the quality of the fabricated DOE. The designs of the various fan-out elements were contributed by our partners from Holoeye. Design values for the diffraction efficiency and UE are taken from simulation with scalar approximation.

A first mask design consisted of 2 level binary elements. It permits investigation of the processing options without the immediate need to fulfill high alignment requirements between the multiple process steps required for multi-level diffractive elements. The design specifications of 4 different DOEs are given in Tab. 2.5. The critical dimensions are set between 1.6 µm and 4.4 µm. Elements G,H and I are 11x11 fan-outs, where the on-axis orders are suppressed for the designs G and I. Element O is splitting the beam in a 6x6 array.

The layout of the mask is shown in Fig. 2.9. After microfabrication, the master wafer is diced into single molds, which correspond to the hexagonal areas. The active areas of the different DOEs are 7.5 mm in diameter for the elements G, H and I. Three different molds are placed on the same hexagonal mold. One hexagonal mold holds only one larger area with a diameter of 17.2 mm. For this, the element O was chosen. For production, it is desired to have different designs on the same mold to safe fabrication costs. In order to test the replication process, the uniformity of the replication quality needs to be evaluated. For better comparison, a larger area with the same structure is used.

More elaborate DOEs are also tested. Every patterning-etching run increases the cost. A multilevel system with 3 masks was designed. The 8 level DOEs G and F are specified in Tab. 2.6. Element F is a linear grating, which splits the incoming beam into 4. This element is interesting since it can be implemented for simulations easier than the design G, which consists of many small details. The layout for the multilevel mask-set is shown

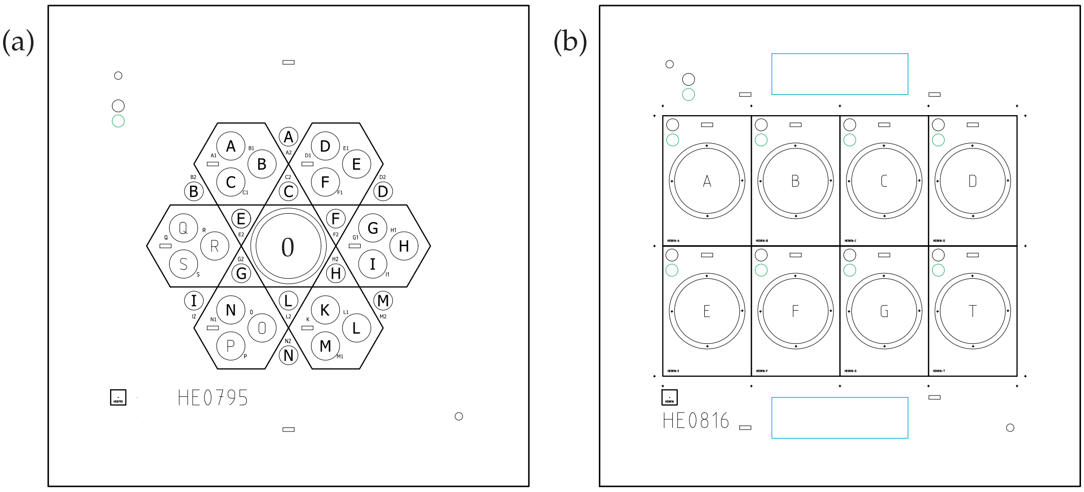

Figure 2.9: 5″ mask layout for (a) hexagonal and (b) rectangular mold inserts.

Phase profile	Diffraction pattern	Design specifications
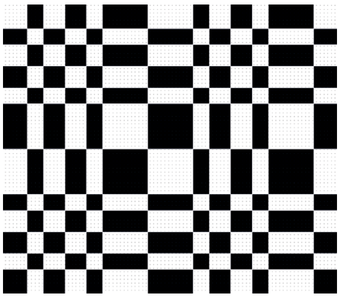	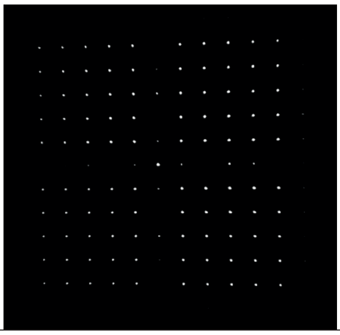	• **name: G** • 11 x 11 beamsplitter • without on-axis orders ([k,0] and [0,m]) • CD = 4.4 µm • Λ = 44.8 µm • design DE = 71.4% • design UE = 5.2%
	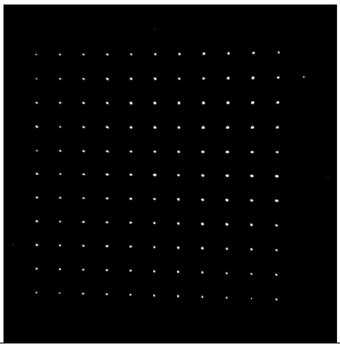	• **name: H** • 11 x 11 beamsplitter • CD = 1.6 µm • Λ = 44.8 µm • design DE = 77.8% • design UE = 1.9%
	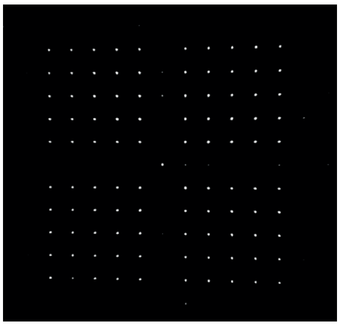	• **name: I** • 11 x 11 beamsplitter • without on-axis orders ([k,0] and [0,m]) • CD = 1.6 µm • Λ = 44.8 µm • design DE = 75.4% • design UE = 1.9%
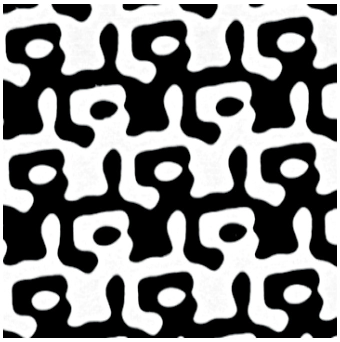	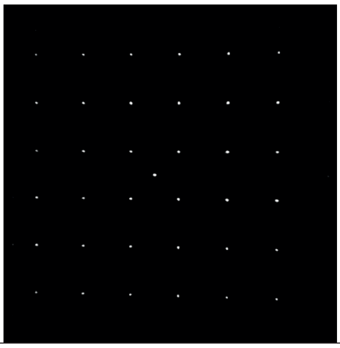	• **name: O** • 6 x 6 beamsplitter • CD = 2.5 µm • Λ = 56.6 µm • design DE = 79% • design UE = 0.5%

Table 2.5: Design specification for DOEs of the 2 level photolithography mask.

in Fig. 2.9 (b). All elements show an area with a diameter of 17.5 mm. The wafer is cut into rectangular molds after microfabrication. The rectangular design was chosen due to the tooling design of the precision glass molding machine.

The use of multiple levels permits higher efficiencies. For 2 level systems, the efficiency is limited to 40.5% for both $+1^{st}$ and -1^{st}. If the diffraction pattern is symmetric around the 0^{th} order, the design orders consist of both $+1^{st}$ and -1^{st} and the theoretical efficiency increases to 81%. For asymmetric diffraction patterns and for efficiencies higher than 80% multilevel DOEs are employed.

For the versatility of precision glass molding, it is also interesting to fabricate DOEs with smaller features. 2 level binary elements with critical dimensions of 400 nm and 800 nm are shown in Tab. 2.7. The features are too small for scalar approximation, so RCWA was used for the simulations. These elements were also placed on rectangular mold inserts. On the molds, additional features with varying structure sizes ranging between 200 nm and 2 µm were added. These molds were patterned with electron beam lithography because the resolution is much higher than for mask photolithography.

Phase profile	Diffraction pattern	Design specifications
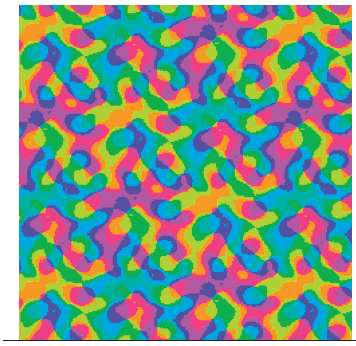	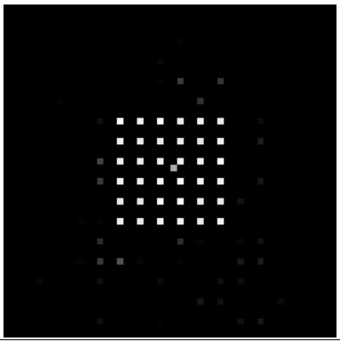	• **name : G** • 6 x 6 beamsplitter in asymmetrical order • 0th order suppressed • CD = 1.8 µm • design DE = 85% • design UE = 1.5%
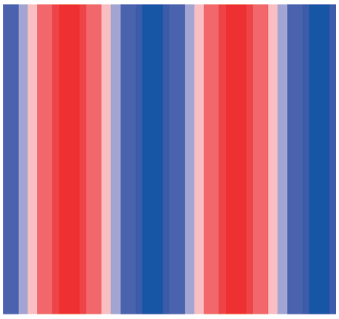	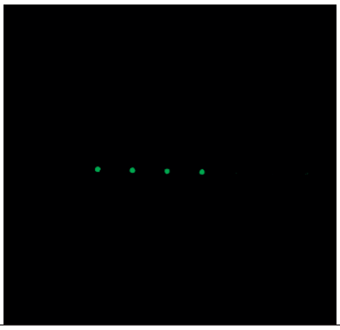	• **name : F** • 1 x 4 beamsplitter • 0th order suppressed • CD = 2 µm • Λ = 50 µm • in TE polarisation • design DE = 86.3% • design UE = 0.2%

Table 2.6: Design specification for the 8 level DOEs with 3 Photolithography masks.

Phase profile	Design specifications
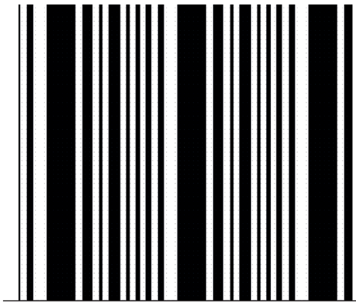	• **name: R** • 1 x 31 beamsplitter • CD = 800 nm • Λ = 29 µm • in TM polarisation (RCWA) • design DE = 83% • design UE = 17.5%
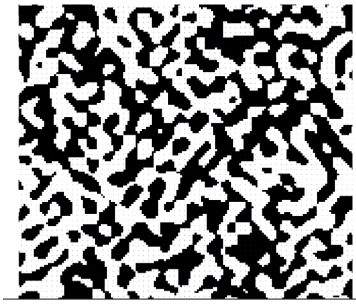	• **name: B** • 31 x 31 beamsplitter • CD = 400 nm • design DE = 62% (RCWA) • design UE = 7.5%

Table 2.7: Design specification for the higher resolution DOEs.

2.3 Limiting Factors of Optical Performance

The design specification for the efficiency and uniformity are never reached for the fabricated elements. Examples of limiting effects are summarized in Tab. 2.8. Both scalar and rigorous models are used to simulate the DOEs discussed here. The scalar approximation is limited to low-aspect-ratio surface profiles, that is small diffraction angles. Due to the fast computational simulation, it is used to design DOEs. Rigorous models like RCWA are much slower. They are used for situations, where the scalar approximation no longer holds, such as polarization dependent effects and subwavelength gratings.

In the center of interest for the work presented here is the investigation of fabrication specifications. These can originate from the mold fabrication e.g. over-/underexposure, etch depth and feature positioning errors or from the molding e.g. partial filling of features. The evaluation can be done by measuring the surface profile or by measurements of the optical performance. The design parameters for optics are given by the shape, uniformity and surface roughness over the whole active surface area.

Also, the fabrication specifications can strongly depend on the design. A low uniformity error is more difficult to achieve for a larger number of spots than for a small spot array. Additionally, the fabrication tolerance is higher for multilevel elements than for 2 level elements. Particular situations such as mask to mask alignment errors can have a significant influence on the power distribution of a multilevel DOE.

The optical performance of the final DOEs will be determined by both the mold fabrication and the precision glass molding. The molded DOEs are compared to directly micromachined DOEs. The aim of this work is to investigate if the replicated DOEs can reach the same quality as the directly micromachined DOEs and to what extent the precision glass molding influences the optical performance. In order to distinguish between errors introduced during mold fabrication and precision glass molding, simulations can be used, where fabrication errors can be turned on and off individually.

design-related effects	- validity of scalar theory for features smaller than 5λ
fabrication-related effects	- etch depth errors - lateral positioning errors - quality of the side walls - surface roughness
operation-related effects	- coherence of source (LED or laser) - wavelength shift, wavelength bandwidth - collimation of source - incidence of the launch beam (shadowing effects) - polarization state of the source

Table 2.8: Examples for limiting factors for diffractive optical elements [Kress2009].

3 Glassy Carbon Mold Fabrication

The performance of the molded diffractive optical element (DOE) depends on the quality of the microstructured mold. The mold sturcture needs to fulfill the same requirements as the directly fabricated DOE in fused silica. The fabrication constraints are the same as the ones discussed in section 2.3.

Tab. 3.1 summarizes the desired qualification of the DOE in glass and thus of the GC mold. The requirements for the mold fabrication are given by the following parameters. The sidewall angle has to be higher than 80°. An estimation can be done based on an evaluation of the wall width from SEM images in top view and the depth measured with a mechanical profilometer (Tencor Alpha-Step 500). The tangent of the sidewall angle is assumed to be the ratio of the depth over the width. The sidewall angle is influenced by the selectivity, which is the ratio of the etch rates between substrate and mask material. A high selectivity is necessary to achieve a high wall verticality and to reduce the mask layer thickness, which also increases the lateral resolution. The surface roughness R_a is measured with an AFM and should be below 20 nm for an optically flat surface.

	Requirement
Mask Material	easy to process, high-resolution, cheap
Structuring Technique	fast
Selectivity GC : Mask	GC $\gg$ Mask
Sidewall Angle (for depth)	$> 80°$
Surface Roughness R_a	< 20 nm
Surface Quality	High (no contamination)

Table 3.1: The requirements for the mold fabrication are given by the sidewall angle, the surface roughness, and the surface quality. A high selectivity of the mask material compared to the GC substrate is preferred.

This section deals with the process development for the microstructuring of GC molds for DOEs. Section 3.3 discusses different mask materials for the microfabrication process. Additionally, the plasma etching conditions are investigated. With this technologies, we fabricated multilevel DOEs, where the results are shown in section 3.4. In order to analyze the resolution limit of the mold fabrication and the glass molding, higher resolution DOEs were fabricated by e-beam lithography and discussed in section 3.5.

3.1 Glassy Carbon

Glassy Carbon (GC) is non-graphitizing carbon, which means that it does not transform into crystalline graphite at very high temperatures of 3000 °C. The name glassy comes from the disordered, amorphous structure at the microscale and its high hardness, because of which it can be highly polished. At the atomic scale, a graphitic microcrystalline structure was found. Transmission electron microscopy showed that GC contains a high amount of fullerene-related nanodomains [Harris2004]. A scheme is given in Fig. 3.1. GC is fabricated by pyrolysis of polymeric precursors in an inert atmosphere. During temperature treatment at ca. 500 °C the organic precursor looses small molecules, such as hydrogen chloride, hydrogen cyanide, water, small hydrocarbons carbon monoxide, and carbon dioxide. For a higher temperature above 700 °C hydrogen leaves the material and carbon-carbon bonds are formed resulting in a highly cross-linked atomic structure. The final treatment can range to temperatures up to 3000 °C. The high-temperature treatment results in glassy carbon with high purity and less than 0.5% content of any other elements.

Harris et al. investigated the microstructure of low-temperature GC prepared at 1000 °C and higher temperature GC prepared at 2800 °C [Harris2004]. The low-temperature GC depicted in Fig. 3.1 (a) shows tightly curled single carbon layers, which surround

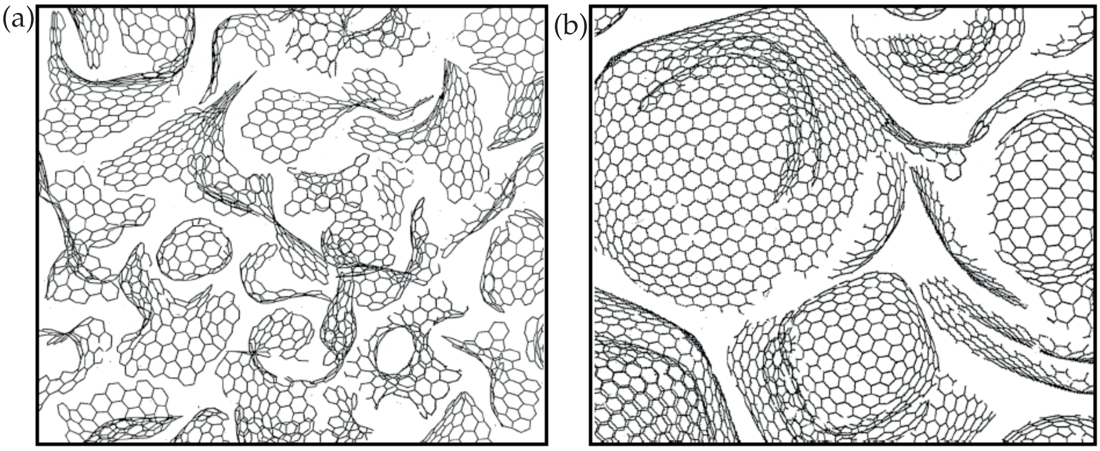

Figure 3.1: Models of the structure of Glassy Carbon at the atomic scale (taken from [Harris2004]): low-temperature pyrolysis results in (a) smaller domains ($\propto$ 1 nm) than high temperature with (b) multiple sheet domains ($\propto$ 5 nm).

micropores with a size of 1 nm in diameter. A higher ordered microstructure can be seen for higher temperature GC in Fig. 3.1 (b). 5 nm large micropores are enclosed by two to four carbon sheets. Brown et al. used scanning tunneling microscopy to investigate the polished and plasma etched GC surfaces [Brown1998]. A low-power plasma etching process enhanced the etching rates for the different structural domains and exposed various domains. A large portion consists of ovid-shaped features with smooth curved surfaces. The size of these features ranges from 1 nm to 38 nm. Some areas show an amorphous glass-like morphology.

Due to the enclosed pores, the density of GC is only 60% of that of monocrystalline graphite. No open pores are found, which makes GC chemical inert even for active oxidizers. It can be operated at temperatures up to 2000 °C in an inert atmosphere. This makes it a valuable material for high-temperature crucibles. Because GC is an isotropic conductor, it is used as an electrode material in electrochemistry. GC is also very bio-compatible and is therefore used as a component in prosthetic devices.

An overview over the properties of GC is given in Tab. 3.2. If GC is used as a mold material, it needs to withstand the harsh conditions during the precision glass molding. An extreme case is the molding of fused silica at ca. 1400 °C, which GC molds have been used for [Youn2009, Mekura2009]. Glass is chemically very reactive in the molding temperature range. The high chemical inertness of glassy carbon allows direct use as a mold material without applying additional antiadhesive coatings (more details in section 4). But the high chemical inertness of glassy carbon makes it difficult to microstructure glassy carbon chemically by etching.

	microstructuring	mold material
high temperature resistance (<2000 °C)		important
high hardness (7 Mohs)	difficult of mechanical structuring	important
low density		
low friction		
low thermal resistance		good (faster heating/cooling)
extreme resistance to chemical attack	difficult for chemical etching	important
impermeability to gases and liquids		important
isotropic	important for chemical etching	

Table 3.2: Properties of glassy carbon. The properties such as high-temperature resistance and chemical inertness make it a good choice for molding of glass, but at the same time, the microstructuring becomes more difficult.

As a substrate, we used 4″ double-side polished glassy carbon wafers with a thickness of 1 mm from Nisshinbo [6]. They show a surface roughness R_a of less than 2 nm (AFM measurements). This high quality is necessary for the use as a mold for diffractive optical elements (DOE). Additionally, we polished already structured GC wafers with a chemical mechanical polishing system (STEAG MECAPOL E460). A typical surface profile after polishing is given in Fig. 3.2. The overall roughness R_a is as low as 1.48 nm, but single scratches with a depth of up to 10 nm are presented on the surface. We believe that single GC particles are broken from the GC wafer surface. During polishing, they are moved over the surface and are hard enough to cause these scratches. The mold lifetime will be increased due to the hardness of GC since the mechanical wear is low. However, this makes GC very brittle and difficult for mechanical machining. The surface finish needs to be optical quality with a roughness R_a below 20 nm. We tested the homogeneity of the GC wafers. A wafer was diced and the cut surface was polished. Scanning electron microscope images (SEM) showed no holes and a high homogeneity over the whole thickness of the substrate.
The cost of a GC wafer from Nisshinbo are 350 SFr (40000 JPY; 2017). The double-side polished glassy carbon wafers were used for testing form both sides.

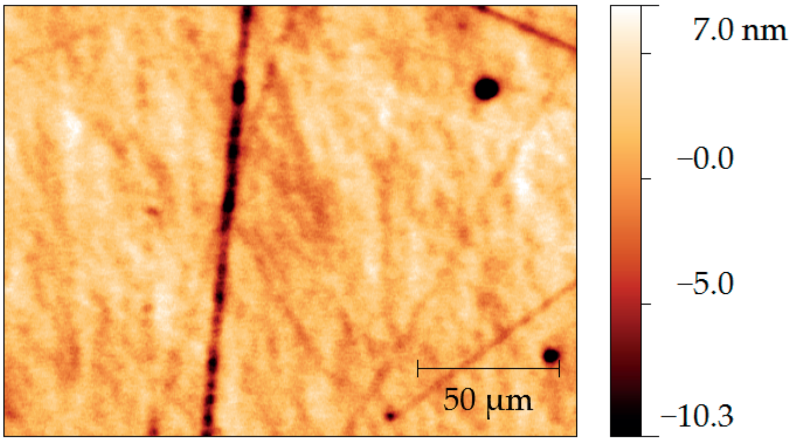

Figure 3.2: Phase shifting interferometry (Veeco Wyko NT1100 [2]) image of a polished GC wafer shows scratches with depths of up to 10 nm.

3.2 State-of-the-art technology for Microstructuring of Glassy Carbon

Different attempts have been used to structure Glassy Carbon in the micrometer range. Most of the processes suffer from a surface roughness higher than 20 nm. The process time is another main limitation. Only processes based on reactive ion etching (RIE) were able to fabricate surfaces with the required surface quality and short enough process times. Table 3.3 shows a summary of different microstructuring processes used for glassy carbon so far. Selected parameters are given where the roughness is of great importance.

Mechanical machining like dicing and grinding has the advantage of continuous surface structuring and can be used also on curved surfaces. Together with polishing very high form accuracy and very high surface quality can be reached. For high consumer markets, these processes are combined with precision glass molding for aspherical lenses. The size of the blade tip determines the minimum feature size and is limited to 20 µm in diameter [Dambon2016]. However, for diffractive optical elements feature sizes down to 100 nm with sharp corners are needed. The surface roughness after the machining of GC is with ca. 70 nm to high for optical applications [Youn2006, Youn2007, Takahashi2007]. Only an additional polishing step enables the optically smooth surface finish. Mechanical machining is thus a limited process for the fabrication of diffractive optical element with considerable large feature sizes.

Laser ablation of GC was regarded with femtosecond laser [Youn2007, Kuhnke2004]and with KrF excimer laser [Youn2007], but shows a roughness higher than 45 nm. Focused ion beam milling results in lower surface roughness, but the writing time can be quite long. Also, the gallium ion implantation causes a variation in depth and an extra annealing step is necessary. The process becomes complicated.

Reactive ion etching (RIE) is used for large area precision manufacturing of diffractive optical elements as a standard technique. But it is limited to planar surfaces. It can also be applied to glassy carbon. Previous research has documented a RIE process with an oxygen plasma [Chen2006, Chen2008, Kuhnke2005, Fredriksson2009]. The major drawback of this approach has been the high surface roughness R_a of 40 nm for 100 nm etch depth [Chen2006] which grows up to 2.5 µm for several hundred microns etch depth [Kuhnke2005].

This high roughness is caused by the so-called "micro masking effect": non-etchable material on the surface changes the local etching rates resulting in a needle-shaped surface topography. The non-etchable material can originate from sputtered material at the radio frequency (RF) electrode cover [Kuhnke2005]. To solve this problem, Youn et al. have proposed a RIE process with a combination of O_2 and SF_6 [Youn2009]. Sulfur hexafluoride is commonly used as a cleaning gas in plasma etching chambers. They choose a gas mixture of SF_6/O_2 at a ratio of 1:4 resulting in a low surface roughness R_a of less than 5 nm. Such surface roughness is acceptable to realize optical components. The amount of SF_6 should be set to a minimum to assure a low surface roughness.

Technology	Working area	Feature Size in µm	Depth in µm	Roughness R_a in nm	Comments and References
Target	large	1-10	0.1-1	<20	
Dicing	large	>20 (blade size)	>50	>70	50 mm /min, only straight lines [Youn2006, Youn2007, Takahashi2007]
Femto-second laser writing	medium	20 (spot size)	50 µm (18 µm /pulse)	45-80	20mm/min (300nm mismatch), vertical sidewalls [Youn2007, Kuhnke2004]
KrF Excimer laser	small	-	200	45-70	better for deep etching [Youn2007]
Focused Ion Beam etching	small	0.004 - 1	0.004 - 1	<20	slow etching speed (example: area 628 µm ^{2}, depth 650 nm, time 105 min), surface contamination with Ga^+ [Takahashi2005, Youn2006, Youn2007]
Reactive Ion Etching O_2	large	5	0.16	40	PR mask [Chen2006]
		100	10	high	Ni mask and lift-off [Chen2008]
		0.11-0.3	0.4	11	Au mask and lift-off [Fredriksson2009]
		50	100	2600	Al mask with laser ablation [Kuhnke2004], micro-masking effect [Kuhnke2005]
		0.5	0.3	7.8	HSQ and EBL [Yasui2008]
Reactive Ion Etching O_2/SF_6	large	0.5	0.9	2	Au mask and EBL [Youn2009], Au mask and photolithography [Mekura2013]
		5	3	low	Si-containing resist [Mekura2012]

Table 3.3: Overview of microstructuring processes for GC and the target parameters in comparison with the investigated processes. Mechanical machining like dicing is limited to considerable large feature sizes. Laser ablation with femtosecond laser and with KrF excimer laser result in roughness higher than 45 nm. Focused ion beam milling results in lower surface roughness, but the writing time can be quite long. RIE process with a combination of O_2 and $/SF_6$ shows very low surface roughness and can be used on large areas.

A further increase will not improve the quality further, but lower the etching rate of GC slightly. Youn at al. chose a gas flow of 20 sccm for SF_6, because the gas flow control of their plasma etching system was not accurate enough below this value.
Based on the approach presented in [Youn2009], this section shows possibilities to microstructuring GC. Their process is depicted in Fig. 3.3. Gold is used as a hard mask. Two additional Ti layers are used to improve the adhesion between the GC substrate and the Au layer, and between the Au layer and the photoresist. Electron beam lithography is used to achieve features down to 350 nm lateral dimension. The hard mask layer is then structured by argon dry etching. Afterwards, the GC was dry etched. Details are given in Tab. 3.4. Finally, the etched GC sample is cleaned in a cerium nitrate aqueous solution to remove the remaining hard mask. The results presented fulfill all requirements for DOE fabrication, where the design parameters for optics are given by the surface roughness, wall shape, uniformity and surface quality (compare Tab. 3.1 for more details). For a success of the replication process, the mold has to fulfill the same requirements as the DOE. However, the approach presented in [Youn2009] uses Au, which is not allowed in our clean room facilities. Inserting wafers with Au layers into a plasma etching machine will contaminate the chambers. This can strongly influence other processes for

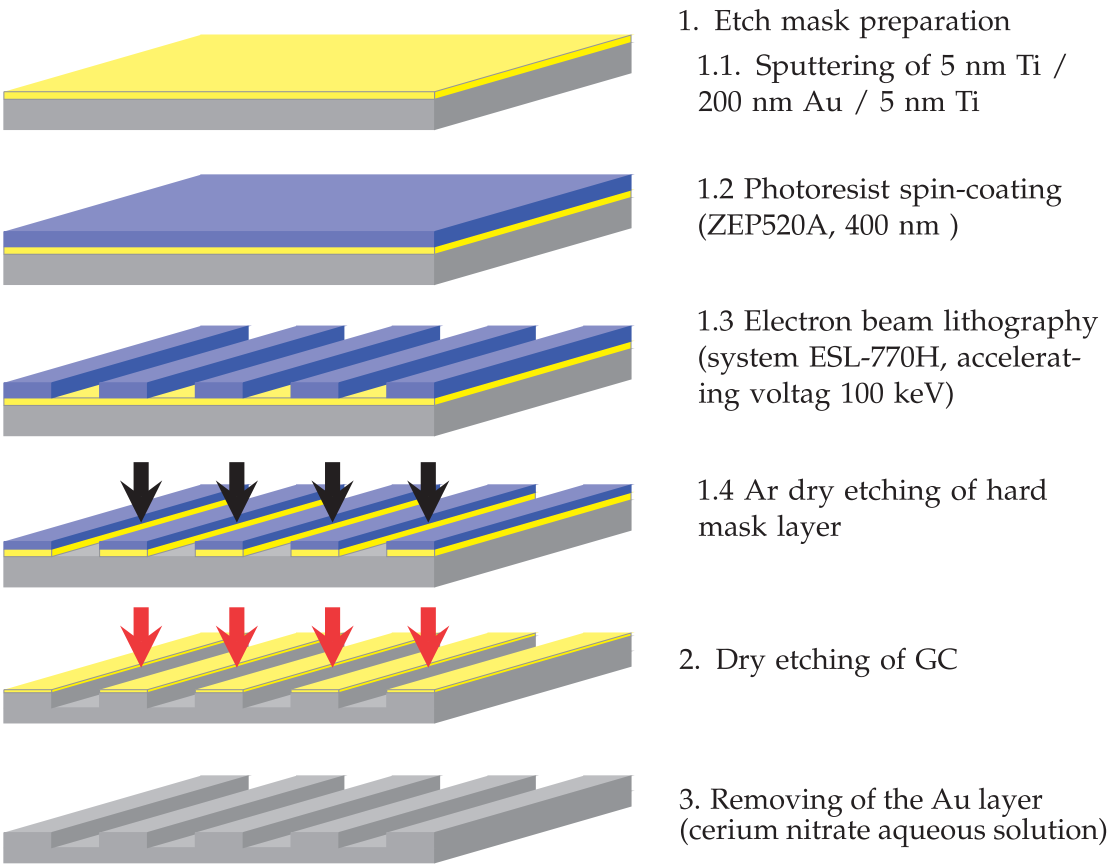

Figure 3.3: Process flow of GC microstructuring taken from Youn et al. [Youn2009] including a gold mask layer and e-beam lithography.

semiconductor devises fabricated in this chamber, since the Au will cause additional doping. Because of this Au is prohibited in the Center of MicroNanoTechnology CMi EPFL Lausanne [2]. In the cleanroom facilities in Microcity EPFL Neuchatel [1] a plasma system is also available, which is used for Si etching with the pseudo Bosch process. An Au contamination of the plasma chamber would mean that the pseudo Bosch process is no longer working. For these reasons, a different process flow for the microstructuring of GC needs to be established.

Machine	parallel platen RIE system (SAMCO, Japan)
Radio frequency (RF) power	200 W
Pressure	5 Pa
Gas flow rates	80 sccm O_2 20 sccm SF_6
GC etch rate	120 nm/min

Table 3.4: Dry etching conditions used by Youn et al. [Youn2009] in process step 2 (Fig. 3.3).

3.3 Process Development with a Binary System

In order to find a working process for the microstructuring of GC, a binary photolithography mask is used. Details of the binary mask design are given in Chap. 2.2.3. We note that the feature sizes are relatively large for DOEs, but we used these designs as a starting point in order to establish a working process. The maximum target etch depth is 692 nm. All GC wafers were etched to have a depth around this value.

First, we will discuss different mask materials for the plasma etching process, which were employed to replace Au as a hard mask. Sections 3.3.1 to 3.3.4 are published in the SPIE conference proceeding [Prater2014]. In Section 3.3.6 the conditions for the plasma etching process are discussed. Finally, we will give a summary of the fabrication process in Chapter 3.3.7. With the established working process, we focus on more advanced DOEs with multilevels in section 3.4, which is published in the SPIE conference proceeding [Prater2015a, Prater2015b]. To improve the resolution we use electron-beam lithography in section 3.5 [Prater2016].

Part of the work presented here was done at the cleanroom facilities at CMi EPFL in Lausanne [2]. This was due to the fact that the OPT laboratory was moved to the new building Microcity EPFL Neuchatel at the end of 2013. The shifted cleanroom at Microcity was only fully operational by mid of 2015. Therefore, we established the whole process including photolithography and RIE etching first at CMi. The multilevel elements were fabricated at CMi. Later the fabrication was done at Microcity. The electron-beam system at Microcity was used for the higher resolution elements, which were fully fabricated at Microcity. Only the thin film deposition was done at CMi.

3.3.1 Photoresist as Mask Material for Reactive Ion Etching

In a first step, we used a positive photoresist (PR) layer (MicroChemicals AZ 1518) as a mask for the RIE of GC. The process flow is depicted in Fig. 3.4. Hexamethyldislazane (HDMS) is used to increase the adhesion between the resist and the GC. The resist was spin-coated on the wafer for a thickness of 2.8 µm. The designed structures were transferred from a quartz chrome mask to the resist via photolithography in hard contact. Then the GC wafer with the patterned photoresist was placed in a SPTS Advanced Plasma System (CMi). Process parameters of the inductively coupled plasma reactive ion etching (ICP-RIE) are 13.56 MHz for the electrodes frequency, a coil power of 950 W, a platen power of 100 W, a platen chiller at 20 °C and a chamber pressure down to 37.5 mTorr. The gas flow rates for O_2 and SF_6 were 40 and 10 sccm. The cooling temperature of the substrate was set to 20 °C. After the etching, the remaining resist was removed with the Remover 1165 (Shipley Microposit).
This process generated microstructured GC (Fig. 3.5) with a very low surface roughness R_a of less than 20 nm (White light interferometer). The obtained selectivity between GC and resist is 1:5 and the wall verticality 37° at 523 nm etch depth. The edges are thus not sharp and the microstructure quality is not sufficient for the use of DOE fabrication.

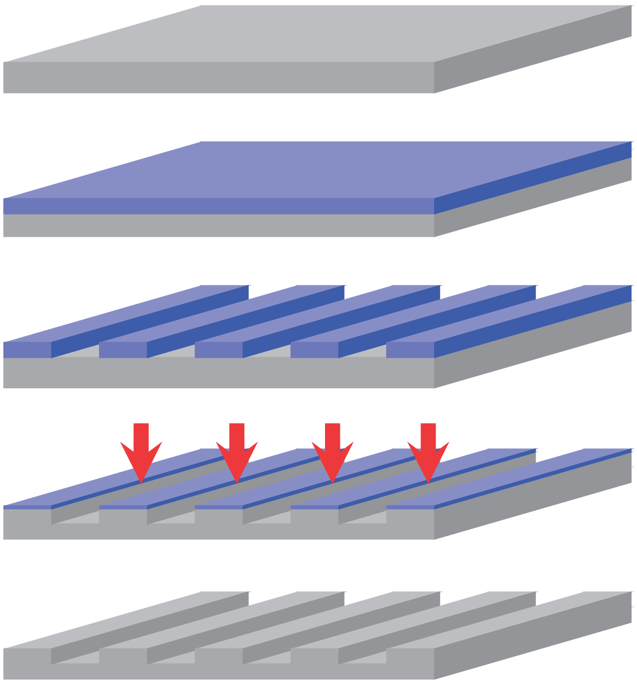

Figure 3.4: Process flow with photoresist as a mask material for microstructuring of GC. Process parameters ICP-RIE step 3. are 13.56 MHz for the electrodes frequency, a coil power of 950 W, a platen power of 100 W, a platen chiller at 20 °C, a chamber pressure down to 37.5 mTorr, backside wafer cooling of 20 °C and gas flow rates of 40 sccm O_2 and 10 sccm SF_6.

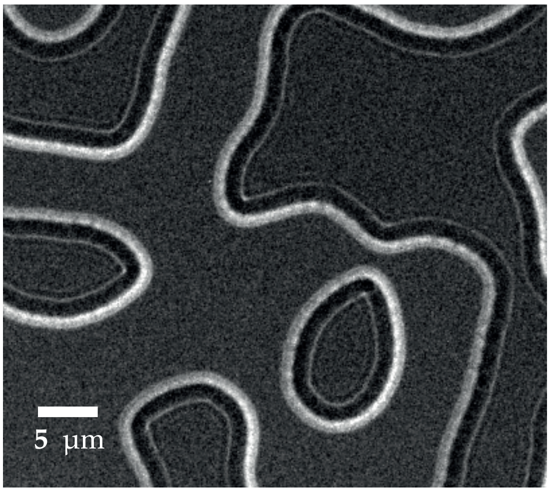

Figure 3.5: Glassy Carbon surface after the microstructuring with a photoresist mask and RIE. A very low surface roughness R_a of less than 20 nm was measured for the 523 nm etched areas. The edges can be seen by the 2 bright lines and are very wide. They have an angle of 37°.

3.3.2 Photoresist as Mask Material for Ion Beam Etching

To increase the selectivity we tested a process based on a photoresist mask and ion beam etching (IBE). An ion beam system Veeco NEXUS IBE-350 (CMi) was used with a beam voltage of 500 V, a beam current of 0.8 A, an electric current density of $1.2\,\mathrm{mA\,cm^{-2}}$ and a tilt angle of 5°. The etching selectivity between the GC and the 1060 nm thick resist increased slightly to 1:2.5. The process results in a slope angle of 61° for an etch depth of 331 nm and a surface roughness R_a of less than 15 nm. The main drawback of this process is the hardening of the resist during the Argon-ion bombardment. This leads to

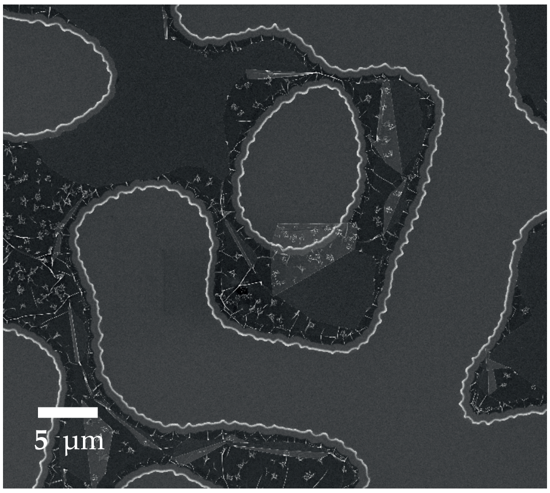

Figure 3.6: Glassy Carbon surface after the microstructuring with a photoresist mask and ion beam etching. The photoresist is hardened during the Argon-ion bombardment and cannot be removed fully with the solvent Shipley 1165 or a piranha etching. The hardened photoresist layers can be seen on the unetched areas.

difficulties for resist removal which cannot be fully accomplished by the solvent Shipley 1165 or a piranha etching (Fig. 3.6). It is recommended to break the hardened resist in an O_2 plasma ashing-step before the wet etching step of the resist. However, this will also etch the GC surface and have the same micro masking effect reported by Youn et al. [Youn2009]. With the ion beam etching in combination with the photoresist, it is thus not the optimal solution to microstructure GC surfaces with high quality.

3.3.3 Aluminum as Mask Material for Reactive Ion Etching

It is a common approach to use a hard mask to increase the selectivity between the substrate and the mask. Therefore, different metals as mask material were applied. The process flow using a hard mask (Fig. 3.18) becomes longer and more demanding in comparison to a process with a resist mask only (Fig. 3.4). Aluminum is a hard mask material used for silicon dry etching and is not chemically etched by the fluorine.

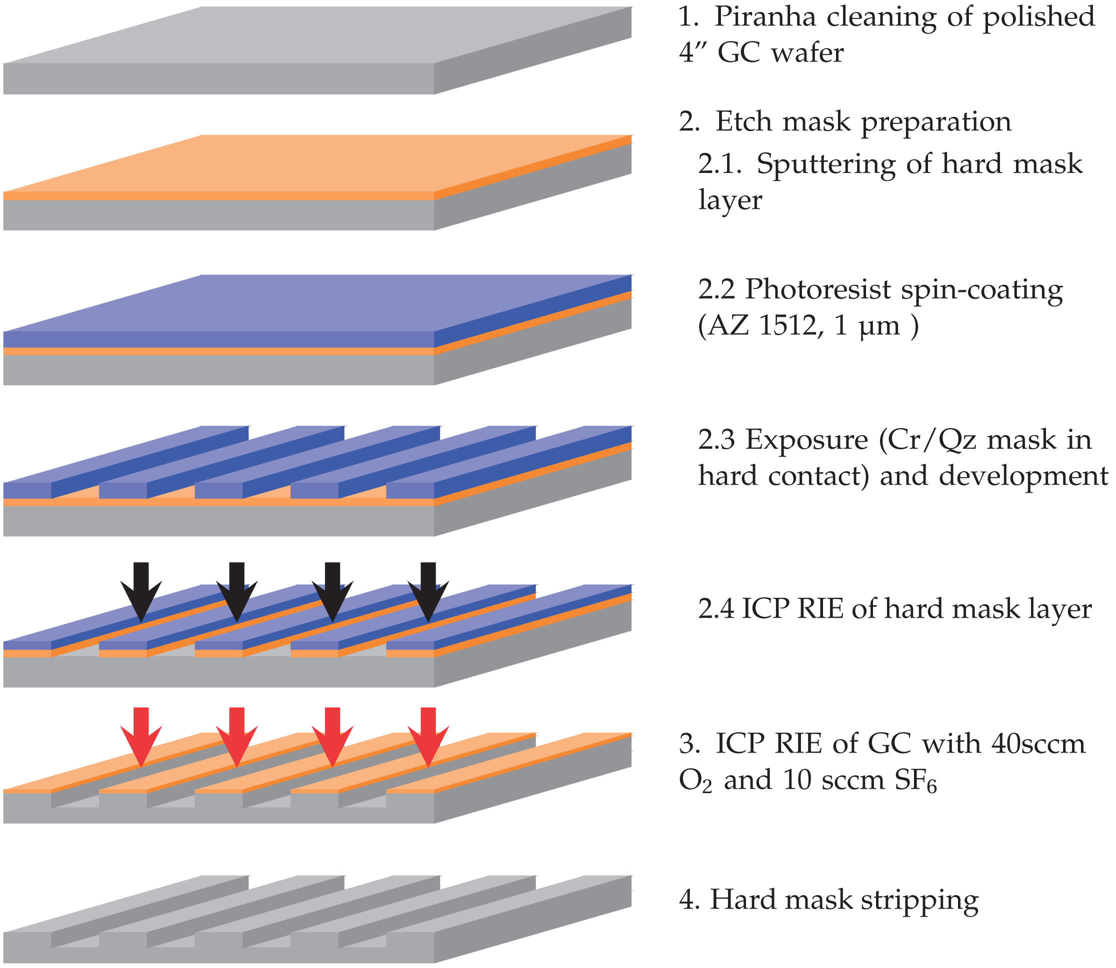

Figure 3.7: Process flow of GC microstructuring with a hard mask. The conditions for the ICP-RIE step 3. are the same as in Fig. 3.4.

A titanium layer of 5 nm was used to increase the adhesion between GC and Al and between Al and photoresist. The layer thickness of Al was set to 200 nm. After the sputtering of the metallic layers, the wafer is spin-coated with the photoresist and exposed with the photolithography mask in hard contact. The pattern is then transferred from the resist to the metallic layer with an ICP-RIE process in a Cl_2/BCl_3 chemistry. After the etching of the hard mask layers, the substrates were rinsed into deionized water and the remaining resist is stripped with Remover 1165 (Shipley Microposit). The GC etching was done in an ICP-RIE system (SPTS Advanced Plasma System) in an O_2 $/SF_6$ chemistry. The etching selectivity between the GC and the aluminum is 1:0.4 and thus much better than the one obtained with the photoresist mask. The Al layer was removed by wet etching in HF(49%):H_2O(1:50).
The GC surface after the microstructuring is shown in Fig. 3.8. This approach fails due to the poor surface quality of the etched GC. Non-volatile particles are present on the whole wafer area and could not be removed by HF or Piranha. The most likely explanation of this is a re-deposited of aluminum fluorine compound on the GC surface which is very resistant and cannot be removed with the O_2 $/SF_6$ RIE.

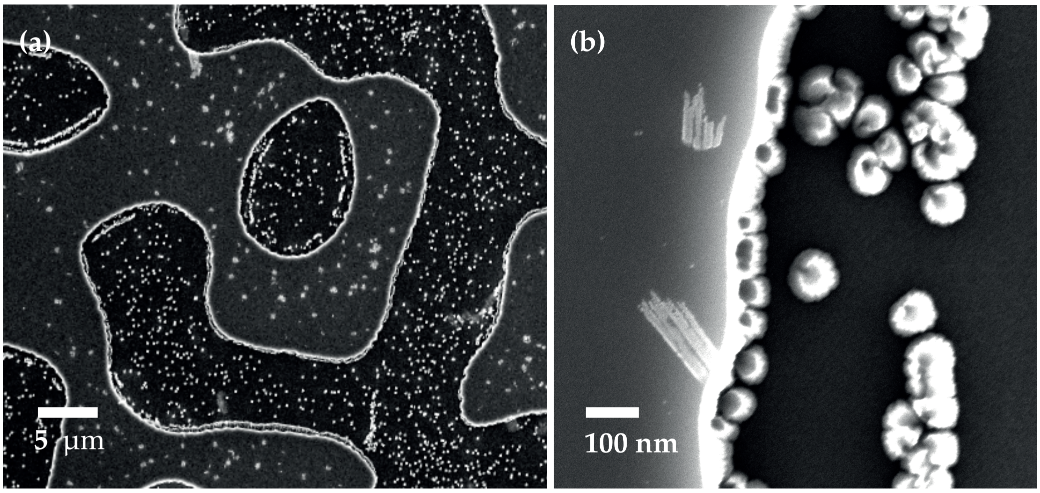

Figure 3.8: Glassy Carbon surface after the microstructuring with an Al mask and RIE. (a) particles are present surface. (b) higher magnification image shows additional features in the etched areas, which could not be removed.

3.3.4 Titanium as Mask Material for Reactive Ion Etching

Instead of Al, we used Ti as a hard mask layer for the etching of glassy carbon. The polished glassy carbon wafer is sputtered with a 500 nm titanium layer. A 1 µm thick photoresist layer (AZ 1512) is spin coated on top and exposed in hard-contact mode. The exposed resist was removed in a developer solution and rinsed in deionized water. The pattern is then transferred from the resist into the Ti layer with the same ICP-RIE process as the aluminum layer. We choose a minimum etching time to ensure a clean glassy carbon surface. We use the same ICP-RIE process as for the Al process to etch the

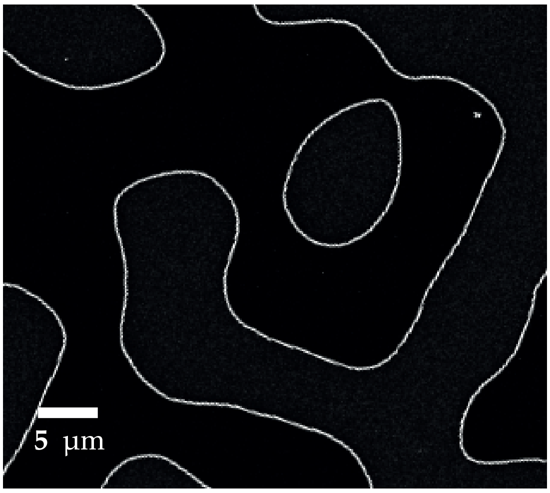

Figure 3.9: Glassy Carbon surface after the microstructuring with a Ti mask and RIE. A particle-free GC surface with an etch depth of 596 nm is seen with a high surface quality.

GC substrate.The last step of the process flow is to remove the remaining mask layer. Ti is wet etched in HF(49%):H_20(1:50).

Figure 3.9 shows a 596 nm deep etched glassy carbon surface fabricated with the Ti hard mask. A particle-free GC surface is seen with a high surface quality. There is hardly a difference between the etched and non-etched surface areas. For a GC etching chemistry of 40 sccm O_2 and SF_6 the parameters are given as: The titanium etch-rate is 1.5 nm/sec. The GC etch rate is 7.36 nm/sec. Therefore, the selectivity GC:Ti is 5:1. The Ti layer thickness of 250 nm was chosen to ensure a maximum etching depth of 1 µm.

The etching of the hard mask layer changes the resist chemically and physically. A hardened surface layer is formed. When this photoresist is removed in a wet etching step, the hardened resist surface layer may fall on top of the substrate surface and is not removed by the remover solution. An example is shown in Fig. 3.10. The titanium can be seen in

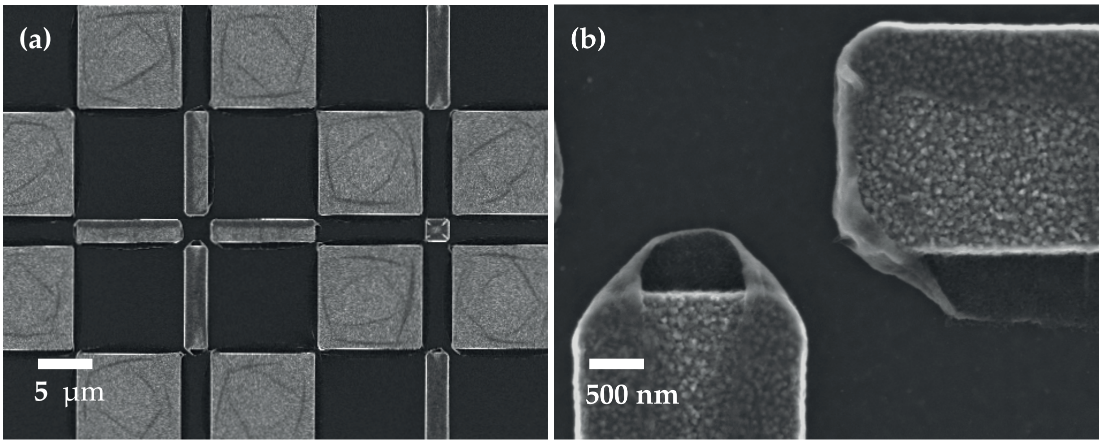

Figure 3.10: GC surface after the etching of the Ti mask. In some cases, residual hardened resist layers are present on the surface after the removal of the photoresist.

the granular areas and the GC surface is seen as the black parts. Grey films are present on parts of the Ti areas and fall partially on the GC areas. This unwanted contamination layer could be removed by a short O_2 plasma etching to break the hardened resist before the wafer is transferred to the wet etching bath. However, an O_2 plasma etching would increase the roughness of the opened glassy carbon regions. That is why, we choose to keep the remaining resist for the glassy carbon etching with O_2/SF_6, where the etching time is long enough to etch the total resist layer.

The quality of the hard mask layer in terms of surface roughness and layer homogeneity will directly influence the edged walls in the GC. A SEM image of the deposited Ti layer is shown in Fig. 3.11 (a). Within a few seconds, titanium forms a TiO_2 grain layer when exposed to air. The thickness of the TiO_2 layer is in the order of nm and results in a roughness R_a of ca. 10 nm. During the opening of the hard mask in the Cl_2/BCl_3 etching, the TiO_2 grains will imprint their shape on the wall shape of the titanium hard mask layer. Therefore, the TiO_2 grains will cause a deviation of the GC walls from a straight line, which can be seen by the etched GC walls in Fig. 3.11 (b). The grains with a size of 70 to 150 nm and the Ti layer thickness of 250 nm will also limit the minimum feature size to ca. 1 µm. For the diffractive optical elements shown here we used photolithography in hard contact, which has a resolution limit of 2 µm. For advanced techniques like electron-beam lithography the resolution is determined by the size of the grains to ca. 1 µm. The grainular texture of the TiO_2 layer can vary over the surface. In Fig. 3.12 a different element is imaged. The deviation of the ideal edge direction is stronger than in Fig. 3.11. To investigate the surface profile of the etched microstructures further, the GC surface was imaged from different perspectives. In Fig. 3.12 (b) a view nearly parallel to the substrate surface is given.

This sample was cut to measure the height profile more accurately. First, we used a dicing saw 1006A from Micro Automation Inc. to cut the 1 mm thick GC substrate by 0.8 mm into the unstructured backside. We then mechanical broke last ca. 0.2 µm by hand to achieve a clean and flat cut edge. The profile of the broken GC surface is given in Fig. 3.12 (c). From the side view, one can see that the walls are much steeper than what we

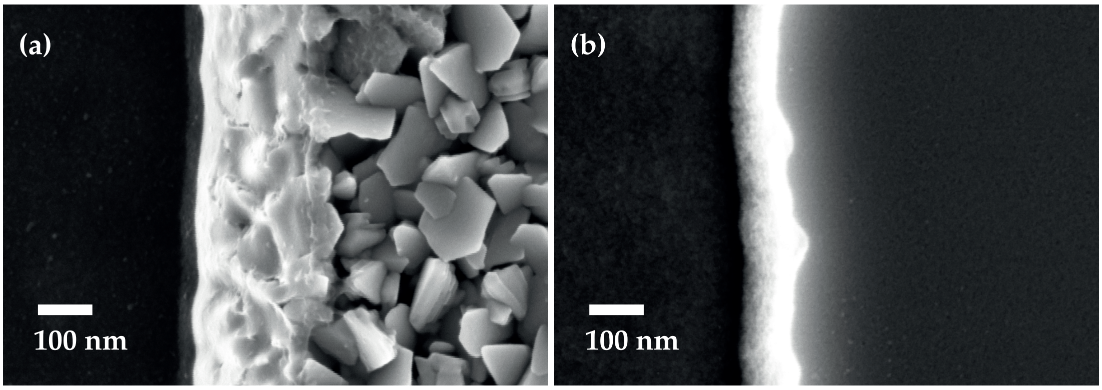

Figure 3.11: The Ti layer mask (a) shows a grainy surface texture, which will result as additional edge roughness of the etched GC surface (b).

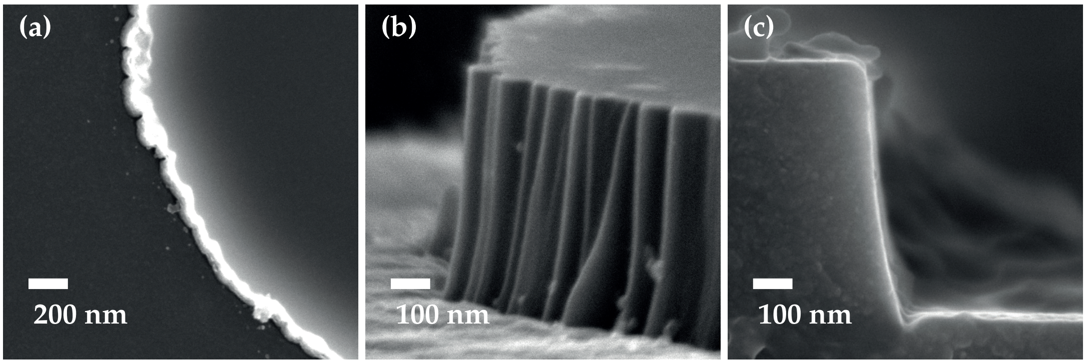

Figure 3.12: SEM images of the 596 nm deep microstructured GC wafer: (a) top view, (b) side view with a tilt angle of 85° and (c) profile of a GC microfeature.

expect from the top view. The walls are very flat at the top part. The steep part of the wall is only 50 nm wide. The verticality is defined as the cosine of the width over the depth. For a depth of 596 nm a verticality of 85° is calculated.
Roughness analysis were performed with an atomic force microscope (AFM) system from Bruker (Dimension FastScan AFM system [2]). In Fig. 3.13 the topographies of

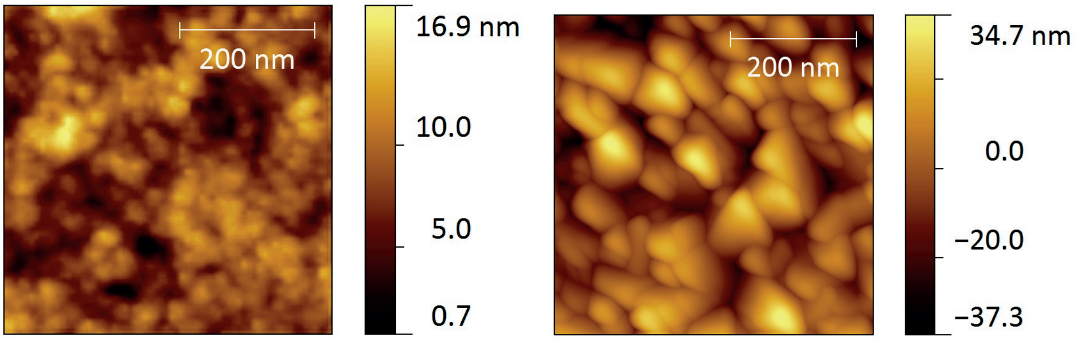

(a) Polished GC R_a=1.73 nm (b) Ti surface R_a=10.6 nm

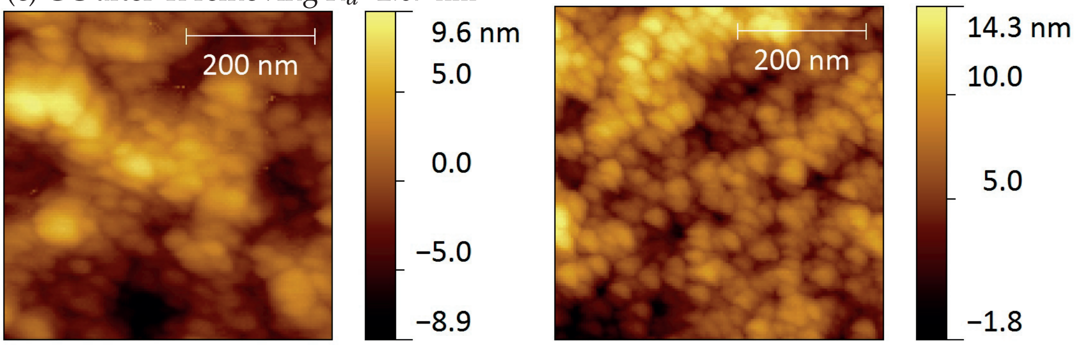

(c) GC after Ti removing R_a=2.07 nm (d) Etched GC surface R_a=2.47 nm

Figure 3.13: Roughness analysis were performed with AFM measurements. The polished GC substrate (a) shows the lowest roughness. The Ti surface has a high roughness due to the TiO_2 grains, which increases the opened GC surface after Ti etching (c). The final GC roughnes for a depth of 523nm (d) is 2.47 nm .

the different process steps are presented. The topography of the glassy carbon shows microdomains. These topographical features can be associated with glassy or more crystalline carbon domains [Harris2004, Brown1998]. The titanium surface has the highest roughness R_a of 10.6 nm caused by the grainy surface texture. The initial roughness of 1.73 nm of the polished wafer is increased during the whole process. The etching of the titanium in the chlorine chemistry enhanced he roughness to 2.07 nm. The final surface roughness is 2.47 nm for an etch depth of 523 nm. The increase in roughness can also be seen in Fig. 3.12 (b): the bottom surface looks rougher than the top part, which is not influenced by the whole micro-structuring process. For a better-controlled batch of samples, the roughness was improved to 2.11 nm for a 730 nm etch depth. This roughness is lower than the requirement of 20 nm and proves the high surface finish of the process.

3.3.5 Si\SiO_2 as Mask Material for Reactive Ion Etching

Next, we will discuss to use Si or SiO_2 as hard mask layers for the RIE of GC. Si and SiO_2 are commonly used in microfabrication and we can profit from processes that are well established. First, a process to deposit the mask layer with a high homogeneity needs to be found. Layer quality strongly depends on the substrate material. Since GC is a very unusual material and has not been used in our cleanroom, no knowledge is available. The surface wetting is e.g. poor, so we expect difficulties with the uniform covering and adhesion of the layers. First, the deposition of SiO_2 layers is discussed. Thereafter, we give details on the deposition of Si layers. Since the Si layer quality is very high, Si layers were further used for the reactive ion etching of GC. We then give information on the optimization of the etching parameters in order to reach a high etch selectivity.

Deposition of SiO_2 layers

A 250 nm thick SiO_2 layer was sputtered with the machine Alliance-Concept DP 650 at CMi. The substrate temperature was kept at 20 °C. After photoresist patterning, the SiO_2 layer was etched with CF_4 ICP-RIE (STS at CMi). The remaining resist was removed with the Shipley Remover 1165. The GC surface with the etched SiO_2 is shown in Fig. 3.14. The layer homogeneity is very poor. The SiO_2 texture is flaky and the SiO_2 edge becomes very wavy. To increase the density of the SiO_2 layer, a higher substrate temperature of 350 °C was tested. For this, the CMi machine SPIDER was used. An improvement in the layer homogeneity was given, but the quality is still not good enough. Additionally, we added O_2 during deposition, since the O_2 changes the SiO_2 composition. After the deposition, the layer lifted immediately of the substrate during handling.

Next, we tested plasma enhanced chemical vapor deposition (PECVD). The machine PlasmaLab 80+ from Oxford instruments was used, which is located at Microcity. The substrate temperature was set to 350 °C. No problems with layer adhesion occurred. The layer surface was very smooth. The result after the GC etching is shown in Fig. 3.15. The GC depth is 530 nm and 92 nm of SiO_2 is etched. This gives a selectivity of GC : SiO_2 of 1 : 0.18, which is comparable to Ti. The etched SiO_2 surface in Fig. 3.15 (b) shows small voids with a size in the 20 nm range. They also cause very wavy walls in the GC substrate.

For electron-beam evaporation, we used the machine EVA600 from Alcatel at CMi (settings: high position, substrate to room temperature and the ion source HRN). The layer homogeneity is very good, which can be seen in Fig. 3.16. Directly after the deposition, the 250 nm SiO_2 layer started to lift of the GC substrate. To improve the adhesion between SiO_2 and the GC substrate it is possible to use a 5 nm thick Ti layer. No tests have been done to prove this concept.

The 3 deposition technologies and their results are summarized in Tab. 3.5. Form the 3 tested process the PECVD gave the best results, but is still not good enough, since the voids in the SiO_2 layer cause severe deviations of the GC wall shapes.

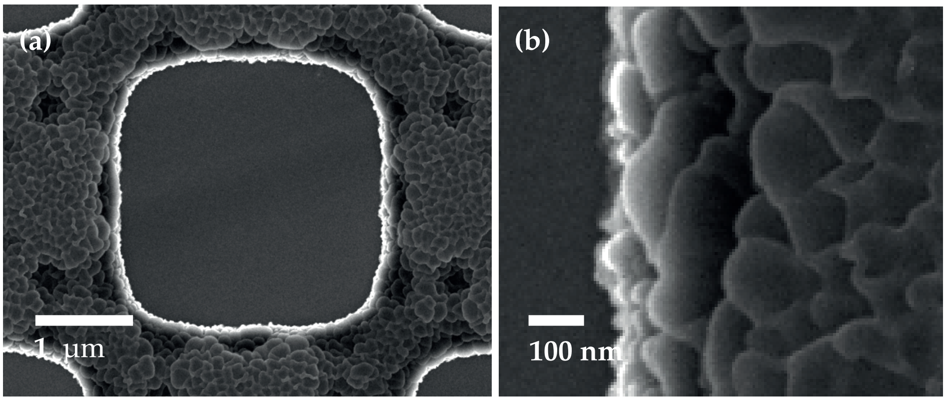

Figure 3.14: The SiO_2 layer was sputtered with DP650 from CMi and etched with CF_4. The poor layer homogeneity can be seen by the flaky texture.

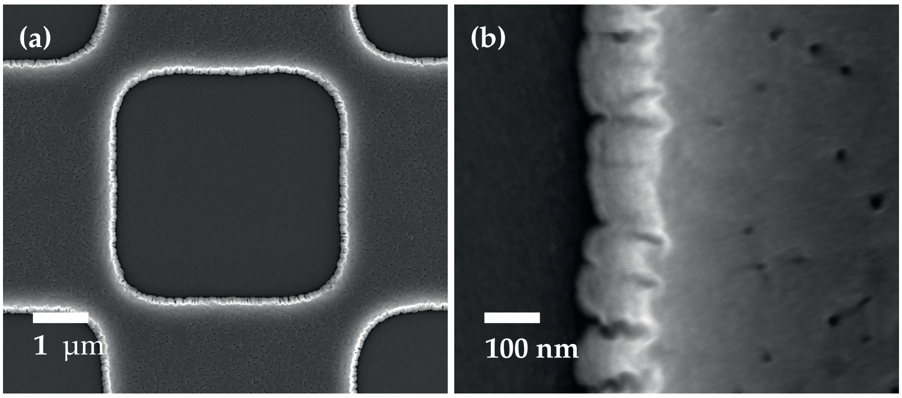

Figure 3.15: Etched GC surface with the remaining SiO_2 layer, which was deposited by PECVD. Small voids in the SiO_2 layer appear during the etching and cause very wavy GC walls.

Process	Machine	Results
Sputtering	Alliance-Concept DP 650 (CMi)	poor layer homogeneity, flaky texture (Fig. 3.14)
Plasma enhanced chemical vapor deposition (PECVD)	PlasmaLab 80+ (Microcity)	poor layer homogeneity, voids (Fig. 3.15)
E-beam evaporation	Leybold-Optics LAB 600 - H (CMi)	poor adhesion, good layer homogeneity (Fig. 3.16)

Table 3.5: Process overview and results for the deposition of a 250 nm thick SiO_2 layer with sputtering, PECVD and evaporation.

Deposition of Si layers

The sputtering of Si layers is done with the machine SPIDER at Cmi because it allows using high temperatures for the substrate, which was set to 350 °C. A first test was done with a layer thickness of 250 nm. The SEM image of the top surface is given in Fig. 3.17 (a) and shows grains with a size of 10 to 30 nm. In a later process optimization step, the layer thickness was reduced to 70 nm. Larger grains in the range of 20 to 50 nm can be seen on the layer surface in Fig. 3.17 (b). Also, the surface does look less smooth than

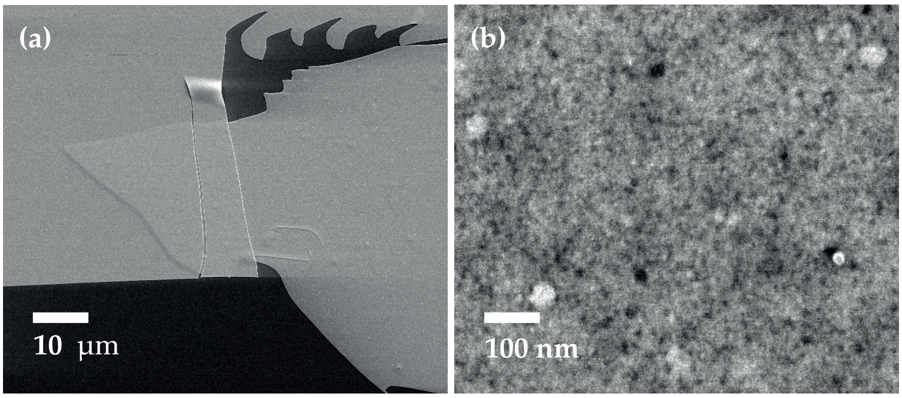

Figure 3.16: The SiO_2 layer deposited with e-beam evaporation has a high layer homogeneity, but shows very bad surface adhesion.

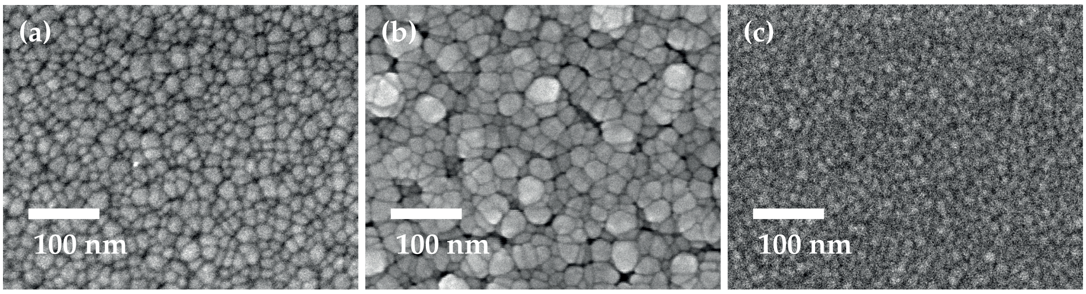

Figure 3.17: SEM images of the top surface of puttered Si layers: (a) 250 nm Si, (b) 70 nm Si and (c) 5 nm Ti with 70 nm Si.

for a 250 nm thickness.

We believe that the surface wetting of GC is very poor. At the beginning of the Si deposition, the Si atoms/clusters migrate away from the GC substrate and form larger domains. When the layer grows and the GC substrate is covered with a Si film, Si is deposited on Si and smaller domains are more likely with a higher layer density.

An additional 5 nm layer of Ti was used to improve the adhesion between the Si and the GC substrate. The surface of the 5 nm Ti/70 nm Si is shown in Fig. 3.17 (c) and a low surface roughness is given. The imaged grains are at the resolution limit of 20 nm of the SEM. Atomic force microscope (AFM) measurements showed that the surface roughness R_a of the 70 nm layer is 1.7 nm and improved to only 0.47 nm for the 5 nm Ti/70 nm Si layer. Thus, a high layer homogeneity can be assumed.

As an alternative for sputtering, we tested PECVD. A deposition of 250 nm Si showed similar results to the sputtered 250 nm Si. A Ti adhesion layer would improve the quality further. The PECVD machine has no Ti target available. Deposition of Ti and Si in 2 different machines is not optimal because the 5 nm Ti layer would form a TiO_2 layer with a grainy texture when exposed to air in a few seconds.

The tested process and their results are summarized in Tab. 3.6. In conclusion, the best layer quality was found for sputtering of 5 nm Ti/70 nm Si layer. This process was used for the microstructuring of GC in the following section.

Process	Machine	Results
Sputtering	SPIDER (CMi) substrate temperature 350 °C 70 nm Si	good adhesion; larger Si grains close to GC surface
	SPIDER (CMi) substrate temperature 350 °C 70 nm Si and 5 nm Ti adhesion layer	very good adhesion due to Ti layer
PECVD	Machine from PV-Lab (Microcity) 70 nm Si (no Ti available)	good adhesion

Table 3.6: Process overview and results for the deposition of a Si layer with sputtering, and PECVD. The best layer quality was found for sputtering of a 5 nm Ti/70 nm Si layer.

Process Development for Si as Mask Material for Reactive Ion Etching

The Si process flow is depicted in Fig. 3.18. A 5 nm Ti layer was used as an adhesion layer between the 70 nm Si and the GC substrate. The deposition was done by sputtering at a substrate temperature 350 °C. The photolithography step is the same as the one employed for the Ti process. For the hard mask opening of Si, we used an ICP-RIE process with CH_3/SF_6 (STS at CMi). The photoresist is not removed for the same reason as for the Ti process: the photoresist develops a hardened top surface during the Si etching, which will fall on the GC surface in the photoresist remover solution. After the ICP-RIE of the GC, Si is removed be wet etching with HNO_3 (70%):HF (49%) : H_2O (50:3:20).

Figure 3.19 shows a GC surface structured with this process. The Si/Ti mask is not removed yet. The surface of the mask layer looks very smooth, no voids or flakes can be seen. This suggests a high layer homogeneity. The GC was etched to a depth of 850 nm. It can also be seen that the wall is very steep. In the SEM images from top view a wall

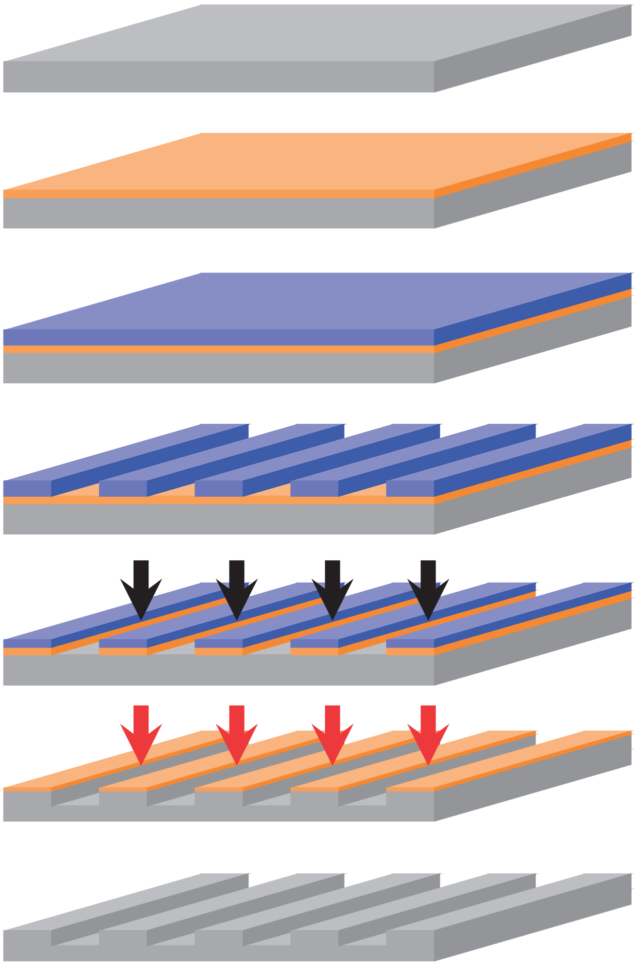

1. Piranha cleaning of polished 4″ GC wafer

2. Etch mask preparation

   2.1. Sputtering of 5 nm Ti and 70 nm Si

   2.2 Photoresist spin-coating (AZ ECI 3007, 530 nm)

   2.3 Exposure (Cr/Qz mask in hard contact) and development

   2.4 ICP RIE of Si with CH_3/SF_6 (STS at CMi)

3. ICP RIE of GC with 45 sccm O_2 and 5 sccm SF_6 **selectivity GC:Si 19:1**

4. Hard mask stripping with wet etching in HNO_3(70%) : HF(49%) : H_2O (50:3:20)

Figure 3.18: Process flow of GC microstructuring with a Si hard mask. The hard mask layer was sputtered for 5 nm Ti/70 nm Si layers.

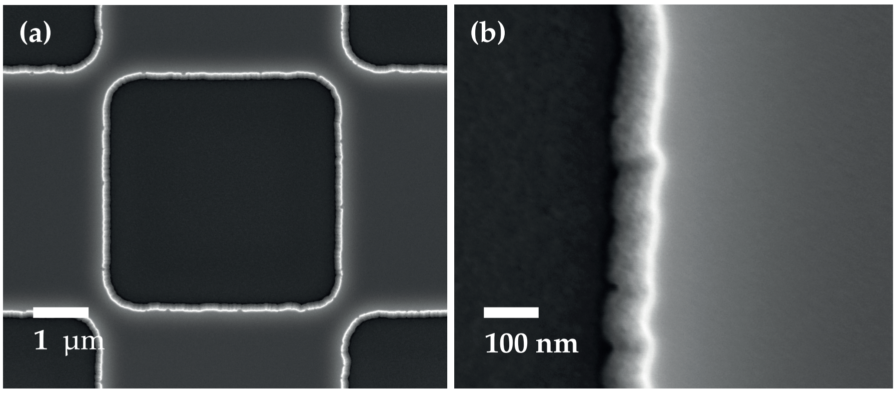

Figure 3.19: GC surface after RIE etching with the remaining Si/Ti layer. The etch depth of GC is 850 nm. The etched Si layer shows no nanofeatures, which suggests a high layer homogeneity.

Figure 3.20: SEM image of the photoresist is taken without an Au coating, which decreases the resolution. The photoresist is after development not perfectly straight.

width of 70 nm can be approximated giving an 83° wall verticality.
The quality of the etched GC surface is comparable to the one obtained with the Ti process. However, a wavy wall shape can clearly be recognized. We believe that the origin is not the inhomogeneity in the silicon layer. Resolution limitations are mostly due to the photolithography in hard contact. In comparison, the photoresist pattern is shown in Fig. 3.20 with the same scale as the microstrucutured GC in Fig. 3.19 (b). The size of the resist waviness corresponded to the waviness in the GC walls. Therefore, using higher-resolution lithography methods for creating the hard mask(s) should be used for creating GC molds with higher accuracy.

For a GC etching chemistry of 40 sccm O_2 and SF_6, the GC to Si selectivity is with 6:1 slightly better than the one obtained for Ti. GC is etched by the O_2 and Si is etched by the SF_6, which is added to ensure a low surface roughness. By changing the gas ratio between the O_2 and SF_6 to 45 sccm and 5 sccm, we could achieve a selectivity of 19:1. AFM measurements showed that the changed ratio of etching gasses did not affect the etched GC surface quality. In both cases, a roughness R_a of 1.7 nm was found.

The etch rates are depicted in Fig. 3.21. The etch rate for GC and Si are 10.5 nm/s and 0.55 nm/s respectively. The etch depth variation between the different etch runs is strong. The maximum deviation from the fit curve was 25 nm. Problem with the SPTS machine accrued mainly after maintenance. It is advised to wait minimum 1 day after the last maintenance service. For diffractive optical elements, an accuracy of ± 5% form the depth is desired. Additionally, the etch rate of GC is very fast. One can only set process time by seconds and the etch rate of 10.5 nm per seconds decreases the accuracy. It is possible to optimize the etch process for a slower etch rate by e.g. decreasing the platen power and/or the coil power (details about the etch process can be found in section 3.3.6).

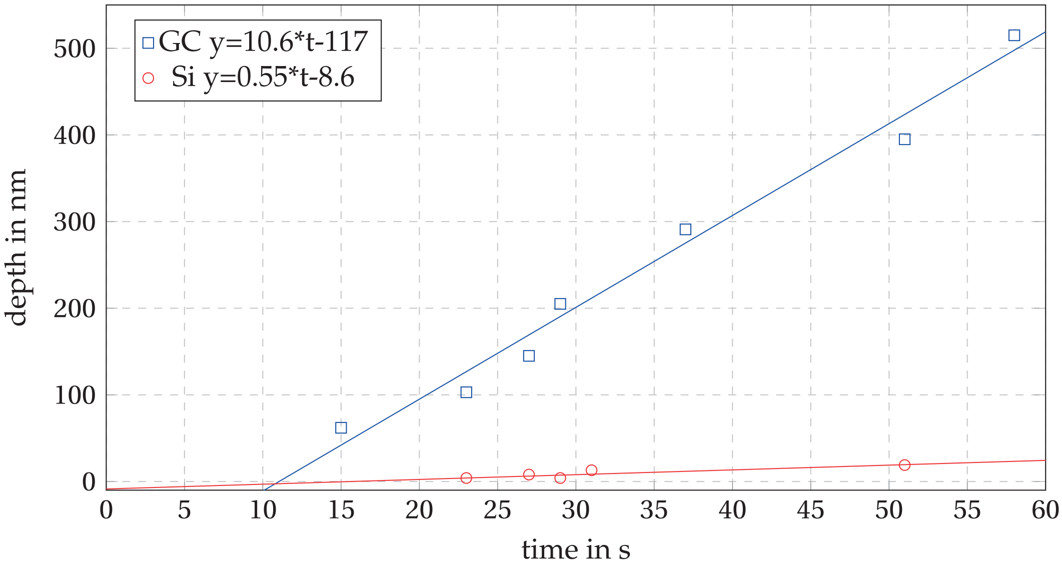

Figure 3.21: Etch rate of GC and the Si hard mask, where 45 sccm O_2 and 5 sccm SF_6 are used during the RIE etching. A very good etch selectivity between GC and Si of 19:1 is reached.

However, the process gave a very good result for the GC microfabrication. The selectivity of 19:1 between the GC and the Si allowed to decrease the Si layer thickness significantly. For a maximum etch depth of 1 µm the etched Si thickness is 53 nm. Thus, we set the Si thickness to only 70 nm. In general, a thinner mask layer gives a better resolution, smaller wall width, and higher wall verticality. We believe that due to the smaller layer thickness and better layer quality the Si process will enable smaller feature sizes than the Ti process. To prove this, further investigations will be done to combine e-beam lithography with the Si hard mask to reach feature sizes well below 1 µm. The approach is discussed in section 3.5.

We believe that the ratio of the O_2 and SF_6 could also be changed in the opposite way: a higher amount of SF_6 will result in a selectivity close to 1 : 1, which would enable a transfer of a continuous relief from the Si hard mask into the GC substrate. First, the photoresist needs to be structured with the continuous relief. Kley et al.[Kley1997] discussed different surface profiling methods like laser-beam writing, electron-beam writing and optical half-tone mask technology. Afterward, the resist profile is copied to the Si hard mask and finally the continuous Si surface is transferred 1 to 1 into the GC substrate with an adopted RIE process.

In order to achieve a high GC surface quality, the homogeneity of the Si layer needs to be excellent. We tested this approach for 2 µm thick Si layers. The 2.4 µm thick photoresist was deformed by a thermal reflow process [Herzig1997] to achieve a continuous test shape. A RIE etching process with the STS machine at CMi EPFL Lausanne was used, which provides a 1:1 selectivity between the photoresist and the Si. The results are shown in Fig. 3.22 (a). A test pattern with 5 µm circles in diameter was etched. A small part of the photoresist is remaining, which can be seen at the center of the circle. The sputtered Si layer shows grains with a maximum size of 250 nm. A Si wafer was etched with the same process and is depicted in Fig. 3.22 (b). The Si wafer shows a much better homogeneity, which indicates that Si etch process is not causing the grain texture of the sputtered Si layer. The grainy texture of the sputtered Si layer is a major limiting factor if it should be used for further form transfer into GC. The surface roughness of the etched GC surfaces will be increased accordingly.

Additional limitations arise from the maximum layer thickness of Si. We found that a thickness of 4 µm can still be deposited. If the layer is too thick, the stress in the layer induced by the temperature variation during deposition might become so high that the layer deforms and lifts off the substrate.

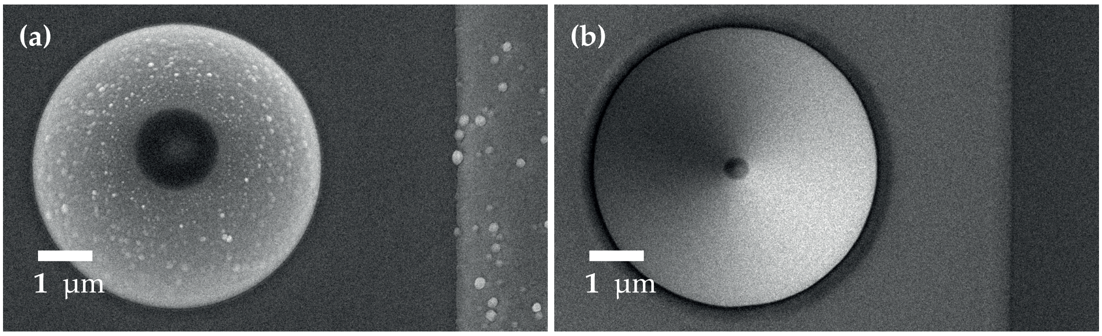

Figure 3.22: Continuous photoresist shape fabricated by a reflow process with 5 µm large circles. The resist shape is transferred into Si: (a) 2 µm Si layer on GC wafer and (b) Si wafer (monocrystalline).

3.3.6 Reactive Ion Etching

Diffractive optical elements are typically fabricated by dry etching. Wet etching of fused silica is isotropic and the substrate material is removed under the photoresist mask resulting in very rounded surface profiles. This becomes more pronounced for smaller feature sizes and with higher aspect ratios. Dry etching can give very repeatable results. With the right conditions, dry etching is highly anisotropic. Dry etching includes both chemical reactions and kinetic removal. The generated plasma includes species that reactive with the substrate material. The reaction products are volatile and are removed from the chamber by the vacuum pumps. Owing to the chemical reaction the etch selectivity is very good. However, wet etching shows typically no directionality and is thus not optimal. Kinetic removal includes the acceleration of ions, which knock atoms out of the substrate. The kinetic removal is very directional, but also a considerable amount of the etch mask can be removed. Reactive ion etching (REI) combines both aspects. The reactive ions are generated in the plasma and are accelerated towards the substrate by a bias voltage, which provides directional etching. The ions react with the substrate material. Thus, the etch selectivity is kept high.
In this work, 2 machines from Surface Technology Systems STS were used. The scheme of STS is given in Fig. 3.23. In order to have more freedom of parameters an inductively coupled plasma is used. A coil around the plasma chamber generates an electro-magnetic field, which defines the plasma to a smaller region. The coil power determines the plasma density. A higher plasma density will e.g. result in a faster etch

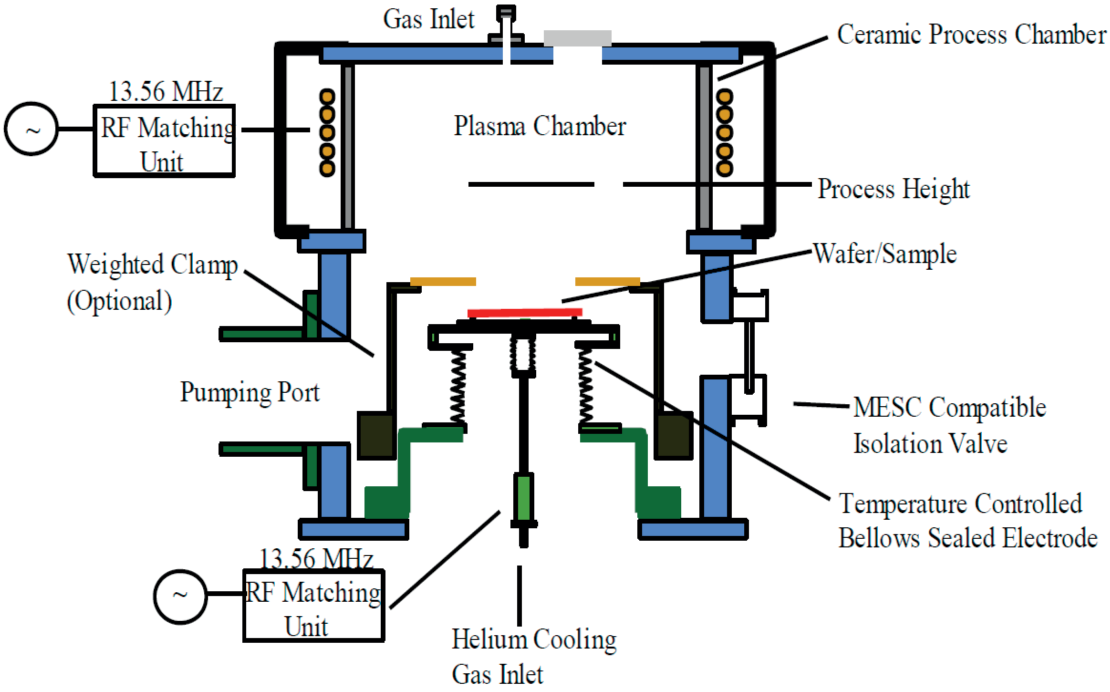

Figure 3.23: Schematic of the STS ICP system (taken from [7]).

rate. The physics is not always well understood since the composition of the plasma species might also change, which can increase or decrease the etch rate of the substrate. The energy of the ions is set by the bias voltage and thus the amount of kinetic etching. The ICP-RIE systems we used are STS at Microcity and SPTS at CMi. The 2 machines are having different chamber geometries and the STS is designed for a smaller pressure range than the SPTS, which is caused by the vacuum pump. A smaller pressure in the chamber allows the ions to move towards the substrate with fewer collisions and thus more directional. Also etch products are faster removed from the substrate surface. But the gas/ions are removed also faster from the plasma, which decreases the etch rate. In some cases, the plasma becomes unstable because the ions are removed too fast from the plasma and cannot create enough new ions by collision.
Youn et al. used a parallel-plate RIE system (SAMCO, Japan) [Youn2009]. The etch conditions are given in Tab. 3.7. As a starting point for finding good etch condition, we use the settings from Youn, which are repeated in Tab. 3.7. A parallel-plate RIE system is used. The etch rate is with 2 nm/s quite slow. We use a ICP-REI system with one more parameter: the coil power. Thus, plasma density and ion energy can be tuned separately. The settings for the SPTS were suggested by CMi stuff (Tab. 3.8 (A)). The gas flow rates of the SPTS were limited below 50 sccm. Therefore the flow rates are set as 40 sccm for O_2 and 10 sccm SF_6, which is maintaining the gas ratio of 4:1 and following the suggestion of Youn et al. The coil power is set to 950 W to generate a high-density plasma for fast etching with a high selectivity. The etch rate of GC is with 7.5 nm/s considerable faster than the one from Youn et al. However, the etch selectivity of GC:Si is only 6:1. By changing the gas ratio of O_2 and SF_6 to 9:1 a much better selectivity was reached with 19:1. Profiles of GC etched with the 2 different gas ratios are shown in Fig. 3.24 (a)-(b). The influence on the edge profile is not noticeable. Wall angles of higher than 80° are reached. Trenching is also present to a minor degree.

Machine	parallel-plate RIE system (SAMCO, Japan)
Radio frequency (RF)	13.56 MHz
Platen power	200 W
Pressure	5 Pa 37.5 mTorr
Gas flow rates O_2	80 sccm
SF_6	20 sccm
GC etch rate	2 nm /s
selectivity GC : Au	20 : 1

Table 3.7: Etching conditions used by Youn et al. [Youn2009] with a 5 nm Ti/ 200 nm Au/ 5 nm Ti hard mask.

Machine	ICP RIE system SPTS (CMi)		ICP RIE system STS (Microcity)
Radio frequency (RF)	13.56 MHz		13.56 MHz
Coil power	950 W		950 W
Platen power	100 W		100 W
Pressure	5 Pa 37.5 mTorr		2.7 Pa 20 mTorr
backside cooling	10 °C		20 °C
Gas flow rates	(A)	(B)	(C)
O_2	40 sccm	45 sccm	45 sccm
SF_6	10 sccm	5 sccm	5 sccm
etch mask	250 nm Si	250 nm Si	5 nm Ti / 70 nm Si
GC etch rate	7.5 nm/s	10.5 nm/s	6.3 nm/s
Si etch rate	1.34 nm/s	0.55 nm/s	1 nm/s
selectivity GC:Si	6 : 1	19 : 1	6 : 1

Table 3.8: Dry etching conditions used for SPTS at CMi and STS at Microcity.

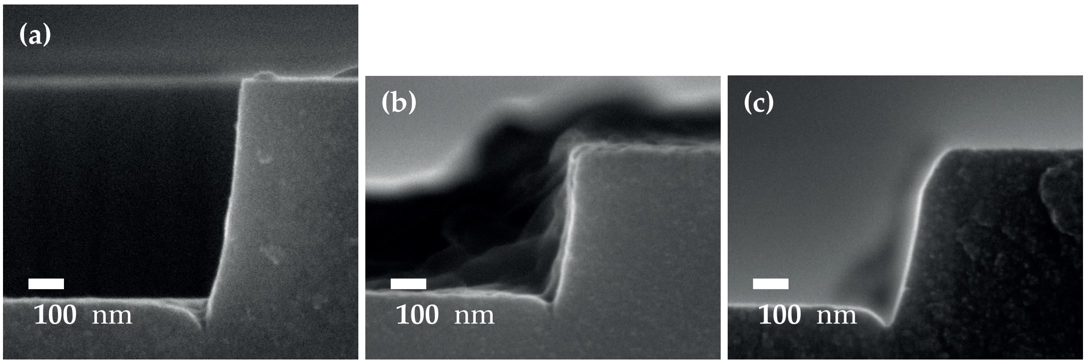

Figure 3.24: GC height profile for 3 different etching conditions: (a) SPTS system (process A) with 250 nm Ti mask, (b) SPTS system with 70 nm Si mask (process B), and (c) STS system with 70 nm Si mask (process C).

The process was transferred to the STS machine at Microcity. The pressure range for this gas flow rates is limited to 5-20 mTorr otherwise the automatic pressure control valve is out of tolerance. The pressure was set to 20 mTorr. The results with the STS were significantly reduced in quality compared to the SPTS. In Fig. 3.24 (c) it can be seen that the wall verticality is reduced and trenching is more pronounced. The etch selectivity is reduced to 6 : 1. The surface roughness is similar to the one obtained with the SPTS. This process was used for the fabrication of higher resolution elements with e-beam lithography (details in section 3.5).

In later etch tests for deep etching a STS process was found that gives an etch selectivity of 17 : 1. A thick Si layer of 2 µm was used to etch 25.8 µm of GC in 72 min. The substrate temperature was reduced to 10 °C, the pressure to 5 mTorr and the platen power was lowered to 50 W. The coil power was kept at the maximum level of the STS because a lower value decreased the selectivity. Additionally, the gas flow rates of 14 sccm O_2 and 1 sccm SF_6 improved the selectivity further. The etching rate of GC reduced to 6 nm/s, which is an advantage for better etch depth control.

The results are depicted in Fig. 3.25. The surface roughness is very low, but the etch walls become rough. During the etching with O_2/SF_6 a passivation layer is deposited on the sidewalls (see Fig. 3.25 (a)), which cannot be chemically removed. This effect can be reduced by e.g. a smaller chamber pressure or a higher substrate temperature, which will increase the surface roughness. A higher substrate temperature of 20 °C will result in a visible micromasking effect. An example with an etch depth of 3.5 µm is given in Fig. 3.26. The surface shows additional grass features, which will increase by further etching.

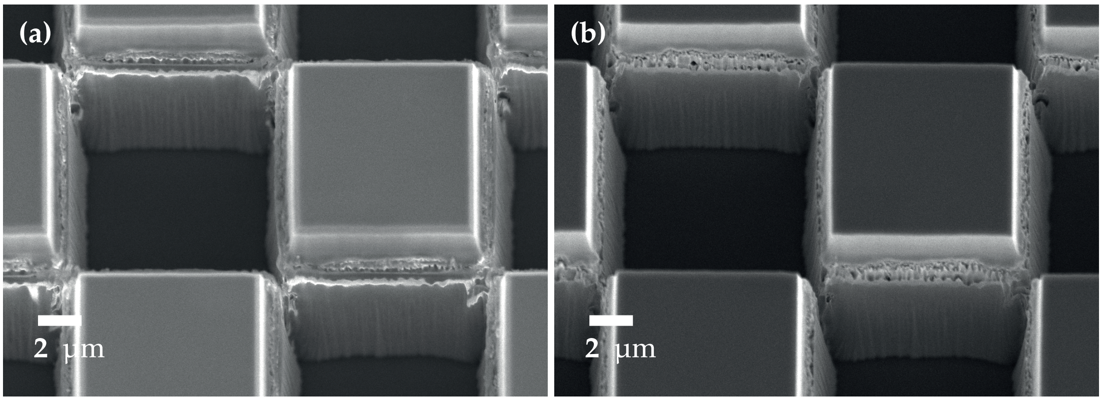

Figure 3.25: Etching of 25.8 µm GC with a 2 µm Si mask: (a) with the remaining Si and (b) final GC surface.

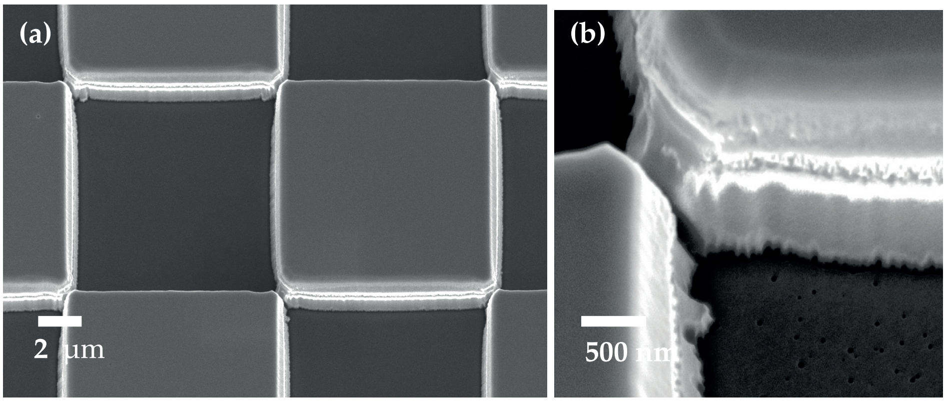

Figure 3.26: Etching of 3.5 µm GC with a 2 µm Si mask at a higher substrate temperature 20 °C compared to Fig. 3.25. The surface shows nm features, which originate from the micromasking effect.

The process is optimized to achieve a high selectivity, a low surface roughness and smooth etch walls. The process for the result in Fig. 3.25 is a compromise between this requirements. The main limitation is the appearing micromasking effect for processes with a higher selectivity.

3.3.7 Summary of Process Development

The process investigated in this work and their results are summarized in Tab. 3.9. The requirements for the diffractive optical elements are also valid for the glassy carbon molds. The sidewall angle is influenced by the selectivity, which is the ratio of the etch rates between substrate and mask material. A high selectivity is necessary to achieve a high wall verticality and to reduce the mask layer thickness, which also increases the lateral resolution. The best results are obtained with a 5 nm Ti/ 70 nm Si mask in combination with RIE. A gas ratio for O_2 to SF_6 of 9:1 significantly improved the etch selectivity (SPTS at CMi).

The 250 nm Ti process also gives acceptable results but has a higher layer roughness caused by the TiO_2 top surface. These features are copied to some extend to the GC microstructures. They can be easily seen as an additional waviness to the otherwise

Mask material	Etching tech.	Selectivity GC : Mask	Wall angle	R_a	Surface Quality
Requirements					
easy to process, high homogeneity		GC ≫ Mask	> 80°	< 20 nm	High (no contamination)
Process overview					
Photoresist 2.8 µm	RIE	**1 : 5**	**37°** (532 nm)	< 20 nm	high
Photoresist 1.06 µm	IBE	**1 : 2.5**	**61°** (331 nm)	< 20 nm	**low, resist not fully removable**
5 nm Ti/ 200 nm Al/ 5 nm Ti	RIE	1 : 0.4	**67°** (460 nm)	**> 20 nm**	**low, residuals in etched region**
250 nm Ti, **grainy surface**	RIE	1 : 0.2	>80° (690 nm)	< 5 nm	high
250 nm SiO_2, **low layer homogeneity**	RIE	1 : 0.18	>80°	< 20 nm	high
70 nm Si (sputtering)	RIE	O_2:SF_6 4:1 1 : 0.17	>85°	< 5 nm	high
		O_2:SF_6 9:1 1 : 0.053			excellent

Table 3.9: Requirements for the diffractive optical elements in comparison to the process results. The results in bolt letters indicate when the process requirements are not met. The best results are obtained with a 70 nm Si mask in combination with a RIE of a gas ratio O_2:SF_6 9:1.

straight lines. The selectivity is with 1 : 0.2 in the same range as for the Si process when the same O_2 to SF_6 gas ratio is used. We note that for a gas ratio of 9:1 the selectivity should also improve. The surface roughness R_a of the GC mold needs to be below 20 nm. For some process this was not met: the Al process resulted in particle contamination in the etched regions, and for the ion beam etching the resist could not be removed.

In the following sections, multilevel DOEs are fabricated with both the Ti process and the Si process. The low layer thickness of 70 nm for Si allows the combination with e-beam lithography for an improved resolution and accuracy.

3.4 Multilevel Fabrication

Multilevel diffractive optical elements were fabricated with 3 photolithography masks for 8 level microstructures. Both the Ti process described in section 3.4.1 and the Si process described in section 3.4.2 were used. The design elements are similar. For each fabrication cycle, one set of 3 masks was ordered from Compugraphix in Jena (Germany). The mask set for the Ti process had the wrong polarity in the alignment mark area, which made a good mask-to-mask alignment very difficult. This problem was corrected for the later mask set, which was used for the Si process. Also, the critical dimensions were increased for some elements. The requirements for the mask-to-mask alignment scale with the critical dimension (CD). These errors are always present in multilevel fabrication technology. Smaller CD and thus a reduced influence of alignment errors allow a better investigation of the influence of the precision glass molding.
The DOE designs, which were fabricated, are given in Tab. 2.6 and act as varying beamsplitting elements. To discuss fabrication results, we will use a more simple design given in Fig. 3.27. It is a blazed grating in one direction and a two spot beamsplitter in the other direction. The edge depth corresponding to a 2π phase shift is defined as h. The first structuring is done for the smallest step h/8, than h/4 and finally the largest step of h/2. This approach minimizes resolution issues by diffraction effects during the

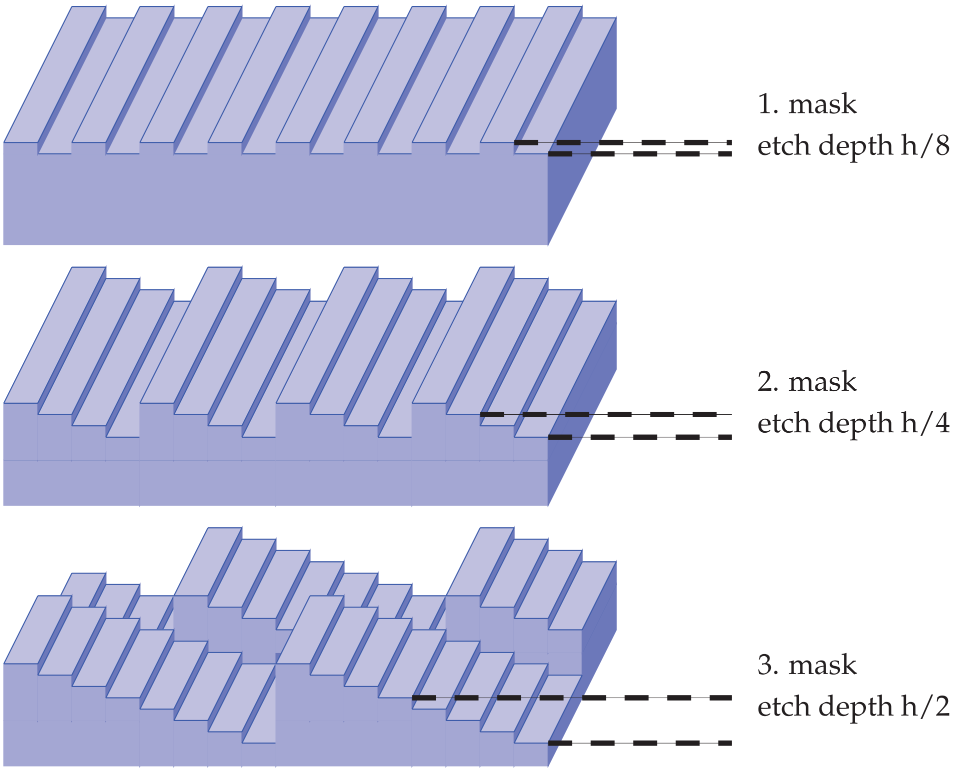

Figure 3.27: Profil of blazed beamsplitter (name A). The first structuring is done for the smallest step h/8, than h/4 and finally the largest step of h/2.

exposure of the resist.
Before the second and third exposure, the mask needs to be overlapped with the already etched surface elements. The 2 main effects are depicted in Fig. 3.28. If we assume a perfect alignment, but an overexposure is introduced, then the linewidth of the photoresist is too narrow Fig. 3.28 (a). The etched lines from the 2 photolithography steps do not overlap perfectly with each other, although the mask-to-mask alignment was perfect.
A more pronounced influence have e.g. mask-to-mask misalignment, for which the accuracy is typically in the range of 0.5 µm. It is very difficult to accomplish higher precision with mask aligners. Figure 3.28 (b) shows how mask misalignment can influence the final etch result. It can be seen that the levels are not perfectly aligned resulting in thin line features. Both errors will result in similar line features.

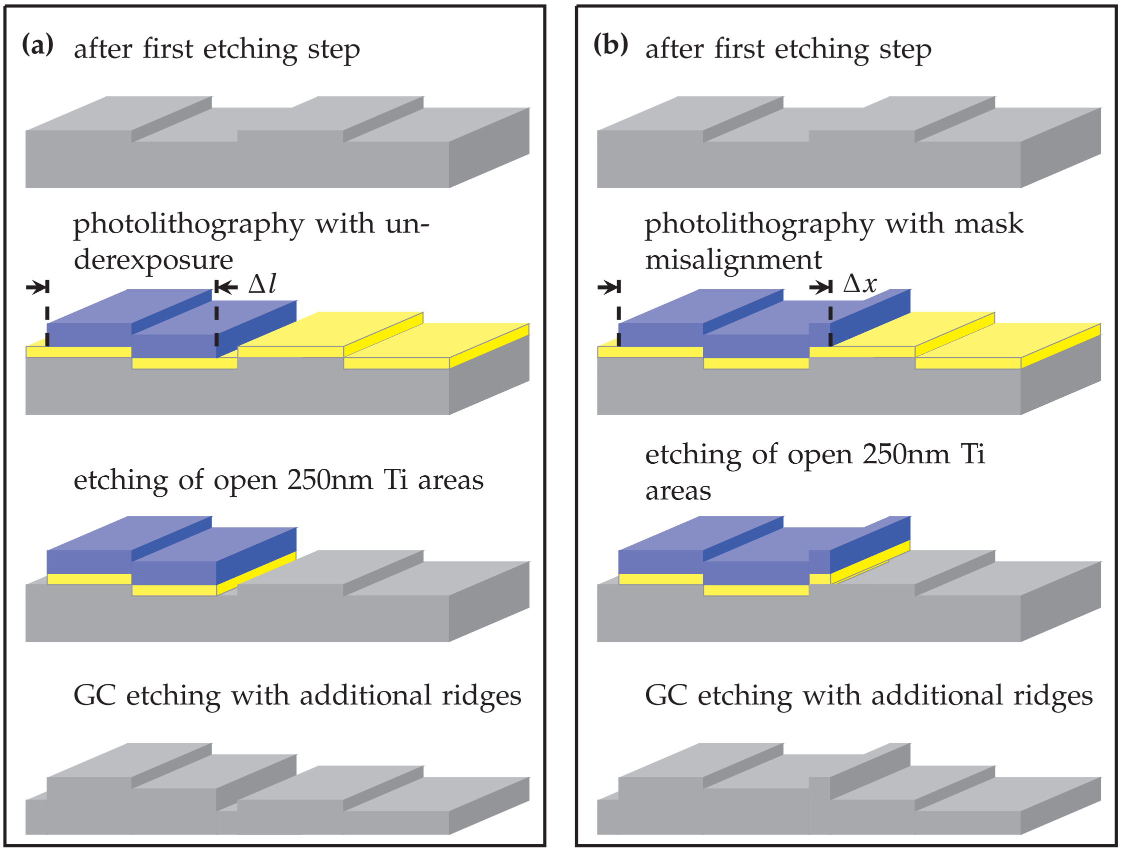

Figure 3.28: Influence of errors introduced during the photolithography for multilevel fabrication: (a) duty cycle and (b) mask misalignment.

3.4.1 Multilevel Fabrication with a Ti hard mask

We introduce an 8 level microstructuring process for glassy carbon molds with standard photolithography and a Ti layer as hard mask for reactive ion etching. We use the process given in section 3.3.4. The results of this section were published in the conference proceeding Photonics West [Prater2015a].
The microstructuring process (Ti layer deposition - photolithography- etching) of the GC was repeated 3 times starting with the smallest height step of the design that was 200 nm. The second etching depth was 435 nm and the last was 890 nm . The average depth for a corresponding half wavelength (π) phase shift is thus 853 nm. The etching rate using the above mentioned parameters was 8.3 nm /s with an etch depth control better than 30 nm. Better control over the etching depth can be accomplished with an adjusted process and much slower etching rates that can come down to typically 1 $\mathrm{nm\,s^{-1}}$.
SEM pictures of the GC surface are shown in Fig. 3.29. The design parameters together with the fabrication results are summarized in Tab. 3.10. The feature dimensions are smaller than the design values, which indicates an underexposure. Also, the shape of the 4 µm squares introduced during the last etch step show strong form deviations, which is very likely caused by the exposure in hard contact. There are misalignment

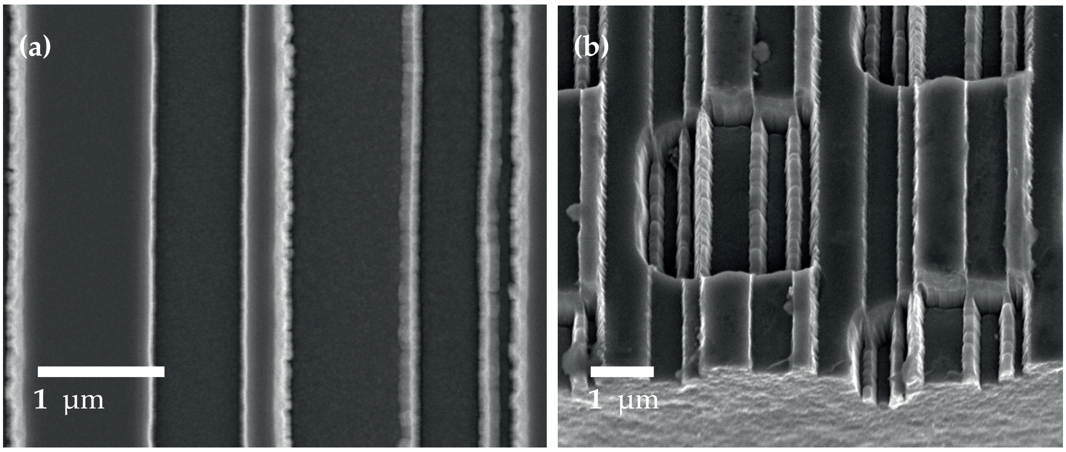

Figure 3.29: (a) GC after 2 etching steps and (b) after 3 etching steps. The design depicted in Fig. 3.27 cannot be recognized in the fabricated element due to too high fabrication errors (details in Tab. 3.10).

		duty cycle		alignment error	
	depth	design	fabrication	Δy	Δx (vertical)
1. mask	220 nm	1 µm lines	0.73 µm		
2. mask	435 nm	2 µm lines	1.8 µm	300 nm	73 nm
3. mask	890 nm	4 µm squares	3.48 µm	-430 nm	-915 nm

Table 3.10: Comparison of design parameters and fabrication results for the element shown in Fig. 3.29. The errors of linewidth and mask-to-mask alignment are in the same range as the critical dimension of 1 µm.

errors with respect to the first etching in the horizontal direction of 300±30 nm for mask 2 and of -430±30 nm for mask 3. In the vertical direction they were -260±30 nm for mask 2 and -1000±30 nm for mask 3. These errors are considerable large with respect to the grating periods of 8 µm and the critical dimension of 1 µm. To avoid such alignment errors advanced alignment techniques on higher generation aligners (<250 nm alignment precision) or electron-beam lithography with misalignment accuracies of less than 100 nm need to be considered. Steppers can reach high alignment accuracy, but they are not considered typically for diffractive optical elements.

In Fig. 3.29 (b) a cross-section of a GC structure is shown. The square areas were etched during the last etching step. Some features etched during the 1st and 2nd fabrication cycle were etched again in the last fabrication cycle. They are placed inside the square areas. When comparing the lines outside the square areas and inside, it can be seen that the lines show different wall shapes. The lines etched 2 times show ridges. This can be explained by the schematic drawing in Fig. 3.30. The step height after the 1st and 2nd etching are 220 nm and 435 nm, respectively which is in the range of the thickness of

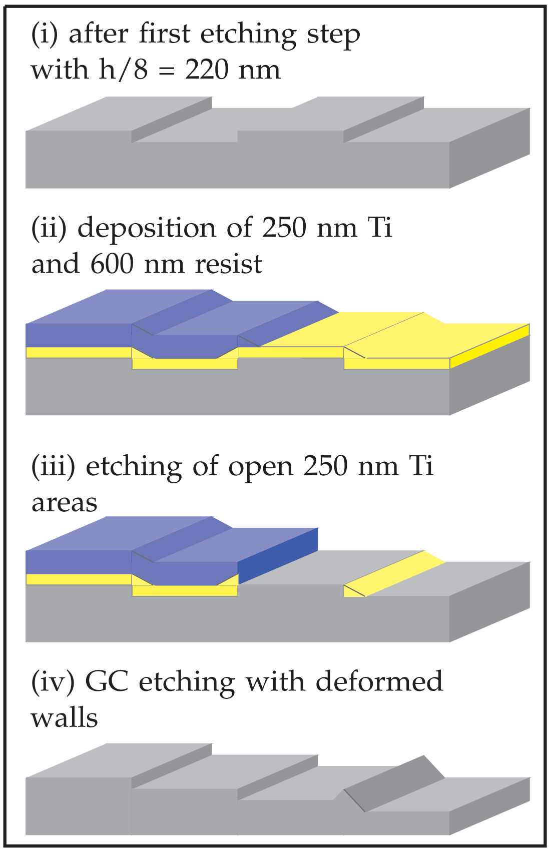

Figure 3.30: Influence of hard mask opening on multilevel fabrication. During etching, not all Ti might be removed (iii), because the Ti layer thickness is in the range of the surface step features. Such additional Ti-mask features will cause standing walls at the position of the edges after the GC etching.

the sputtered Ti layer of 250 nm. Close to an edge an increased effective thickness of Ti with respect to the vertical etching direction will be deposited in Fig. 3.30 (ii). During etching, not all Ti might be removed at the edges in Fig. 3.30 (iii). Such additional Ti-mask features will cause standing walls at the position of the edges after the GC etching process (see Fig. 3.30 (iv)). To clear the Ti mask layer uniformly on the exposed areas it is possible to etch the Ti longer. However, this will change the size of the Ti areas and thus the size of the final GC microstructures.
The standard solution is to use a lift-off process [Hatzakis1969]. With this the, Ti is fully removed in the resist covered regions. The Ti layer of 250 nm is much thicker than typical hard mask layers in the range of 30-100 nm. It is possible to use a negative photoresist with a thickness 2 times larger than the Ti layer, to find a working lift-off process. This will, however, reduce the resolution further and increase the complexity of the process. The Si hard mask offers higher selectivity and thus thinner layers can be used. We, therefore continue the multilevel fabrication with the Si process introduced in section 3.4.2.

3.4.2 Multilevel Fabrication with a Si hard mask

We use the process with a 70 nm thick Si mask layer, which was described in section 3.3.5. The results of this section are published in the SPIE conference proceeding [Prater2015b]. A blazed element with a period of $\Lambda = 12$ µm and a critical dimension of CD = 1.5 µm was fabricated, for which SEM images are shown in Fig. 3.31. The design depicted in Fig. 3.27 can clearly be recognized indicated the good fabrication quality. The design parameters together with the fabrication results are summarized in Tab. 3.11. The errors of linewidth and mask-to-mask alignment are much smaller than the critical dimension of 1.5 µm. The mask-to-mask alignment errors are below 155 nm, which represents the absolute limit of the mask lithography.

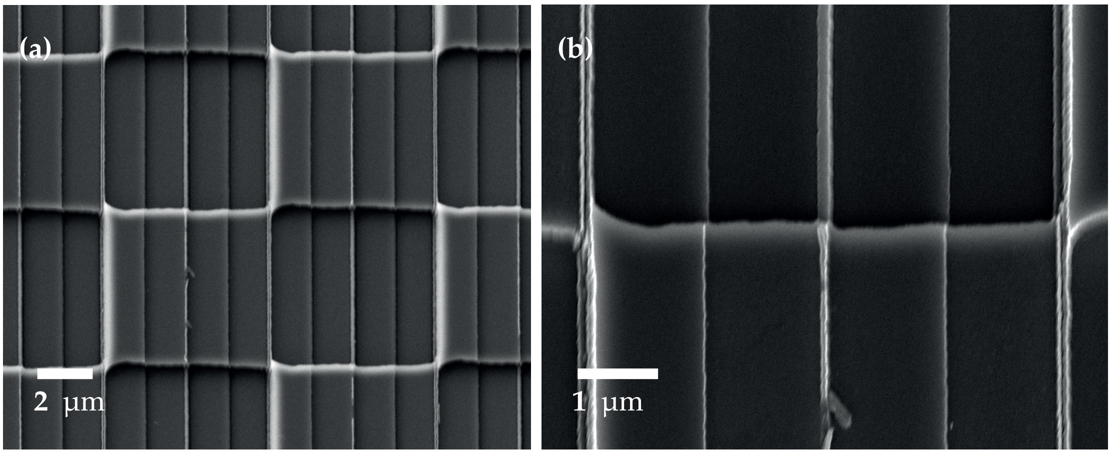

Figure 3.31: GC after 3 etching steps and Si hard mask. The design depicted in Fig. 3.27 can clearly be recognized indicated the good fabrication quality.

In Fig. 3.31 (b) small ridge features caused by duty cycle errors and/or mask-to-mask alignment errors can be seen. Their dimensions are in the nm range. They are, thus, very fragile and prone to break easily during precision glass molding. We believe that this is not a problem, since this features are not included in the design.
Due to the smaller layer thickness of 70 nm, no problems with clearing the Si mask occurred. In comparison to the results obtained with the Ti process, no ridges in multiple edged walls can be found. The process based on a 70 nm thick Si hard mask is capable of fabricating GC molds with a high quality comparable to state-of-the-art technology.

		duty cycle		alignment error	
	depth	design	fabrication	Δy	Δx (vertical)
1. mask	103 nm	1.5 µm lines	1.3 µm		
2. mask	205 nm	3 µm lines	2.81 µm	-115 nm	50 nm
3. mask	395 nm	6 µm squares	5.78 µm	155 nm	50 nm

Table 3.11: Comparison of design parameters and results obtained with the Si process for the element shown in Fig. 3.31. The errors of linewidth and mask-to-mask alignment are much smaller than the critical dimension of 1.5 µm.

3.5 Electron-Beam Lithography

We use the process with a 70 nm thick Si mask layer, which was described in section 3.3.5, in combination with electron beam lithography. This section is published in the SPIE conference proceeding [Prater2016a]. The process layout is shown in Fig. 3.32. After the Si sputtering, we use HMDS as an adhesion promoter for the e-beam photoresist ZEP520 (50% solution), which was spin-coated with a thickness of 158 nm. The resist is then exposed with a Raith 150 e-beam lithography system. The aperture was set to 30 µm and the write field to 100 µm. The resist is developed in Amyl-Acetate during 55 s and thereafter rinsed in a solution of 90:10 MiBK:IPA. The dry etching of the Si layer and the GC substrates are done by a STS Multiplex ICP machine. The gases SF_6 and C_3F_8 are used for anisotropic etching of the Si layer. The GC substrates are etched with a gas mixture of 45 sccm O_2 and 5 sccm SF_6. The chamber pressure is set to 20 mTorr. We use a coil power of 950 W and a platen power of 100 W. The GC substrate is etched with an

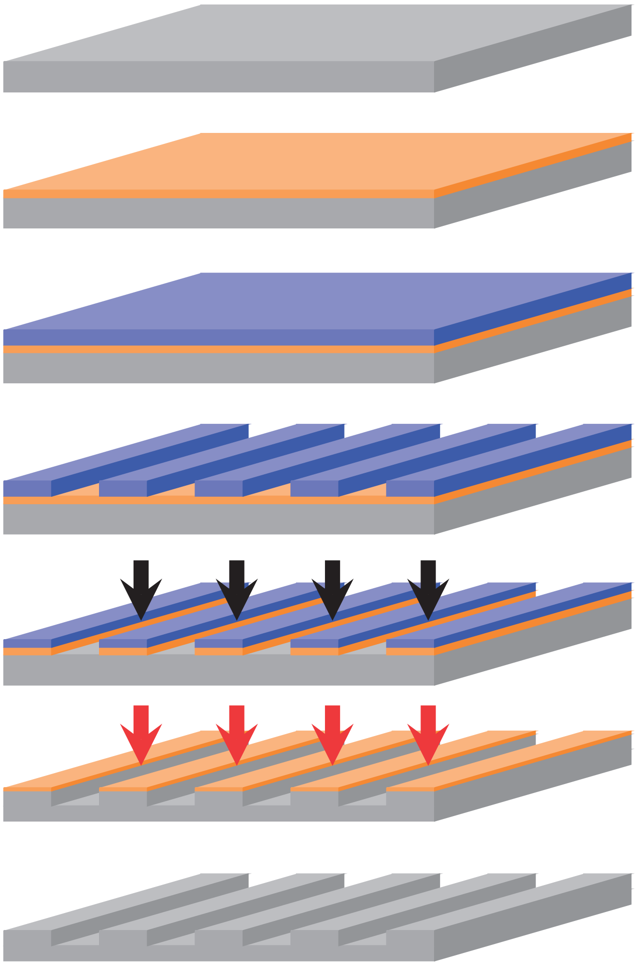

1. Piranha cleaning of polished 4″ GC wafer
2. Etch mask preparation
   2.1. Sputtering of 5 nm Ti and 70 nm
   2.2 Photoresist spin-coating of ZEP520 (50% solution), 158 nm thickness
   2.3 Exposure with e-beam system Raith 150 and development
   2.4 ICP RIE of Si
3. ICP RIE of GC with 45 sccm O_2 and 5 sccm SF_6 **selectivity GC : Si 6 : 1**
4. Hard mask stripping

Figure 3.32: Process flow of GC microstructuring with electron beam lithography for higher resolution elements.

etch rate of 6.3 nm/s and the selectivity to the Si is around 6:1. After the dry etching, the remaining Si layer is removed in a developer AZ 400 bath, which is heated to 60 °C to increase the etching rate to a reasonable speed. A final cleaning in Piranha removes the photoresist residuals.

In this study, we fabricated two different types of structures: a DOE and resolution test patterns. The total size of the GC mold is 24 mm by 36 mm. The mold was etched to depth of 485 nm. The active area of the DOE is 4 mm^2. SEM images of the DOE are shown in Fig. 3.33. The optical functionality is a 1:31 beamsplitter. The period is 29 µm with a critical dimension of 800 nm. For a fabricated depth of 485 nm, this gives an aspect ratio of 0.6, which has to be replicated. The exposure conditions were optimized to achieve an accuracy of 2% (± 20 nm) between the design values and the fabricated line widths because the performance of the DOE can be significantly influenced by changing the position of the transition points [Jahns1989, Shea2004].

The resolution test patterns consist of lines with various widths, which range from 2 µm down to 250 nm. For an etch depth of 485 nm, these correspond to aspect ratios from 0.24

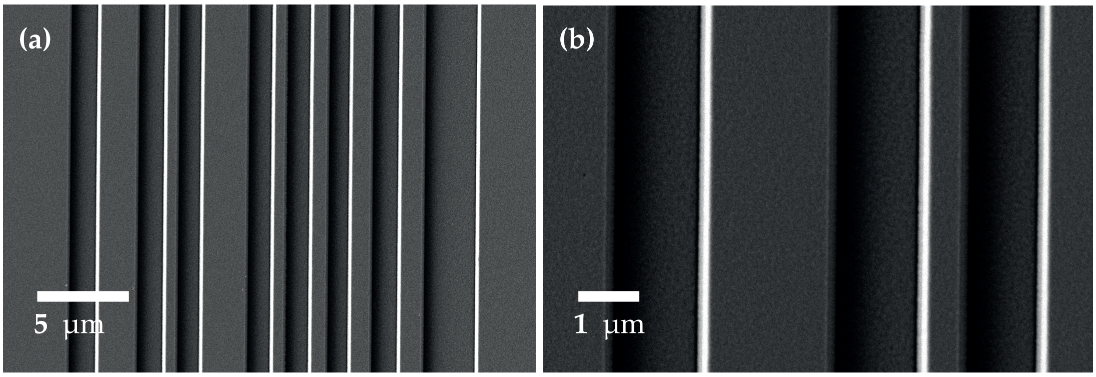

Figure 3.33: SEM image of the fabricated GC mold with the beamsplitter R (design from Tab. 2.7)

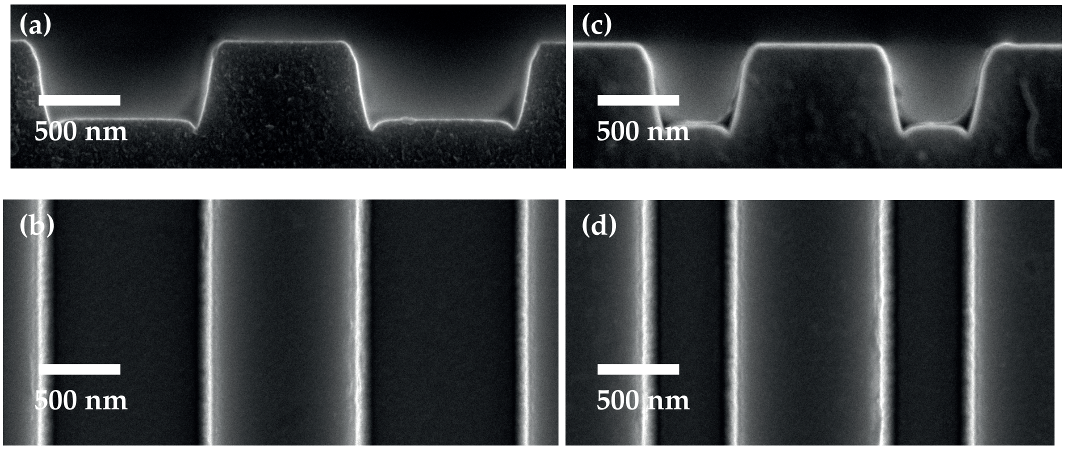

Figure 3.34: SEM images of lines with a linewidth of 1.04 µm (a)-(b) and 0.54 µm (c)-(d). (b) and (d) show the top view of the GC surface. The molds were diced and the height profiles are given in (a) and (c), where the GC substrate in on the bottom.

to 1.94. The length of the lines are 3 mm. After molding we cut the molds to access their height profiles, which can then be compared with the molded glass. Examples of the fabricated mold are depicted in Fig. 3.34. The linewidth of the resolution lines is 1.04 µm for (a)-(b) and 0.54 µm for (c)-(d). The molds were diced into the unstructured surface until ca. 200 µm to the structured side. The final cut was done by manually breaking the mold in order to achieve a flat cut edge. The height profiles in Fig. 3.34 (a) and (c) show a considerable amount of trenching. The wall verticality is 82° ± 2°. Due to the e-beam lithography, the wall waviness seen before with the mask lithography (details in Fig. 3.19 and 3.20) is decreased significantly. This allows to fabricate features down to 250 nm with high accuracy.

3.6 Summary of Glassy Carbon Microfabrication

First, we discussed different mask materials for the plasma etching process of glassy carbon (GC). The process presented by Youn et al. [Youn2009] was used as a starting point, where Au is used as a hard mask. In order to find a working process, a binary photolithography mask with large CD was employed. The requirements for the diffractive optical elements are also valid for the glassy carbon molds. The sidewall angle is influenced by the selectivity, which is the ratio of the etch rates between substrate and mask material. A high selectivity is necessary to achieve a high wall verticality and to reduce the mask layer thickness, which also increases the lateral resolution. The best results are obtained with a 5 nm Ti/ 70 nm Si mask in combination with RIE. A gas ratio for O_2 to SF_6 of 9:1 significantly improved the etch selectivity (SPTS at CMi). The 250 nm Ti process also gives acceptable results but has a higher layer roughness caused by the TiO_2 top surface. These features are copied to some extend to the GC microstructures. They can be easily seen as an additional waviness to the otherwise straight lines.

In the following multilevel DOEs were fabricated with both the Ti process and the Si process. Problems with clearing the Ti hard mask layer occurred because the layer thickness of 250 nm was in the range of the etched steps. Very good results were obtained with the Si mask material both in terms of design representation and alignment accuracy. The low layer thickness of 70 nm for Si allowed the combination with e-beam lithography for an improved resolution and accuracy. A diffractive optical element with a critical dimension of 800 nm and an aspect ratio of 0.6 was fabricated. Additional lines with feature sizes down to 250 nm were also realized. These results show that it is possible to microstructure GC molds with a wide range of binary optics designs and with a high accuracy.

4 Precision Glass Molding

This Chapter deals with the precision glass molding of diffractive optical elements. All molding experiments were carried out by our partners at the Fraunhofer Institute for Production Technology (IPT, Aachen Germany). The measurement and analysis will be the main subject here and were mainly done at EPFL. The glassy carbon (GC) molds were fabricated in the EPFL cleanrooms. Two different glass materials were tested: a low transition temperature T_g glass: L-BAL42 from OHARA and a very high T_g glass: fused silica.

First, section 4.1 will give an overview of available technologies for precision replication of optical components. The molding set-up and procedure are explained in section 4.2. To get a better understanding of the molding mechanisms, the properties of the mold material and the glass in the temperature range of the molding are discussed in section 4.3. Of special interest are the influence of the viscosity and the coefficients of thermal expansion. A discussion of the optimization of the molding settings is given in section 4.4. The influence of the thermal properties during molding is important and examples of experimental observations will be given. Section 4.5 analysis the characteristics necessary for a good mold material. A comparison of glassy carbon and fused silica as mold materials will be done. The fused silica mold was fabricated by an external supplier and exhibits a high quality due to the e-beam lithography employed. To test the temperature limits of precision glass molding with glassy carbon molds fused silica was molded at 1400 °C in section 4.6. Of special interest are the minimal feature size and the maximum aspect ratio that can be molded with high accuracy. Therefore, a diffractive optical element with a critical dimension of 800 nm was be replicated in L-BAL42 in section 4.7.

4.1 State-of-the-art Technology

Replication is a common technology for mass production. The demand for precision manufacturing is growing, which is reflected by the replication accuracy and quality. A key application can be found for optical components made of plastic and glass.

Surface geometries range from refractive elements like aspheric lenses with mm sizes to micro- and nanosized surfaces for diffractive optical elements (DOE). A range of different technologies has been developed, which depend on the optical material and the surface geometry. For ’smooth’ refractive surfaces the preferred choices are plastic injection molding and precision glass molding with mechanically machined mold inserts [Mertus2012]. The technologies involved are described in Tab. 4.1.

optical material	replication technology	mold material	mold machining technology
plastic and very low T_g glasses (<400 °C)	plastic injection molding	electroless Nickel	single point diamond turning
glass	precision glass molding	carbide or ceramic molds with inert coatings (e.g. Pt-Ir)	precision diamond grinding and polishing

Table 4.1: Replication technologies for refractive optical components [Mertus2012]. Single point diamond turning can be used for the more ductile material nickel, but cannot be used for temperatures higher than 400 °C. Carbide or ceramic molds can withstand temperatures needed for precision glass molding.

The choice of the mold material depends on the temperature during replication. Electroless nickel undergoes a phase transition at temperatures of ca. 400 °C, where crystalline phase grains form. The grain topography adds to the machined surface and increases the surface roughness. Therefore, a more temperature stable material needs to be used for precision glass molding. Tungsten carbide (WC) is preferred, because of its high temperature resistance and high hardness, which exceeds that of nickel. A high hardness has the advantage of longer mold lifetimes and causes a cost reduction per unit especially for high-volume manufacturing. However, the cost of the mold inserts is higher for WC than for nickel.

The 2 main technologies for the mechanical structuring of the mold surface are single point diamond turning and precision diamond grinding. Single point diamond turning can be used for more ductile materials such as nickel. The size of the diamond tip can be very small from 25 µm to 500 µm. For harder materials like tungsten carbide, the wear of the machining tool can be very high. Therefore, precision diamond grinding is used for tungsten carbide. The grinding wheel consist of many microscope sized diamond particles. The accuracy of single point diamond turning is higher than for precision diamond grinding, because of the less predictable wear of the grinding wheel [Dambon2016, Mertus2012].

The machining of the surface will show a tooling grove pattern, which results in additional surface roughness. Due to the ductility of nickel, diamond turned surfaces can be very smooth. Tungsten carbide is more brittle. To achieve an optically flat surface, tungsten carbide molds are typically polished after machining.

Mechanical machining of the molds is limited in terms of the minimum size, that can be shaped with diamond tools. Single point diamond turning has been successfully used to fabricate v-grooves and pyramids in the µm range [Yan2009b]. The design is limited to straight lines. Precision diamond grinding of tungsten carbide molds needs an additional polishing step and can, thus, not be used for microfabrication. Therefore, mechanical machining is not commonly used to fabricate molds with diffractive optical designs. The state-of-the-art technologies involved for the fabrication of micro- and nanostructured optical elements [Hansen2011, Gale2005] are described in Tab. 4.2.

optical material	replication technology	mold material	mold machining technology
plastic and very low T_g glasses (<400 °C)	plastic injection molding, soft lithography and hot embossing	electroless Nickel	electroforming (Si wafer as master)
		PDMS	casting process (Si wafer as master)
glass	precision glass molding	carbide or fused silica	cleanroom technology

Table 4.2: Replication technologies for diffractive optical components [Hansen2011, Gale2005]. The mold fabrication for plastic components is based on replication of a Si master, which was microstructured with cleanroom technology or laser ablation [Kang2004].

Plastic injection molding involves the injection of liquid plastic material into a cold mold insert under high pressure. The cycle times are very short. Soft lithography can replicate feature sizes down to the nm range. This includes UV embossing and nano imprint lithography. High aspect ratio features can be fabricated with hot embossing, which includes heating of the polymer until a viscous state and pressing under moderate pressure. It is an isothermal process. Hot embossing is characterized by short flow distances and lower shear stress in comparison to plastic injection molding [Wor2009]. The main differences of these technologies lie in the cycle time, feature size and aspect ratios, which can be realized.

The mold fabrication for plastic components is based on replication of a Si master. This is taking advantage of a large amount of available process for Si wafers. The Si wafers themselves are not used as molds, because they are too brittle to withstand the high pressure repeatably [Kang2004]. The structuring is done by either cleanroom technology or laser ablation of a photoresist coated on the Si wafer. The Si wafer is coated with a thin conducting layer as pretreatment. Electroforming of nickel or copper is used to make metal masters. The silicon wafer is etched afterward. Soft tools made out of PDMS, PES, and epoxy are also available. The liquid PDMS is poured on the Si wafer typically with SU8 microfeatures and solidified by a heat treatment. These mold materials cannot withstand the temperatures during precision glass molding.

Precision glass molding is the equivalent to hot embossing for plastic components. The viscosity is higher than for polymer materials during replication. Precision glass molding is commercially used for optical components such as aspherical lenses, lens arrays and freeform lenses. Shrinkage errors and changes in the refractive index introduced during the molding can effect the optical performance significantly. This can be compensated by adopting the initial mold shape by an iteration approach or by reliable simulations [Klocke2012].

Precision glass molding for diffractive optical elements is not yet established in industry, because no mold material is available that can both withstand the molding conditions and can be micromachined with the desired microfeatures in optical quality. The necessary characteristics of the mold material are:

- high temperature resistance for 400 °C - 800 °C and if possible 1400 °C for fused silica;
- high hardness, which allows low wear, less deformation of the mold and long mold lifetime;
- chemical inert to allow an easy separation of mold and glass after molding.

The choice of the mold material is very limited. Table 4.3 compares different mold material for precision glass molding with diffractive optical elements. Nickel is very temperature limited, because it experiences a phase transition at around 400 °C [Mertus2012]. Copper-nickel alloys show a better temperature resistance than Ni, but they are more difficult to microstructure [He2011]. Tungsten carbide can be structured by precision diamond grinding for refractive surfaces down to feature sizes of 10 µm. To overcome this limitation an adaption with cleanroom technology has been tested [Kang2004, Choi2004]. The tungsten carbide molds were pressure formed from tungsten carbide powder on a Si master and a following sintering process. The grain texture results in high surface roughness. A polishing procedure showed good results, but limits the possible designs further.

Komori et al. conducted adhesion tests for glass molding [Komori2008]. They showed that Si molds adhere strongly. The best results were given for chemical vapor deposited diamond (CVD), when a flat mold was used. However, molding of microstructured elements showed broken glass features for higher filling conditions. The microstructuring of diamond is done with focused ion beam etching, which is not practical for large area fabrication, because of the very slow writing times. The fabrication costs of thick CVD layers on large areas are also very high. The texture of the diamond layer shows polycrystalline grains in the µm range, which is not ideal.

Antiadhesion coatings can improve the easy release of the mold significantly. A carbon coating was successfully used for a SiC mold [Mori2009]. But adhesion problems appeared when the filling rate was close to 100%. The coating needs to be uniformly applied to the surface including the e.g. very steep flanks. Depending on the type of coating the layer thickness can range from 50 nm to 300 nm, which can cause a significant feature rounding for µm features. Also, the thermal expansion during molding is different between mold and coating and will eventually cause a failure of the coating and therefore limits the mold lifetime. It is thus preferred to avoid coatings.

Glassy Carbon and CVD diamond are the only materials which do not need coatings.

material	temperature resistance	hardness	chemical inert	microstructuring process	molding tests	references
Nickel	**<400**°C **(phase transition)**	low	coating needed	electroplating of Si wafer	very low T_g glass	[Mertus2012]
Copper nickel alloy	better than Ni	better than Ni	coating required, 250 nm Pt-Ir	**single point diamond turning**	P-SK57 (T_g=550 °C)	[He2011]
Tungsten carbide (WC)	<800 °C	high	coating needed (Pt-Ir, carbon)	**precision diamond grinding, feature size > 20 µm**	LF5 Schott (T_g=415 °C)	[Mertus2012, Wolz2015]
Si	<800 °C	**too brittle**	**coating needed,** 45 nm **graphene,** 50 nm $\mathbf{Si_4Ni_3}$	cleanroom technology based	P-LASF47 Schott (T_g=530 °C)	[He2013, Hung2009, Kang2004, Komori2008]
SiC	good	good	**coating needed,** 50 nm **graphene coating**	cleanroom technology compatible	K-PSK100 (T_g=420 °C)	[Mori2009]
Fused silica	< 800 °C	good	**coating needed,** 250 nm **Pt-Ir**	cleanroom technology compatible	K-PG325 Sumita (T_g=285 °C)	[Yi2006]
CVD diamond	very good	very good	very good	**focused ion beam etching too slow for large areas**	Pyrex at 690 °C	[Komori2008]
Glassy Carbon	<2000 °C	very good	very good	very good	fused silica, borosilicate glass, Al at 660 °C	[Youn2009, Mekura2009] [Mekura2013, Komori2008]

Table 4.3: Comparison of mold material for precision glass molding with diffractive optical elements. The characteristics of the mold material are given by the temperature resistance, hardness, chemical inertness, and compatibility with microstructuring technologies. The criteria that are not fulfilled are highlighted with bold letters.

Glassy Carbon can be microstructured with high quality in the micrometer regime on a wafer scale and has been successfully used for molding of low T_g glass and fused silica [Youn2009, Mekura2009, Mekura2013]. It is the preferred material for glass molding and was therefore chosen for this work. As an alternative fused silica was tested.

4.2 Molding Process Set-up

In the following, we will explain briefly the process flow of precision glass molding. Details can be found in [Chen2008]. Two Toshiba machines were used, which are shown in Fig 4.1. They are employed for different temperature ranges: the GMP-211V can be operated until temperatures up to 800 °C and the GMP-207HV until (T≤1400 °C). For this temperature range, the tooling is mainly made of Carbon-based materials.

Figure 4.1: Molding machines at IPT Aachen (Germany): (left) Toshiba GMP-207HV (T≤1400 °C) and (right) Toshiba GMP-211V (T≤800 °C)

The standard molding process for an aspherical lens is depicted in Fig. 4.2. The glass preform is polished to optical quality. The preform has already a shape close to the final shape. Otherwise too much material needs to be moved and the high pressure generated at limited areas results in fracture or deformation of mold and/or glass. For the replication of diffractive optical elements, flat molds based on wafer-technology were fabricated. The glass preforms are, thus, flat plates with a diameter of ca. 22 mm. They are first cleaned in an ethanol bath and then in an ultrasonic bath with isopropanol. Drying was accomplished with a nitrogen gun.

The two molds are fixed to the upper and lower flanges, where the lower flange can be moved with µm precision. The glass preform is placed on the lower mold (step 1). The sealed chamber is then evacuated and flood by an inert gas, here nitrogen (step 2). In the first stage of the molding, the glass preform and the molds are heated up above the glass transition temperature T_g with infrared heaters (step 3). Once the molding

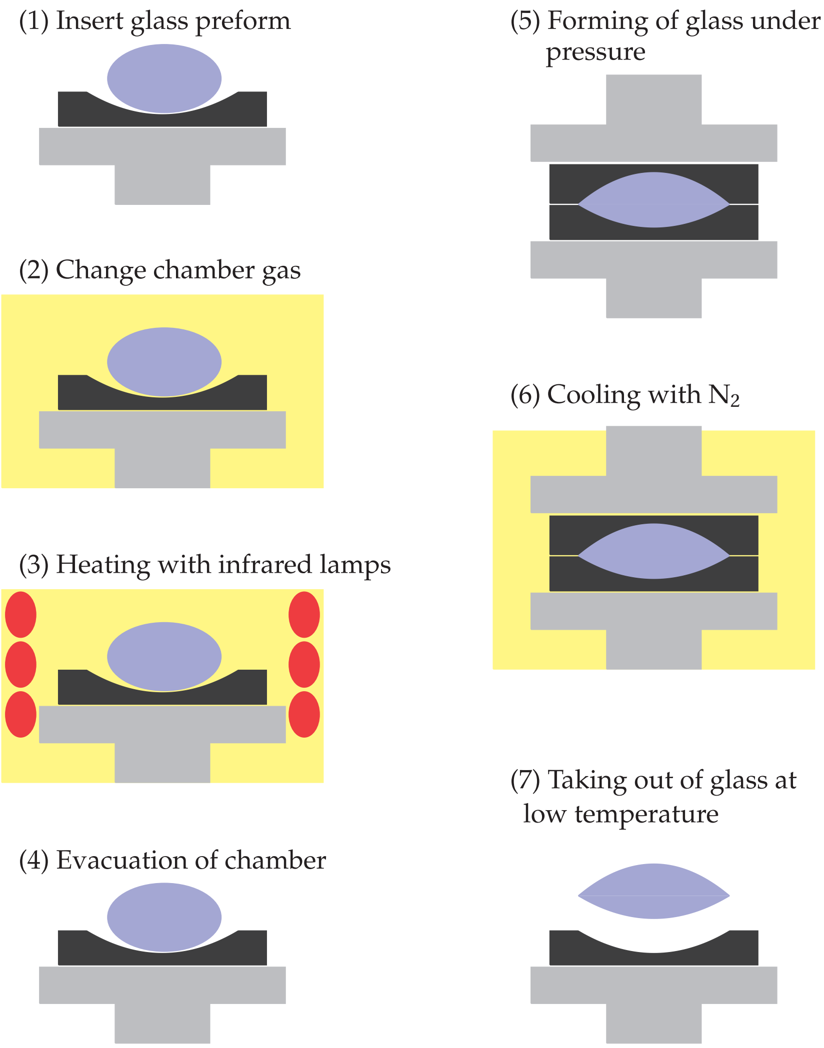
(1) Insert glass preform

(2) Change chamber gas

(3) Heating with infrared lamps

(4) Evacuation of chamber

(5) Forming of glass under pressure

(6) Cooling with N_2

(7) Taking out of glass at low temperature

Figure 4.2: Molding process for an aspherical lens.

temperature is reached, the system is kept at this temperature for a certain period of time to homogenize.

The molding is done by pressing the glass preform with a constant pressure (step 5). To avoid inclusion of nitrogen the chambers is under vacuum during the molding. Afterwards, the pressure is reduced and the system is slowly cooled down below the glass transition temperature. This controlled cooling stage is used to avoid deformations of the glass and to reduce possible tensions in the glass. Then the pressure is released and the system can now be cooled down fast to room temperature (step 6). Finally, the glass is removed from the molding chamber (step 7). The process time for a whole molding cycle can be between 15 and 25 minutes depending on the geometry and the total size of the optics.

Process parameters that need to be predefined are the process time, pressure and temperature during the molding step (5). Table 4.4 summarizes the parameter range possible

	parameter range of GMP-207HV	parameter range for L-BAL42
time	no limit	120 s - 360 s
pressure	≤ 20 kN	0.5 kN - 7 kN
temperature	≤ 800 °C	550 °C - 570 °C

Table 4.4: Process parameters for precision glass molding during the molding step (5): the parameter range possible for GMP-207HV and the investigated parameter range for the low T_g glass L-BAL42 form OHARA.

with the system GMP-207HV. The glass used mainly in this work is a low T_g glass from OHARA. The investigated parameters are also given in Tab. 4.4. Additionally, the controlled cooling has to be defined by the separation temperature, the cooling time and the reduced pressure. Although the main pressing phase is over, the glass can still deform in this phase, since the temperature is around T_g.

The tooling has to be modified for the mold fixation of flat molds. Two different configurations shown in Fig. 4.3 were used. First, we used a configuration with no extra tooling. A stack consisting of the mold, the glass preform, and the bearing plate is placed in a sealed chamber (Fig.4.3 (a)). The bearing plate consists of a metal plate with an anti-adhesion layer. It is heavy enough to ensure that the glass mold stack does not move during the molding. For this configuration, the glass is always in contact with the two mold surfaces. Only after a handling temperature of around 100 °C is reached mold and glass are separated from each other by the operator.

An optimized system is given in Fig.4.3 (b), where the microstructured GC mold is fixed to the upper flange. This configuration has an important advantage: mold and glass can be separated at an arbitrary temperature simply be lowering the lower flange.

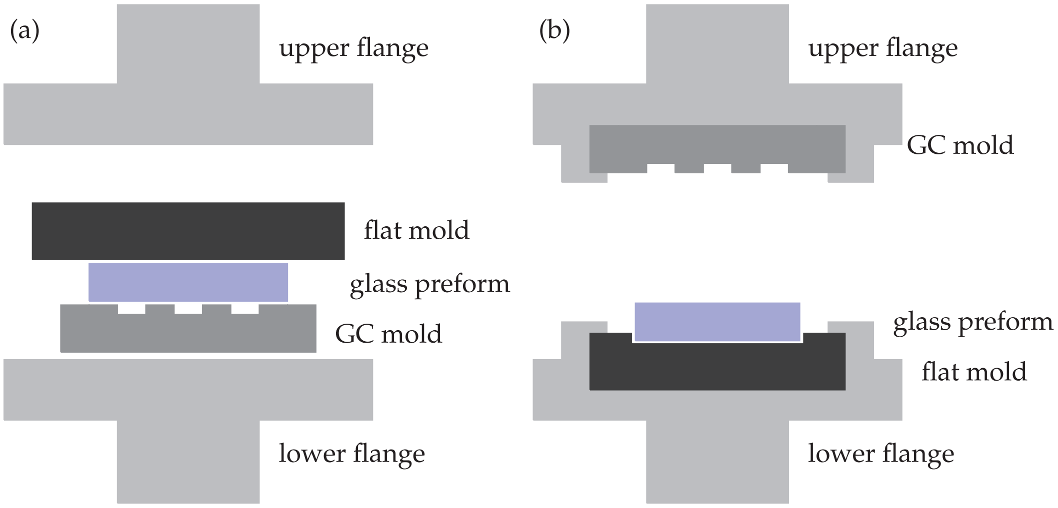

Figure 4.3: Contact between the glass and molding surfaces with two different configurations: (a) loose stack and (b) GC mold fixed to machine flange.

4.3 Glass Properties

To get a better insight into the molding mechanisms we will discuss the properties of the mold material and the glass in the temperature range of the molding. For low temperatures the glass has is a short window of elastic deformation and the glass is brittle. In the high-temperature range, the glass becomes a viscous liquid. Between this two regions, the glass behaves like a viscoelastic material. The deformability of the glass is best described in terms of the viscosity η. The higher the temperature the smaller becomes the viscosity and the less force is necessary to perform a certain deformation. At a viscosity $log(\eta)$ equal to 7.6 the glass deforms rapidly under its own weight, which is identified as the softening point SP. Additionally, a volume change can be seen during the molding. The thermal volume expansion for L-BAL42 from OHARA is depicted in Fig. 4.4. The glass volume increases linearly in the low-temperature range. A strong increase in the thermal expansion can be seen for a temperature T_g, which is referred to as the glass transition temperature. The volume increases until the Yield point At, after which the volume starts to shrink again. The main temperature point for L-BAL42 and fused silica SQ-1 from Schott are summarized in Tab. 4.5.

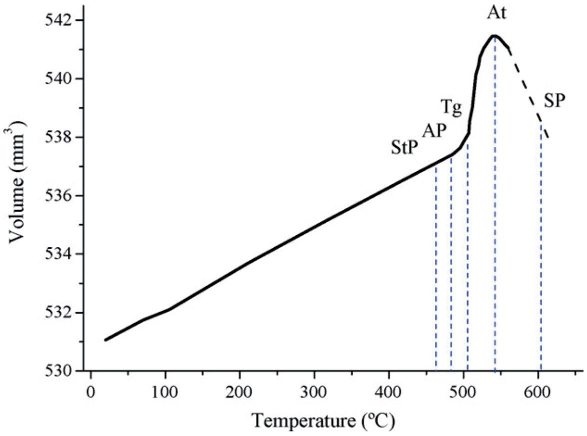

Figure 4.4: Temperature dependency of volume change for the glass L-BAL42 (taken from [Yan2009])

Temperature Point	Definition	L-BAL42	SQ-1
Strain Point StP	$log(\eta) = 14.5$	467 °C	970 °C
Annealing Point AP	$log(\eta) = 13$	494 °C	1075 °C
Glass transition temperature T_g	point where linear expansion changes to nonlinear	506 °C	
Yield Point At	max. Volume	538 °C	
	$log(\eta) = 9$	564 °C	1437 °C
Softening Point SP	$log(\eta) = 7.6$	607 °C	1580 °C

Table 4.5: Thermal properties of L-BAL42 (OHARA) [3] and fused silica SQ-1 (Schott) [4]. The recommending molding temperature is for $log(\eta)$ around 9.

4.3.1 Viscosity

Glass molding is typically done at a temperature between At and SP. OHARA is recommending molding at a temperature, for which $log(\eta)$ is equal to 9. For L-BAL42 this is the case at 564 °C [3]. The temperature dependency of the viscosity can be described by the Vogel-Flucker-Tammann-equation:

$$log(\eta) = A - \frac{B}{T - T_0}, \tag{4.1}$$

where A, B and T_0 are fit parameters from experimental data. These parameters are given in Tab. 4.6 and used for the plots of the viscosity in Fig. 4.5. These dependencies give a good starting point for the molding settings. Molding for L-BAL42 should be done at around 564 °C and molding of SQ-1 at 1437 °C. Since the Toshiba machine GMP-207HV can only be operated until 1400 °C, one can expect a lower molding quality unless much longer molding times or pressures are used. For microstructures with smaller features and larger aspect-ratios, a lower filling might be seen.

	L-BAL42	SQ-1
A	5.87	-23.89
B	234.6	$1.078 * 10^5$
T_0	490	-1842
temperature range of fitting	550 °C - 590 °C	970 °C - 1580 °C

Table 4.6: Coefficients of the Vogel-Flucker-Tammann-equation for L-BAL42 (taken from [Yan2009]) and SQ-1 [4].

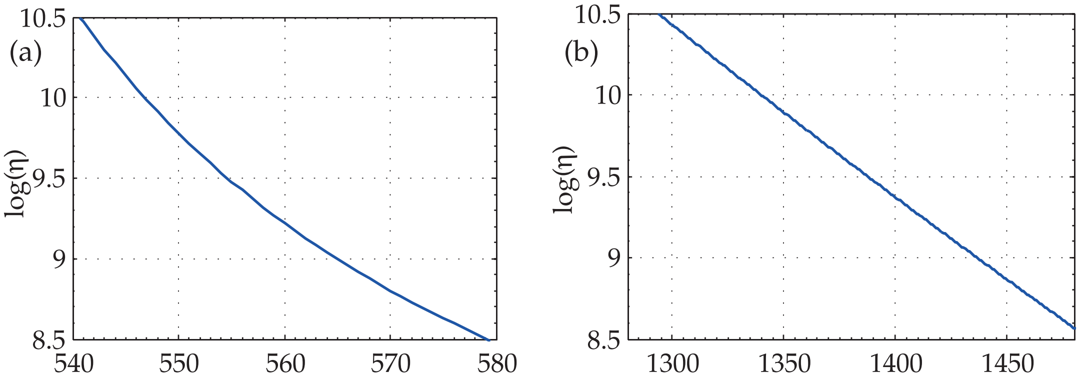

Figure 4.5: Temperature dependency of viscosity for the glass (a) L-BAL42 and (b) SQ1 with the coefficients given in Tab. 4.6.

Cavity filling for hot embossing of PMMA has been discussed by [Wor2009]. An estimation for effective filling is given for the minimum applied pressure drop Δp as

$$\Delta p = \frac{8 v_{mold} L \eta(\overline{\gamma})}{r^2}, \tag{4.2}$$

- r ... radius of cavity
- v_{mold} ... mold velocity
- L ... length of cavity
- η ... shear- and temperature-dependent viscosity ($\overline{\gamma}$ shear velocity)
- temperature of polymer.

This estimation is done for cylindrical cavities. The molding pressure needs to be increased proportional to the feature size by $1/r^2$ and proportional to the cavity length L. A strong influence is given by the temperature. According to Fig. 4.5 (a) the viscosity $log(\eta)$ of L-BAL42 increases from 8.8 for 570 °C to 9.78 for 550 °C. In order to compensate, the pressure needs to be increased by 1 order of magnitude for a temperature change of 20 °C.

4.3.2 Refractive Index Change

When the glass is cooled down fast, the volume does not shrink back to the same initial volume due to thermal relaxation [Yan2009]. In Fig. 4.4 the volume expansion during heating is shown. The volume graph during cooling is located therefore above the heating curve. This depends on the cooling rate. Because the volume of the molded glass is larger than the glass preform, the density and thus the refractive index of the molded glass is lower. The supplier OHARA gives values for the refractive index change in the data sheet [3]. A diagram of this relationship is depicted in Fig. 4.6 (a). For a wavelength of 656 nm and phase change of π the step height is given in Fig. 4.6 (b). Thus, the optimal step height needs to be increased by 2.4 nm for a cooling rate of 0.5 °C/s and by 2.7 nm for 1 °C/s. This is below the accuracy of the plasma etching. We can safely state that a refractive index change does not need to be included into the design of diffractive optical elements.

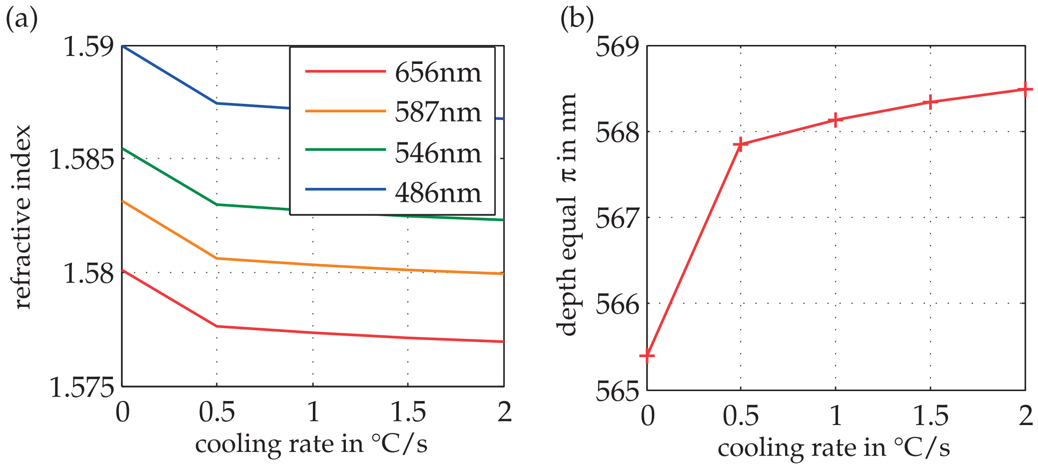

Figure 4.6: (a) refractive index change of L-BAL42 due to volume shrinkage and the corresponding change of optimal etch depth for π phase shift at a wavelength of 656 nm.

4.3.3 Coefficient of Thermal Expansion

The temperature dependent volume change can be described by the coefficient of thermal expansion (CTE), which is defined as the slope of the volume change. Values of the CTE for L-BAL42 can be found in the datasheet [3]. The CTE of L-BAL42 in the linear temperature regime is $88 \times 10^{-7}\,\mathrm{K}^{-1}$ (for 100 °C to 300 °C). The CTE of the mold material GC is $22 \times 10^{-7}\,\mathrm{K}^{-1}$ in the temperature range of interest. The influence of the CTE during the molding is schematically explained in Fig. 4.7. At the molding temperature, the size of the active areas are the same for glass and mold. During the cooling until the separation temperature, glass and mold shrink. The radius of the active area for the glass L-BAL42 is R_{glass} and for the GC mold R_{GC}. The difference in the thermal extension coefficient between the glass and the GC cause a stronger shrinkage of the glass in respect to the mold. The difference in size is given by $R_{GC} - R_{glass}$.

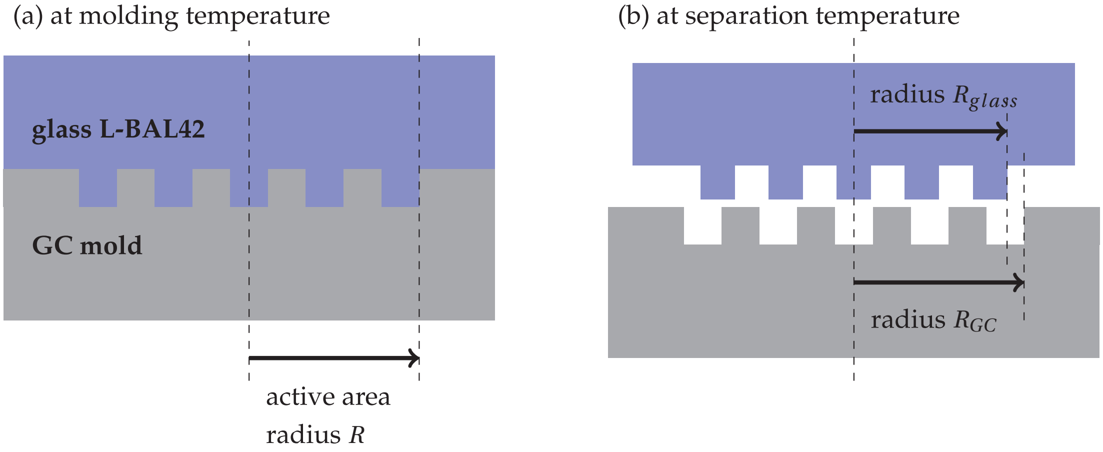

Figure 4.7: At the molding temperature the size of the active areas are the same for glass and mold (a). The glass L-BAL42 shrinks more than the mold (b).

To estimate the influence of the cooling, we will assume a uniform volume shrinkage in all directions. If the molding setup with a mold-glass-stack (Fig. 4.3 (a)) is used, glass and mold stay in contact from the molding temperature 565 °C until around 100 °C, where they can be separated manually. The linear shrinkage of GC ΔR_{GC} for a radius of 8.5 mm is around 8.4 µm. The estimation for L-BAL42 is more difficult, because of the nonlinear volume change in the molding range. We use the CTE given in Tab. 4.7 in the following:

$$\Delta R = R + \int_{T_1}^{T_2} \mathrm{CTE}(T) \cdot R \cdot dT.$$

Unfortunately, the CTE was not available for temperatures higher than 540 °C. The Yield Point, which is defined as the temperature of max. volume, is given at 538 °C. For this point, the CTE is 0. For higher temperatures CTE becomes negative. To get a rough estimation, we will assume that CTE is $-454 \times 10^{-7}\,\mathrm{K}^{-1}$ for temperatures higher 540 °C. The linear shrinkage of L-BAL42 is thus 41.4 µm for 8.5 mm length. The difference between mold and glass is thus 33.2 µm. This is clearly a problem for the molding of microstructure with a minimum structure size in the submicrometer range. The induced stress can cause breaking of edges of the GC and scratching of the surface of the glass. In the worst case, whole elements of the GC and glass might be quarried out.

It is desirable to separate mold and glass early during the cooling stage. The molding machine was therefore modified so that the GC mold could be fixed to the upper machine arm (configuration Fig. 4.3 (b)). Thus, it is possible to separate mold and glass at a much higher temperature than before. The cooling from the molding temperature 565 °C until the glass separation temperature of 450 °C will cause the glass to shrinkage 15.3 µm and the GC 1.7 µm. The difference of mold and glass is therefore only 13.6 µm, which is nearly 3 times smaller than for the stack configuration.

The used glass is already one of the optical glasses with the lowest expansion coefficient. In contrast to other application, for DOEs the glass is chosen due to its optical characteristic. For imprinting microfluidic parts in bio-MEMS applications Pyrex glass was successfully molded with GC molds by [Mekura2012, Mekura2013, Takahashi2005, Takahashi2007]. Pyrex glass is a low-thermal expansion borosilicate glass, but it is not an optical glass. The CTE is $32.5 \times 10^{-7}\,\mathrm{K}^{-1}$ in the linear range and T_g is 560 °C [Wor2009]. In this work, fused silica was also molded. The CTE of fused silica is with $5.1 \times 10^{-7}\,\mathrm{K}^{-1}$ smaller than the CTE of GC with $22 \times 10^{-7}\,\mathrm{K}^{-1}$. We expect that fused silica will shrink more than the GC mold during cooling. For the higher temperature machine Toshiba GMP-207HV no tooling was available to fix the mold to the upper flange. The temperature range, for which mold an fused silica stayed in contact, is from ca. 1400 °C to 100 °C and thus very large. We believe that the thermal shrinkage during the cooling can be the main limiting factor for precision glass molding. In the next section, we will discuss experimental observations concerning the molding quality.

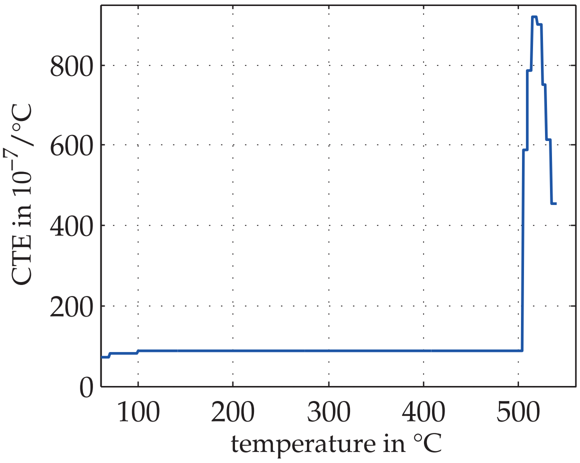

T in °C	CTE in $10^{-7}\,\mathrm{K}^{-1}$
-30 ↔ 70	72
100 ↔ 300	88
505 ↔ 510	589
510 ↔ 515	786
515 ↔ 520	919
520 ↔ 525	900
525 ↔ 530	750
530 ↔ 535	613
535 ↔ 540	454

Table 4.7: Thermal properties of L-BAL42 [3].

4.3.4 Oxidation

In the high-temperature regime needed for the glass molding, the surface of many materials show a tendency to oxidize. The oxidized material can diffuse into the glass. This causes the glass to stick to the mold and can make demolding very difficult. The lifetime of the mold can be significantly reduced. Therefore, the glass and mold need to be under an oxygen-free environment during the molding process (including heating, pressing and cooling) [Davim2017].

This can be suppressed by a nitrogen environment, which is easy to operate. A better working approach is to work under vacuum, but this has the disadvantage of a higher cost. The machine GMP211 by Toshiba Machine Co. Ltd. is operating under vacuum. Trace amounts of oxygen are present in the chamber, that can be sufficient to oxidize the mold surface during on single molding process [Georgiadis2015]. Glass is an oxide material itself. Oxygen can diffuse towards the glass mold interface. Also, oxygen can diffuse in the molding chamber atmosphere and react with the mold surface.

One approach to prevent these effects is to coat the mold surface. Additional diffusion processes in the thin coating layers can change the antiadhesive properties and need to be considered. Materials that are not reacting with oxygen are preferred. An example is Platinum-Iridium (Pl-Ir).

Carbon-based materials like diamond-like carbon (DLC) and glassy carbon are more prone to oxidization. It would be preferred to use a non-oxidizing coating for these materials. But the antiadhesive carbon surface properties would be lost by applying a coating. It is not clear how strong the influence of the oxidization is. Lifetime tests need to be performed and careful surface inspections need to be performed.

4.4 Optimization of the Molding Settings

For the first molding tests, we used glassy carbon molds fabricated with the Ti process (details 3.3.4). The depth was etched to 690 nm. The process parameters for the molding are summarized in Tab. 4.8. The stack configuration was used, which means that the mold and glass stayed in contact from the molding temperature of 570 °C to ca. 100 °C. The viscosity for 570 °C is with $10^{8.8}$ Pa s very low and should allow a good filling of the

GC mold	depth 690 nm
glass	L-BAL42
configuration	stack (Fig. 4.3 (a))
molding temperature	570 °C
molding time	90 s
molding pressure	0.8 kN
after molding time	180 s
after molding pressure	0.5 kN

Table 4.8: Parameters for molding experiment A.

microstructures. Images of the mold and the replicated L-BAL42 glass are shown in Fig. 4.8. Three different diffractive optical designs were placed on the same mold, which are named with the 3 markers ′D1′, ′E1′ and ′F1′. The critical dimension (smallest structure) were 2 µm for ′D1′ and ′E1′ and 20 µm for ′F1′. It is desired to place multiple DOE designs on the same mold to improve the cost efficiency. The areas between the DOEs are unstructured and show the polished surface quality. The pictures of the mold and the glass in Fig. 4.8 show that the microstructured areas are not uniform. Both show similar patterns. Deviations can be seen especially at the outskirt area of the microstructured

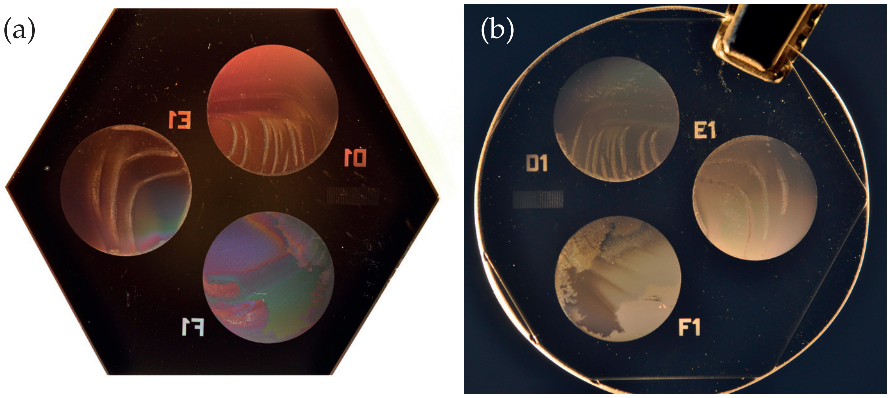

Figure 4.8: Images of the GC mold and glass of molding experiment A (parameters given in Tab. 4.8).

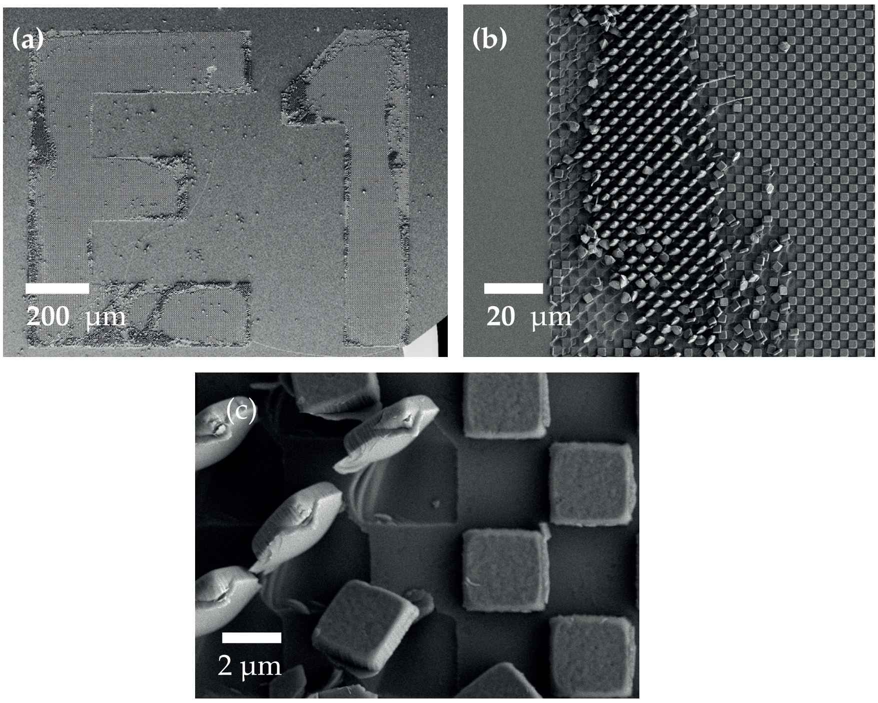

Figure 4.9: SEM images of the glass of experiment A (parameters given in Tab. 4.8) in the region ′E1′ in Fig.4.8 (b). Rapture of the 3 µm wide squares can be seen at the borders of the structured areas.

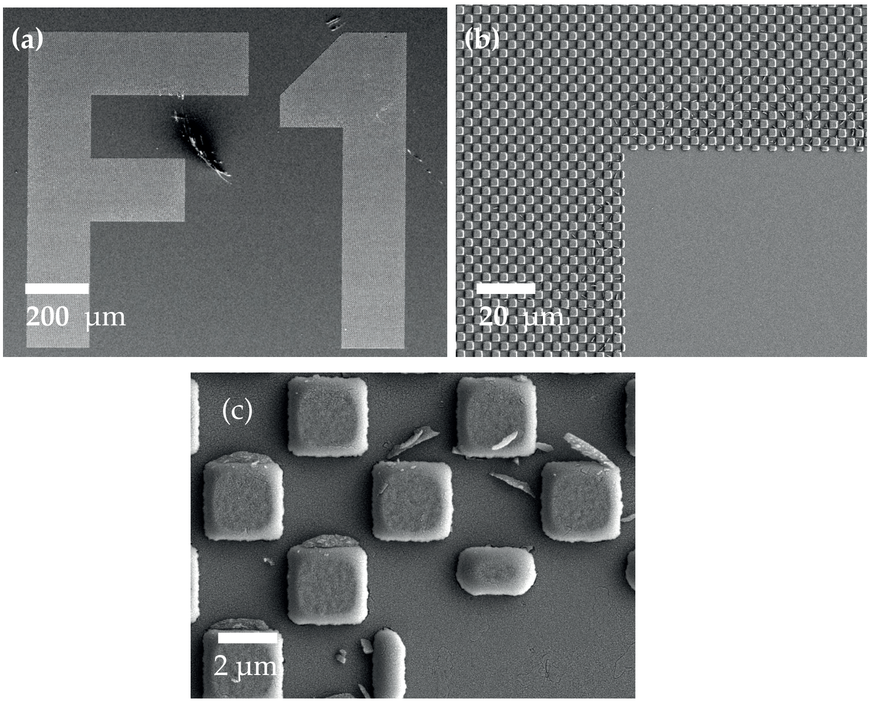

Figure 4.10: SEM images of the glass of experiment A (parameters given in Tab. 4.8) in the region ′F1′ in Fig.4.8 (b). The filling is lower than for the regions ′E1′. Small particles are present on the surface originating from the broken GC features.

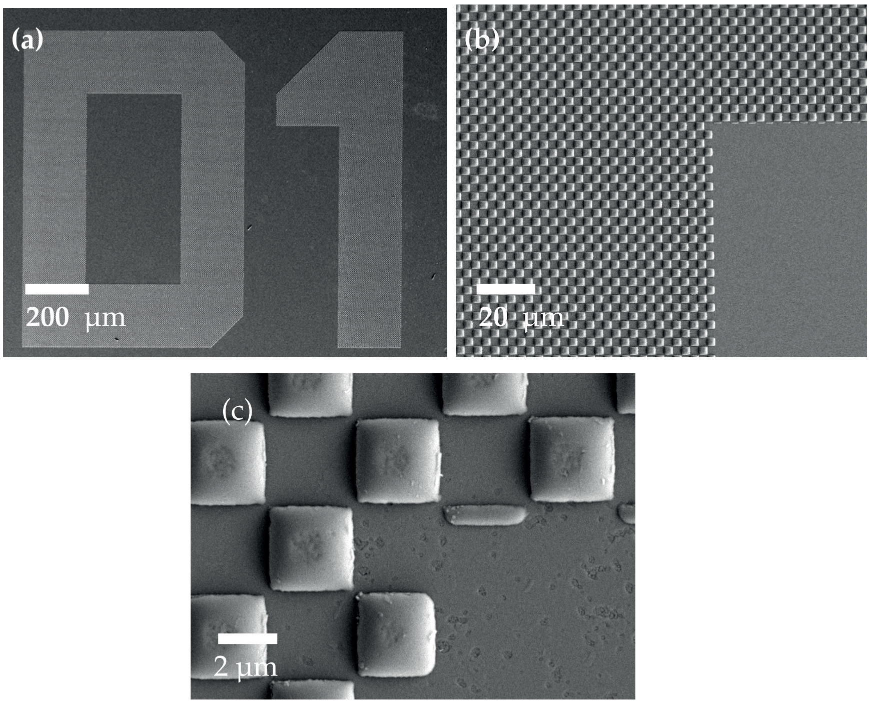

Figure 4.11: SEM images of the glass of experiment A (parameters given in Tab. 4.8) in the region ′D1′ in Fig.4.8 (b). No damage to the square pattern can be seen, but the filling is lower than for the regions ′E1′ and ′F1′.

regions.
In order to test the area dependency of the replication quality, we compare the markers, since the 3 circle areas exhibit different patterns. The markers consist of a chess pattern with 3 µm wide squares. SEM images for all three markers are shown in Fig. 4.9 - 4.11. For the marker ′E1′ in Fig. 4.9 (a) a large amount of the microfeatures is broken. This is especially the case for the outskirt areas. Also, parts of the mold were broken during the molding. In some areas of the glass the square pattern is standing in a collective pattern (Fig. 4.9 (b)). We believe this is caused by the different thermal shrinkage of mold and glass during the cooling step. The glass L-BAL42 shrinks more than the GC mold. The center of the glass is located downwards from the element ′E1′. The glass is moving towards this direction with respect to the mold. The glass in the unstructured areas around element ′E1′ can slide freely over the GC mold, whereas the microstructured areas are more mechanically interlocked with each other. Thus, a stress is built up at the interface of flat and microstructured areas. If the stress is high enough, it can cause the rapture of the holding microfeatures. The direction of the standing pattern in Fig. 4.9 (b) and (c) corresponds to the glass mold movement: the left flat area is moving downwards causing the microstructured features to be flipped upwards with a small tilt in the border direction. The same deformation/rapture behavior was found for the outskirt areas of the large DOE areas in Fig. 4.8.
For the 2 other markers ′F1′ and ′D1′ much less deformation can be seen. The filling of marker ′F1′ is lower than for the regions ′D1′ and a considerable edge rounding is present. Small particles in Fig. 4.10 (c) are present on the surface originating from broken GC features. No damage to the square pattern of marker ′D1′ can be seen in Fig. 4.11, but the filling is lower than for the regions ′D1′ and ′F1′. Additional side profiles were taken for features of the markers ′F1′ and ′E1′, which are given in Fig. 4.12. The best filling can be seen for marker ′E1′, because the edges of the features are very sharp. The walls of the replicated glass in Fig. 4.12 show the same waviness as the GC mold (Fig. 3.12 (b)). This indicates that precision glass molding can replicate features in the nm range.
We believe that there is a connection between the filling rate of the microstructures and the appearance of deformation/rapture: for higher filling, the features are more prone

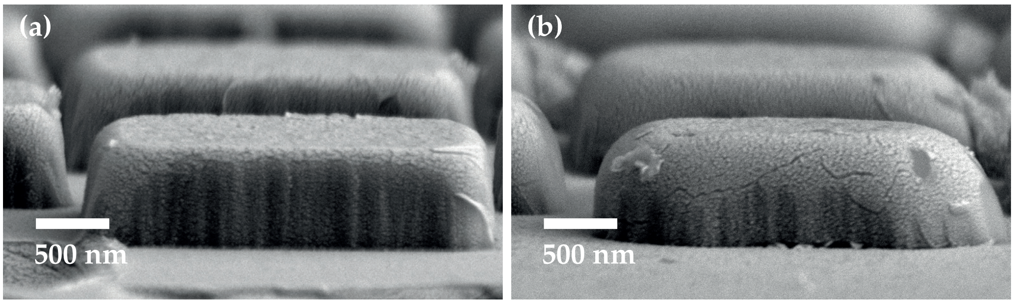

Figure 4.12: Side view images of marker features for (a) region ′E1′ and (b) region ′F1′ with a tilt angle of 5°.

to be deformed. A better filling means that the contact surface between the glass and mold is higher and thus the holding of the microstructured areas increases, therefore increasing the stress built-up at the interface to flat and microstructured areas.
We did not observe a chemical sticking between the mold and glass for any experiment. Only deformations and raptures were seen. For one experiment, where a multilevel DOEs was replicated, a large part of the mold was broken and attached to the glass. An image of the mold is given in Fig. 4.13. Only the microstructured area was broken. After ca. 30 min the GC part jumped away from the glass surface. The GC part showed an unchanged microstructured surface. It is very likely that the thermally induced stress caused a mechanical clamping between the connected microstructured surface of glass and mold. The stress was released like a string and allowed the GC part to be moved away in an abrupt movement.

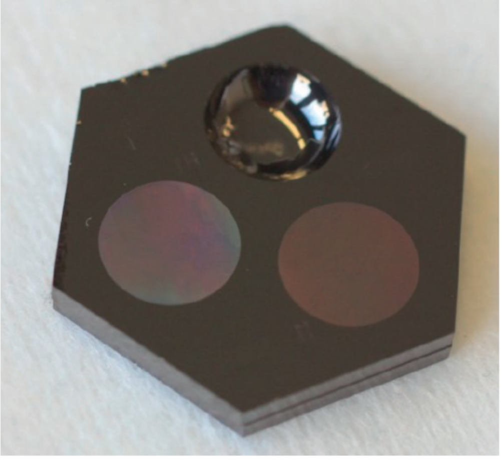

Figure 4.13: Attachment of GC mold to L-BAL42 during molding resulting in the rapture of a large structured area,

The only other case, for which demolding was problematic, occurred for the molding of micro-Fresnel lenses. A 17 mm large area with the center of the lens corresponding to the center of the mold was used. The only way to separate mold and glass was by mechanical force and resulted in breaking of the glass and/or mold into parts with mm size. The symmetry of the Fresnel lens corresponds with the shrinkage direction. We believe that this symmetry increases the effect of mechanical clamping.
To avoid problems of deformation and mechanical clamping the different shrinkage behavior of glass and mold during the cooling step needs to be minimized. It is important to separate the glass from the mold at a temperatures as high as possible. Therefore, experiments with a special holder were performed, where the separation temperature was increased to 450 °C. The temperature needs to be well below T_g to avoid the glass to reflow by itself.
Special design can also improve the replication quality. For DOE designs, where a high filling quality is not necessary, molding parameters for a lower filling should be used. This can be realized by using a lower molding temperature and/or shorter molding

times. To avoid the stress built-up at flat to microstructured interfaces, large areas are preferred. The filling of the whole mold surface can be done with the DOE design or with special spacer structures. Also, non-center symmetric designs are easier to demold than center symmetric designs.

The large area element O, which was introduced in Tab. 2.5, has a diameter of 17 mm. The molding conditions are given in Tab. 4.9, where the main difference to experiment A (Tab. 4.8) is a lower temperature of 555 °C. Photos of the mold and glass are given in Fig. 4.14 . Both glass and mold look much more uniform than experiment A, which indicates a more homogenous replication quality with less rapture/deformation problems. SEM images at the middle of the DOE area are shown in Fig. 4.15 (b)-(c). For comparison, the equivalent features on the GC mold are also given. A good replication quality can be seen. The glass edges look sharp and no broken particles are present.
We can investigate the area dependency by looking at different positions on the glass in Fig. 4.16. The features at the border of the glass look different and less similar to the GC mold. They are less filled at the border areas. They also show deformation due to glass

GC mold glass configuration	depth 690 nm L-BAL42 stack (Fig. 4.3 (a))
molding temperature molding time molding pressure	555 °C 120 s 1.2 kN
after molding time after molding pressure	180 s 0.5 kN

Table 4.9: Parameters for molding experiment O.

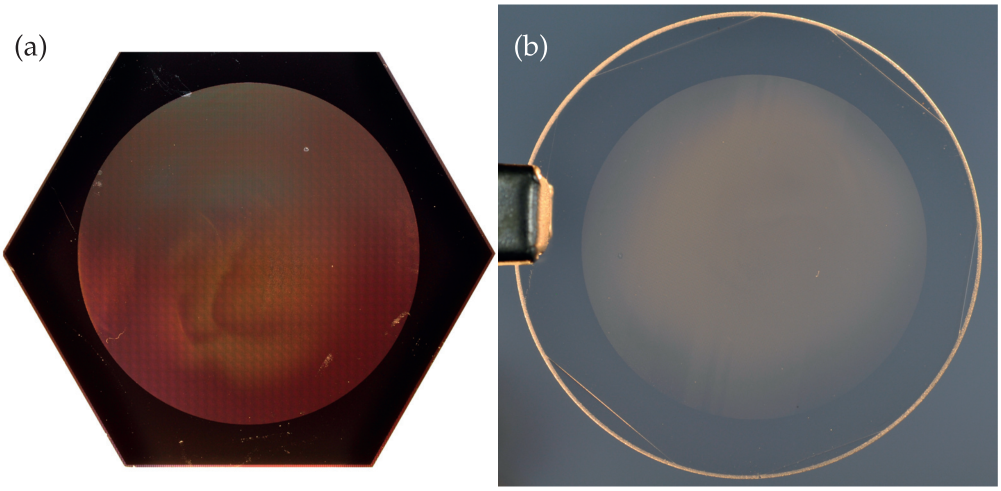

Figure 4.14: Images of the GC mold and glass of molding experiment B (parameters given in Tab. 4.9).

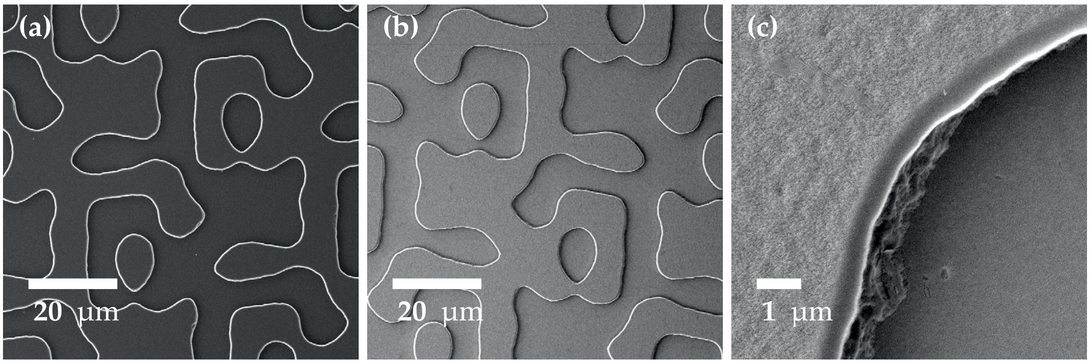

Figure 4.15: SEM images of molding experiment B for (a) the GC mold and (b)-(c) the glass in the center of the element.

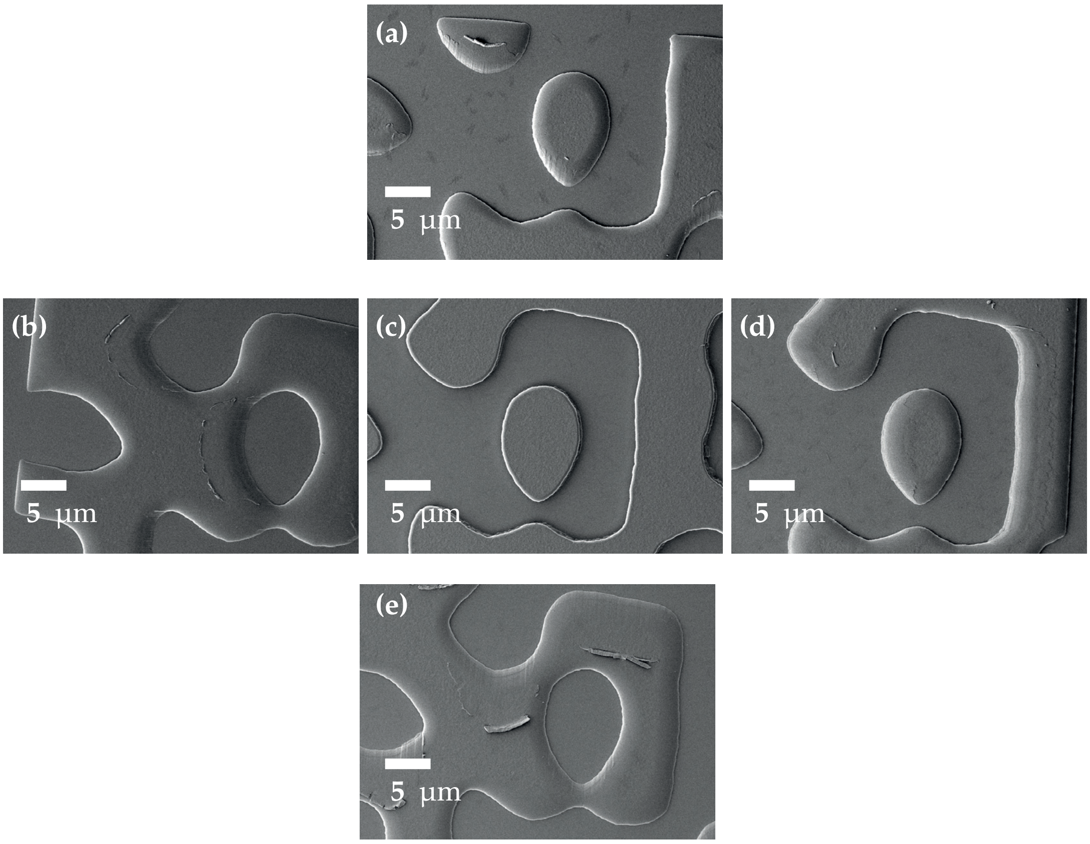

Figure 4.16: SEM images of molding experiment B (settings Tab. 4.9) at different locations on the glass area: (c) center (same position as Fig. 4.15) and the four border positions (a) top, (b) left, (d) right and (d) bottom, which show deformation due to glass movement against the mold.

movement against the mold. Glass material was moved in the direction away from the glass center. The outstanding glass edge facing the glass center were deformed. This is due to the different thermal shrinkage. The material displacement can be measured in Fig. 4.16 and is (a) top 3 µm, (b) left 4.8 µm, (d) right 6.6 µm and (e) bottom 9.1 µm.
An estimation of the length difference was done in section 4.3.3. If the temperature range from 565 °C to 100 °C over the area radius of 8.5 mm is considered, the glass shrinks by 33.2 µm more than the GC mold. The deformations in Fig. 4.16 at the outer areas are more likely to appear in the higher temperature range, where the glass acts like a viscoelastic material. If the temperature range is limited by 565 °C to 450 °C, the glass to mold difference reduces to only 15.3 µm. This value is in the same order of magnitude as the experimentally observed deformations. A more detailed analysis of the molding temperature on the amount of shrinkage is not possible, since the exact CTE is not known for temperatures higher than the Yield Point of 538 °C.
The microfeatures at the outer areas show less filling and exhibit more rounded edges. Simulations of mold filling for hot embossing of mold size 26 mm x 66 mm were discussed by Worgull [Wor2009]. The pressure distribution over the area is parabolic. This gives the available pressure to fill the microfeatures at a defined distance from the center. Worgull found that the maximum pressure is present at the center of the mold [Wor2009]. Therefore, the microfeatures of the same size are first filled in the center of the mold and slower in areas further away from the center. This explanation agrees well with our findings. In order to find good molding parameters, it is, thus, important to investigate the filling at the center and at the border of the molded glass.

A new machine configuration, where the mold is fixed to the upper flange, is tested. This allows for an earlier separation of mold and glass. A multilevel mold with a depth of 700 nm, which was fabricated with the Si process, was used. The critical dimension is 1.5 µm. The process parameters are summarized in Tab. 4.10. The molding temperature is set to 565 °C, for which the viscosity is ca. 10^9 Pa s. This corresponds to the recommended temperature of the supplier OHARA. The separation temperature is 450 °C.
For a molding time of 120 s, the results are depicted in Fig. 4.17. A longer molding time of 240 s was needed to achieve a better filling. The SEM images in Fig. 4.18 show very

GC mold glass configuration	depth 700 nm L-BAL42 fixed mold (Fig. 4.3 (b))
molding temperature molding time molding pressure	565 °C 120 s and 240 s 1 kN
separation temperature	450 °C

Table 4.10: Parameters for molding experiment for multilevel design A.

steep walls. A better area uniformity for the fixed holder experiment in Fig. 4.17 can be seen than for the stack configuration in Fig. 4.16. No fracture or deformation appears for the fixed holder. The high replication accuracy of Fig. 4.18 and the uniform replication result over an 18 mm area shows that a high quality for the molding of DOE can be achieved. It is essential to optimize the molding parameters for a high form accuracy and a minimal amount of thermal shrinkage effects.

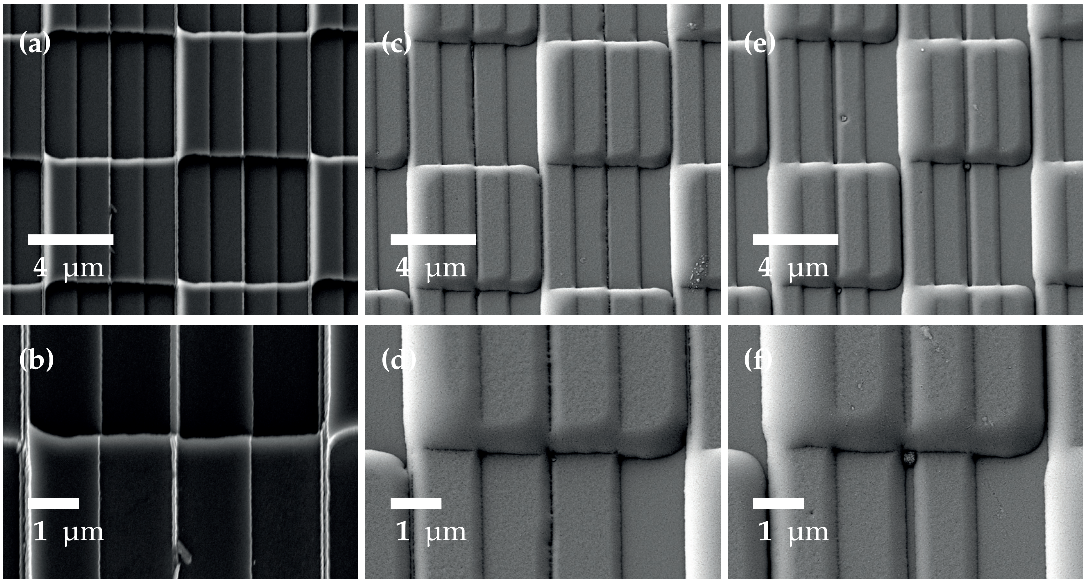

Figure 4.17: Area dependency fixed mold, (a)-(b)mold center, (c)-(d) glass center and (e)-(f) glass out.

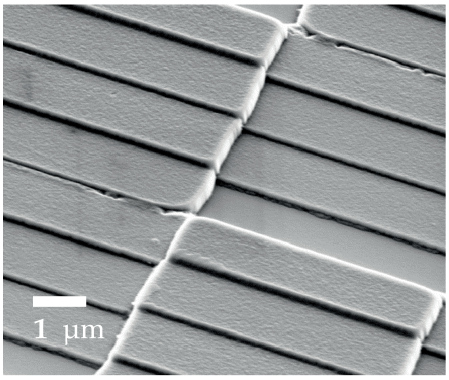

Figure 4.18: Molding the same element as in Fig. 4.17 with a longer process time of 240 s results in a very good replication quality.

4.5 Comparison of Mold Materials

As discussed in section 4.1 the preferred characteristics for the mold material are:

- high temperature resistance for 400 °C - 800 °C and 1400 °C for fused silica;
- high hardness for low wear, less mold deformation and longer mold lifetime;
- chemical inert to allow an easy separation of mold and glass after molding;
- microstructuring process with optical quality (e.g. CD ≈ 1 µm, $R_a < 20$ nm).

As mold materials glassy carbon (GC) and fused silica are testes against these criteria. For fused silica, an anti-adhesion layer Pt-Ir needed to be applied. The results of this section are published in the journal paper [Prater2016].

4.5.1 Glassy Carbon as Mold Material

For all molding experiments, the GC molds could be separated from the glass without effort. No chemical binding was observed. This was expected owing to the excellent anti-adhesion properties of GC. It is thus not necessary to use additional coatings.
For most of our experiments, we used the same mold between 1 and 10 times. This was done mostly to see the influence of individual molding parameters. In order to analyze the durability of the GC molds, we conducted 50 cycles with the same mold. The molding parameters are summarized in Tab. 4.11. We used similar parameters as the optimized parameters from the last section 4.4. The mold filling showed small edge rounding in comparison to the critical dimension of 2.5 µm. The molding temperature was 555 °C and the separation temperature was 450 °C (mold-glass configuration 4.3 (b)). The element O, which was used for the mold lifetime test, acts like a 6x6 beamsplitter. Optical measurements were conducted to measure the 6x6 design order efficiency, the 0^{th} efficiency, and the uniformity error. A change in the optical performance could be found. The performance quality degrades mainly for the first 3 replications. The uniformity error UE, the efficiency of the 0^{th} order and the efficiency of the design orders increased. The performance of replicas 3 to 50 stays constant.
SEM images in Fig. 4.19 (a) showed that the mold was slightly damaged. Replica 1

GC mold glass configuration	depth 525nm L-BAL42 holder (Fig. 4.3 (b))
molding temperature molding time molding pressure	565 °C 120 s 1 kN
after molding time after molding pressure separation temperature	180 s 0.5 kN 450 °C

Table 4.11: Molding parameters for lifetime test with element O.

shows no degeneration depicted in Fig. 4.19 (b). Whereas replica 2 in Fig. 4.19 (c) shows the corresponding broken part of the mold. Fig. 4.20 shows the mold in comparison with replica 2 in higher magnification. Although the position is not exactly the same, it can be stated that the size and shape of the broken edge correspond. The replica shows two

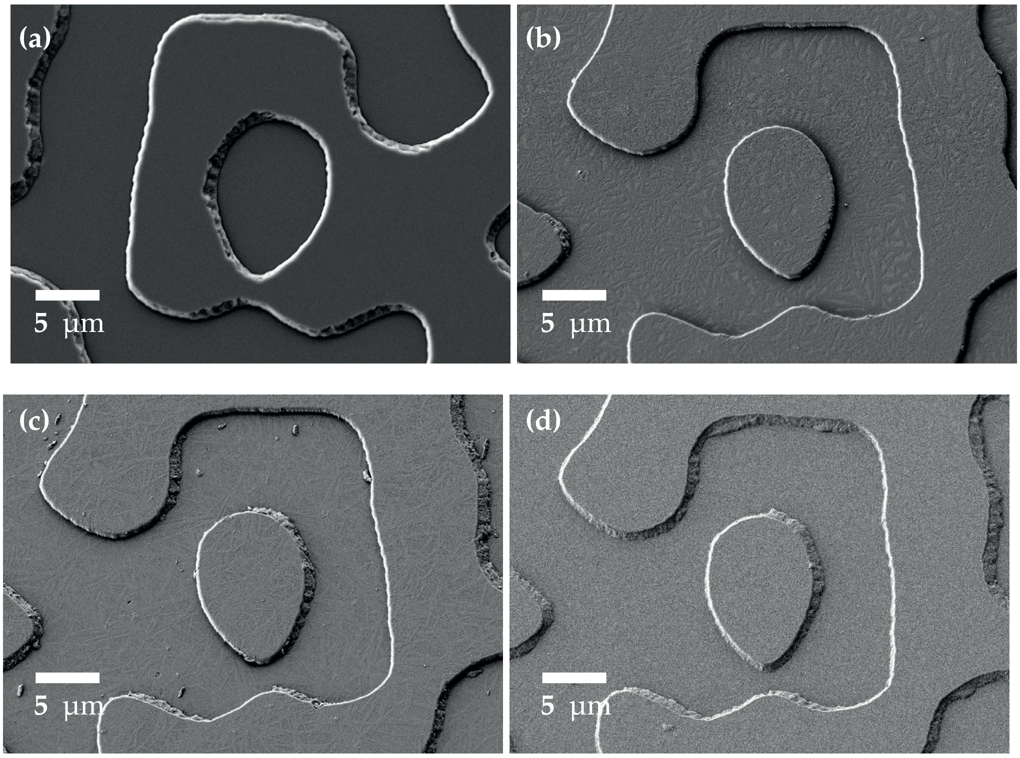

Figure 4.19: (a) SEM images of GC mold after 50 replication cycles and of 1^{st} replication (b), 2^{nd} replication (c) and 50^{th} replication (d). The 1^{st} replication reproduces perfectly the designed structure, but the mold is damaged during demolding. In subsequent moldings, the replica shows degeneration, which does not change for many cycles.

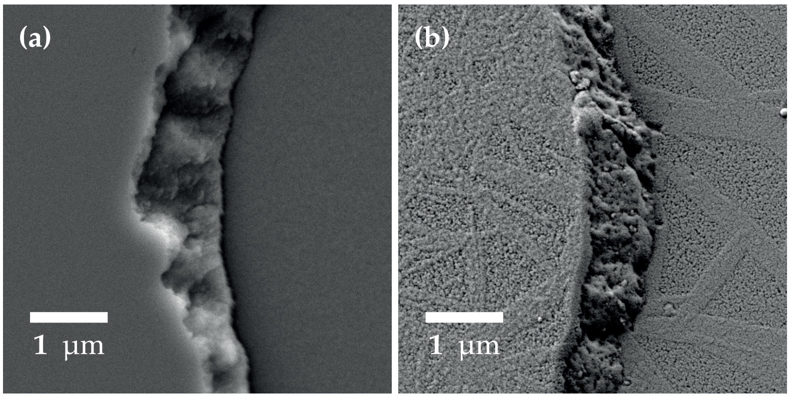

Figure 4.20: (a) Higher magnification SEM images of GC mold after 50 replication cycles and of 2^{nd} replication (b) showing the edge damage. The glass surface was sputtered with 10 nm Au, which causes the rough surface appearance.

different textures at the edge: lower roughness features are glass and higher roughness features are broken GC mold parts sticking to the glass.
We believe that the problem is caused by a lateral movement of the upper molding arm during demolding, causing the partial breakage of the GC mold features. After the first replication, the replicas did not show any alterations anymore. Replica 50 given in Fig. 4.19 (d) shows the same features as replica 2. Even with the present problem, one can see that the molding was stable after the first few runs. The machine was modified in a way that the microstructured mold is fixed to the upper arm. The arm movement needs to be controlled very accurately during demolding. This is not foreseen in the standard mold settings. We note that this problem did not occur for other mold experiments with the fixed mold configuration. Examples of very good replication with the fixed mold configuration can be found in Fig. 4.17 and 4.18 in section 4.4.
The GC mold was fabricated with the Si process. The depth was etched to 525 nm. AFM measurements of the mold show that the roughness does not significantly change. The roughness R_a of the etched surface after mold fabrication was 2.3 nm and after 50 replications 2.6 nm. The results of the AFM measurement are depicted in Fig. 4.21. The surface roughness of (a) polished GC mold was found to be 0.596 nm and for (b) the replicated glass0.59 nm. Therefore, the surface roughness of the mold is very well imprinted on the glass. We believe that the scratches on the glass surface seen in Fig. 4.21 (b) are caused by a glass-to-mold movement during the cooling period.
Additionally, no change of the texture like holes could be seen on the GC mold surface. GC is thermally stable enough to mold the glass L-BAL42 at 555 °C. This shows that GC molds have the potential for multiple use of more than 50 replication cycles.

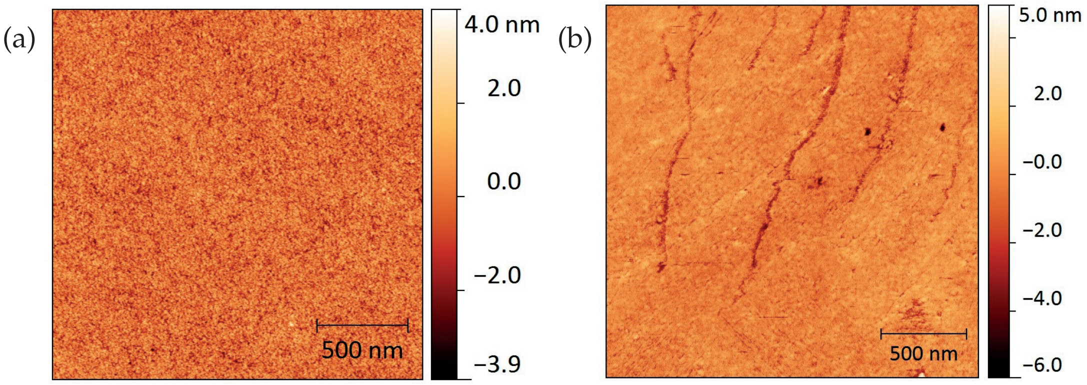

Figure 4.21: AFM measurements of the surface topography of (a) polished GC mold (R_a = 0.596 nm) and (b) the corresponding replicated glass (R_a = 0.59 nm).

4.5.2 Fused Silica as Mold Material

To compare our approach to coated molds, we tested a fused silica mold, which was fabricated by an external supplier. This mold exhibits a high structure quality due to the e-beam lithography employed and is used as a state-of-the-art reference. SEM images of the molding with a fused silica masters are given in Fig. 4.22. The design is the same as on the binary mask H. Due to the e-beam lithography the accuracy of the edge position is much higher. The pixelated shape is caused by the sequential exposure with the e-beam. The molding parameters are given in Tab. 4.12. In order to use fused silica masters for precision glass molding, anti-adhesion coatings are required. The fused silica masters were sputtered with 15 nm thick Platinum-Iridium (Pt-Ir) layer, the typical material choice for such a case. The fused silica master was coated at IPT Aachen (Germany). Figure 4.22(a)-(b) show the fused silica master after the coating. The sidewall of the etch step is not uniformly coated. It shows a higher roughness than the flat surface. Coating techniques such as sputtering give very uniform coatings, but are very directional in depositions. A good sidewall coating is difficult to achieve.

This fused silica master was used to mold L-BAL42 at a temperature of 570 °C and a pressure of 0.8 kN. The stack configuration of Fig. 4.3 (b) was used consisting of the microstructured fused silica master on the bottom, the glass preform and a flat tungsten carbide mold on the top.

The SEM images (Fig. 4.22(c)-(d)) of the master after molding shown severe change. In some regions of the mold large pieces of L-BAL42 are broken and stick to the fused silica mold. They can be clearly identified thanks to the different material contrast in the SEM. The replicated glass in Fig. 4.22(e)-(f) shows the corresponding missing parts. The high temperature of 570 °C results in a low viscosity of $10^{8.8}$Pa s and allows a very good mold filling. The microfeatures of the molded glass in Fig. 4.22 (f) show very steep edges and thus a good replication accuracy.

In the higher magnification images of the fused silica mold, it can be seen that a part of the Pt-Ir coating is missing at the edges. It is thus more difficult to separate the fused silica mold and glass. Because the filling was very good at the edges, the glass and mold were in contact at the edges. We believe that the damage of the coating is decreased for lower filling conditions. The wear of the fused silica molds is very high. Only a

glass configuration	L-BAL42 stack (Fig. 4.3 (a))
molding temperature molding time molding pressure	570 °C 90 s 0.8 kN
after molding time after molding pressure	180 s 0.5 kN

Table 4.12: Molding parameters used for a fused silica master with a 14 nm Pt-Ir antiadhesion layer.

few cycles are possible, usually less than 5. A thicker Pt-Ir antiadhesion coating would increase the lifetime of the mold, but the quality of the micro-structured mold would degrade due to the edge rounding. Typical layer thickness is ca. 300 nm.
The coefficient of thermal expansion of fused silica is $5.1 \times 10^{-7}\,\mathrm{K}^{-1}$ (25 °C - 600 °C), which is 4 times smaller than for glassy carbon. This will increase the shrinkage difference between glass and mold during the cooling. The coating lifetime is also influenced by the thermal shrinkage [Mertus2012]. During each molding cycle, the thermal expansion difference between mold and coating can cause deformation and cracks in the coating

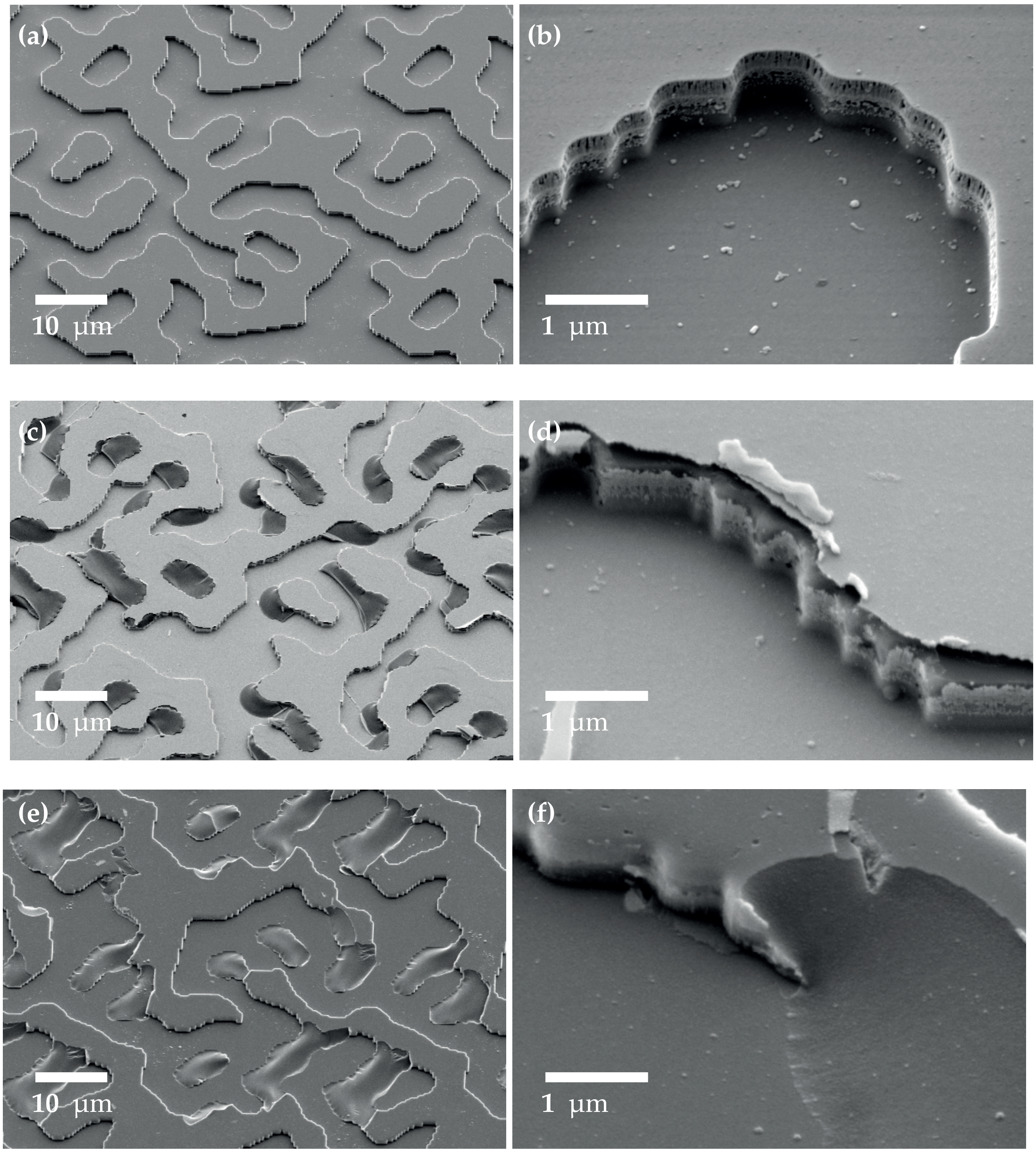

Figure 4.22: SEM images of the fused silica master (design H) after coating with Pt-Ir (a)-(b) and after molding (c)-(d) in comparison to molded glass (e)-(f) (carbon coated for SEM imaging).

layer.
In comparison, we found the GC molds more robust, offer a much longer mold lifetime and do not require a coating, which would increase the cost, have e.g. a smaller lifetime and degrade the quality.

4.6 High Temperature Glass Molding

Fused silica has a wider wavelength range for transmission than low and mid-T_g glasses such as L-BAL42 from OHARA. It is chemically very stable and withstands a higher range of temperatures. For our work, we used SQ1 from Schott [4]. A viscosity of 10^9 Pa s is reached at a temperature of 1437 °C, which is necessary for an effective mold filling. The coefficient of thermal expansion is with $5.1 \times 10^{-7}\,\mathrm{K}^{-1}$ (25 °C - 600 °C) 4 times lower than for GC.
The molding parameters are given in Tab. 4.13. An 8 level mold with a depth of 1.05 µm, which was fabricated with the Si process, was used. The mold was tested before for L-BAL42, during which smaller features introduced by mask-to-mask misalignment were pulled out. Since this features are not included in the design, the damage should not change the performance significantly.
The molding temperature was set to 1400 °C, which is the limit of the Toshiba machine GMP-207HV. In order to compensate for the higher viscosity, the pressure was increased to 2 kN. The SEM images of the mold after the microfabrication and the 1st fused silica

GC mold	1.05 µm
glass	SQ1
configuration	stack (Fig. 4.3 (a))
molding temperature	1400 °C
molding time	240 s
molding pressure	2 kN
after molding time	240 s
after molding pressure	0.5 kN

Table 4.13: Parameters for molding of fused silica at very high temperatures.

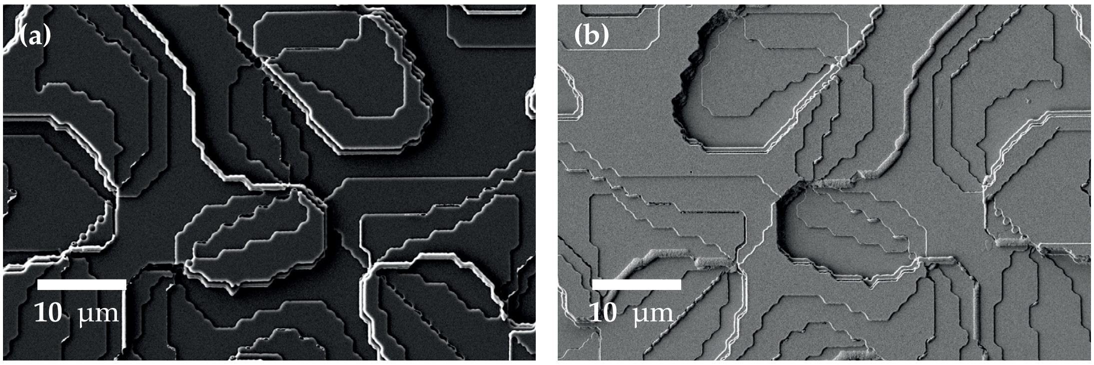

Figure 4.23: SEM images of the GC mold before molding (a) and the 1st replicated SQ-1 (b).

replication are shown in Fig. 4.23. The replication accuracy is good and the surface shape is clearly visible.
Photos of the mold after the 3^{rd} molding cycles and the 3^{rd} fused silica replica are given in Fig. 4.24. Both mold and fused silica surfaces do appear less uniform. A closer look at the SEM images shows a particle contamination on the mold and the fused silica sample. An area with a large amount of particles is given in Fig. 4.25. One part of the glassy carbon surface in Fig. 4.25 (a) is broken and appears at the corresponding position on the fused silica surface. It seems that the mold surface changes and becomes more sticking to the fused silica during the molding. In the extreme cases, large areas of GC are broken and stick to the fused silica (and vice versa), which can be seen by the $\propto$ 100 µm large black particles on the fused silica surface in Fig. 4.24 (b).
Images of the GC mold are given in Fig. 4.26 before the molding (a) and after molding (b)-(c) at two positions with a small amount of particles. The surface of the mold appears rougher after the molding in comparison to the microfabricated mold. A change in the GC mold surface could also be found at areas, where no glass was in contact with the mold.
In order to investigate the origin of the particles, we used x-ray analysis at the SEM Merlin at CMi. The results showed that the particles consist of SiO_2. The surface chemistry of the GC mold shows large amounts of Carbon and small amounts of Oxygen.

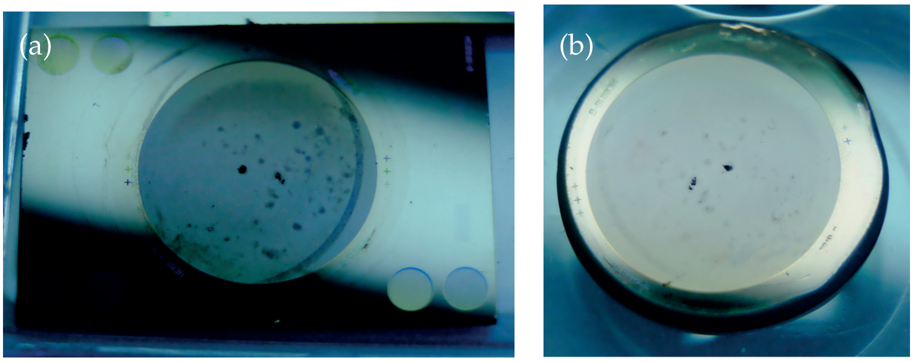

Figure 4.24: (a) GC mold after 3^{rd} molding cycles and (b) corresponding 3^{rd} fused silica replica.

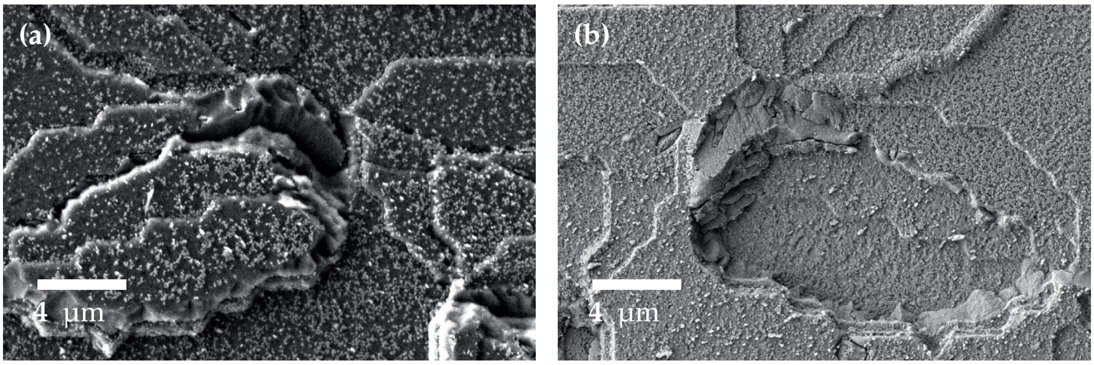

Figure 4.25: SEM images after 3^{rd} cycles of replication with (a) GC mold and (b) replicated fused silica.

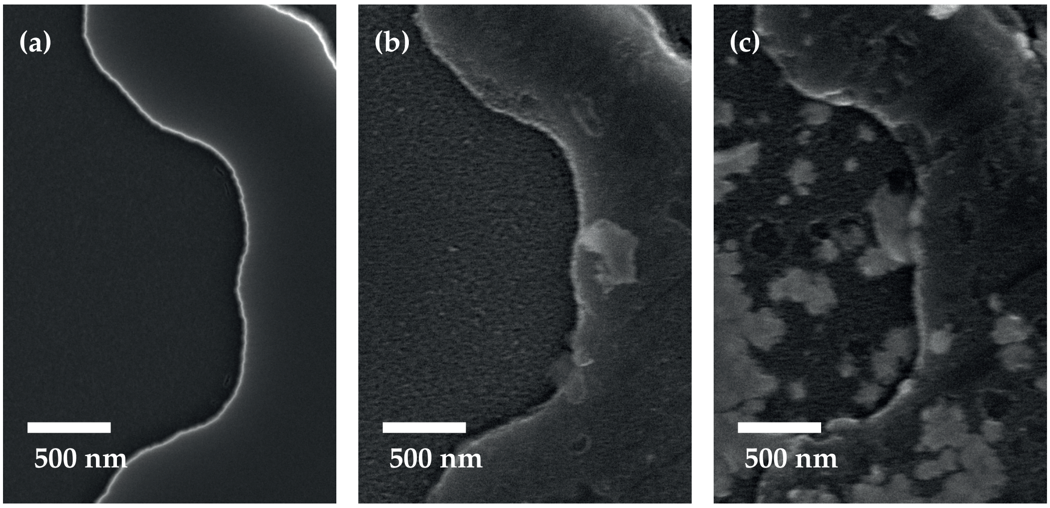

Figure 4.26: SEM images of the GC mold before molding (a) and after molding (b)-(c) at two different regions.

The Oxygen is always present on surfaces, since it attaches in oxygen containing atmospheres. We cannot measure a change in the oxygen contact and assume that the GC surface did not chemically change.
The particle contamination and changed surface morphology could be caused by oxidization of the GC surface. The GC surface can react with O_2 to volatile CO_2, which cannot be measured with our set-up. The origin of the O_2 can be either a small amount of O_2 present in the molding chamber or by O_2 diffusion from the glass. The temperature for fused silica molding is with 1400 °C much higher than for the molding of L-BAL42. It is crucial that the GC is in an inert atmosphere, otherwise the carbon is reacting with O_2 and the GC surface slowly degrades. Holes appear on the surface causing a higher surface roughness. The increased surface roughness or a possible change in the surface chemistry might increase the adhesion between the fused silica and the GC to an extent, where no glass release is possible anymore and thus causing parts of the GC and/or glass to break. The degradation of the GC mold is repeated for each molding cycle. This would explain, why the first replication showed a good replication and fracture appeared only for later replications.
Since the modification of the GC mold surface is seen also in areas not covered by the glass, we believe that the O_2 content in the atmosphere plays a significant role. We suggest that this mold failure mechanism could be suppressed by controlling the atmosphere in the molding chamber better. No investigation was done to prove this theory because of limited access to the molding machines. We conclude that molding of fused silica with high accuracy is possible, but the lifetime of the glassy carbon mold is very limited in our case.

4.7 Resolution Limit of Glass Molding

From the application point of view, it is important to know the limits of precision glass molding. Of special interest are the minimal feature size and the maximum aspect ratio that can be molded with high accuracy. The glassy carbon molds were fabricated with the Si mask in combination with electron-beam lithography, which allows feature sizes below 1 µm (details of the mold fabrication can be found in section 3.5). The results of this section are published in the conference proceedings [Prater2016a].

The molding conditions for the glass L-BAL42 are given in Tab. 4.14. The pressure was set to 1 kN for all experiments. Two temperatures and 3 different times were used. The temperatures are 565 °C and 568 °C, which will result in a viscosity log(η) of 8.998 and 8.878. These viscosity values are very close to each other. We expect therefore similar results.

Photos of the mold and the replica **565°C-120s** are shown in Fig. 4.27. The total size of the GC mold is 24 mm by 36 mm. We fabricated two different types of structures: a diffractive optical element (DOE) and resolution test patterns. The optical functionality of the DOE is a 1:31 beamsplitter (design details of element R are given in Tab. 2.7). The period is 29 µm with a critical dimension of 800 nm. For a fabricated depth of 485 nm this gives an aspect ratio of 0.6 that has to be replicated. The active area of the linear beamsplitter is 2 mm by 2 mm and can be seen in Fig 4.27 (a) by the large square area.

GC mold glass configuration	depth 485 nm L-BAL42 fixed (Fig. 4.3 (b))
molding temperature molding time molding pressure	565 °C, 568 °C 120 s, 240 s, 360 s 1 kN
after molding time after molding pressure	180 s 0.5 kN

Table 4.14: Parameters for molding for a high-resolution glassy carbon mold.

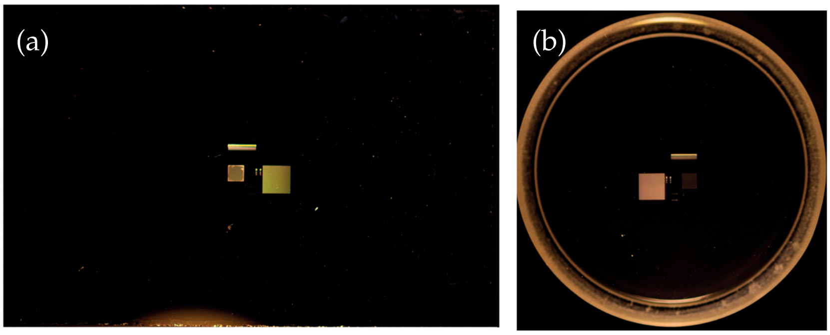

Figure 4.27: Images of the GC mold and glass with high resolution features including a 2 mm by 2 mm large area of the DOE R and 2 mm long lines with different linewidths for resolution limitation tests.

In order to get a more general idea of the molding quality, we added resolution lines with linewidth ranging from 2 µm down to 250 nm. For an etch depth of 485 nm, these correspond to aspect ratios from 0.24 to 1.94. For each linewidth, we used 10 lines with a distance equal to the linewidth and a length of 2 mm. The resolution test patterns can be seen in Fig 4.27 (a) by the large rectangular area on the top.

After molding, we cut the mold and glass to access their height profiles, which can then be compared with each other. Figure 4.28 (a) shows the height profile of the GC mold feature with a width of 1.5 µm. The GC substrate is shown up-side-down to have a better understanding of the glass filling behavior. The wall verticality of the mold microfeatures is 82° ± 2°. The replica **568°C-120s**, which was molded at 568 °C for a duration of 120 s, is given in Fig. 4.28 (b) of a 1.5 µm resolution line and in Fig. 4.28 (c) for a 1.5 µm wide line included in the DOE. The profiles of the resolution line and the DOE line show very different filling rates. The resolution line is well replicated. The line feature of the DOE was measured at the center of the 2 mm by 2 mm area. The glass touches the glassy carbon only at the very center of the line. It appears that the glass filling rate depends also on the structure around the element. If we want to investigate the filling behavior for large area structuring, the resolution lines fabricated on the mold are not good representatives. In the following, we concentrate only on the large area DOE.

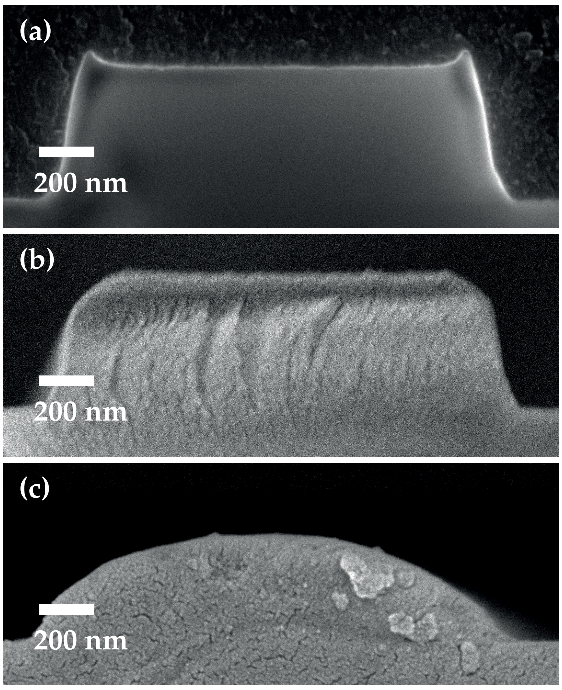

Figure 4.28: Height profile of 1.5 µm wide lines for (a) the GC mold and glass (120s, 568 °C) with single lines (b) and element R (c).

SEM images of the GC mold and the glass samples for 6 different molding conditions are shown in Fig. 4.29. A part of the DOE with a period of 29 µm is imaged. The largest linewidth is 2.9 µm. The narrowest line is 1.15 µm with an 800 nm long distance to the next line. The glass profiles are taken at the center of the 2 mm by 2 mm area. After dicing the surface of the cut was not sufficiently flat for good imaging. Therefore, all samples needed to be polished to a very good quality. We used the Allied High Tech MultiPrep polishing machine at Microcity. The lowest diamond grain size of the disk film was 0.25 µm. The glass was sputtered with Au for SEM imaging. During the polishing, glass particles are removed from the polishing cut and redeposit on the microstructured surface. The particles in the SEM images are due to this.

From the SEM images in Fig. 4.29 it can be seen that the sample **568°C-120s** shows the lowest filling rate. As expected longer molding times result in a better filling. To better compare the profiles we use Matlab. An example is given in Fig. 4.30 for the sample **565°C-120s**. The blue curve corresponds to the extracted height profile. The glass was sputtered with a 10 nm thick layer of Au for SEM imaging. The accuracy is ca. ± 20 nm.

(a) GC mold

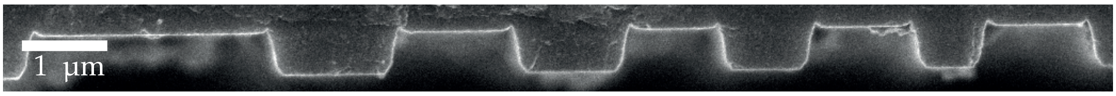

(b) 120 s and 565 °C

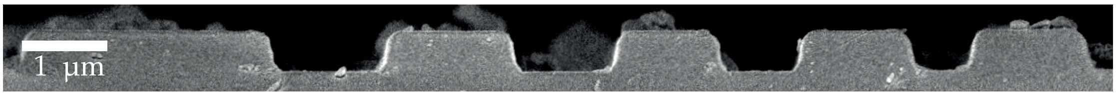

(c) 240 s and 565 °C

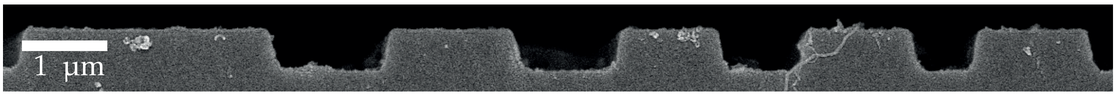

(d) 360 s and 565 °C

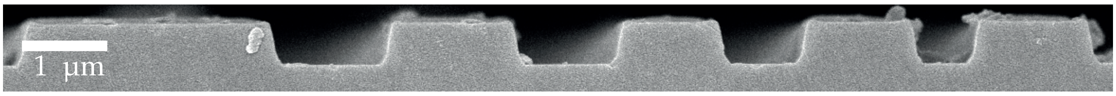

(e) 120 s and 568 °C

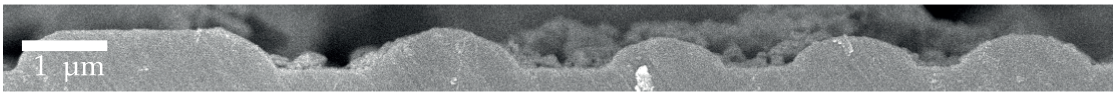

(f) 240 s and 568 °C

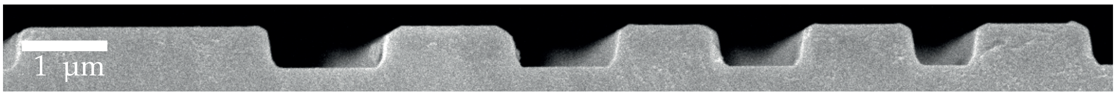

(g) 360 s and 568 °C

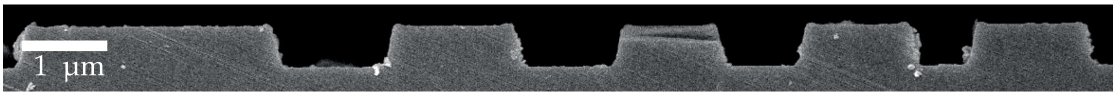

Figure 4.29: SEM images of the GC mold (a) (substrate on the top) and glass (b)-(g) with high-resolution features of element R.

The extracted height profiles are depicted in Fig. 4.31. The mold profile is shown up-side-down for better comparison. The depth of the mold is 485 nm. Features from the trenching effect appear on the mold profile, which can be seen by the 'ears' at the corners. Only the sample **565°C-120s** shows a low filling rate. It is expected that a higher temperature with the same molding time will result in a better replication. This is not the case when comparing the samples **565°C-120s** and **568°C-120s**. It is not clear if this effect is caused by an unwanted mold setting. To confirm the result, the experiment needs to be repeated, which was not possible in this work.

For all other samples expect **565°C-120s** good filling was achieved. The glass reached the flat part of the mold. Differences are only present at the corner rounding. A longer molding time causes a better filling in the edge corners. The best filling is achieved for the samples **565°C-360s** and **568°C-360s** with the longest molding times. Both samples are filling the trenching ears. The temperature difference of 3° has a small influence.

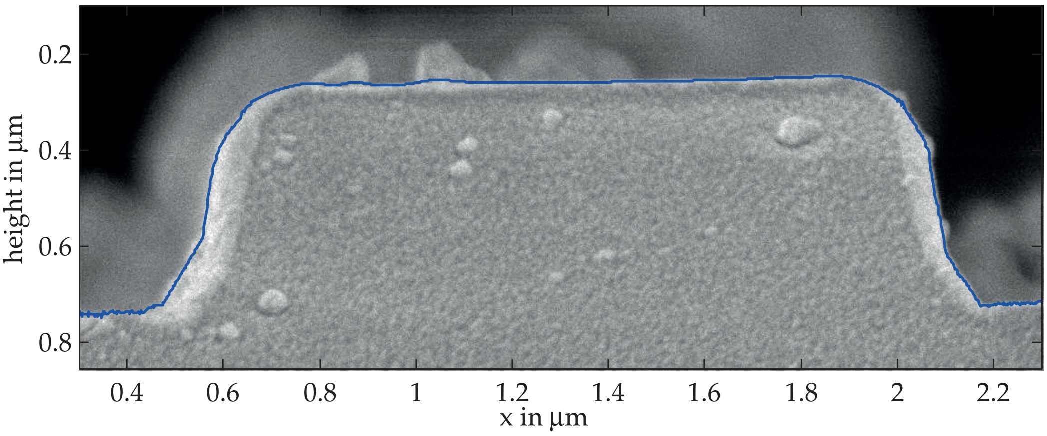

Figure 4.30: The height profile is extracted from the SEM images with Matlab. Example for 120 s and 565 °C.

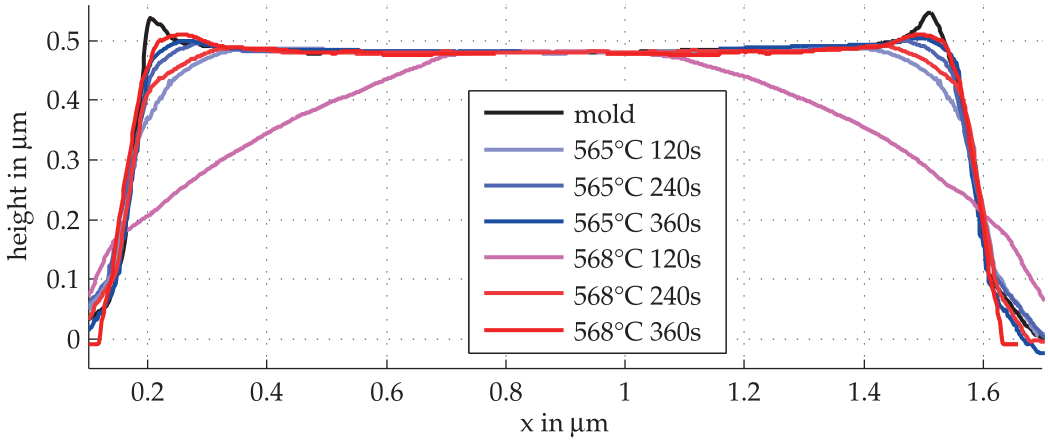

Figure 4.31: Extracted height profiles from the SEM images for the line element with 1.45 µm width. Mold filling is very close to the mold for longer molding times.

The good correspondence of the mold and glass shows that a temperature of 565 °C and a molding time of 360 s is sufficient to mold this diffractive optical element with high replication accuracy. The analysis of the molded glass profiles gives a good idea of the molding quality, but the more important investigation has to be done in terms of optical performance. The results of the optical performance of the elements presented here are discussed in section 5.2.2.

The measured glass profiles will be used for simulations. For the DOE design R lines with linewidths ranging from 2.9 µm to 1.15 µm need to be molded. The profiles of the 8 different lines are plotted together in Fig. 4.32. The measurement was done at the center of the DOE area. For both samples **565°C-360s** and **568°C-240s**, the glass profile was independent of the linewidth. This is seen for all molding tests. We note that designs with stronger variations in the feature size could show different glass profiles. This effect also depends on the molding parameters and the typ of glass.

Finally, the replication quality was investigated at different positions of the DOE. We found that the uniformity over a length of 2 mm is very good. Deviations could be found for same replications in the close vicinity of the border of the DOE area. An example is given in Fig. 4.33 for 1.45 µm wide lines.

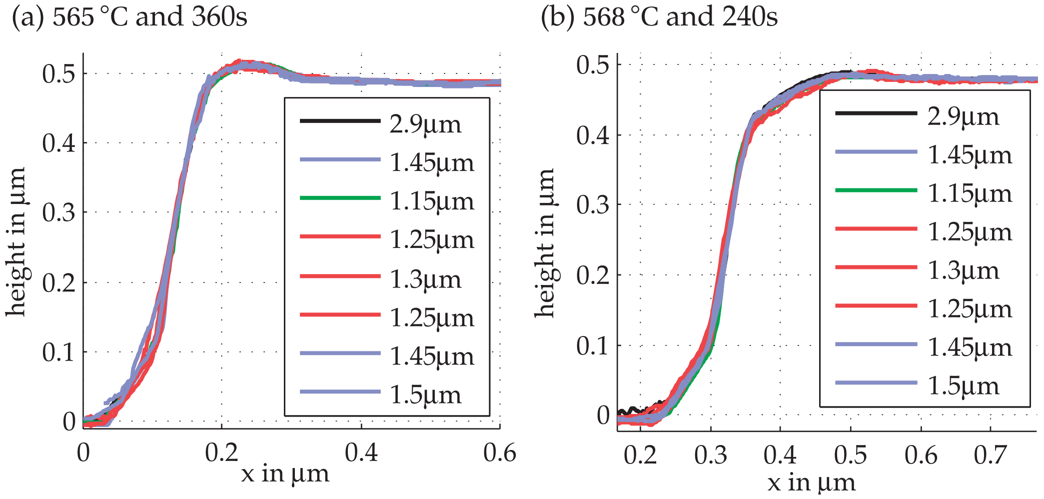

Figure 4.32: Profile of lines with different widths at the center of the DOE for 2 different molding conditions (a) and (b).

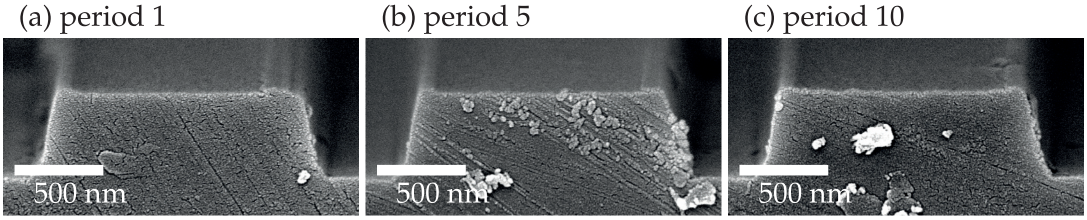

Figure 4.33: Height profile of glass **568°C-360s** at different positions of element R starting from the left side of the element.

The center of the microstructured area lies to the right and the flat unstructured area is positioned to the left of the depicted features. This molding experiment showed very high filling rate. The feature in the first period next to the flat area in Fig. 4.33 (a) shows deformation of the trenching corner. The more the features are located near the center of the area (b) and (c) the less this effect can be seen. We believe that the problem occurred due to a thermal shrinkage movement or the flanch movement of the lower flanch was not perfectly vertical. We found this area dependent effect to be the strongest variation for all samples. Therefore, we conclude that the area uniformity over the tested length of 2 mm is very good.

4.8 Summary

The fabricated glassy carbon molds were used for precision glass molding of a low T_g glass L-BAL42 (OHARA) and for fused silica molding. All molding experiments were carried out by our partners at the Fraunhofer Institute for Production Technology (IPT). L-BAL42 was chosen because of its low coefficient of thermal extension. During the cooling of the precision glass molding the mold and glass stay in contact, otherwise the glass would be still too liquid to maintain its molded shape. The shrinkage mismatch of the mold and glass will cause a stress built-up especially at transition zones between flat areas and microstructured areas, which in the most extreme cases cause rapture and/or deformation of the microsurfaces. We found that releasing the glass at elevated temperature (in our experiments 450 °C) can greatly reduce the damage. The molding set-up needed to be modified to fix the glassy carbon mold to the upper molding flanch. Very good replication results were obtained for L-BAL42 molded at 655 °C. The homogeneity over a microstructured area with a diameter of 17 mm was sufficiently good.

A fused silica mold with a 15 nm Pt-Ir anti-adhesion coating was tested for the molding of L-BAL42. The lifetime of the mold is less than 5 cycles, because the adhesion problems between glass and mold occurred resulting in the breakage of glass microfeatures. In comparison, we found that GC is more robust, offers a much longer mold lifetime and does not require a coating, which would increase the cost, have e.g. a smaller lifetime and degrade the quality.

Strong mold wear of the glassy carbon mold was found for the molding of fused silica at very high temperatures. We found that molding of fused silica with high accuracy is possible. Further investigations have to be done to improve the lifetime of the glassy carbon mold.

A high-resolution diffractive optical element with a critical dimension of 800 nm and an aspect ratio of 0.6 could be molded with high accuracy into L-BAL42. We could thus prove the potential of precision glass molding with high-resolution glassy carbon molds.

5 Optical Performance

In this chapter, the quality of the molded diffractive optical elements (DOEs) is discussed in terms of optical performance. First, we will introduce the set-up used for the characterization in section 5.1. Thereafter, the results of 2 level binary elements are discussed in section 5.2. These include the low-resolution elements in section 5.2.1, for which the glassy carbon molds were fabricated with mask photolithography and the high-resolution elements in section 5.2.2, which were fabricated with e-beam lithography.

For a deeper understanding, the measurement results are accompanied by simulation results. For the low-resolution elements, simulations based on Fraunhofer approximation are sufficient. For a correct representation of the high-resolution elements rigorous methods are used. Different fabrication errors are analyzed. During the mold fabrication errors such as duty cycle errors, form deviation and etch depth errors can be introduced. The molding is analyzed in more detail for the high-resolution elements since height profiles of the molded elements were available from the SEM images and can be included in the simulations. Last, the multilevel elements are analyzed in section 5.3. For these elements, mask-to-mask misalignment errors are introduced during mold fabrication and show a strong influence on the final performance of the molded DOEs.

5.1 Measurement Set-up

Our project partner Holoeye contributed the optical measurements. The set-up is depicted in Fig. 5.1. It is a goniometer set-up with a power meter. The sample is placed on a sample table. Laser sources of different wavelength are placed on the table. For the measurement, the collimated laser light is sent through the DOE. A power meter is placed below the DOE. The distance between the sample and the power can be up to 2 m. The distance is large enough so that the power distribution is considered to be measured in the far field and that the orders are well separated in space. The spacing of the orders needs to be larger than the size of the power meter. The power meter measures the power of each diffraction order individually with very high dynamical range. It is mounted on an x-y stage in order to move to the individual orders. The power of the orders of interest can thus be measured automatically. The power without the DOE is measured as a reference and the power in the design orders is compared to this number. The minimum value that can be measured is 0.1% of the incoming laser beam. The accuracy of the diffraction efficiency is 12% for the absolute values and 5% for the relative distribution.

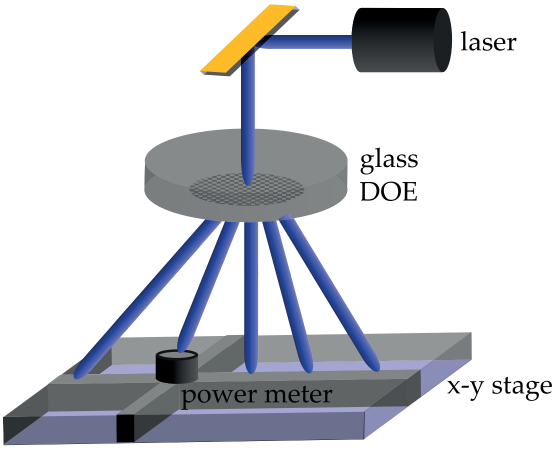

Figure 5.1: Set-up for the optical performance measurements.

5.2 Two Level Binary Structures

5.2.1 Low-Resolution Elements Fabricated with Mask Photolithography

First, the optical performance of the low-resolution elements, which were fabricated with mask photolithography, are discussed. The designs of the elements are given in Tab. 2.5. Element O works as a 6x6 beamsplitter and G as a 11x11 beamsplitter. The critical dimensions are 4.4 µm for G and 2.5 µm for O.

The molding results of element O were discussed in Chapter 4.4. The molding temperature was set to 555 °C. For the element G, a slightly lower temperature of 550 °C needed to be employed to prevent fracture of the glass-mold microstructures. The fabrication details of G are summarized in Tab. 5.2. The comparison of the mold (a) and (c) to the molded glass surface (b) and (d) shows that a good replication quality is reached.

The optical performance of both DOEs is summarized in Tab. 5.1. Both molds were fabricated on the same wafer. The depth of the GC mold was 690nm. The 0^{th} order efficiency is very low for element O with 0.05%. The uniformity error is with 2.5% slightly higher than the theoretical uniformity error of 0.05%. Also, the eff. is with 71.2% very close to the theoretical value. Therefore, precision glass molding can be used to fabricate this element with very good fidelity.

The optical performance of element G is worse than for element O. The uniformity error is 11.9% and thus much higher than the design value of 5.2%. Also, the 0^{th} order efficiency is with 2% considerably higher than the average order power of 0.62%. This can either be caused by a phase mismatch or errors in the structure positions. The phase mismatch is typically caused by an operation wavelength to etching height mismatch. Since precision glass molding is employed, it is also possible that the glass is not completely filling in the mold resulting in a noticeable smaller grating height.

In order to simulate element G, Fraunhofer approximation can be used (see section

element	G	O
	11x11 beamsplitter	6x6 beamsplitter
SEM images	Tab. 5.2 (b) and (d)	Fig. 4.16
replication T	550 °C	555 °C
replication time	180s	180s
replication pressure	1kN	0.9kN
meas. wavelength	750nm	839nm
Oth order	2%	0.05%
design UE	5.2%	0.5%
meas. UE	11.9%	2.8%
theor. eff	64.4%	71.3%
meas. eff.	62.4%	71.2%

Table 5.1: Optical performance of replicas with design G and O. The theoretical design efficiency include a reflection loss of 5% per surface.

sample reference name:	**binary-G-LBAL42**

mask design	
mold insert	hexagonal form Fig. 2.9(a)
optical design	binary DOE 11x11 beamsplitter Tab. 2.5 G

mold fabrication: M1-G	
ICP machine	SPTS CMi
process	250nm Ti mask
photolithography	hard contact
depth	690 nm

precision glass molding	
machine	Toshiba GMP-211V
holder	stack configuration Fig. 4.3 (a)
glass	L-BAL42
molding time	180 s
pressure	1 kN
molding T	550 °C
separation T	100 °C

GC mold	replica
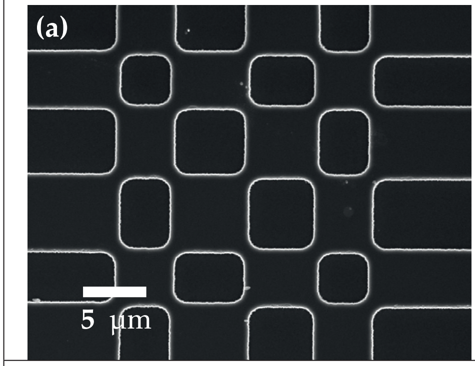	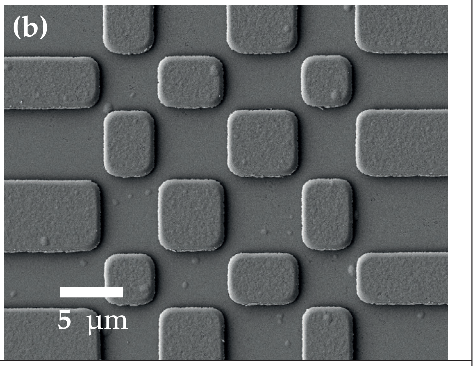
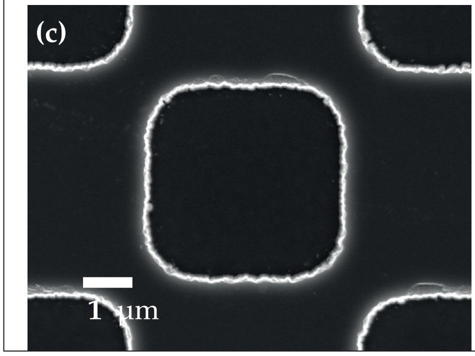	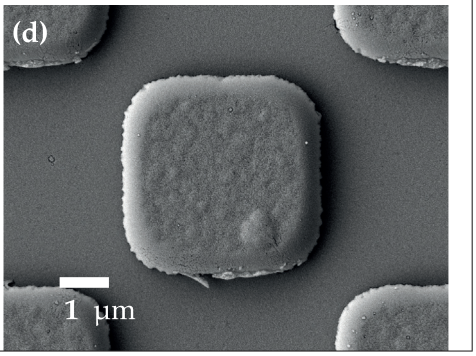

Table 5.2: Design parameters and fabrication results of sample Binary-G-LBAL42. The mold was fabricated with a 2 level design on a photolithography mask. The glass material L-BAL42 was molded 550 °C, which is lower than 564 °C, the recommended temperature of the supplier.

2.1.1). The phase profile consisting of areas with a phase difference of π is depicted in Fig. 5.2 (a). The measurement wavelength of 750 nm leads to a phase mismatch of 6.2 %. Thus, the 0^{th} order efficiency reads as 0.95 % for the simulation result in Fig. 5.2 (b). The uniformity error of the simulated diffraction pattern does not change due to the phase offset. As stated in chapter 2.2.2, phase mismatch errors have no influence on the uniformity error, but the positions of the structure areas determine the uniformity error. From the SEM images in Tab. 5.2, an underexposure and corner rounding can be seen. This errors are already present in the mold. The radius of the corner rounding is ca. 1.06 µm and the photoresist was slightly underexposed resulting in duty cycle smaller

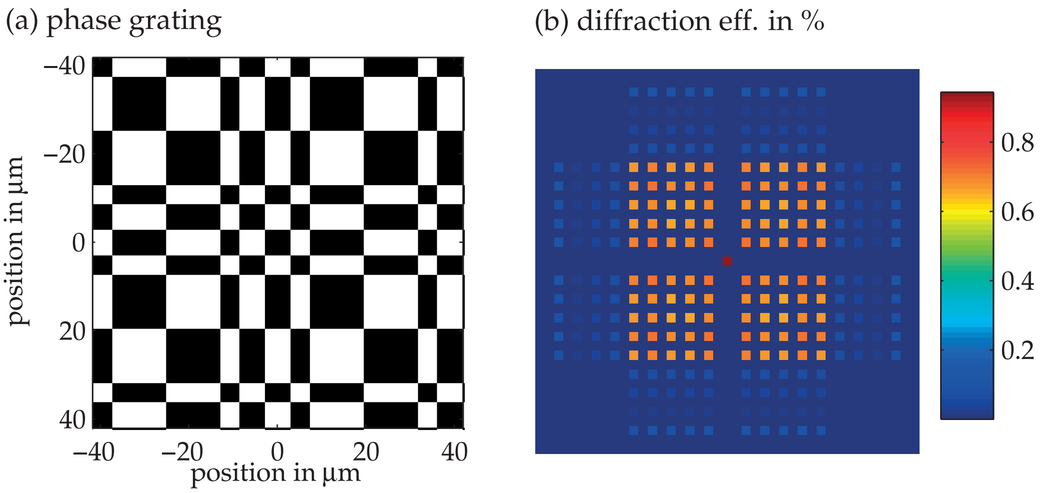

Figure 5.2: Simulation of 11x11 beamsplitter G with Fraunhofer approximation: (a) implementation of phase distribution and (b) the corresponding diffraction pattern in the far field. The phase step of the DOE includes the ratio of fabricated DOE depth and the π depth 650nm for the measured wavelength 750nm with the glass L-BAL42.

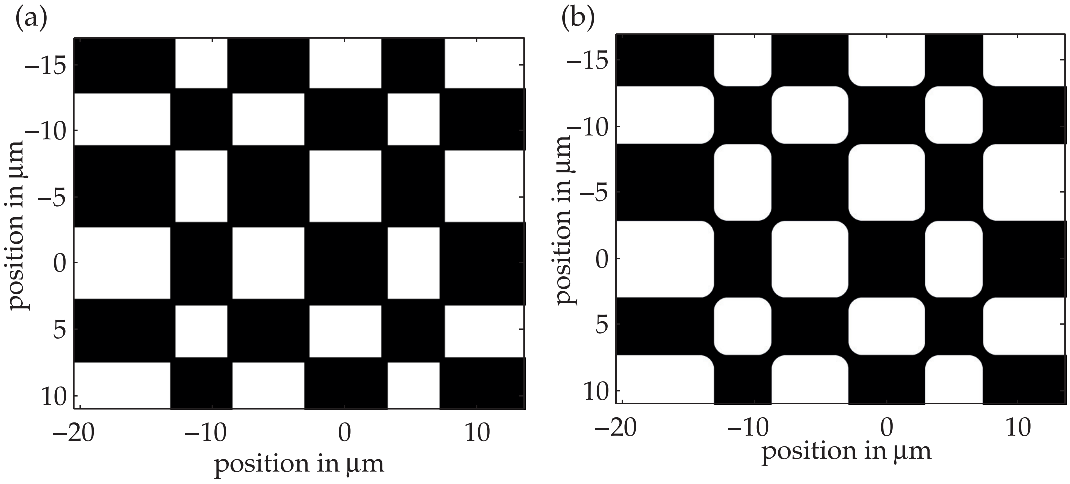

Figure 5.3: Phase of DOE with (a) duty cycle of -405nm and (b) corner rounding of 1.09 µm radius. The values of duty cycle and corner rounding are taken from the SEM images shown in Tab. 5.2 (b).

by −409 nm.

The simulated phase profiles including corner rounding and duty cycle are given in Fig. 5.3. The results of the simulations show that the duty cycle error will result in a minor increase of the uniformity error to 5.3% and a strong increase in the 0^{th} order efficiency to 2.08%. The corner rounding influences only the uniformity error, which is with 9.6% very close to the measured uniformity error of 11.9%. The efficiency of the design orders changes only by 1.5%. Thus the corner rounding and duty cycle error introduced by the mold can cause the lower optical performance of element G. In order to simulate the molding influence, height profiles of the molded glass need to be measured and included in the simulations. For 2-dimensional elements like element G, this not easily done.

In summary, the optical performance of element O is good and agrees well with the expectation. However, the optical performance is limited for element G, where a high uniformity error of 11.9% was measured. The errors in duty cycle and corner rounding are caused by the photolithography process of the GC mold and influence the optical performance of element G strongly. We can use equation 2.21, which is repeated here, to analyze the 2 different DOEs:

$$UE \approx \frac{8\sqrt{2}}{\sqrt{\eta}} S^{3/2} \frac{1}{Q}.$$

The relative position error is given by: $Q = \frac{\Lambda}{\Delta x}$. Thus, the uniformity error increases for a larger number of spots S, if the same accuracy of the structure positioning Δx is kept. Element G has with 11x11 spots a much larger number of beams than element O with 6x6. In order to decrease the uniformity error for element G, the accuracy of the mold fabrication has to be improved. This can be done by using e-beam lithography. This technology also allows the fabrication of smaller features, which can be used to reach larger diffraction angles.

5.2.2 High-Resolution Elements Fabricated with Electron-Beam Lithography

This section discusses the high-resolution diffractive optical element R, which acts like a 1-dimensional 31 beamsplitter. The design parameters are here repeated in Tab. 5.3. Electron-beam lithography was used to improve the accuracy of the GC mold microstructering and to fabricate features down to 800 nm. The results of the molding were given in section 4.7.

In order to have a comparison to state of the art technology, an element with the same design was made available by Holoeye. The reference element consists of a fused silica substrate, which was microstructured with e-beam lithography and direct plasma etching. The depth of the element is 580 nm. The optical measurements were done with a wavelength of 515 nm in TM polarization. The power distribution is depicted in Fig. 5.4. The orders are normalized to the average power of the 31 design orders ranging from -15^{th} to 15^{th} order. Additionally, the accuracy of the measurement, which is 5% of the relative order power, is given with the gray area.

Simulation results, which are based on RCWA, are also shown. An ideal surface shape was assumed with no structure position errors. The etch depth of 580 nm is corresponding to the fabricated DOE. The power distribution of the simulation and the measurement agree well with each other. The uniformity error of the fabricated fused silica DOE is with 20.7% very good. For the simulation, a very low 0^{th} order of 0.49% of the average order power can be seen. If the 0^{th} order is not considered, the UE of the simulation is given by 21.5%. For a better wavelength to depth match, a minimum uniformity error of 19.37% can be expected from the simulations.
The efficiency is higher for fused silica than for L-BAL42 since the reflection coefficient is lower by ca. 1.5% for each surface. It is thus not useful to compare the efficiency of the reference element in fused silica with the efficiency of L-BAL42 DOEs. The measured efficiency is compared to values obtained with the simulations.

Phase profile	Design specifications
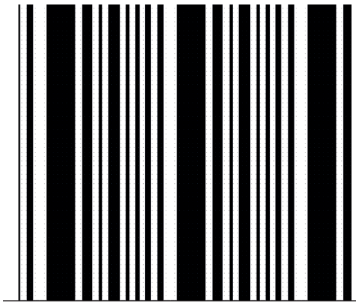	• **name: R** • 1 x 31 beamsplitter • CD = 800 nm • $\Lambda = 29$ µm • in TM polarisation (RCWA) • design DE = 83% • design UE = 17.5%

Table 5.3: Design specification for the higher resolution DOE R.

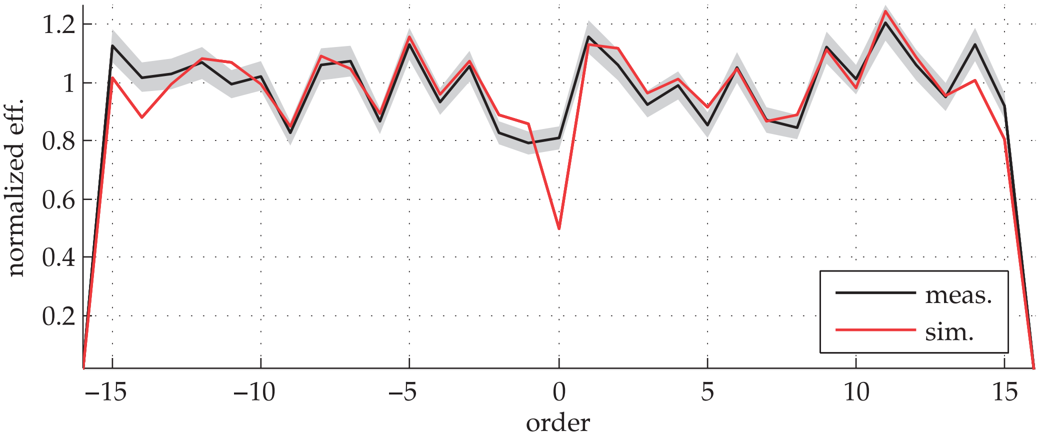

Figure 5.4: Optical performance of a fused silica element is used as reference of state of the art technology. The grey area represents the accuracy of the measurement, which is 5% of the relative order power.

In section 4.7 6 molded DOEs in the glass L-BAL42 were analyzed by SEM imaging. The optical performance of 4 elements, whose height profiles are given in Fig. 5.5, are discussed in this section. The sample **568°C-120s** shows a low filling. A very good corner filling is seen for the elements **565°C-360s** and **568°C-360s** . Their profiles are nearly identical and thus a similar optical performance is expected. The element **568°C-240s** shows a small corner rounding. The optical performances of these 4 elements are summarized in Tab. 5.4. Their diffraction distributions are depicted in Fig. 5.6. The element **568°C-120s**, for which a low mold filling was seen, shows a very high 0^{th} order of 14% with respect to the average order power. From the SEM images, an average height of only 360 nm could be seen. A simulated binary element with this height results in a 0^{th} order efficiency of 8.6% with respect to the average order power. The low filling of the mold is thus clearly seen in its low optical performance.
The elements **565°C-360s**, **568°C-240s** and **568°C-360s** show similar power distribution and are given separately in Fig. 5.7. The distributions are very close to each other.

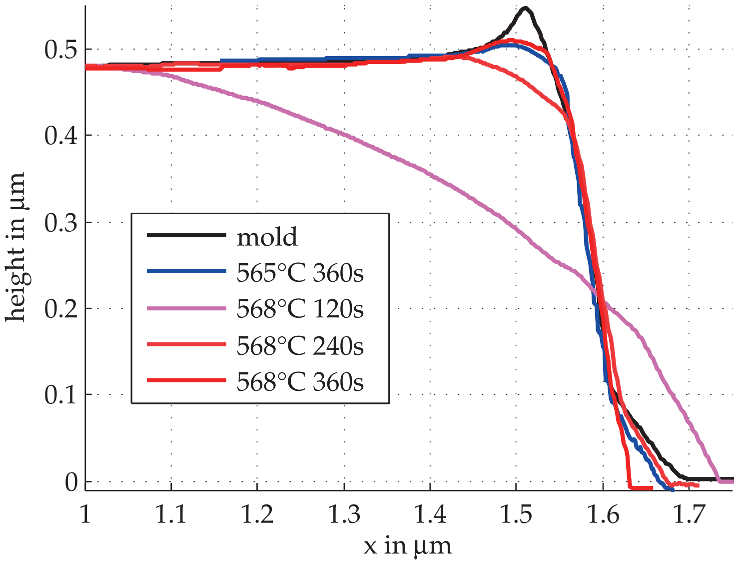

Figure 5.5: Height profiles of 4 different molding conditions, which were introduced in section 4.7. The sample **568°C-120s** shows a low structure accuracy. The profiles of the samples **565°C-360s** and **568°C-360s** are nearly identical.

replication T	565 °C	568 °C		
replication time	360 s	120 s	240 s	360 s
meas. wavelength	594 nm			
0^{th} order	2.48%	26.33%	3.01%	2.49%
UE	24.69%	80.83%	22.6%	27.4%
theor. eff	74.76%			
meas. eff.	69.28%	58.72%	72.18%	71.47%

Table 5.4: Optical performance of 4 replicas with design element R. Highest efficiency and lowest uniformity error is reached with element **568°C-240s**

The strongest order 11 does not vary, but the lowest order +15th is changing for the 3 elements. For element **568°C-240s** a slightly higher 0th order efficiency is seen. The smallest uniformity error of 22.6% is achieved with element **568°C-240s**. The optical performance of this element is very good and close to the performance of the reference element in fused silica. This proves that precision glass molding can be used to fabricate high quality DOEs with a critical dimension of 800 nm and aspect-ratios of 0.6.
The optical performance is influenced by both the mold fabrication and the precision glass molding. With the help of the SEM images, it is possible to include the height profiles in the simulation and thus better distinguish between fabrication constraints of mold fabrication and molding. In the next section, RCWA simulations are used to analyze these questions in more detail.

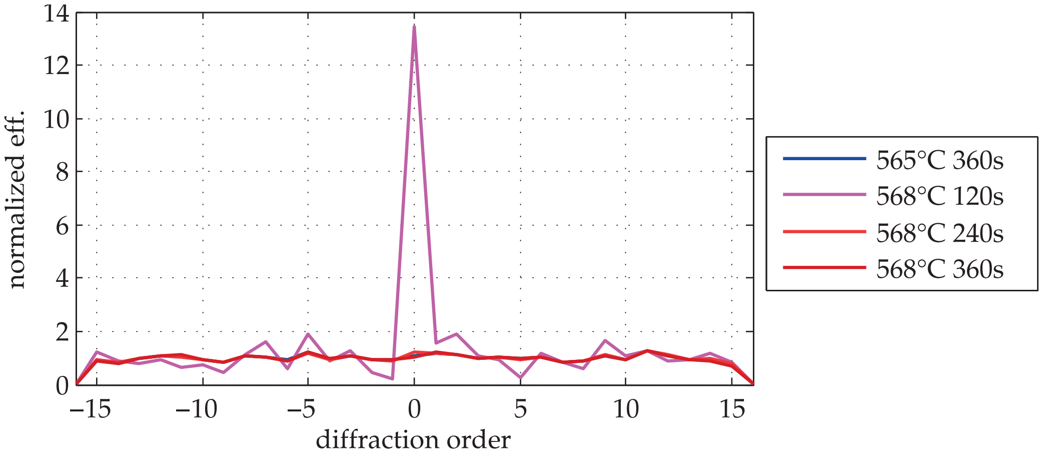

Figure 5.6: Diffraction pattern of 4 different elements. Element **568°C-120s** results in a very high 0th order of 14% with respect to the average order power. The elements **565°C-360s**, **568°C-240s** and **568°C-360s** show similar power distribution and are given separately in Fig. 5.7.

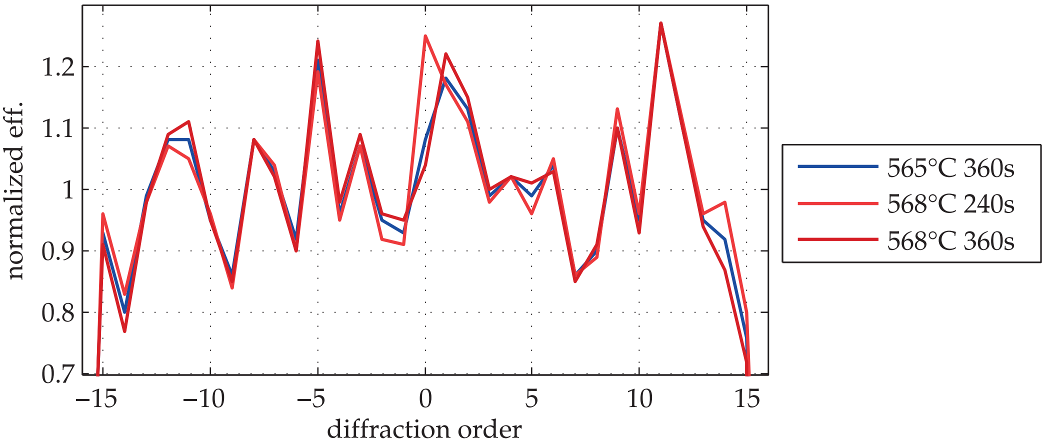

Figure 5.7: Diffraction efficiency of the 3 best replicated elements from Fig. 5.6. Uniformity error is determined by +15th order, where the lowest uniformity error 22.6% is achieved with element **568°C-240s**.

Implementation of RCWA Simulations

The rigorous coupled wave analysis (RCWA) was introduced in section 2.1.2. The critical size of element R is 800 nm, which is in the range of the operation wavelength 594 nm. It is thus not possible to use Fraunhofer approximation for accurate simulation of this element and rigorous methods are necessary. The diffraction pattern is polarization dependent and the design was optimized for TM polarization. In the RCWA simulation, we used the same wavelength 594 nm as in the measurement. The refractive index for L-BAL42 at this wavelength was used with a surrounding in air (n=1). To simplify the simulation we only use 1 interface. The second interface can be included by adding reflection loss with the Fresnel coefficient. This gives a value for the efficiency that is comparable to the measurements. To compare the order distribution it is better to use average values, which are normalized to the average value of the design orders. In Tab. 5.4 it can be seen that the measurement efficiencies are ca. 2.5% to 4.5% lower than the simulation results. The simulations do not include surface roughness, which will cause losses in the diffraction efficiency and increase stray light.

The input of the phase grating surface is depicted in Fig. 5.8 (a). The red line represents the continuous surface profile. For the RCWA simulation, discrete layers need to be defined. For an ideal 2 level binary element, it is sufficient to use 3 layers. Figure 5.8 (b) shows the order power for a depth of 509 nm. A low uniformity error of 20.77% is given. For this simulations, the number of Fourier orders is set to 250. As stated in section 2.1.2 the number of Fourier orders determines the accuracy of the simulations. Therefore, the efficiency and uniformity error in dependency of the number of Fourier orders were analyzed to analyze the fidelity of the approach. The results are shown in

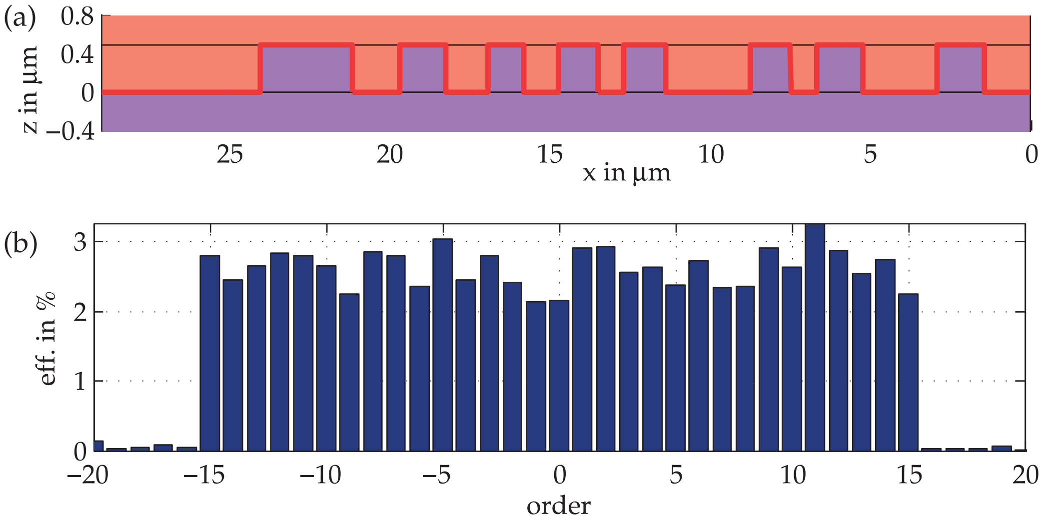

Figure 5.8: (a) Profile of designed phase grating can be implemented with 3 layers only. The first 5 lines are equal to the SEM images discussed in section 4 shown in Fig. 4.29. The corresponding diffraction pattern (b) in TM polarization with 31 orders gives an efficiency of 81.67% and uniformity error of 20.77% (250 Fourier orders, $\lambda = 594$ nm, depth 509 nm).

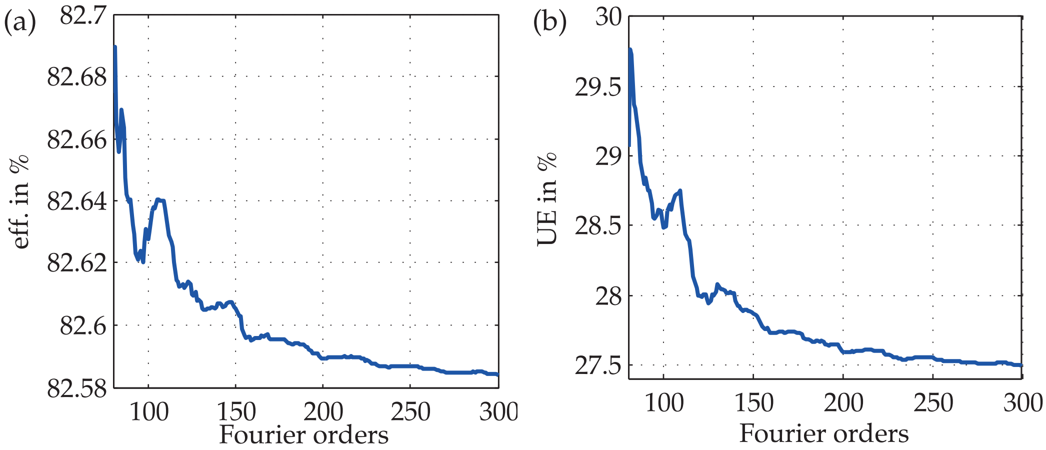

Figure 5.9: Dependency of the efficiency and UE on the number of Fourier orders used for the simulations: for 250 Fourier orders an accuracy of 0.002% for (a) the efficiency and an accuracy of 0.05% for the UE is reached.

Fig. 5.9. Between 80 and 300 Fourier orders the efficiency of the 31 design orders does change only be 0.1%. The variation around 250 Fourier orders is as small as ±0.001%, which represents the accuracy of the design efficiency. For an accurate simulation of the efficiency, a lower number of Fourier orders would be sufficient. However, the uniformity error shows a stronger dependency on the number of Fourier orders. The accuracy of the uniformity error for 250 Fourier orders is ±0.05%. For all further simulations, we use 250 Fourier orders.

We want to replace the ideal profile in Fig. 5.8 (a) with the measured profile of the molded DOEs from Fig. 4.32. The linewidths in one period vary from 2.9 µm to 1.15 µm. A comparison showed that the height profiles are similar for all linewidths in a period. We thus only need to load one profile for each molding setting. The implementation procedure is explained in Fig. 5.10. First, the measured height profile (a) of the molded DOE replaces the ideal profile (b). The position of the edge is critical since it will change the linewidth. The position, at which the measured profile reaches half of the height, is considered at the ideal edge position.

The implementation for RCWA simulation needs layer definition, where the number of layer needs to be chosen accordingly. A low number of layers 10 (c) will speed up the simulations, but a good representation of the real profile might require more layers 100 (d). The RCWA method also allows using a different thickness for each layer. The algorithm to define the layers is included in software package "Reticolo" and works with a fixed thickness. We chose to use this algorithm with 2 different thickness definitions and use the 9 thicker layers for the bottom and the thin layer definition at the top, where it replaces one thick layer. The features at the top are flatter and change stronger for the different molding settings.

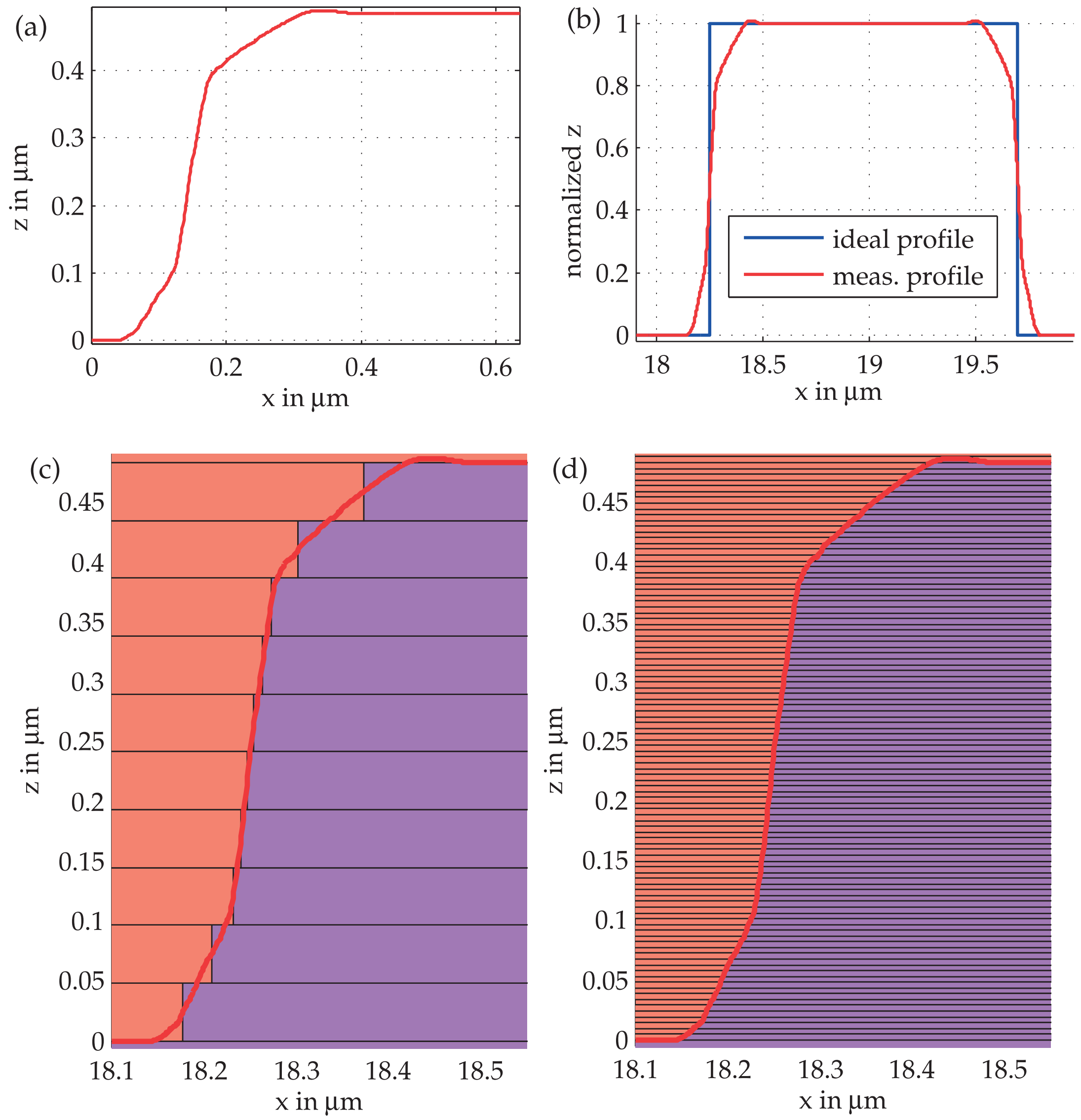

Figure 5.10: Measured height profile (a) of the molded DOE can replace the ideal profile (b). The implementation for RCWA simulation needs layer definition, where the number of layer needs to be chosen accordingly. A low number of layers 10 (c) will speed up the simulations, but a good representation of the real profile might require more layers 100 (d).

Results of RCWA Simulations

First, we will discuss the element R with ideal profile shape given in Fig. 5.8 (a). The influence of the duty cycle and etch depth are depicted in Fig. 5.11. After the fabrication, the depth of the mold was measured with a mechanical profilometer Tencor Alpha-Step 500. The depth was found to be (483 ± 10) nm and should be the same for the molded glass surface. The duty cycle was taken from the SEM images. Since the walls of the features were not straight, the half-width maximum was used as a reference. For the sample **568°C-240s** the average duty cycle is (39 ± 40) nm and for the GC mold (18 ± 40) nm. In Fig. 5.11 the measurement diffraction pattern of sample **565°C-240s** is also shown, which had the best optical performance. The strongest correlation between the measurement and the simulation can be seen for a step height of 483 nm and a duty cycle of 40 nm, which corresponds well with the values of the measured dimensions. Figure 5.12 gives more details of the performance change for a depth and duty cycle variation. The highest efficiency is reached for low depth values. With an increase in the depth more and more power is transferred from the 0^{th} order to higher orders. Only a part of this power is distributed between the other 30 design orders, which results

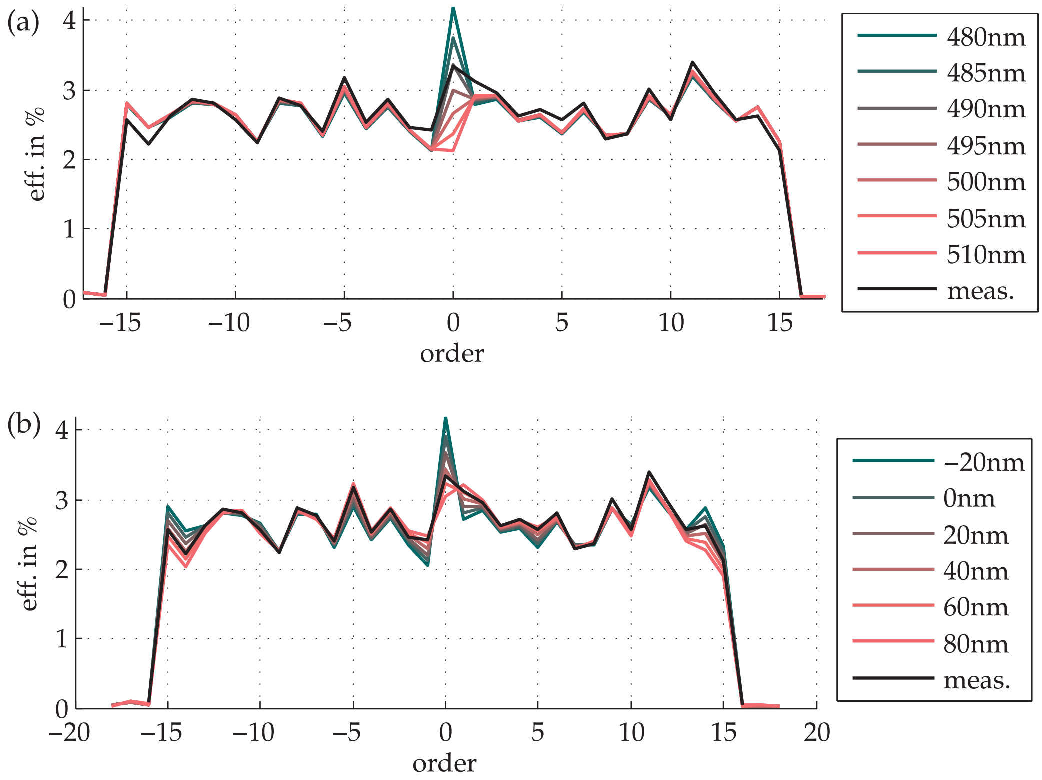

Figure 5.11: Simulation of element R with ideal profile shape (see Fig. 5.8 (a)) in comparison to the measurement of element **568°C-240s**. A change in the step heights (a) (duty cycle 0) only influences the 0^{th} order efficiency, whereas the duty cycle (b) (step height 483 nm) has a strong influence on the efficiency of the off-axis orders.

in an efficiency drop of 2.5% between a depth of 480 nm and 520 nm. The change of the power distribution of the off-axis orders does not vary significantly due to a height variation. The dependency of the uniformity error on the step height is mainly caused by the strong variation of the 0^{th} order efficiency (Fig. 5.12 (c)).
The duty cycle has a strong influence on the uniformity error. The simulations were done with a fixed depth of 483 nm, where a stronger 0^{th} order efficiency causes a higher

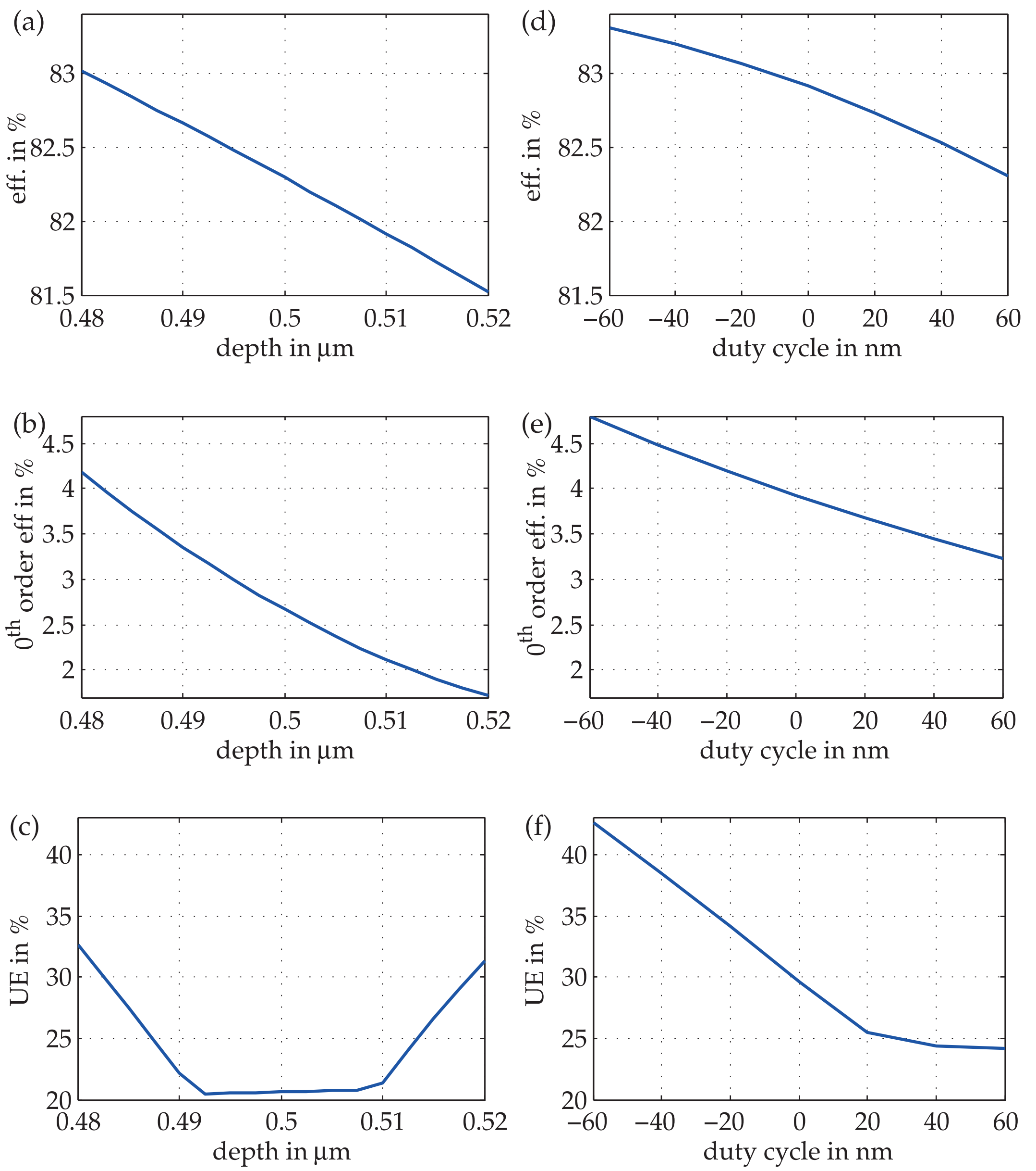

Figure 5.12: Simulation of element R given in Fig. 5.11 with varying depth (a)-(c) (duty cycle 0) and varying duty cycle (d)-(f) (depth 483 nm) has influence on the efficiency of the 31 design order, the efficiency of the 0^{th} order and the uniformity error.

uniformity error. This can be compensated by choosing a higher duty cycle (Fig. 5.12 (f)). Deviations of the measured power distribution with respect to the simulation can be categorized in 0^{th} order changes and off-axis order changes. The off-axis order changes can only be caused by duty cycle errors. A 0^{th} change can be caused by both height errors and duty cycle errors. The molded profiles are different to each other only by the corner filling. This can be both seen as a height change and a duty cycle change. The optical measurements given in Fig. 5.7 showed both variations in the 0^{th} order and the off-axis orders.

The simulation results for an ideal edge profile and the molded profiles are given in Fig. 5.13. It can be seen that the edge profile of fabricated elements changes the power distribution in some extent. The strongest difference is given for the 0^{th} order. Element **568°C-240s** holds a small edge rounding, which causes an effective lower height and thus a higher 0^{th} order efficiency. The mold surface showed a significant trenching. The glass of the samples **565°C-360s** and **568°C-360s** filled part of the trenching area. The effective height is therefore higher than the flat area of the mold with 483 nm and the 0^{th} order efficiency decreases in comparison to the ideal edge. The trenching features can be suppressed by an optimized plasma etching process or by choosing a lower mold filling point.

The power distribution of the ideal edge agrees the best with the distribution of elements **565°C-360s** and **568°C-360s**, which showed the best filling. Experiments **565°C-360s** and **568°C-360s** show very similar results due to similar height profiles. Figure 5.14 compares the measurement with the simulation, where the SEM height profiles from Fig. 5.5 are included. The simulation results with the molded profiles agree better with the measurement than the simulation results with the ideal profiles. A lower filling and thus lower height will also cause a higher diffraction efficiency according to Fig. 5.11 (a). This explains the higher diffraction efficiency for element **568°C-240s**.

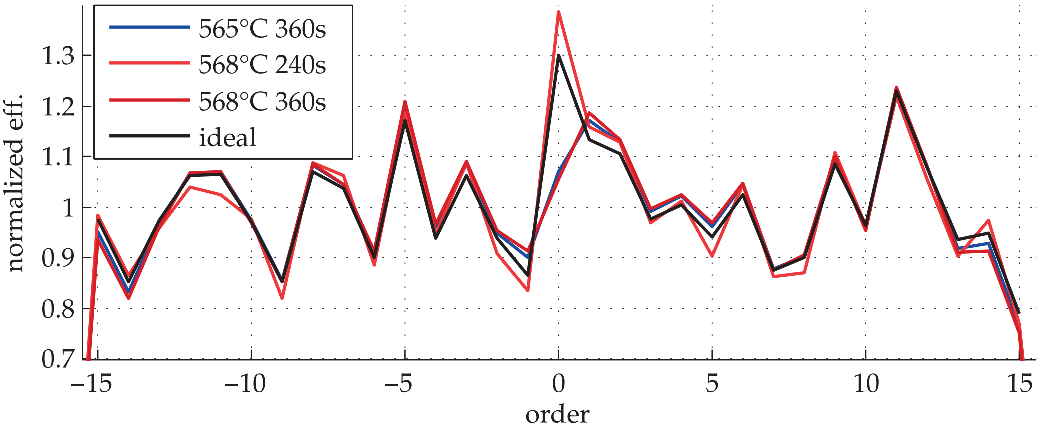

Figure 5.13: Simulation with SEM height profiles of 3 different molding results shown in Fig. 5.5. The efficiencies are normalized to the average order efficiency of the 31 design orders for better comparison. Experiments **565°C-360s** and **568°C-360s** show very similar results due to similar height profiles.

(a) 565 °C 360s

meas.	$\text{eff}_{31} = 69.28\%$	UE = 24.69%	$\text{eff}_0 = 2.48\%$
sim. SEM	$\text{eff}_{31} = 77.09\%$	UE = 23.6%	$\text{eff}_0 = 2.67\%$

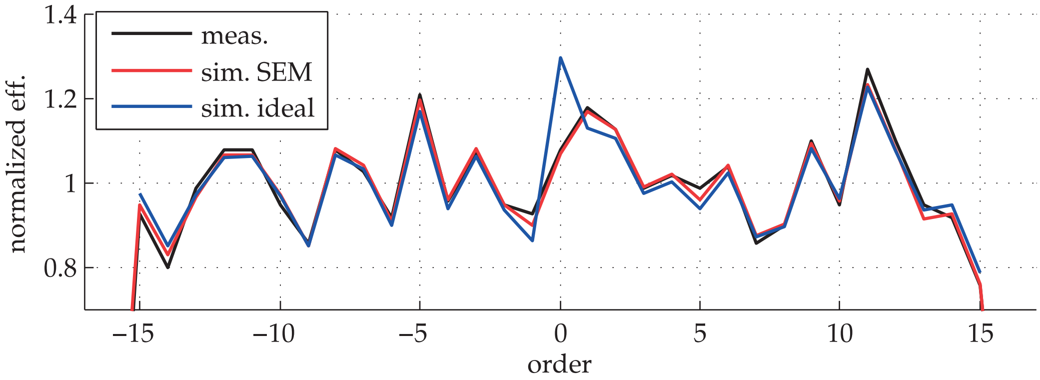

(b) 568 °C 240s

meas.	$\text{eff}_{31} = 72.18\%$	UE = 22.6%	$\text{eff}_0 = 3.01\%$
sim. SEM	$\text{eff}_{31} = 76.75\%$	UE = 28.5% (without 0^{th} 22.6%)	$\text{eff}_0 = 3.43$ %

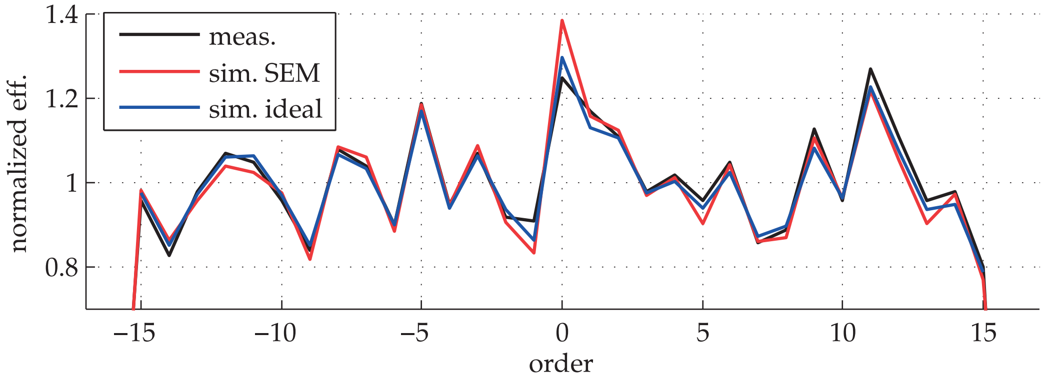

(c) 568 °C 360s

meas.	$\text{eff}_{31} = 71.47\%$	UE = 27.4%	$\text{eff}_0 = 2.49\%$
sim. SEM	$\text{eff}_{31} = 76.97\%$	UE = 24.4%	$\text{eff}_0 = 2.62\%$

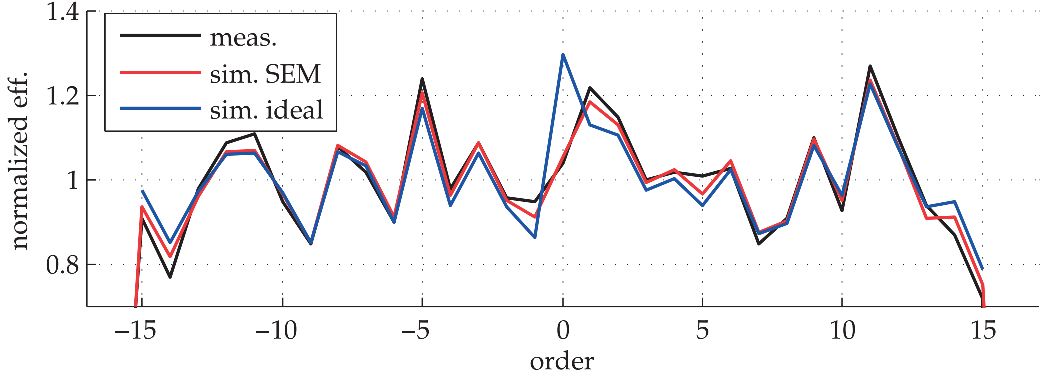

Figure 5.14: Simulation with SEM height profiles shown in Fig. 5.5 in comparison to measurement. The efficiencies are normalized to the average order efficiency of the 31 design orders for better comparison. The power distributions of simulations are in good agreement with measurement results. However, the efficiencies of the simulations do not show the same tendency as the measurements.

The element **568°C-240s** suffers from a higher 0^{th}. For the simulations, this results in a higher uniformity error of 28.5%. A deviation of the 0^{th} order can be compensated by choosing a better step height for the GC mold. If we excluded the 0^{th} order and only consider the 30 off-axis design orders, a low uniformity error of the simulations of 22.6% is reached, which agrees very well with the measurement.

In summary, it was shown that precision glass molding with high-quality GC molds can be used to fabricate DOEs with state-of-the-art quality. We showed that a similar optical performance to a reference element in fused silica was reached. A high-quality GC mold was fabricated with e-beam lithography, which allowed the good performance of the molded DOE. The optical measurements are in good agreement with the simulations based on RCWA, where the measurement values for depth 483 nm and duty cycle error of 40 nm were used. The profiles of the molded DOEs were included in the simulations and showed that feature roundings have a similar effect as etch depth errors and duty cycle errors. The molding settings such as time and temperature can be used to reach the optimal height profile. Mold errors such as trenching can be compensated during molding by choosing a lower mold filling.

5.3 Multilevel Structures

In order to test our replication approach for a more demanding diffractive optical elements, we microstructured multilevel GC wafers. The wafers have different etching depths, but were structured with the same process based on a Si hard mask, which was introduced in section 3.4.2. Each wafer carried 8 different DOE designs. For the analysis, 2 designs were chosen: a 2D beamsplitter and a linear beamsplitter.

5.3.1 Two-dimensional Beamsplitter

The test element G is given in Tab. 2.6, which acts as a 6x6 beamsplitter in asymmetric order. Mold M8-G was used for molding of the glass L-BAL42 and fused silica. Details of the fabrication chain both for mold fabrication and precision glass molding are given in Tab. 5.6 for L-BAL42 and in Tab. 5.7 for fused silica (FS). The second mold M11-G was only employed for L-BAL42 (Tab. 5.8).

SEM images of the fabricated GC mold M8-G are shown in the left column of Tab. 5.6 and illustrate the impact of alignment errors. It can be seen that the levels are not perfectly aligned resulting in thin line features. The misalignment for the mold M8-G in the horizontal direction is in the range of 100 nm, for the vertical direction it is higher with 200 nm to 500 nm. The alignment errors of the second mold M11-G were below 160 nm and thus significantly lower than for mold M8-G. However, all alignment errors lay in the accuracy of the used mask aligner, which is given as 0.5 µm.

The results of the optical performance tests are shown in Table 5.5. The power of the 0^{th} order is close to 0 indicating that the test wavelengths and the etch depths are chosen accordingly. The diffraction efficiency for the 6x6 beamsplitter is theoretically 85.15%. To compare with the measurement we include a Fresnel reflection loss for each surface. The measured efficiencies are 67% for the replicas **multi-8-G-LBAL42** and **multi-8-G-FS**. The replica of mold M11-G has a slightly higher efficiency of 70%. The efficiencies are thus 10% below the design efficiency. The uniformity error for sample multi-8-G-LBAL42 is with 19% similar to the sample multi-11-G-LBAL42 with 21%. However, the UE of the fused silica replica multi-8-G-FS with 40% is considerably higher. Since the same mold was used for multi-8-G-LBAL42 and multi-8-G-FS, the error must come from the replication process.

For all given replications is the measured UE much higher than the design value of 1.4%. From the SEM images for mold and corresponding replica in Tab. 5.6-5.8, it can be seen that the replication is of good quality. Errors that can influence the optical performance are either introduced by the mold fabrication or the replication process. Most prominent are the mold specifications given by mask-mask alignment errors, duty cycle errors and form deviations given by the hard contact mode during exposure. From the measurements, it can be seen that mold M8-G has much higher alignment errors than mold M11-G. The similar optical performance does not represent this difference. For the here discussed two-dimensional DOE, it is very difficult to give parameters for the fabricated duty cycle and form deviations. Also owing to the complex surface shape, accurate simulations with considerable computational effort are very difficult to do.

sample	**multi-8-G-LBAL42** Tab. 5.6	**multi-8-G-FS** Tab. 5.7	**multi-11-G-LBAL42** Tab. 5.8
Mold	M8-G	M8-G	M11-G
glass	L-BAL42	SQ-1	L-BAL42
λx	687 nm	659 nm	452 nm
0^{th} (meas.)	< 0.1%		0.1%
UE (theo.)	1.4%	1.4%	1.4%
UE (meas.)	19%	40%	21%
Fresnel loss	5.04%	3.45%	5.24%
DE (theo.)	76.78%	79.38%	76.46%
DE (meas.)	67%	67%	70% - 72%
$\frac{\text{DE(meas.)}}{\text{DE(theo.)}}$	87.3%	84.4%	91.5%-94%

Table 5.5: Optical performance of 6x6 beamsplitter design G. The mold M8-G was used for precision glass molding of both fused silica and L-BAL42. Mold M11-G was only used for precision glass molding of L-BAL42. The replica of fused silica shows with 40% the highest uniformity error. Both L-BAL42 show similar optical performance and the uniformity error is considerable higher than the design uniformity error.

sample reference name: multi-8-G-LBAL42

mask design	
mold insert	rectangular form Fig. 2.9(b)
optical design	multilevel DOE 6x6 beamsplitter Tab. 2.6 G

precision glass molding	
machine	Toshiba GMP-211V
holder	fixed mold Fig. 4.3 (b)
glass	L-BAL42
molding time	240 s
pressure	1 kN
molding T	565 °C
separation T	450 °C

mold fabrication: M8-G	
ICP machine	SPTS CMi
process	70nm Si mask
photolithography	hard contact

		alignment error	
	depth	Δx	Δy
1. mask	161 nm		
2. mask	285 nm	35 nm	460 nm
3. mask	603 nm	-80 nm	-200 nm

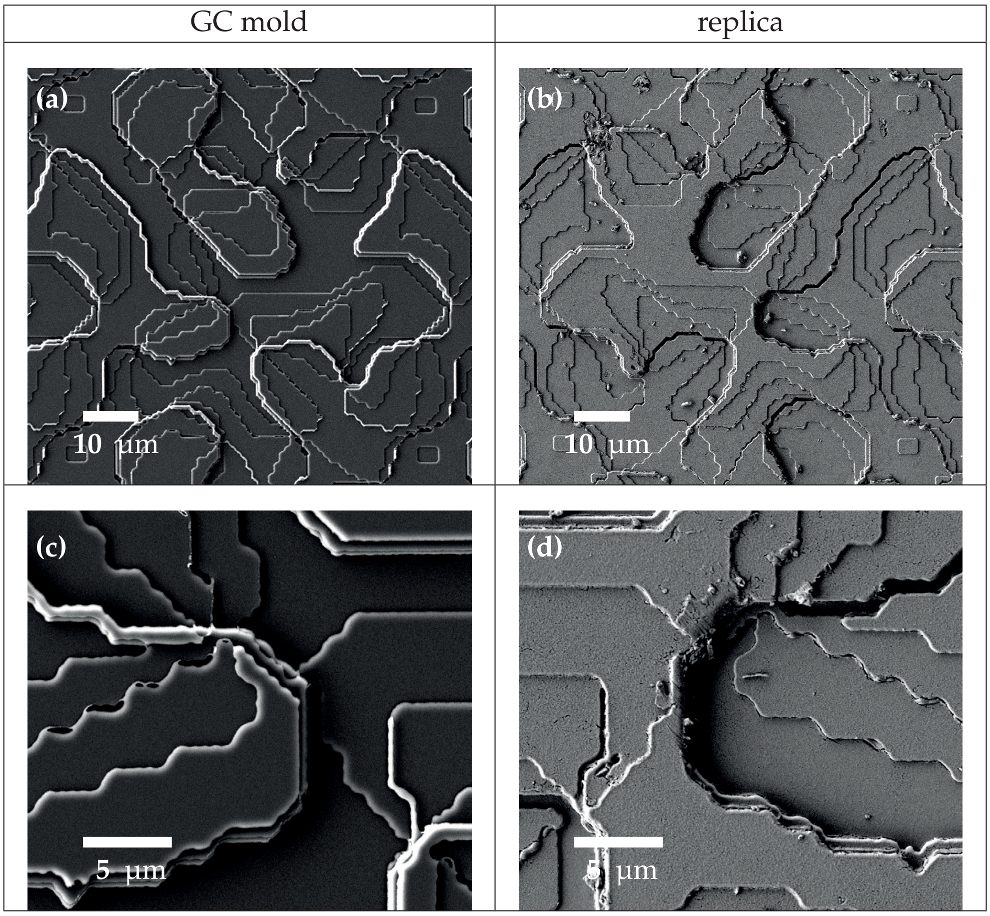

Table 5.6: Design parameters and fabrication results of sample multi-8-G-LBAL42. The alignment errors of the molds are 460 nm and -200 nm in the vertical direction and can be seen also in the replicated glass surface.

sample reference name:	**multi-8-G-FS**

mask design	
mold insert	rectangular form Fig. 2.9(b)
optical design	multilevel DOE 6x6 beamsplitter Tab. 2.6 G

precision glass molding	
machine	Toshiba GMP-207H
holder	glass stack Fig. 4.3 (a)
glass	fused silica SQ-1
molding time	240 s
pressure	3 kN
molding T	1400 °C
separation T	room temperature

mold fabrication: M8-G	
ICP machine	SPTS CMi
process	70nm Si mask
photolithography	hard contact

		alignment error	
	depth	Δx	Δy
1. mask	161 nm		
2. mask	285 nm	35 nm	460 nm
3. mask	603 nm	-80 nm	-200 nm

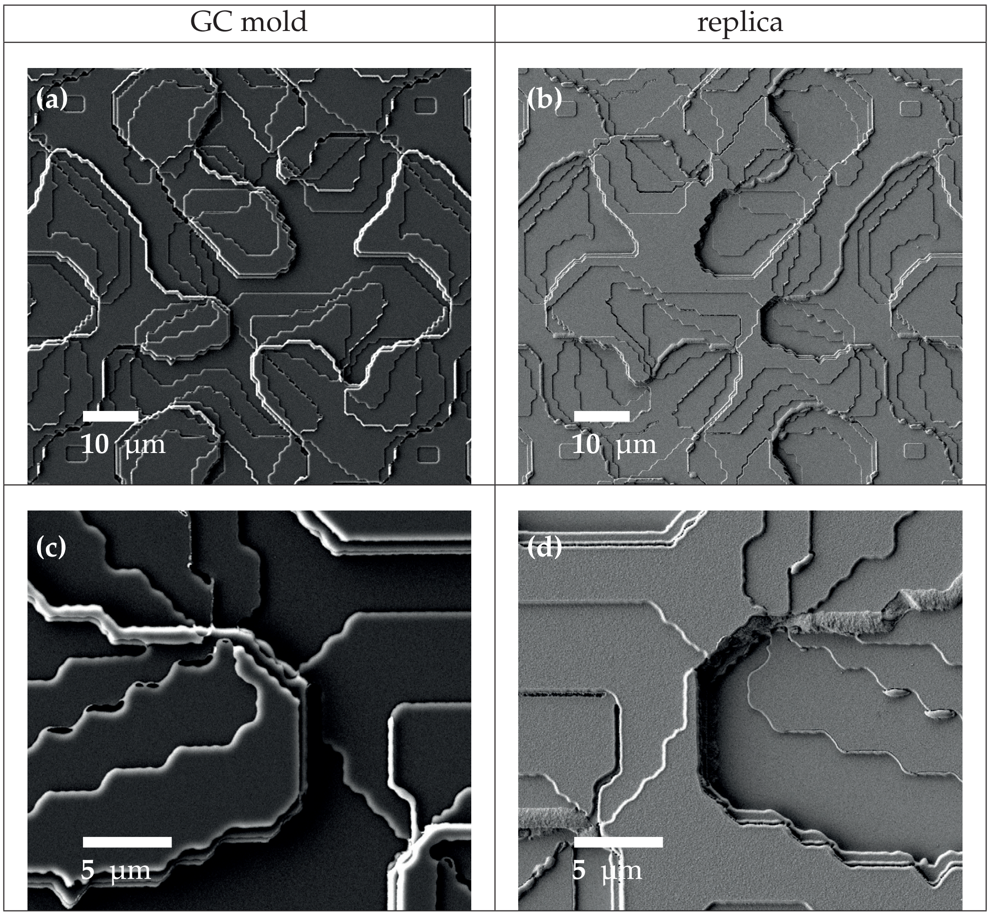

Table 5.7: Design parameters and fabrication results of sample multi-8-G-FS. The same mold as for multi-8-G-LBAL42 in Tab. 5.6 was used to mold fused silica.

sample reference name:	**multi-11-G-LBAL42**

mask design	
mold insert	rectangular form Fig. 2.9(b)
optical design	multilevel DOE 6x6 beamsplitter Tab. 2.6 G

mold fabrication: M11-G	
ICP machine	SPTS CMi
process	70nm Si mask
photolithography	hard contact

		alignment error	
	depth	Δx	Δy
1. mask	103 nm		
2. mask	205 nm	73 nm	115 nm
3. mask	395 nm	-125 nm	-155 nm

precision glass molding	
machine	Toshiba GMP-211V
holder	fixed mold Fig. 4.3 (b)
glass	L-BAL42
molding time	240 s
pressure	1 kN
molding T	565 °C
separation T	450 °C

GC mold
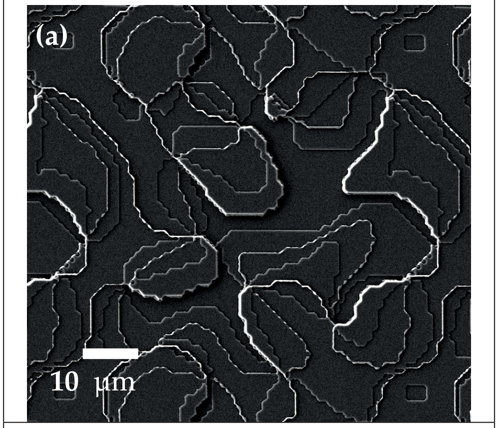
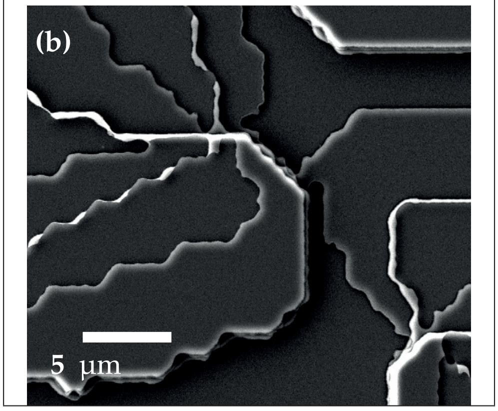

Table 5.8: Design parameters and fabrication results of sample multi-11-G-LBAL42. The alignment error are less than 155 nm and thus smaller than for mold M8-G.

5.3.2 One-dimensional Beamsplitter

In this section, we will discuss a one-dimensional beamsplitter. The diffractive optical element F acts as a 1x4 beamsplitter (design details in Tab. 2.6). The design orders are -3^{rd}, -1^{st}, 1^{st} and 3^{rd}. We used this element for simulation because it is easier to implement in Matlab and the computational time for 1D elements are moderate. A scheme of the fabrication procedure is depicted in Fig. 5.15. Three masks were used for the fabrication, which are illustrated above the wafer. The structures of each mask are etched with different etch depths. First, the mask with the smallest etch depth h/8 was etched, then the second highest etch depth h/4 and last the highest etch depth h/2. The height h refers to the depth, for which a phase difference of π can be achieved. The smallest features are 2 µm and are present in the mask h/8.

Two molds were fabricated with the same set of masks. The mold M11-F was used for glass molding of L-BAL42 (Tab. 5.9). The second mold M8-F was also used for L-BAL42 with the second molding conditions (Tab. 5.10). After the L-BAL42 replication, this mold was also used for high-temperature replication of fused silica (Tab. 5.11).

Fabrication errors introduced during mold fabrication are etch-depth errors, mask-to-mask misalignment errors, the wall verticality (angle between the substrate surface and the etched wall) and the duty cycle, which is the fabricated line width in comparison to the design width. For example, an underexposed photoresist will result in thinner lines in the final mold structure. Qualification of the shape deviations due to diffraction during exposure is difficult to evaluate but can have a considerable impact on the optical performance of the final DOE in glass.

The given values for the fabricated molds are measured at the center of the 17 mm wide DOE areas. The mask-to-mask misalignment errors for mold M11-F are with -58 nm and 73 nm much lower than for mold M8-F with - 150 nm and 500 nm. The accuracy of mask aligners is circa 500 nm. Mask-to-mask alignment errors can vary strongly between wafers. This error can be approximated as a shift in the line profile for the simulations but will vary over the DOE area.

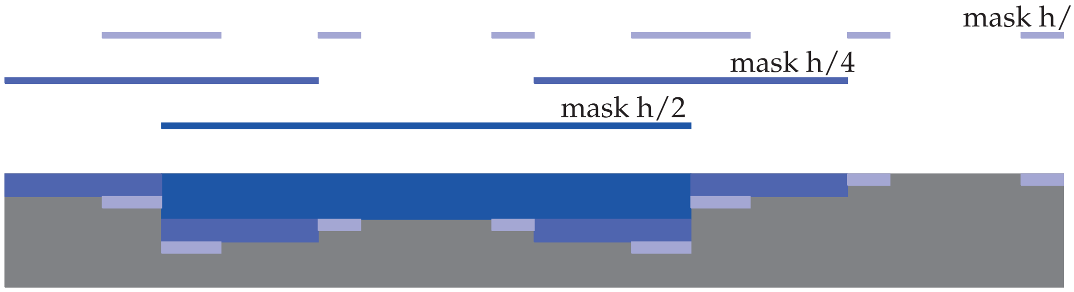

Figure 5.15: Multilevel fabrication of element F with a period of 50 µm. 3 Masks were used for the fabrication, which is illustrated above the wafer. The structures of each mask are etched with different etch depths. First, the mask with the smallest etch depth h/8 was etched, then the second highest etch depth h/4 and last the highest etch depth h/2. The height h refers to the depth, for which a phase difference of 2π can be achieved.

sample reference name: multi-11-F-LBAL42

mask design	
mold insert	rectangular form Fig. 2.9(b)
optical design	multilevel DOE 1x4 beamsplitter Tab. 2.6 F

precision glass molding	
machine	Toshiba GMP-211V
holder	fixed mold Fig. 4.3 (b)
glass	L-BAL42
molding time	240 s
pressure	1 kN
molding T	565 °C
separation T	450 °C

mold fabrication: M11-F	
ICP machine	SPTS CMi
process	70nm Si mask
photolithography	hard contact

	depth	alignment Δx
1. mask	109 nm	
2. mask	208 nm	-58 nm
3. mask	383 nm	73 nm

	duty cycle	
	design	fabrication
1. mask	25 µm	25 µm
2. mask	14.6 µm	14.45 µm
3. mask	5.6 µm 2 µm	5.3 µm 1.75 µm

Table 5.9: Design parameters and fabrication results of sample multi-11-F-LBAL42. The alignment errors are less than 100nm and thus much smaller than for mold M8-F.

sample reference name: multi-8-F-LBAL42

mask design	
mold insert	rectangular form Fig. 2.9(b)
optical design	multilevel DOE 1x4 beamsplitter Tab. 2.6 F

precision glass molding	
machine	Toshiba GMP-211V
holder	fixed mold Fig. 4.3 (b)
glass	L-BAL42
molding time	240 s
pressure	1 kN
molding T	565 °C
separation T	450 °C

mold fabrication: M8-F	
ICP machine	SPTS CMi
process	70nm Si mask
photolithography	hard contact

	depth	alignment Δx
1. mask	153 nm	
2. mask	280 nm	-150 nm
3. mask	585 nm	500 nm

	duty cycle	
	design	fabrication
1. mask	25 µm	25 µm
2. mask	14.6 µm	14.3 µm
3. mask	5.6 µm 2 µm	5.25 µm 1.97 µm

GC mold	replica
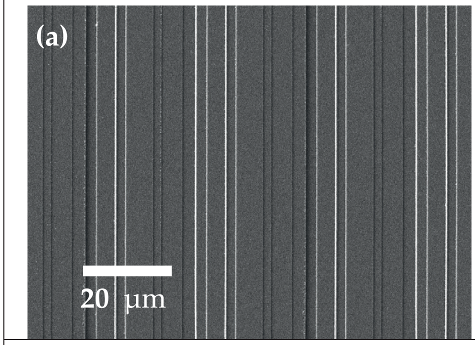	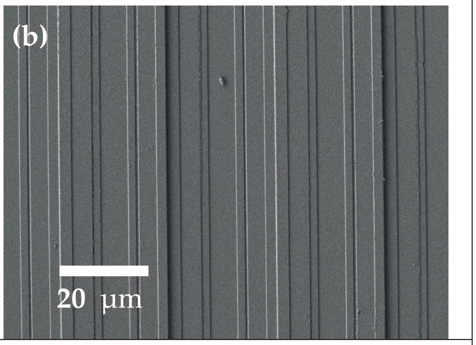
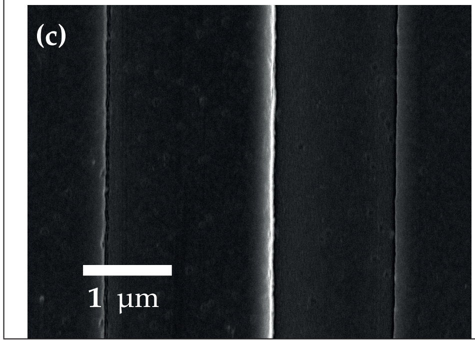	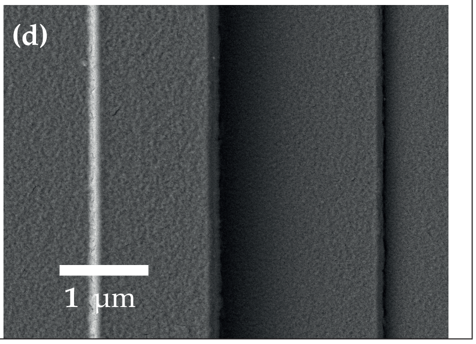

Table 5.10: Design parameters and fabrication results of sample multi-8-F-LBAL42. The alignment errors are with -150 nm and 500 nm considerable large in comparison to the critical dimension of 2 µm.

sample reference name: multi-8-F-FS

mask design	
mold insert	rectangular form Fig. 2.9(b)
optical design	multilevel DOE 1x4 beamsplitter Tab. 2.6 F

precision glass molding	
machine	Toshiba GMP-207H
holder	glass stack Fig. 4.3 (a)
glass	SQ-1
molding time	240 s
pressure	3 kN
molding T	1400 °C
separation T	room temperature

mold fabrication: M8-F	
ICP machine	SPTS CMi
process	70nm Si mask
photolithography	hard contact

	depth	alignment Δx
1. mask	153 nm	
2. mask	280 nm	-150 nm
3. mask	585 nm	500 nm

	duty cycle	
	design	fabrication
1. mask	25 µm	25 µm
2. mask	14.6 µm	14.3 µm
3. mask	5.6 µm 2 µm	5.25 µm 1.97 µm

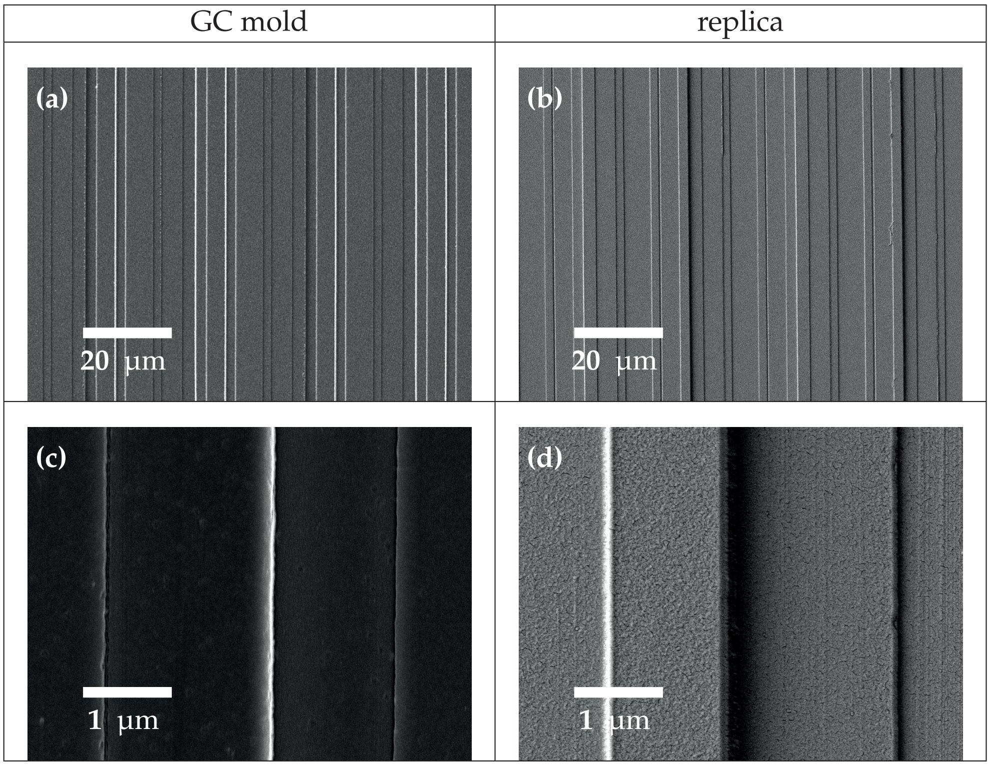

Table 5.11: Design parameters and fabrication results of sample multi-8-F-FS. The same mold as for multi-8-F-LBAL42 in Tab. 5.10 was used to mold fused silica.

From SEM images at different positions, it could be seen that the linewidth varies at different positions. The exposure mode was set to hard contact because vacuum contact was not available for the used tool. Therefore, the distance between the mask and the photoresist can vary strongly and diffraction effects can alter the exposed photoresist shape significantly.

The etch depth was measured for 50 µm wide lines which were placed at different positions of the wafer. The etch depth is changing in the direction perpendicular to the wafer flat. This is caused by the SPTS plasma etching. We note that this problem can be minimized for optimized etching conditions. A variation of max. 1% of the etch depth over an active area of 17 mm was observed.

The optical performance of the L-BAL42 DOE for mold M11-F is given in Tab. 5.12. The wavelength used for the measurement was 488 nm. The power is normalized to the average power of the 4 design orders for better comparison. The diffraction efficiency was with 73.5% very close to the design value of 74.8%. The overall performance is very good. A low UE of 4.8% could be observed at the center of the element. However, a variation of the 4 design orders over the area could be observed. The UE is between 4% and 10%. This may be caused by a variation of the depth, line-to-line shift and duty cycle over the area.

The diffraction pattern for the design orders is shown in Fig. 5.16 (a) for the direction parallel to the flat and in Fig. 5.16 (b) for the direction perpendicular to the flat. In the perpendicular direction the $\pm 3^{rd}$ exchange power with the $\pm 1^{st}$ orders. The down position shows a power decrease for the $\pm 1^{st}$ orders. However, the power in the + orders stays equal to the - order. In the direction parallel to the flat (Fig. 5.16 (a)) the symmetry around the 0^{th} order changes. The optical performance of the replicated DOEs for mold M8-F are given in Tab. 5.13. The wavelength used for the measurement was 687 nm for L-BAL42 and 532 nm for fused silica. In both cases a high eff. of 74% was achieved. Additionally, a strong asymmetry around the 0^{th} order can be seen. Thus, the UE is with

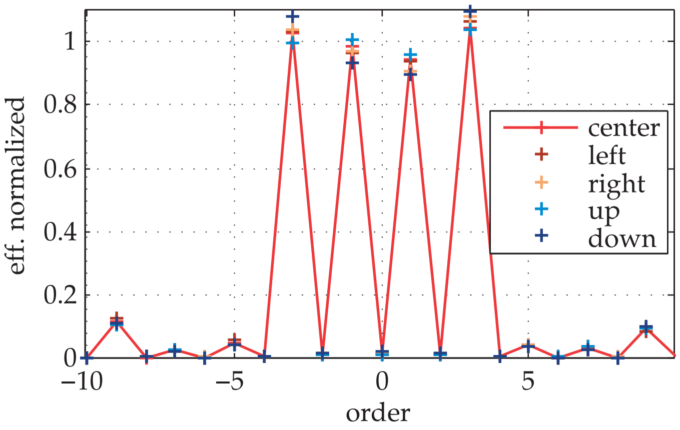

λ = 488 nm

	eff.
meas	73.5%
sim.	74.8%

position	UE
center	4.8%
left	6.2%
right	8.7%
up	4.1%
down	9.9%

Table 5.12: Power distribution in the 4 design orders measured for sample **multi-11-F-LBAL42** (Details in Tab. 5.9) with test wavelength 488nm in TE polarization.

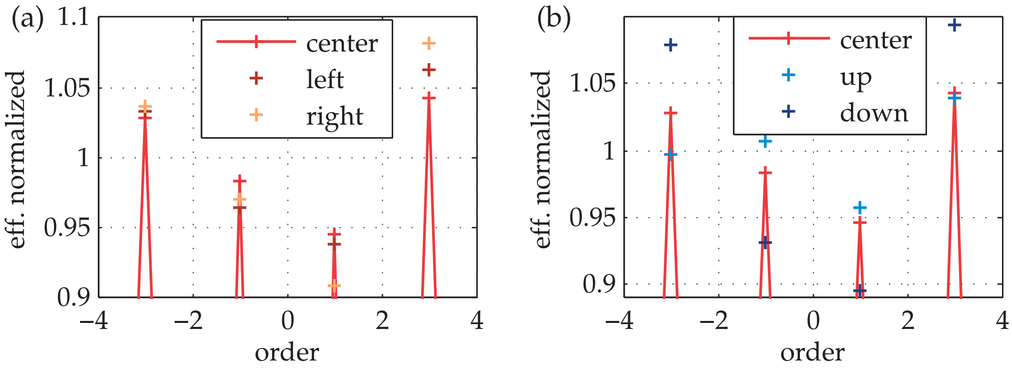

Figure 5.16: Magnification of Tab. 5.12. The order distributions are compared with each other in the horizontal direction (a) and in the vertical direction (b).

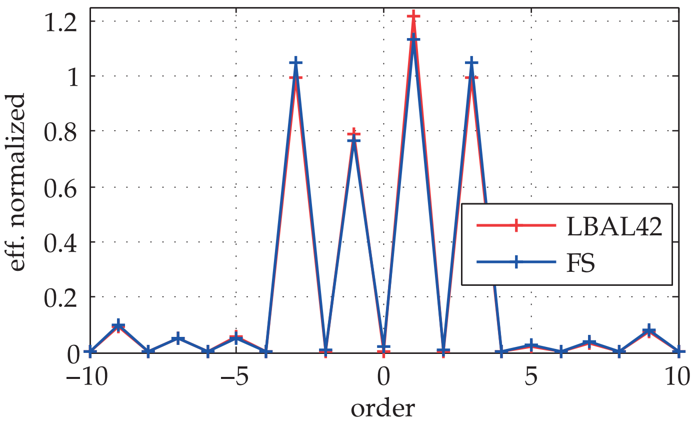

λ = 687 nm for L-BAL42
λ = 532 nm for fused silica

efficiency

	L-BAL42	fused silica
meas.	74%	74%
sim.	76.7%	78.8%

	UE	0th
L-BAL42	21.2%	0.087%
fused silica	19.3%	0.19%
design	0.5%	0%

Table 5.13: Power distribution in the 4 design orders measured for sample **multi-8-F-LBAL42** and sample **multi-8-F-FS** in TE polarization (Details in Tab. 5.10).

21.2% for L-BAL42 and 19.3% much higher than for the replicas of mold M11-F.
The optical performance is for both replicas very similar. However, the L-BAL42 replica gives a higher contribution to the $\pm 1^{th}$ orders in comparison to $\pm 3^{th}$ orders than the fused silica replica. The SEM images of the replicas given in Tab. 5.10 and 5.11 prove that a very good replication quality is reached. Thus we believe that the different optical performance is not resulting from the molding. We note that the different wavelength to etch depth matching can also cause the difference in the optical performance since the two samples were measured with two different wavelengths.
Since both replicas show the same asymmetric power distribution, it can be stated that the cause of this problem is already present in the mold. The mold M8-F suffers from significantly higher mask-to-mask misalignment errors of up to 500 nm than mold M11-F. This might be the reason for the increased UE.
Although it can be safely stated that the mold exhibits the same variations of depth, duty cycle and line-to-line shift as mold M11-F, the replicas of M8-F show no area dependence of the optical performance.

From the measurement alone it is not possible to determine which fabrication error coming from both mold fabrication and molding results in what kind of change in the optical performance. To understand each fabrication error, we perform simulations, where one error can be independently turned off and on.

5.3.3 RCWA Simulations of a 1D Beamsplitter

Implementation of RCWA Simulations

For the simulation of the 1D beamsplitter, we use RCWA (see section 2.1.2 for details). Paraxial Fourier optics cannot be used to simulate the fabricated DOEs since the smallest feature sizes due to e.g. misalignment are smaller than the wavelength.
The implemented DOE is shown in Fig. 5.17(a). It is given by 8 height levels and 7 layers. For a wavelength of 488 nm and L-BAL42, the lowest uniformity error is achieved for a surface depth 824 nm, which is equal to 2π. One layer has thus a thickness of 103 nm. The diffraction pattern in TE polarization is shown in Fig. 5.17(b). The UE is 0.051%, the efficiency of the 4 design orders is 74.8% and the 0^{th} order efficiency is as low as 0.0075%.
The number of Fourier orders was set to 160. Fig. 5.18 depicts the dependency of the order efficiency on the number of Fourier orders used in the RCWA simulations. The stability is reached for 160 Fourier orders. From this graph, it can be seen that the accuracy is circa 0.01% for the diffraction efficiency.
Different fabrication constraints can be included in the simulation. The etch depth of the 3 etch steps can be included by changing the layer thicknesses individually. The duty cycle and mask alignment errors are taken into account by changing the positions of the phase steps. The molding is considered by changing the step profile. This can only be done by increasing the number of layers accordingly. In the following, only fabrication errors introduced by the mold are considered.

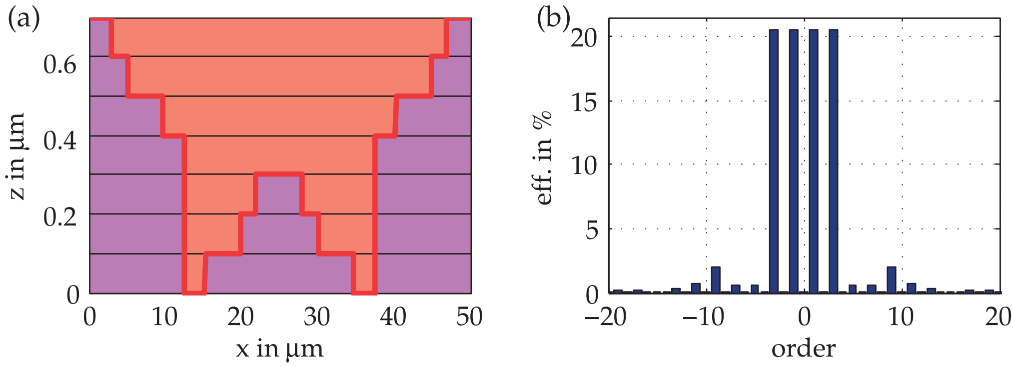

Figure 5.17: Phase profile (a) of element F with critical dimension 2 µm consists of 7 layers (8 discrete levels). The corresponding diffraction pattern (b) is simulated for a wavelength of 488nm, the glass L-BAL42 and with a depth of 827nm, which is equal to 2π.

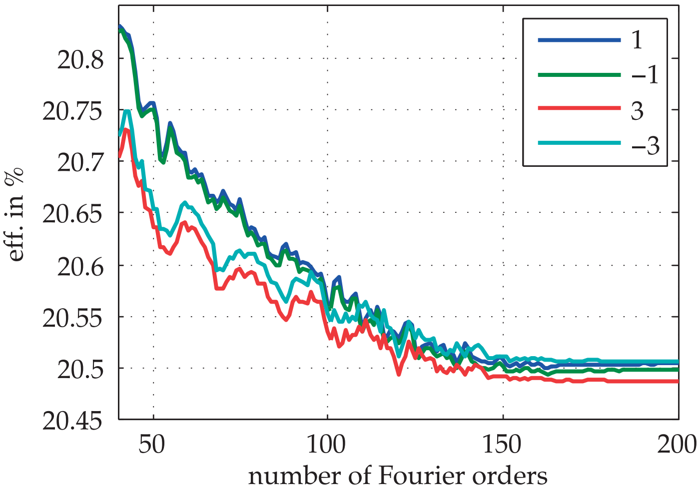

Figure 5.18: Convergence analysis of RCWA. The accuracy of the order efficiency depends on the number of Fourier orders used in the RCWA simulations. The simulation result reaches a stable value for a number of Fourier orders higher than 160 (accuracy ±0.01%).

Results of RCWA Simulations

First, we will include all fabrication constraints and compare them to the measurement results for **multi-8-F-LBAL42**, **multi-8-F-FS** and **multi-11-F-LBAL42**. They are given in Tab. 5.14 for **multi-11-F-LBAL42** and for the replicas **multi-8-F-LBAL42** and **multi-8-F-FS** in Tab. 5.15 and in Tab. 5.16.
In order to compare the simulations with the measurements better, the orders were normalized to the average of the 4 design orders. The simulations match well with the measurement results. The best result was obtained for **multi-11-F-LBAL42**. The simulated UE is with 4.08% very close to the measurement with 4.8%. The 4 design orders show a small asymmetry around the 0^{th} order. For the 2 replicas with the second mold M8-F, a much stronger asymmetry can be seen, which is both present in the measurement and the simulations. To find the cause of this high UE, the individual fabrication constraints will be simulated.

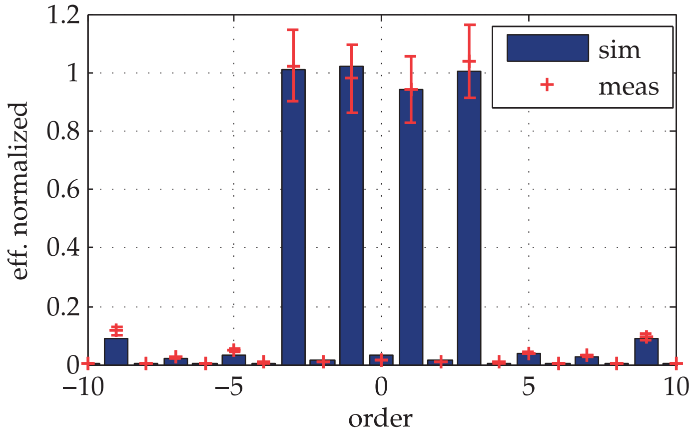

λ = 488 nm
depths from Tab. 5.9
duty cycle from Tab. 5.9
alignment from Tab. 5.9

	sim.	meas.
UE	4.08%	4.8%
eff.	74.8%	73.5%

Table 5.14: Simulation results in comparison to optical performance measurement for sample multi-11-F-LBAL42.

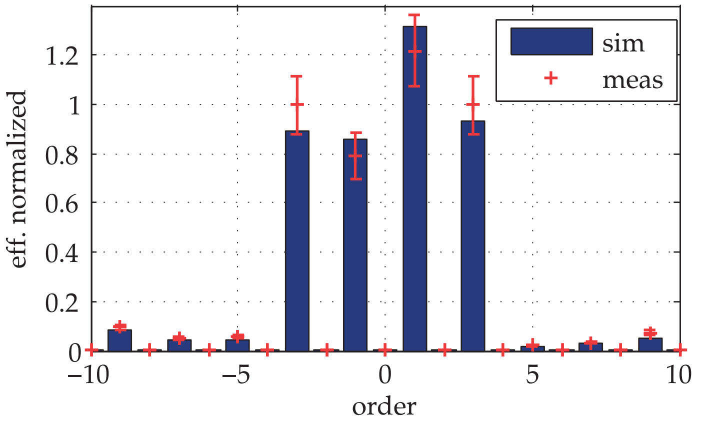

λ = 687 nm
depths from Tab. 5.10
duty cycle from Tab. 5.10
alignment from Tab. 5.10

	sim.	meas.
UE	21.1%	21.2%
eff.	76.7%	74%

Table 5.15: Simulation results in comparison to optical performance measurement for sample multi-8-F-LBAL42.

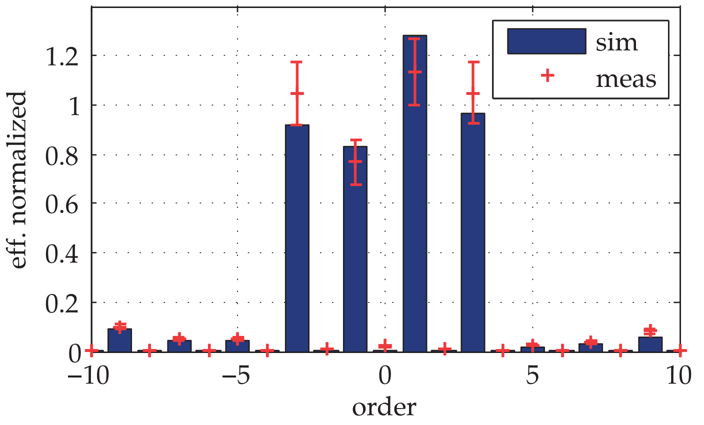

λ = 532 nm
depths from Tab. 5.11
duty cycle from Tab. 5.11
alignment from Tab. 5.11

	sim.	meas.
UE	21.4%	19.3%
eff.	78.8%	74%

Table 5.16: Simulation results in comparison to optical performance measurement for sample multi-8-F-FS.

If we consider a grating with ideal duty cycle and no alignment error but etch depths equivalent to the fabricated DOEs, UE of 5.08% for **multi-8-F-LBAL42** and 1.9% for **multi-11-F-LBAL42** are reached. The results are summarized in Tab. 5.17. The simulated UEs are smaller than the measurement values. Also, no asymmetry around the 0^{th} is introduced by the etch depth variation. Thus, the etch depth variation is not the only parameter, which defines the optical performance.

	multi-11-F-LBAL42	**multi-8-F-LBAL42**	**multi-8-F-FS**
mask h/8	109 nm	153 nm	153 nm
mask h/4	208 nm	280 nm	280 nm
mask h/2	383 nm	585 nm	585 nm
λ	488 nm	687 nm	532 nm
UE sim.	1.9%	5.08%	2%
UE meas.	4.8%	21.2%	19.3%

Table 5.17: Simulation of the etch depths given for the fabricated DOEs (no alignment errors and no linewidth errors assumed).

The dependency of the profile height can be considered by a total scaling of the surface and of the 3 individual etch steps. In Fig. 5.19 the dependency of the diffraction efficiency on the height change is drawn. L-BAL42 and 488nm wavelength are assumed. For 2 level beamsplitters the UE does not vary strongly with the etch step. For the here discussed multilevel DOE, this is not the case. A change of the height from 824 nm to 844 nm increases the UE from 0.044% to 2.9%. If one limits the UE to 5% the depth error needs to be below ±35 nm, which is equal to an accuracy of 4.2% for the etch depth. Accuracies below 10% are very demanding to achieve.

Since 3 etch steps are needed, also the individual depth variations are of interest. It can be seen that h/2 and h/8 depths do have a very small influence on the UE. They play a role for the diffraction efficiency. However, the h/4 etch depth determines the UE. For a UE below 5% the etch depth needs to be as good as 206 nm ± 8.6 nm, which is equal to an accuracy of 4.18% for the etch depth.

For all height variations, one can see that the diffraction pattern remains symmetric. That means the 1st is equally strong as the -1st orders and the 3rd to the -3^{rd} order. A change in the height will only exchange the power between $\pm 3^{rd}$ and $\pm 1^{rd}$ orders. The same variation can be seen in the optical performances for the two replicas of mold M8-F in Fig. 5.13. Thus, we can assume that the different optical performance is caused by a different wavelength height matching.

(a) variation of total height

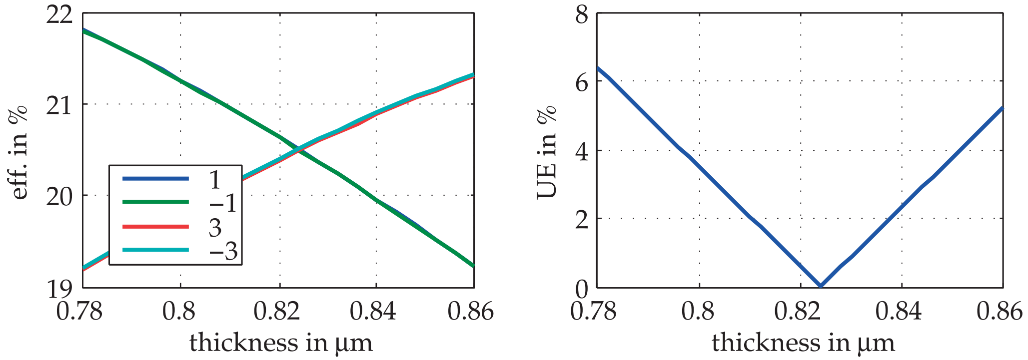

(b) variation of h/2 height

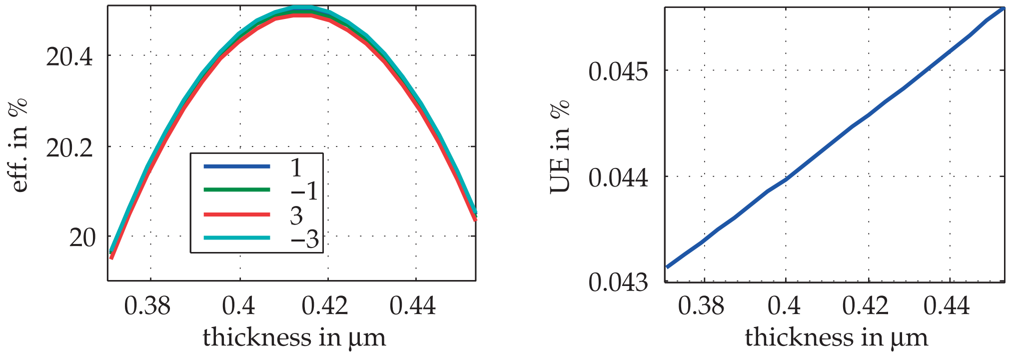

(c) variation of h/4 height

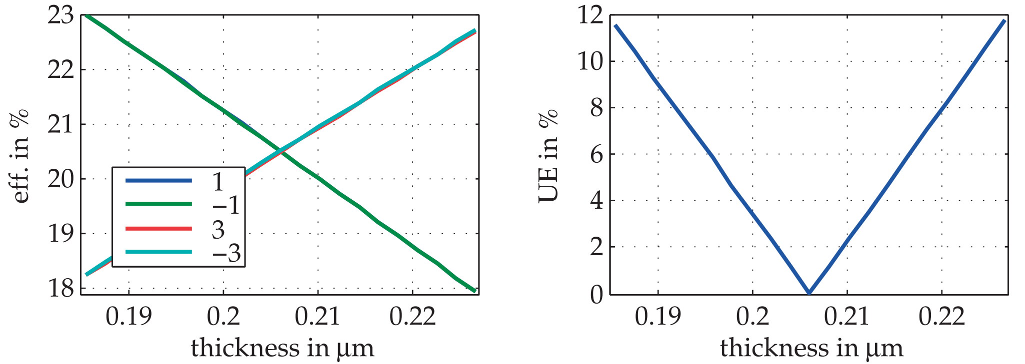

(d) variation of h/8 height

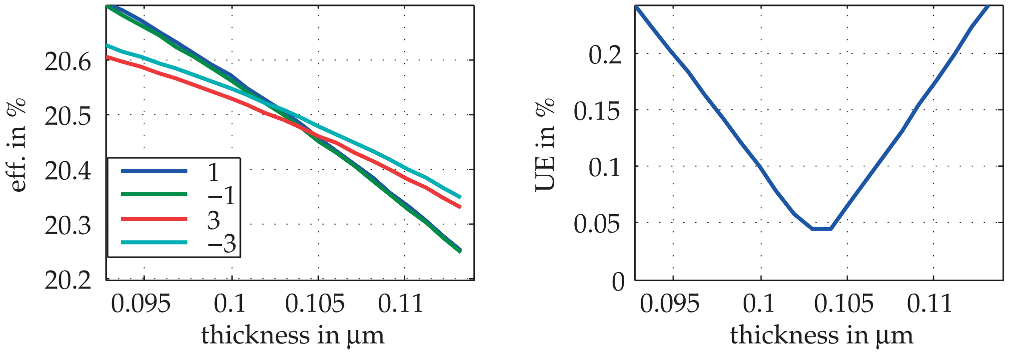

Figure 5.19: Simulation of height variation for a L-BAL42 DOE with 488 nm wavelength: strongest change of UE for second etch depth h/4.

A considerable variation of the etch depth was found for the direction perpendicular to the flat. The change is 4.25% of the depth over a distance of 17 mm. Comparing the etch depth variation with the accuracy limitation of the simulations, one can expect a UE variation in the order of 5% for the optical performance measurements. This agrees well with the area dependency of multi-11-F-LBAL42 given in Tab. 5.12 and Fig. 5.16 (b). The simulations show that both -3^{rd} and the $+3^{rd}$ order increase with thickness by the same amount. Also, -1^{st} and 1^{st}order behave in the same way. The symmetry is not changing. The same behavior can be seen in the measurement results from Fig. 5.16 (b). For the replicas of mold M8-F, this area dependency was not observed (Tab. 5.13). We performed the same height variation like in Fig. 5.19 (a), but included the error for duty cycle and alignment error. The power distribution and UE are given in Fig. 5.20 (c)-(d). The power distribution of replica multi-8-F-LBAL42 shows that the 1^{st} order is much stronger than the other 3 orders. This difference is not changed a lot by the variation of the thickness. Thus, we assume that for already high UE much smaller area dependency will be seen.

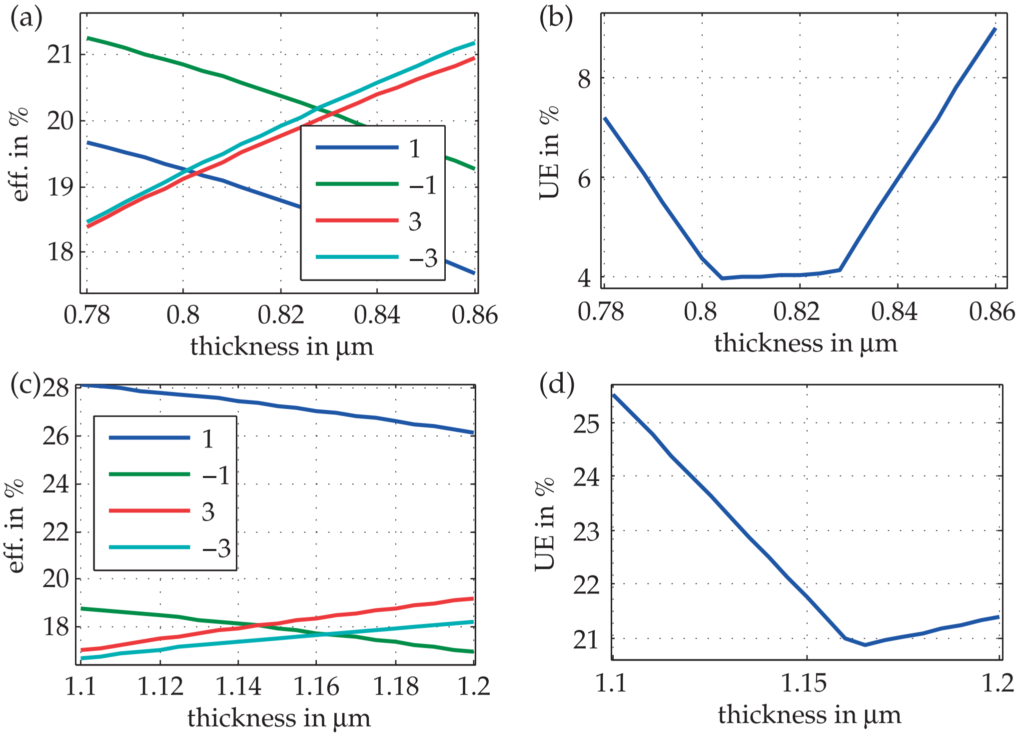

Figure 5.20: Simulation of height variation for multi-11-F-LBAL42 (a)-(b) and multi-8-F-LBAL42 (c)-(d) including alignment error and duty cycle.

The influence of the duty cycle is illustrated in Fig. 5.21. 4 different linewidths are given in the design: 2 µm and 5.6 µm for the first mask h/8, 14.6 µm for mask h/4 and 25 µm for mask h/2. From the power distribution, it can be seen that the change is symmetric around the 0^{th} order. The UE increases up to 3%.

If we consider a grating with ideal etch depth and no alignment error, but duty cycle errors equivalent to the fabricated DOEs, UE of 2.7% for **multi-8-F-LBAL42** and 0.54% for **multi-11-F-LBAL42** are reached. The results are summarized in Tab. 5.18. The simulated UE is much smaller than the measurement values. Thus, the achieved duty cycle is of minor importance to the optical performance in contrast to the other fabrication constraints.

	multi-11-F-LBAL42	**multi-8-F-LBAL42**	**multi-8-F-FS**
line 25 µm	25 µm	25 µm	25 µm
line 14.6 µm	14.45 µm	14.3 µm	14.3 µm
line 5.6 µm	5.3 µm	5.35 µm	5.35 µm
line 2 µm	1.75 µm	1.97 µm	1.97 µm
UE sim.	0.54%	2.7%	0.64%
UE meas.	4.8%	21.2%	19.3%

Table 5.18: Simulation of linewidth errors given for the fabricated DOEs (no alignment error, ideal etch depth assumed).

(a) 25 µm line

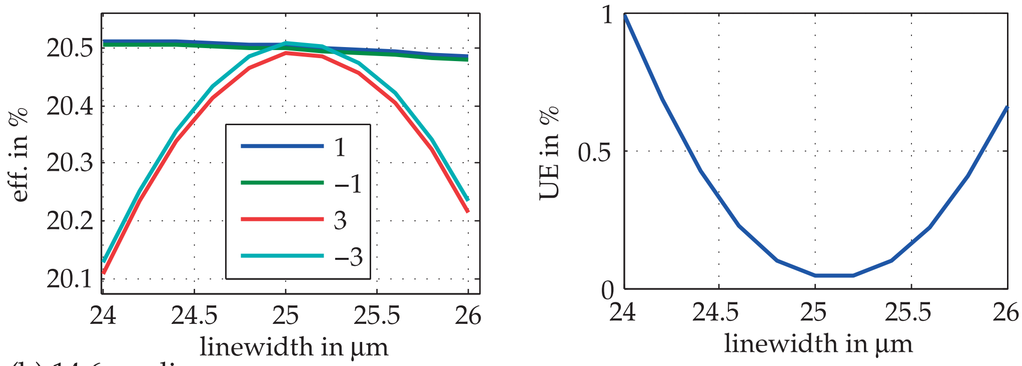

(b) 14.6 µm line

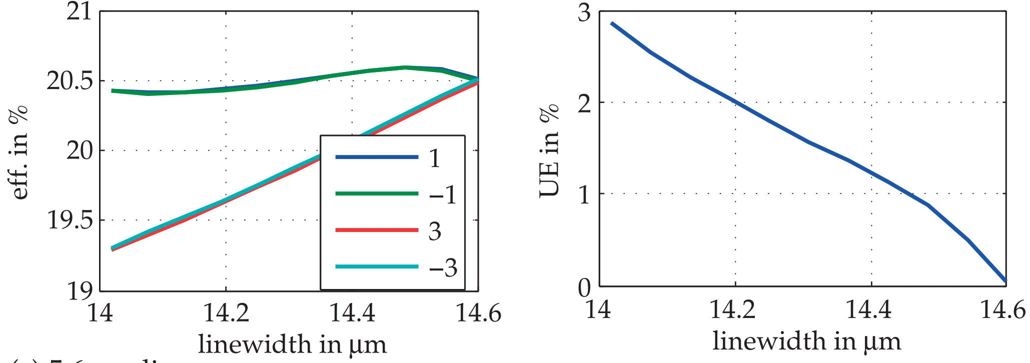

(c) 5.6 µm line

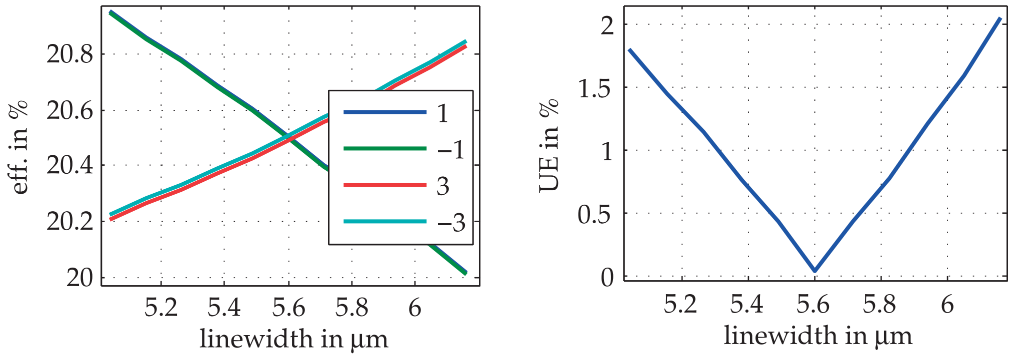

(d) 2 µm line

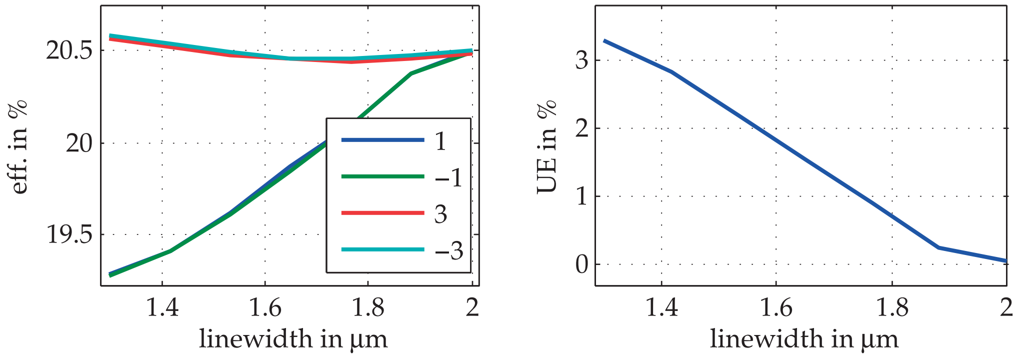

Figure 5.21: Simulation of duty cycle variation for a L-BAL42 DOE with 488 nm wavelength.

If we consider a grating with ideal etch depth and duty cycle, but alignment errors equivalent to the fabricated DOEs, we reach very high UE (Tab. 5.19). The simulated values are very close to the measurement results. The power distribution for only alignment errors of sample **multi-8-F-LBAL42** is shown in Fig. 5.22. The measurement agrees very well with the simulation, even better than the simulation for all 3 fabrication errors given in Fig. 5.15. Since only alignment errors are considered, we can state that the main limiting factor for the investigated DOE is the mask-to-mask misalignment.

	multi-11-F-LBAL42	**multi-8-F-LBAL42**	**multi-8-F-FS**
mask h/4	-58 nm	-150 nm	-150 nm
mask h/2	73 nm	500 nm	500 nm
UE sim.	4.2%	21.5%	21.8%
UE meas.	4.8%	21.2%	19.3%

Table 5.19: Simulation of alignment errors given for the fabricated DOEs (no linewidth errors, ideal etch depth assumed).

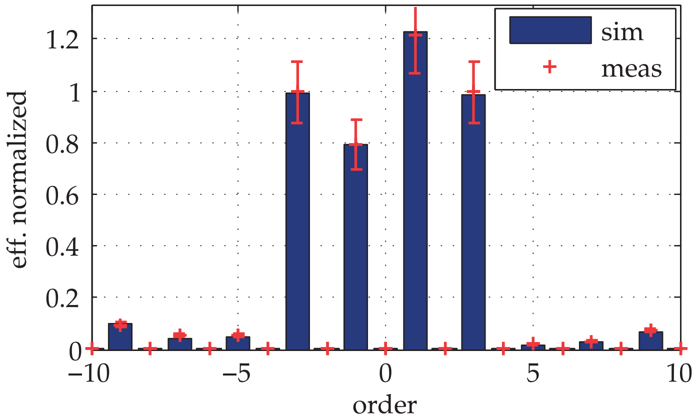

Figure 5.22: Comparison of simulation and measurement of element **multi-8-F-LBAL42** are in good agreement. For the simulation the following parameters are used: glass L-BAL42, 687nm, no linewidth errors, ideal etch depths and alignment errors of -150 nm and 500 nm.

The mask-to-mask alignment can be done with an accuracy better than 500 nm. The change of the power distribution for the alignment of the second mask h/4 to the first mask is given in Fig. 5.23 (b) and for the third mask h/2 in Fig. 5.23 (a). In the range of interest (500 nm) a strong increase of the UE can be seen. In order to maintain a UE below 5%, the second mask h/4 needs to be aligned with a shift smaller than 145 nm and the third mask h/2 with a shift below 190 nm. If both mask alignment errors are simulated the tolerances become tighter (Fig. 5.23 (c)). For a shift in the same directions, both shifts need to be below 210 nm. Shifts in opposite direction need to be below 75 nm. This is much smaller than the accuracy of the mask aligner. In contrast to the etch depth error and the duty cycle, a significant asymmetry can be seen for alignment errors.

(a) mask h/2

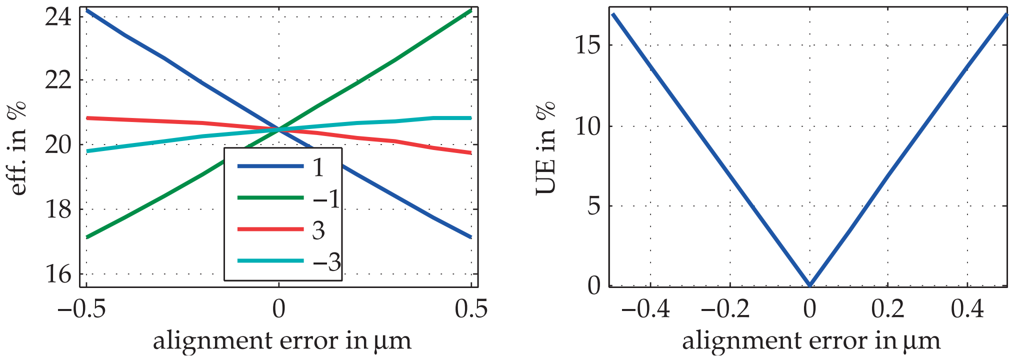

(b) mask h/4

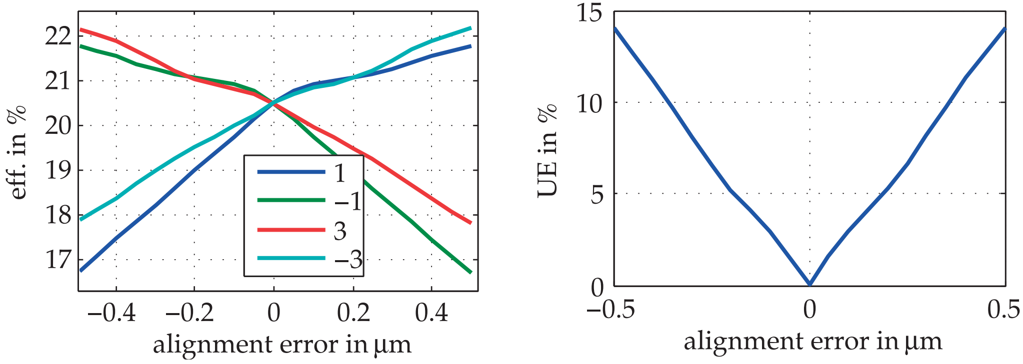

(c) UE in % for mask h/2 and h/4

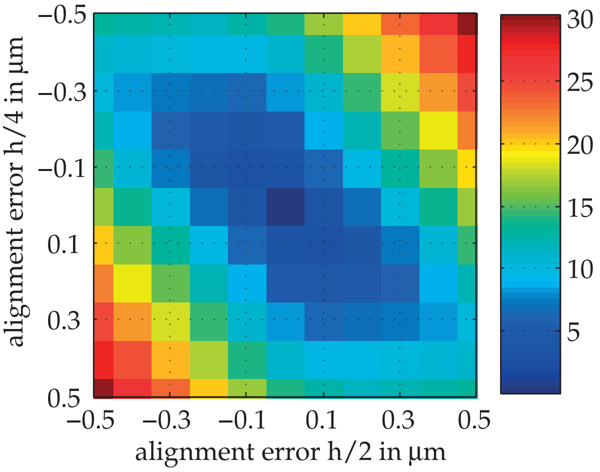

Figure 5.23: Simulation of alignment errors for a L-BAL42 DOE with 488 nm wavelength.

5.3.4 Summary

For our simulations, we use RCWA (Details in Section 2.1.2). Fabrication constraints such as etch depth, duty cycle, and mask-to-mask alignment were considered. The simulated results for the uniformity error are summarized in Tab. 5.20. The simulated DOEs give uniformity errors of 4.08% for **multi-11-F-LBAL42**, 21.1% for **multi-8-F-LBAL42** and 21.4% for **multi-8-F-FS**, which are in excellent agreement with the measurement results. To find the main limiting factor, each fabrication error is simulated individually. From these results, one can see that the biggest contribution to the uniformity error comes from the mask-to-mask alignment error. The simulated uniformity error for only mask-to-mask alignment is the highest with 4.2% for **multi-11-F-LBAL42**, 21.5% for **multi-8-F-LBAL42** and 21.4% for **multi-8-F-FS**.

Miller et al. found that mask alignment represents the main limiting factor, not the etch depth accuracy [Miller1993]. Our findings agree with their analysis. This also explains why the uniformity error for the replica of mold M8-F is much bigger than the replicas of mold M11-F: the misalignment of M8-F is with 500 nm and -150 nm much larger than the misalignment of M11-F with 73 nm and −58 nm.

A uniformity error of below 5% is desired in industry, but this required an alignment accuracy of at least 100 nm. This tight fabrication tolerance cannot be guaranteed with multiple exposure photolithography. On the other hand, once a master is fabricated the optical performance will be very stable between multiple replicas. Thus, multiple masters could be fabricated and only those with sufficient quality could be used for precision glass molding.

	multi-11-F-LBAL42	**multi-8-F-LBAL42**	**multi-8-F-FS**
λ	488 nm	687 nm	532 nm
mask h/8	109 nm	153 nm	153 nm
mask h/4	208 nm	280 nm	280 nm
mask h/2	383 nm	585 nm	585 nm
UE sim.	1.9%	5.08%	2%
line 25 µm	25 µm	25 µm	25 µm
line 14.6 µm	14.45 µm	14.3 µm	14.3 µm
line 5.6 µm	5.3 µm	5.35 µm	5.35 µm
line 2 µm	1.75 µm	1.97 µm	1.97 µm
UE sim.	0.54%	2.7%	0.64%
mask h/4	-58 nm	-150 nm	-150 nm
mask h/2	73 nm	500 nm	500 nm
UE sim.	4.2%	21.5%	21.8%
UE sim.(all)	4.08%	21.1%	21.4%
UE meas.	4.8%	21.2%	19.3%

Table 5.20: Simulation of etch depth, linewidth errors and alignment errors given for the fabricated DOEs.

Alternatively, electron-beam lithography can offer an accuracy of 50 nm but is too expensive for mass production. The approach to use precision glass molding with an e-beam structured master can divide this costs on multiple fabricated DOEs.
Although the 6x6 and the 1x4 beamsplitter have similar misalignment errors (deviations over the wafer area have to be taken into account), but the uniformity errors do not show the same tendency. To simulate the 2D beamsplitter accurately we would need to consider the shape deviations caused by diffraction during exposure. We believe that this source of error plays a significant role and contribute to the high uniformity error. In case of the linear beamsplitter, the diffraction effect is included by the duty cycle. The efficiency for our test element is much less sensitive to misalignment errors than the uniformity error. We note that it is not possible to give general fabrication tolerances for DOEs. Each design has to be analyzed separately.
Implementing the shapes introduced during molding is difficult. For simplicity, we simulate the molding influence by a decrease of the wall verticality. For glass **multi-11-F-LBAL42** in ideal conditions, the uniformity error is 0.15% for 90° wall verticality. Even a decrease to 45° changes the uniformity error only to 0.13%. From this results, we can conclude that the quality of the DOE does not significantly change due to molding unless strong deformations during the cooling stage occur.

5.4 Conclusion

In this chapter, the quality of the molded diffractive optical elements (DOEs) was discussed in terms of optical performance. Three different types of DOEs were tested: 2 level binary elements with low and high-resolution and multilevel elements. For the low-resolution elements the glassy carbon molds were fabricated with mask photolithography. A 6x6 beamsplitter showed good results given in a low uniformity error. A 11x11 beamsplitter achieved a higher uniformity error. The limiting factor of the performance was given by the resolution limit of the mask lithography, which was seen by structure deformation and duty cycle errors.

In order to improve the accuracy of the mold fabrication molds were fabricated by e-beam lithography. This technology also allows the fabrication of smaller features, which can be used to reach larger diffraction angles. It was shown that precision glass molding with high-quality GC molds can be used to fabricate DOEs with state-of-the-art quality. We showed that a similar optical performance to a reference element in fused silica was reached. The simulations based on RCWA are in good agreement with the measurements. The profiles of the molded DOEs were included in the simulations and showed that feature roundings have a similar effect as etch depth errors and duty cycle errors. The molding settings such as time and temperature can be used to reach the optimal height profile. Mold errors such as trenching can be compensated during molding by choosing a lower mold filling.

Last, the multilevel elements were analyzed. For these elements, mask-to-mask misalignment errors are introduced during mold fabrication and show a strong influence on the final performance of the molded DOEs.

6 Conclusion

The aim of this work was to find a suitable mold material for precision glass molding of diffractive optical elements (DOEs) and to find the limiting factors in terms of minimal feature size and maximum aspect-ratio, which can one hand be structured on the mold and on the other hand be replicated accurately in glass. We chose to test glassy carbon and fused silica as potential mold materials. Precision glass molding of DOEs could allow a strong decrease of the cost compared to direct fabricated elements if the mold lifetime is high enough and the quality of the DOEs comparable to state-of-the-art technology.

Different kinds of test elements were used to analyze the potential of our approach. These include 2 level binary elements with low and high critical dimensions and 8 level binary elements. The optical functionalities are beamsplitting elements, which allowed an easy interpretation of the quality by the parameters of efficiency and uniformity error.

We could expand the available processes for the glassy carbon microfabrication. First, other hard mask materials for the plasma etching of glassy carbon were tested, where Si was found to give very good results. This allowed minimizing the resolution limit of the microstructuring by using electron-beam lithography. Si allows the combination with already available processes. A uniform deposition of the hard mask layer is essential for a high form accuracy. We investigated continuous surface relief structuring and fabricated multilevel DOEs with 8 levels.

Precision glass molding was conducted for 2 glass materials: L-BAL42 from OHARA and fused silica SQ1 from SCHOTT. L-BAL42 is used, because of the low coefficient of thermal expansion.The quality of the molding was investigated by scanning electron microscope images of the mold surface and the corresponding glass replication. We investigated the influence of the thermal shrinkage of the glass in respect to the mold material for microrelief surfaces. In contrast to molding of aspherical lens, where the shrinkage can be compensated by the mold design [Klocke2012], the shrinkage can have a significant influence on the lifetime of the mold. The dimension of the shrinkage is in the micrometer range and thus close to the feature sizes of the DOEs. Mold failure due to rapture and/or deformation of mold and glass was seen. This is especially important for small features with high aspect-ratios on large areas, which are more fragile. Also, larger area and transition zones between flat and microstructured areas are more prone to this failure mechanism. We found that it is essential to release the glass from the mold at a high enough temperature. The tooling of the molding machines needs to be therefore adapted.

An important outcome came from testing fused silica as an alternative mold material since microfabrication processes are easier available than for glassy carbon. However, the coating of the fused silica has a very limited lifetime. A 15 nm thin layer of Pt-Ir was used. Thicker layers would increase the coating lifetime but can cause a significant feature rounding, if the layer thickness is in the order of the critical dimension of the DOEs. The breakage of the coating layer becomes more severe if a high filling rate and higher aspect-ratios are used. We believe that a mold with an anti-adhesion layer is not applicable and cost-efficient for the molding of DOEs.

In contrast, we found that glassy carbon molds allow always an easy glass release and therefore do not need a coating. We conducted 50 molding cycles without a noticeable change of the glassy carbon surface properties. Feature size as small as 800 nm with an aspect ratio of 0.6 could be molded into L-BAL42 with high accuracy. This shows clearly that glassy carbon has the potential for large volume replication.

Glassy carbon was tested for molding fused silica at 1400 °C. The glassy carbon surface degrades significantly after 3 replications. Further tests need to be conducted to clarify the reason for this failure. We believe that the atmosphere in the molding chamber needs to be controlled more carefully.

The final evaluation of our approach is done by testing the optical performance and comparing our results with state-of-the-art technology. The main question of this work was to investigate if the molding influence is significant or if the performance is mainly determined by the mold surface structuring. Simulations were the key tool to link the individual steps with the final optical performance.

We found that the optical performance of 2 level binary DOEs fabricated with mask photolithography is determined by the quality of the mold structuring. Due to the employed mask photolithography, the main limitations are given by form deviations and the etch depth accuracy. We tested 8 level binary DOEs and found that the mold surface especially the mask-to-mask alignment errors determine the optical performance. These elements show critical dimensions of 2 µm and higher. Only for one DOE with a critical dimension of 800 nm could a significant influence of the molding be seen. The glass profiles for different filling rates are showing corner roundings in the 10 nm range. This has a similar effect as a change of the etch depth. Since the material position changes only at the etch step position, a similar effect to a duty cycle change can be seen. By varying the molding parameters like temperature and time we could mold this high-resolution DOE with high accuracy and showed that the optical performance is comparable to state-of-the-art technology with fused silica.

The main findings of this thesis are:

- for the first time consideration of the complete product cycle,
- large area molding of DOEs with GC,
- increase of microstructuring technologies for GC,
- investigation of different glass materials for optical applications,
- remarkable quality for high performance DOE, which is comparable to state of the art SiO_2 etching,
- improvement of minimum resolution to 800 nm and maximum aspect ratio to 0.6,
- lifetime-test proves long lifetime of the GC molds and promoting a low cost fabrication technology,
- confirmation of the suitability of GC as an excellent mold material for nm feature sizes with precision glass molding,
- the industrial process is now ready.

We justified that glassy carbon molds can be used for precision glass molding of diffractive optical elements. A mold lifetime of at least 50 cycles is possible, which is important for a cost-efficient fabrication method. The molding cycle time was between 15 to 25 min for the here presented results. We believe that this cycle time can limit the cost of the molded DOEs significantly. More cost efficient molding process by e.g. parallelization are needed, which are beyond the scope of this work.

Acronyms

AFM	Atomic force microscope
CD	Critical dimension
CTE	Coefficient of thermal expansion
DOE	Diffractive optical element
EBL	electron beam lithography
FS	fused silica
GC	Glassy Carbon
HMDS	Hexamethyldislazane
IBE	Ion Beam Etching
PR	Photoresist
SEM	Scanning electron microscope
T_g	Glass transition temperature
RCWA	Rigorous Coupled Wave Analysis
RF	Radio frequency
RIE	Reactive ion etching
λ	Wavelength
Λ	Grating period
η	Diffraction efficiency
m	Diffraction order
θ_m	Diffraction angle of diffraction order m
M	Number of Fourier orders
N	Number of discrete levels

$\mathbf{S}$	Number of phase transition per period
$\Delta\mathbf{x}$	Positioning error of phase transition position
ϵ	Phase scaling error

Bibliography

[Brown1998] N. M. D. Brown, N. Cui and A. McKinley, *A study of the topography of a glassy carbon surface following low-power radio-frequency oxygen plasma treatment*, Appl. Surf. Sci. 133, 157–165 (1998).

[Chen2006] Y. Chen, A.Y. Yi, F. Klocke, G. Pongs, and A. Demmer, *Manufacturing of glass diffractive optics by use of molding process,* ASPE 2006, 395-398 (2006).

[Chen2008] Y. Chen, A. Y. Yi, D. Yao, F. Klocke, and G. Pongs, *A reflow process for glass microlens array fabrication by use of precision compression molding,* J. Micromechanics Microengineering 18, 055022 (2008).

[Choi2004] W. Choi, J. Lee, W.-B. Kim, B.-K. Min, S. Kang and S.-J. Lee, *Design and fabrication of tungsten carbide mold with micro patterns imprinted by micro lithography,* J. Micromech. Microeng. 14, 1519–1525 (2004).

[Dambon2016] O. Dambon, M. Doetz, J. Dukwen, *Entwicklung technologisch fundierter Richtlinien zur ressourcenschonenden Produktion der nächsten Generation von Glasoptiken,* Apprimus Verlag, Aachen, ISBN:978-3-86359-433-6 (2016).

[Dammann1977] H. Dammann and E. Klotz, *Coherent Optical Generation and Inspection of Two-dimensional Periodic Structures,* Optica Acta: International Journal of Optics, 24:4, 505-515,(1977).

[Davim2017] J. P. Davim *Microfabrication and Precision Engineering,* Woodhead Publishing (2017).

[Fredriksson2009] H. Fredriksson, D. Chakarov and B. Kasemo, *Patterning of highly oriented pyrolytic graphite and glassy carbon surfaces by nanolithography and oxygen plasma etching,* Carbon 47, 1335–1342 (2009).

[Gale1997] M. T. Gale, *Replication Techniques for Diffractive Optical Elements,* Microelectronic Engineering 34 (3–4), 321–39 (1997).

[Gale2002] M. T. Gale, *Diffractive optics and micro-optics production technology in Europe,* OSA Trends in Optics and Photonics (TOPS), Diffractive Optics and Micro-Optics, OSA Technical Digest 75, 18-20 (2002).

[Gale2005] M. T. Gale, C. Gimkiewicz, S. Obi, M. Schnieper, J. Söchtig, H. Thiele, and S. Westenhöfer, *Replication Technology for Optical Microsystems,* Optics and Lasers in Engineering, Optics in Switzerland, 43 (3–5), 373–86 (2005).

[Georgiadis2015] K. Georgiadis, *The Failure Mechanisms of Coated Precision Glass Molding Tools,* D82 Diss. RWTH Achen University, Germany (2015).

[Goodman1996] J. W. Goodman, *Introduction to Fourier Optics,* McGraw-Hill Companies, INC., second edition (1996).

[Hansen2011] H. N. Hansen, R. J. Hocken, and G. Tosello, *Replication of Micro and Nano Surface Geometries,* CIRP Annals - Manufacturing Technology 60 (2), 695–714 (2011).

[Hans2014] L. E. Hans, K. Prater, C. Kilchoer, T. Scharf, H. P. Herzig and A. Hermerschmidt, *Wafer-level micro-structuring of glassy carbon,* Proc. SPIE 8974, 89740Y (2014).

[Harris2004] P. J. F. Harris, *Fullerene-related structure of commercial glassy carbons,* Philos. Mag. 84, 3159–3167 (2004).

[Hatzakis1969] M. Hatzakis, *Electron Resists for Microcircuit and Mask Production,* J. Electrochem. Soc. 116, 1033 (1969).

[He2011] P. He, F. Wang, L. Li, K. Georgiadis, O. Dambon, F. Klocke and A. Y. Yi, *Development of a low-cost high precision fabrication process for glass hybrid aspherical diffractive lenses,* J. Opt. 13, 085703 (2011).

[He2013] P. He, L. Li, J. Yu, W. Huang, Y.-C. Yen, L. J. Lee, and A. Y. Yi, *Graphene-coated Si mold for precision glass optics molding,* Opt. Let. 2625, Vol. 38, 14 (2013).

[Henry2010] M. D. Henry, *ICP Etching of Silicon for Micro and Nanoscale Devices,* Ph.D. thesis, California Institute of Technology, (2010).

[Herzig1997] H. P. Herzig, *Micro-Optics: Elements, Systems and Applications,* Taylor & Francis, London (1997).

[Huenten2010] M. Hünten, F. Klocke and O. Dambon, *Precision glass molding. An integrative approach for the production of high precision micro-optics,* Adv. Fabr. Technol. Micronano Opt. Photonics III Paper, 75910X (2010).

[Hugonin2005] J.P. Hugonin and P. Lalanne, *Reticolo software for grating analysis,* Institut d'Optique, Orsay, France (2005).

[Hung2009] Y. M. Hung, Y. J. Lu, and C.K. Sung, *Microstructure patterning on glass substrate by imprinting process,* Microelectronic Engineering 86, 577–582 (2009).

[Jahns1989] J. Jahns, M. M. Downs, M. E. Prise, N. Streibl, and S. J. Walker, *Dammann gratings for laser beam shaping,* Optical Engineering 28(12), 1267 -1275 (1989).

[Kang2004] S. Kang, *Replication Technology for Micro/Nano Optical Components,* Japanese Journal of Applied Physics 43, 5706–5716 (2004).

[Kemme2010] S. A. Kemme, *Microoptics and Nanooptics Fabrication,* CRC Press, USA (2010).

[Kley1997] E.B. Kley, *Continuous profile writing by electron and optical lithography,* Microelectronic Engineering 34, 261-298 (1997).

[Klocke2012] F. Klocke, F. Wang, Y. Wang, G. Liu, O. Dambon, and A. Y. Yi, *Development of a Flexible and Reliable Numerical Simulation for Precision Glass Molding of Complex Glass Optics,* Proc. of SPIE Vol. 8416, 841603-1 (2012).

[Komori2008] M. Komori, H. Uchiyama, H. Takebe, T. Kusuura, K. Kobayashi, H Kuwahara and T. Tsuchiya, *Micro/nanoimprinting of glass under high temperature using a CVD diamond mold,* J. Micromech. Microeng. 18,065013 (2008).

[Kress2009] B. C. Kress and P. Meyrueis, *Applied Digital Optics, from Micro-Optics to Nanophotonics,* John Wiley & Sons, Chichester, UK (2009).

[Kuhnke2004] M. Kuhnke, Th. Lippert, E. Ortelli, G.G. Scherer, and A. Wokaun, *Microstructuring of Glassy Carbon: Comparison of Laser Machining and Reactive Ion Etching,* Thin Solid Films 453-454, 36–41 (2004).

[Kuhnke2005] M. Kuhnke, Th. Lippert, E. Ortelli, G.G. Scherer, and A. Wokaun, *Micro-Fabrication of flow field channels in glassy carbon by a combined laser and reactive ion etching process,* Surf. Coat. Technol. 200, 730–733 (2005).

[Mekura2009] H. Mekaru, C. Okuyama, A. Ueno, and M. Takahashi, *Thermal imprinting on quartz fiber using glasslike carbon mold,* J. Vac. Sci. Technol. B 27, 2820–2825 (2009).

[Mekura2012] H. Mekaru, C. Okuyama and A. Ueno, *Control of inclination angle of glass-like carbon mold by defocus UV exposure on Si-containing photoresist,* J. Vac. Sci. Technol. B 30, 06FB12 (2012).

[Mekura2013] H. Mekaru, C. Okuyama and A. Ueno, *Fabrication of glass-like carbon molds to imprint on glass materials by MEMS processing technologies,* Microsyst. Technol. 19, 315–323 (2013).

[Mertus2012] L. Mertus and A. Symmons, *Implications of Diamond-Turned vs. Diamond Ground Molds Fabrication Technologie on Precision-Molded Optics,* Proc. of SPIE 8489, 848902 (2012).

[Miller1993] J. M. Miller, M. R. Taghizadeh, J. Turunen and N. Ross, *Multilevel-grating array generators: fabrication error analysis and experiments,* Applied optics 32.14, 2519-2525 (1993).

[Moharam1995] M. G. Moharam, Eric B. Grann, Drew A. Pommet, and T. K. Gaylord, *Formulation for stable and efficient implementation of the rigorous coupled-wave analysis of binary gratings,* JOSAA 12, 1068 (1995).

[Mori2008] T. Mori, K. Hasegawa, T. Hatano, H. Kasa, K. Kintaka, and J. Nishii, *Surface-relief gratings with high spatial frequency fabricated using direct glass imprinting process,* Opt. Lett. 33(5), 428–430 (2008).

[Mori2009] T. Mori, Y. Kimoto, H. Kasa, K. Kintaka, N. Hotou, J. Nishii, and Y. Hirai, *Mold Design and Fabrication for Surface Relief Gratings by Glass Nanoimprint,* Japanese Journal of Applied Physics 48, 06FH20 (2009).

[Palagushkin1998] A. N. Palagushkin, M. V. Politov, S. A. Prokopenko, A. L. Mikaelian, A. N. Arlamenkov, B. S. Kiselyov and V. A. Shkitin, *Fabrication of multilevel HOEs using direct e-beam writing,* Proc. SPIE 3348, 76–82 (1998).

[Prater2014] K. Prater, J. Dukwen, T. Scharf, H. P. Herzig and A. Hermerschmidt, *Surface micro-structuring of glassy carbon for precision glass molding of diffractive optical elements,* Proc. SPIE 9192, 919211 (2014).

[Prater2015a] K. Prater, J. Dukwen, T. Scharf, H. P. Herzig, S. Plöger, A. Hermerschmidt, *Multilevel micro-structuring of glassy carbon for precision glass molding of diffractive optical elements,* Proc. SPIE 9374, 937410 (2015).

[Prater2015b] K. Prater, J. Dukwen, T. Scharf, H. P. Herzig, S. Plöger, A. Hermerschmidt, *Multilevel micro-structuring of glassy carbon molds for precision glass molding,* Proc. SPIE 9628, 96281M (2015).

[Prater2016] K. Prater, J. Dukwen, T. Scharf, H. P. Herzig, S. Plöger, and A. Hermerschmidt, *Micro-structuring of glassy carbon for precision glass molding of binary diffractive optical elements,* Opt. Mater. Express 6, 3407-3416 (2016).

[Prater2016a] K. Prater, J. Dukwen, T. Scharf, H. P. Herzig, S. Plöger, and A. Hermerschmidt, *Precision glass molding of high-resolution diffractive optical elements,* SPIE 9888, 98880U (2016).

[Prokopenko1998] S. A. Prokopenko, A. N. Palagushkin, A. L. Mikaelian, B. S. Kiselyov and V. A. Shkitin, *Computer simulation of 2D multiple-level phase beamsplitter fabrication errors,* Proc. SPIE 3348, 83–93 (1998).

[Saleh1991] B. E. A. Saleh and M. C. Teich, *Fundamentals of Photonics,* John Wiley & Sons, Inc., USA (1991).

[Sankur1995] H. Sankur, E. Motamedi, R. Hall, W.J. Gunning, and M. Khoshnevisan, *Fabrication of refractive microlens arrays,* Proc. SPIE 2383, 179 (1995).

[Shea2004] D. C. O'Shea, T. J. Suleski, A. D. Kathman, and D. W. Prather, *Diffractive Optics: Design, Fabrication, and Test,* SPIE Press (2004).

[Takahashi2005] M. Takahashi, K. Sugimoto, and R. Maeda, *Nanoimprint of Glass Materials with Glassy Carbon Molds Fabricated by Focused-Ion-Beam Etching,* Jpn. J. Appl. Phys. 44, 5600 (2005).

[Takahashi2007] M. Takahashi, Y. Murakoshi, R. Maeda, and K. Hasegawa, *Large area micro hot embossing of Pyrex glass with GC mold machined by dicing,* Microsyst. Technol. 13, 379–384 (2007).

[Wolz2015] M. Wolz, U. Blöcher, G. Dross, J. Schmitt, C. Bischoff, and U. Umhofer *Manufacture of refractive and diffractive beam-shaping elements in higher quantities using glass molding technology,* Proc. of SPIE Vol. 9343, 93431Z (2015).

[Wor2009] M. Worgull, *Hot Embossing: Theory and Technology of Microreplication,* Elsevier (2009).

[Voelz2011] D. Voelz, *Computational Fourier Optics* SPIE Press, Tutorial Texts in Optical Engineering Volume TT89, Washington (2011).

[Yan2009] J. Yan, T. Zhou, J. Masuda, and T. Kuriyagawa, *Modeling high-temperature glass molding process by coupling heat transfer and viscous deformation analysis,* Precision Engineering, 33(2), 150-159 (2009).

[Yan2009b] J. Yan, T. Oowada, T. Zhou, and T. Kuriyagawa *Precision machining of microstructures on electroless-plated NiP surface for molding glass components,* Journal of Materials Processing Technology, 4802-4808 (2009).

[Yasui2008] M. Yasui, Y. Sugiyama, M. Takahashi, S. Kaneko, J. Uegaki, Y. Hirabayashi, K. Sugimoto, and R. Maeda, *Fabrication of Glassy Carbon Molds Using Hydrogen Silsesquioxane Patterned by Electron Beam Lithography as O2 Dry Etching Mask,* Japanese Journal of Applied Physics 47 (6S), 5167 (2008).

[Yi2006] A. Y. Yi, Y. Chen, F. Klocke, G. Pongs, A. Demmer, D. Grewell and A. Benatar, *A high volume precision compression molding process of glass diffractive optics by use of a micromachined fused silica wafer mold and low Tg optical glass,* J. Micromech. Microeng. 16(10), 2000-2005 (2006).

[Youn2006] S. W. Youn, M. Takahashi, H. Goto, and R. Maeda, *Microstructuring of Glassy Carbon Mold for Glass Embossing – Comparison of Focused Ion Beam, Nano/femtosecond-Pulsed Laser and Mechanical Machining,* Microelectronic Engineering 83 (11–12), 2482–92 (2006).

[Youn2007] S. W. Youn, , M. Takahashi, H. Goto, and R. Maeda, *Fabrication of Micro-Mold for Glass Embossing Using Focused Ion Beam, Femto-Second Laser, Excimer Laser and Dicing Techniques,* Journal of Materials Processing Technology, 3rd International Conference on Advanced Forming and Die Manufacturing Technology, 187–188, 326–30 (2007).

[Youn2009] S. W. Youn, A. Ueno, M. Takahashi, and R. Maeda, *A process of glassy carbon etching without the micro masking effect for the fabrication of a mold with a high-quality surface* J. Micromechanics Microengineering 19, 125010 (2009).

[1] http://microcity.epfl.ch/cleanroom-en

[2] https://cmi.epfl.ch

[3] http://www.oharacorp.com/pdf/elbal42.pdf

[4] http://www.sico.at/assets/files/Datenblatt%20Sico%20Englisch.pdf

[5] http://refractiveindex.info

[6] https://www.nisshinbo-chem.co.jp/english/products/carbon/glass.html

[7] http://www.purdue.edu/discoverypark/birck/files/STS_AOE_DRIE_Trends.pdf

Karin Prater

Cirriculum Vitae

Rue de la Maladière 71b
2002 Neuchâtel - Suisse
☎ *+41 76 264 69 75*
✉ *karin.prater@epfl.ch*
École Polytechnique Fédérale de Lausanne (EPFL)

Education

2013–2017 **PhD Student**, *On the Limits of Precision Glass Molding for Diffractive Optical Elements*, École Polytechnique Fédérale de Lausanne (EPFL), EPFL STI IMT OPT, Neuchâtel, Switzerland.

2006–2012 **Diploma in Physics with specialization in Photonics**, *Thesis: Vortex Light Bullets*, Friedrich-Schiller-Universität, Jena, Germany.

Internships and Work Experience

2012–2013 **Research assistant**, *Institute of Applied Physics*, Friedrich-Schiller-Universität , Jena, Germany.

2005–2006 Work and Travel New Zealand

Research Interests

Photonics

- Diffractive Optical Elements,
- Rigorous Coupled Wave Analysis (RCWA),
- Nonlinear Fiber Optics

Microfabrication

- Dry Etching
- Thin Film Deposition
- Photolithography (including e-beam Lithography),

Skills and Competences

Computer skills: Matlab, LATEX, MS Office, Labview, Basic Knowledge in C/C++, Unix.

Languages

- German (Native)
- English (Fluent)
- French (Fluent)

Other Skills Work Experience in Industrial Project (CTI Project Switzerland):

- Costumer Orientation,
- Taking Initiative,
- Good Organization and Communication Skills.

Publications

Journal Publications

[1] K. Prater, J. Dukwen, To. Scharf, H. P. Herzig, S. Plöger, and A. Hermerschmidt, *Micro-structuring of glassy carbon for precision glass molding of binary diffractive optical elements,* Opt. Mater. Express 6, 3407-3416 (2016).

[2] To be submitted: *Potential of Precision Glass Molding for Diffractive Optical Elements.*

Conference Proceedings

[1] L. E. Hans,K. Prater, C. Kilchoer, T. Scharf, H. P. Herzig and A. Hermerschmidt, *Wafer-level micro-structuring of glassy carbon,* Photonics West, Proc. SPIE 8974, 89740Y (2014).

[2] K. Prater, J. Dukwen, T. Scharf, H. P. Herzig and A. Hermerschmidt, *Surface micro-structuring of glassy carbon for precision glass molding of diffractive optical elements,* SPIE Optics and Photonics, Proc. SPIE 9192, 919211 (2014).

[3] K. Prater, J. Dukwen, T. Scharf, H. P. Herzig, S. Plöger, A. Hermerschmidt, *Multilevel micro-structuring of glassy carbon for precision glass molding of diffractive optical elements,*Photonics West, Proc. SPIE 9374, 937410 (2015).

[4] K. Prater, J. Dukwen, T. Scharf, H. P. Herzig, S. Plöger, A. Hermerschmidt, *Multilevel micro-structuring of glassy carbon molds for precision glass molding,* Optical Systems Design, Proc. SPIE 9628, 96281M (2015).

[5] K. Prater, J. Dukwen, T. Scharf, H. P. Herzig, S. Plöger, and A. Hermerschmidt, *Precision glass molding of high-resolution diffractive optical elements,* Micro-Optics, Proc. SPIE 9888, 98880U (2016).

Conference Contributions

[1] K. Prater, J. Dukwen, T. Scharf, H. P. Herzig, S. Plöger, and A. Hermerschmidt, *Glassy Carbon Molds for Precision Glass Molding of Diffractive Optical elements,* EOSAM conference (2014).

[2] K. Prater, T. Scharf, H.P. Herzig, C. Rytka, P.M. Kristiansen, *Glassy Carbon Masters for Plastic Injection Molding,* Polymer Replication on Nanoscale PRN2016 (2016).

[3] T. Scharf, K. Prater, J. Dukwen, H. P. Herzig, S. Plöger, and A. Hermerschmidt, *Precision glass molding of high-resolution diffractive optical elements,* Micro and nano engineering MNE (2016).

Others

[1] O. Dambon, M. Doetz, J. Dukwen, *Entwicklung technologisch fundierter Richtlinien zur ressourcenschonenden Produktion der nächsten Generation von Glasoptiken,* Apprimus Verlag, Aachen, ISBN:978-3-86359-433-6 (2016).

[2] K. Prater, J. Dukwen, *Guide4Diffractive – Replikative Fertigung von diffraktiven Glasoptiken,* wt-online 11/12-2014, 763-768 (2014).

References

I. Prof. Hans Peter Herzig
EPFL STI IMT OPT
Rue de la Maladière 71b, CP 526
CH-2002 Neuchâtel 2
Phone +41 21 69 54270, +41 21 69 54330

II. Dr. Toralf Scharf
EPFL STI IMT NAM
ELG 237
CH-1015 Lausanne
Phone +41 21 69 54286

III. Dr. Falk Eilenberger
Fraunhofer-Institut IOF
Albert-Einstein-Str. 7
07745 Jena, GERMANY
Phone +49 3641 807 207